Synthesis and characterization of bismuth doped strontium oxide powder and thin films

By

Mogahid Hassan Mohammed Abdelrehman

(B.Sc. Hons.)

A dissertation submitted in fulfilment of the requirements for the degree

MASTER OF SCIENCE

in the

Faculty of Natural and Agricultural Sciences

Department of Physics

at the

University of the Free State

Republic of South Africa

Promoter: Prof. H.C. Swart

Co-Promoter: Prof. R. E. Kroon

Co-Promoter: Dr. Abdelrhman Yousif Mohmmed Ahmed

Co-Promoter: Dr. Hassan Abdelhalim Abdallah Seed Ahmed

January 2019

Acknowledgements

With great pleasure, I would like to thank the Almighty Allah for everything that he has given to me, for his blessing and guidance to finish this work. I would also like to thank the following individuals:

- **Prof. H. C. Swart** (promoter) for always encouraging, supporting and guiding me throughout the study. The study could not have been a success without him. Prof, thanks for giving me the opportunity into the world of research and for addressing my shortcomings politely. Thank you a lot.
- **Prof. R. E. Kroon** (Co-promoter) who has supported me throughout my thesis with his dedication, patience and knowledge. I have learned a lot on the technical aspects of research from you.
- **Dr. Abdelrhman Yousif Mohmmed** (Co-promoter) whose encouragement, guidance and support from the beginning to the end, enabled me to develop an understanding of the subject.
- **Dr. Hassan Abdelhalim Abdallah Seed Ahmed** (Co-promoter) for his invaluable advices and contributions to this work.
- **Prof. E. Coetsee-Hugo** for assisting me with XPS measurement, **Dr. M. M. Duvenhage** for assisting with ToF-SIMS measurement, **Dr. Edward Lee** for assisting with SEM and EDS measurements, **Mr. Emad Hasabeldaim** for assisting with CL degradation measurement, **Mr. Lucas Erasmus** for his assistance in doing PLD thin films and **Mr. Nadir Azhari** for assisting with AFM measurement.
- **Prof. Valentin Craciun** for assistance in preparing some PLD samples with excimer lasers at the national institute for laser, plasma and radiation physics, Bucharest-Magurele, Romania.
- I thank all staff members of the Department of Physics (UFS) and postgraduate students for a good social environment and fruitful academic discussions.
- I would like to thank my colleague **Mr. Babiker Mohammed**, **Mr. Mohammed Musa** and **Dr. Ogugua Simon Nnalue**.

- The acknowledgement would be incomplete if I do not express my gratitude to the two secretaries of the Department of Physics, UFS, for providing me with help during this study, **Ms. Karen Cronje** and **Mrs. Yolandie Fick**.
- South African Research Chairs Initiative (SARChI) chair and the cluster program of the University of the Free State for financial support, and I am also greatly indebted to the African Laser Center (ALC) for financial support.
- To my lovely family and all my friends: Thank you very much for your valuable support and your words of encouragement in difficulties.

Dedicated to my lovely parents, Hassan Mohammed and Alsittia Mohammed for their endless love, encouragement and constant love have sustained me throughout my life.

To my brothers and sisters, for their support and encouragement

Abstract

The main aim of this project was to investigate the synthesis and characterization of bismuth-doped strontium oxide powder and thin films. Firstly the luminescent properties and stability under electron beam irradiation of the SrO:Bi^{3+} phosphor powder were investigated and secondly the luminescent properties of SrO:Bi^{3+} thin films prepared by different techniques were studied.

The luminescence from Bi^{3+} ions can be useful in obtaining blue to red emitting phosphors by using different hosts, when excited by ultraviolet (UV) light due to efficient conversion to longer wavelengths. The energy levels of Bi^{3+} ions are host dependent. Bi^{3+} is a low cost activator, which provide strong absorption of UV light and can be efficiently converted to longer wavelengths. These emissions are related to the $^3P_1 - {}^1S_0$ or $^1P_1 - {}^1S_0$ transitions of Bi^{3+} ions, which are strongly dependent on the host.

The alkali-earth oxide phosphors offer a potential low-cost alternative to lanthanide-based blue phosphors. Bi^{3+} doped strontium oxide (SrO:Bi) phosphor powders were synthesized by the sol-gel combustion method using metal nitrates as precursors and citric acid as fuel. A wide range of temperatures (800 - 1200 °C) and concentrations of Bi^{3+} (0.05 - 0.7 mol%) were used to determine the optimum sample annealing temperature and Bi^{3+} concentration. The optimum doping concentration, for a fixed annealing temperature of 1200 °C (2 h), was found to be 0.2 mol% and a further increase in the Bi^{3+}concentration resulted in concentration quenching. Samples of this concentration were annealed at various temperatures and the optimum annealing temperature was found to be 1100 °C (2 h). The X-ray diffraction patterns (XRD) corresponded with the well-known face-centered cubic structure of SrO after high-temperature annealing that ranged between 1100 °C up to 1200 °C. Below 1100 °C strontium hydroxide peaks were also present. Williamson-Hall plots showed that the crystallite size was in the range of ~180 nm. Diffuse reflectance measurements of the pure host material showed it was strongly reflecting (~100%) down to a wavelength of about 230 nm, but when doped with Bi^{3+} an absorption band at 275 nm was observed that increased with increasing Bi^{3+} concentration. Scanning electron

microscopy (SEM) revealed a cubic morphology and the grain size increased with annealing temperature.

Photoluminescence (PL) measurements indicated that the phosphor exhibited efficient blue emission around 445 nm under UV excitation, which also occurred for electron irradiation, but slightly shifted about 5 nm to a longer wavelength. PL results showed that the emission intensity did increase with an increase in the annealing temperature up to 1100 °C. The increased intensities were attributed to two factors. The first one is due to a combination of the decrease of the $Sr(OH)_2$, and the second one segregation/diffusion of the Bi^{3+} ions from the bulk to populate the surfaces of the particles with a consequent loss in Bi^{3+} due to volatile species as a result of the increased annealing temperature. The intensity increased up to 1100 °C due to a decrease in the hydroxyl concentration and thereafter at higher temperatures resulted in a Bi^{3+} deficiency from the sample's surface and therefore leading to a decrease in the dopant concentration.

Auger electron spectroscopy (AES) was employed to analyze the surface chemical composition of the powder after pumping to a vacuum pressure of 2.6×10^{-8} Torr and back-filling the vacuum system with O_2 to a pressure of 1.0×10^{-7} Torr. The presence of all major elements of SrO, namely Sr and O were confirmed, but Bi^{3+} was not observed due to its low concentration. Cl and C were also detected as contaminations on the surface. X-ray photoelectron spectroscopy (XPS) results for the $Sr_{1-x}O:Bi_{x=0.002}$ sample also indicated the presence of the major components Sr and O of this material and some contaminations on the surface. By simultaneous monitoring of the cathodoluminescence (CL) and AES peak-to-peak heights over time for 22 h, the CL degradation of the phosphor was investigated. The slight decrease of the CL intensity (less than 20%) was due to the removal of C from the surface due to the electron stimulated surface chemical reactions (ESSCRs) which took place during electron bombardment. During the ESSCR process, the electron beam dissociates the O_2 and other background species such as H_2O to atomic species which subsequently react with C to form volatile compounds (CO_X, CH_4, etc.). The CL intensity reduced slightly more and at a higher rate in the O_2 back-filled environment than in vacuum during the degradation studies, due to the reaction of O_2 with the adventitious C at a higher rate to form volatile compounds on the surface of the irradiated sample. The SrO was found

to be stable under electron irradiation. XPS results indicated surface contaminated elements were completely removed after degradation.

An important application for phosphors is to make thin films for devices such as plasma displays and light emitting diodes. $Sr_{1-x}O:Bi_{x=0.002}$ phosphor thin films were prepared by spin coating and pulsed laser deposition (PLD). Spin coating samples were obtained by sequentially depositing 10 layers at 3000 rpm for 30 s and then annealed at various substrate temperatures. The optimum annealing temperature was found to be 900 °C (2 h). For all thin films samples, XRD showed the thin film had a strong (111) preferential orientation on the cubic phase. The results imply that the crystallite size of the sol–gel-derived films increased slightly with the increasing annealing temperatures. The morphology of the samples was determined by SEM and atomic force microscopy (AFM). The main PL emission peak position of the thin films prepared by spin coating showed a shift to shorter wavelengths at 430 nm, if compared to the main PL peak position of the powder at 445 nm.

Thin films were prepared by PLD of $Sr_{1-x}O:Bi_{x=0.002}$ phosphor optimized for blue luminescence. The powder was pressed into a PLD target, which was annealed at 200 °C for 2 h in air to remove all adventitious water containing species. Thin films were then successfully fabricated by PLD in vacuum or an O_2 working atmosphere on Si (100) substrates. Films were deposited using different types of excimer lasers namely a KrF laser (248 nm) with energy 300 mJ/pulse and a ArF laser (193 nm) with energy 150 mJ/pulse with the constant substrate temperature at 300 °C and deposited at different substrate temperatures using a Nd:YAG laser (266 nm) with energy 33.3 mJ/pulse. The microstructures and PL of these films were found to be highly dependent on the substrate temperature. XRD of the thin films obtained with the different types of excimer lasers showed the thin films also had a strong (111) preferential orientation on the cubic phase. XRD of the films deposited using the Nd:YAG laser in O_2 showed that the crystallinity increased with an increase in the substrate temperature, changing from amorphous to a cubic structure. At the highest temperature of 500 °C, the 111 and 200 SrO peaks were almost the same height, as in the powder. However, for 350 °C and 200 °C, the 200 peak was much smaller, which suggests some preferential orientation for films prepared at lower substrate temperatures. All films deposited in vacuum were amorphous. All the SEM

images show a very rough thin film surface that comprises of rounded irregular particles of different sizes and shapes, which were not uniformly distributed and which do not seem to be highly dependent on the substrate temperature. AFM results showed that the surface roughness decreased as the substrate temperature increased. The optimum substrate temperatures for the maximum luminescence (both (PL) and (CL)) were 200 °C and 50 °C for deposition in O_2 and vacuum, respectively. The main PL emission peak position of all the PLD thin films showed a shift to shorter wavelengths at 427 nm, when compared to the powder (445 nm). The optical properties of the powder and thin films showed different results because the Bi^{3+} ion is very sensitive towards its environment. Time of flight secondary ion mass spectroscopy (ToF SIMS) depth profiles for the samples deposited in O_2 or vacuum at different substrate temperatures look similar, except for a slight thickness variation. The PLD fabrication technique is suggested to be the best technique to fabricate the SrO:Bi^{3+} phosphor thin films.

Keywords and acronyms

Keywords

Phosphor, powder, thin films, strontium oxide, bismuth, sol-gel combustion method, pulsed laser deposition, spin coating, annealing, photoluminescence and cathodoluminescence.

Acronyms

AES Auger electron spectroscopy

AFM Atomic force microscopy

APPH Auger peak-to-peak heights

CRT Cathode ray tube

CL Cathodoluminescence

EDS Energy dispersive spectroscopy

ESSCR Electron stimulated surface chemical reaction

FED Field emission display

FWHM Full width at half maximum

JCPDS Joint Committee on Powder Diffraction Standards

LCD Liquid crystal display

LED Light-emitting diode

PL Photoluminescence

PLD Pulsed laser deposition

PMT Photomultiplier tube

SEM Scanning electron microscopy

ToF-SIMS Time-of-flight secondary ion mass spectroscopy

UV-Vis Ultraviolet-visible

XPS X-ray photoelectron spectroscopy

XRD X-ray diffraction

Table of Contents

Acknowledgements ..... **ii**

Abstract ..... **....v**

Keywords and acronyms ..... **ix**

List of figures ..... **xvi**

List of Tables ..... **xxii**

1: Introduction

1.1 General overview **1**

1.2 Motivation ..... Error! Bookmark not defined.

1.3 Research aims **3**

1.4 Thesis layout **4**

1.5 References **5**

2: Background information

2.1 Background of Phosphors **6**

2.2 Classification of phosphors **7**

2.3 Types of light emission **8**

2.3.1 Incandescence **8**

2.3.2 Luminescence **9**

2.3.2.1 Fluorescence **10**

2.3.2.2 Phosphorescence **10**

2.3.2.3 Photoluminescence **11**

2.3.2.4 Cathodoluminescence **11**

2.3.2.5 Other types of luminescence **12**

2.4 Applications of phosphors **12**

2.4.1 Light emitting diodes **13**

2.4.1.1 LEDs efficiency **14**

2.4.1.2 LEDs Applications **15**

2.4.1.3 Advantages of using LEDs **16**

2.4.1.4 Disadvantages of using LEDs **16**

2.4.2 Field emission displays (FEDs) **17**

2.4.2.1 Advantages and disadvantesges of using FEDs **18**

2.5 SrO host **19**

2.6 Bismuth **22**

2.7 References **24**

3: Synthesis Techniques

3.1 Combustion synthesis (CS) **29**

3.1.1 Types of combustion synthesis **30**

3.1.2 Sol-gel combustion technique **30**

3.1.2.1 The principle for sol-gel combustion **31**

3.1.2.2 Advantages of the Sol-gel combustion process **33**

3.1.2.3 Limitations of the Sol-gel combustion process **34**

3.2 Sol-gel process for thin film deposition **35**

3.3 Spin coating technique **37**

3.4 Pulsed laser deposition (PLD) technique **39**

3.4.1 The growth of thin films by PLD **40**

3.4.2 Advantages and disadvantages of PLD **44**

3.5 References **46**

4: Characterization techniques

4.1 Introduction **49**

4.2 X-ray diffraction (XRD) **50**

4.2.1 Bragg's law of diffraction **52**

4.3 Scanning Electron Microscopy (SEM) **54**

4.4 Energy dispersive X-rays spectroscopy **56**

4.5 UV-Vis spectroscopy **58**

4.5.1 Absorption measurements **57**

4.5.2 Determination of the energy band gap using reflection measurements **59**

4.6 Photoluminescence spectroscopy **61**

4.7 Cathodoluminescence spectroscopy (CL) **64**

4.8 Auger electron spectroscopy (AES) system **66**

4.9 X-ray photoelectron spectroscopy (XPS) **68**

4.10 Atomic Force Microscopy (AFM) **71**

4.11 Time-of-Flight Secondary Ion Mass Spectrometry (ToF-SIMS) **73**

4.12 References **76**

5: Luminescence properties of Bi doped SrO powder

5.1 Introduction **80**

5.2 Sample preparation **82**

5.3 Characterization **82**

5.4 Results and discussion **83**

5.4.1 Structure and morphology **83**

5.4.2 Diffuse reflection spectra and band gap calculations **87**

5.4.3 Luminescence properties **88**

5.4.3.1 Photoluminescence properties **88**

5.4.3.2 Cathodoluminescence properties **94**

5.5 Conclusion **95**

5.6 References **96**

6: Surface analysis and cathodoluminescence degradation of Bi doped SrO powder

6.1 Introduction **99**

6.2 Sample preparation **100**

6.3 Characterization **101**

6.4 Results and discussion **101**

6.4.1 Structure and morphology **101**

6.4.2 Luminescence properties **103**

6.4.3 Surface analysis and CL degradation **107**

6.5 Conclusion **113**

6.6 References **113**

7: Comparison of SrO:Bi phosphor thin films fabricated by spin coating and pulsed laser deposition

7.1 Introduction **117**

7.2 Experimental procedure **119**

7.2.1 Sample preparation **119**

7.2.2 Characterization technique **120**

7.3 Results and discussion **121**

7.3.1 XRD Analysis **121**

7.3.2 Photoluminescence (PL) study **123**

7.3.3 Surface morphology **127**

7.3.3.1 Scanning electron microscopy **127**

7.3.3.2 Atomic force microscope **128**

7.4 Conclusion..... **133**

7.5 References **133**

8: Effect of background atmosphere and substrate temperature on SrO:Bi thin films produced using pulsed laser deposition

8.1 Introduction **137**

8.2 Experimental **138**

8.3 Results and discussion..... **140**

8.3.1 Structural analysis **140**

8.3.2 Elemental composition analysis (EDS)..... **142**

8.3.3 Surface morphology **144**

8.3.3.1 Scanning electron microscopy **144**

8.3.3.2 Atomic force microscopy..... **146**

8.3.4 Photoluminescence (PL) properties **149**

8.3.5 Cathodoluminescence properties..... **152**

8.3.6 ToF-SIMS analysis..... **155**

8.4 Conclusion..... **161**

8.5 References **161**

Chapter 9: Conclusion

9.1 Summary **166**

9.2 Suggestions for future work **169**

9.3 Research presentations and publications..... **170**

9.3.1 Presentation at conferences/Workshops..... **170**

9.3.2 List of publications include **170**

List of figures

Figure 2.1: Representation of the luminescence process: (a) activator (A) in a host (H) and (b) sensitizer (S) and activator (A) in a host (H)…….....**8**

Figure 2.2: Different types of incandescence (a) the sun, (b) bar of iron that glows red under radiant heat from gas flames and (c) an ordinary bulb **9**

Figure 2.3: Jablonski energy diagram for absorption, fluorescence and phosphorescence **10**

Figure 2.4: The basic process of photon generation **14**

Figure 2.5: The basic components of a FED.....**18**

Figure 2.5: FED packaging **18**

Figure 2.7: The crystal structure of SrO similar to NaCl or rock salt type with space group Fm3m (in Hermann-Mauguin notation) **20**

Figure 3.1: Schematic diagram of the preparation of nanocrystalline SrO powder by sol-gel combustion process.....**32**

Figure 3.2: The equipment used for the combustion method: (a) stirring, (b) preheated to 250 °C for 30 min, (c) dark brown powder, (d) annealed at various temperatures, (e) fine white powder.....**33**

Figure 3.3: Steps involve in the processing routes to obtain coatings by sol-gel method.....**35**

Figure 3.4: Schematic diagrams to synthesize the $Sr_{1-x}O:Bi_{x=0.002\%}$ phosphor by using the sol-gel method and to prepare the thin films by spin-coating.....**36**

Figure 3.5: Stages of the spin coating technique.....**38**

Figure 3.6: Spin coating SPEN 150 from Semiconductor Production System at the Department of Physics of the University of the Free State.....**39**

Figure 3.7: A schematic of the laser ablation process and its stages up to thin film formation.....**41**

Figure 3.8: Difference between long (nanosecond) pulse and femtosecond pulse laser ablation.....**43**

Figure 3.9: Schematic diagram of the PLD system.....**44**

Figure 3.10: PLD system at the Department of Physics of the University of the Free State.....**46**

Figure 4.1: Schematic diagram of an X-ray diffractometer.....**50**

Figure 4.2: The characteristic X-ray emission obtained from a copper (Cu) target with a nickel (Ni) filter.....**51**

Figure 4.3: Schematic diagram of Bragg diffraction from a set of arrangements atoms.....**52**

Figure 4.4: Bruker D8 Advance X-ray diffractometer at the Department of Physics, University of the Free State.....**54**

Figure 4.5: Schematic presentation of the field emission scanning electron microscopy.....**55**

Figure 4.6: JEOL JSM-7800F system a typical SEM instrument, showing the electron column, sample chamber, EDS detector, electronics console, and visual display monitors, University of the Free State.....**56**

Figure 4.7: Schematic of emitted characteristic X-rays in an atom.....**57**

Figure 4.8: Incident and transmitted light.....**58**

Figure 4.9: Schematic of a dual-beam UV-Visible spectrophotometer.....**59**

Figure 4.10: The Lambda 950 UV-Vis (Perkin Elmer Lamb) spectrophotometer at the Department of Physics, University of the Free State.....**60**

Figure 4.11: Simplified schematic energy diagram showing the excitation and emission involved in the photoluminescence process.....**61**

Figure 4.12: Schematic diagram of PL spectrometer.....**62**

Figure 4.13: Schematic diagram of the PL system with a He-Cd laser with a fixed wavelength of 325 nm.....**63**

Figure 4.14: Varian Cary-Eclipse fluorescent spectroscopy at the Department of Physics, University of the Free State.....**63**

Figure 4.15: A typical PL laser system with an excitation wavelength of 325 nm at the Department of Physics, University of the Free State.....**64**

Figure 4.16: The different beam current as a function moving distance of the edge of the Faraday cup.....**66**

Figure 4.17: PHI, model 549, AES unit at the Department of Physics, University of the Free State.....**67**

Figure 4.18: Schematic diagram of the XPS technique.....**69**

Figure 4.19: PHI 5000 Versaprobe II Scanning XPS Microprobe.....**71**

Figure 4.20: Schematic diagram of the setup of an AFM system.....**72**

Figure 4.21: The Shimadzu SPM-9600 AFM system at the Department of Physics, University of the Free State.....**73**

Figure 4.22: Schematic diagram of the principle of mass separation.....**74**

Figure 4.23: Schematic diagram for the ToF-SIMS technique.....**76**

Figure 4.24: A photograph of the ToF-SIMS5 at the Department of Physics, University of the Free State.....**76**

Figure 5.1: (a) XRD patterns of $Sr_{1-x}O:Bi_x$ for different concentration of Bi annealed at 1200 °C. (b) XRD patterns of $Sr_{1-x}O:Bi_x$ phosphor powder after different annealing temperatures for Bi concentration fixed at 0.2 mol%.....**84**

Figure 5.2: The unit cell of SrO.....**85**

Figure 5.3: Williamson–Hall plots.....**86**

Figure 5.4: SEM images for the $Sr_{1-x}O:Bi_{x=0.002}$ samples annealed at (a) 1100 °C and (b) 1200 °C.....**87**

Figure 5.5: Diffuse reflection spectra of $Sr_{1-x}O:Bi_x$ samples annealed at 1200 °C. The inset shows a Tauc plot to determine the band gap.....**88**

Figure 5.6: PL excitation and emission spectra of $Sr_{1-x}O:Bi_x$ phosphor for different concentrations of Bi^{3+} annealed at 1200 °C. The inset shows the maximum PL intensity (at 445 nm) as a function of Bi^{3+} concentration. **89**

Figure 5.7: (a) Schematic diagram of the energy levels of the Bi^{3+} ion, and (b) Gaussian fitting of the emission band of $Sr_{1-x}O:Bi_{x=0.002}$.....**91**

Figure 5.8: PL excitation and emission spectra of $Sr_{1-x}O:Bi_{x=0.002}$ after different annealing temperatures. The inset shows the maximum PL intensity of 445 nm as a function of annealing temperature.....**93**

Figure 5.9: The CL emission intensities versus wavelength for the $Sr_{1-x}O:Bi_{x=0.002}$ obtained after annealing at the different temperatures. The inset shows the maximum CL intensity as a function of annealing temperature.....**94**

Figure 6.1: (a) Shows the XRD pattern of $Sr_{1-x}O:Bi_{x=0.002}$ powder annealed at 1100 °C and standard JCPDS data file no. 06-0520, (b) the unit cell of SrO and (c) represent the SEM micrograph of the $Sr_{1-x}O:Bi_{x=0.002}$ powder annealed at 1100 °C.....**102**

Figure 6.2: (a) Emission spectra of $Sr_{1-x}O:Bi_{x=0.002}$ annealedat 1100 °C obtained by using the xenon lamp at 360 nm and electron beams with beam voltages of 2.5 keV and 5 keV. (b) PL excitation and emission by using 260 nm and 360 nm and (c) CIE coordinates for emission.....**105**

Figure 6.3: AES spectra of the $Sr_{1-x}O:Bi_{x=0.002}$ powder before and after electron-beam bombardment in (a) a vacuum base pressure of 2.6×10^{-8} Torr, and (b) backfilled with oxygen up to a pressure of 1.0×10^{-7} Torr.....**106**

Figure 6.4: APPHs as a function of electron beam dose in (a) a vacuum base pressure of 2.6×10^{-8} Torr, and (b) backfilled with oxygen up to a pressure of 3.5×10^{-7} Torr.....**107**

Figure 6.5: CL Intensity as a function of electron dose exposure at (a) a vacuum base pressure of 2.6×10^{-8} Torr, and (b) backfilled with oxygen until a pressure of 3.5×10^{-7} Torr. The insets represent the CL spectra before and after degradation.....**108**

Figure 6.6: XPS survey spectra of SrO:Bi before sputtering and after 120 s of Ar^+ sputtering (a) un degradation and (b) after degradation.....**109**

Figure 6.7: Deconvolution of the Sr^{2+} XPS peak of $Sr_{1-x}O:Bi_{x=0.002}$ (a) and (b) un-degradated, (c) and (d) degraded $Sr_{1-x}O:Bi_{x=0.002}$ as indicated before and after sputtering.....**110**

Figure 6.8: Deconvolution of O 1s XPS peak of $Sr_{1-x}O:Bi_{x=0.002}$ (a) and (b) un-degradation, (c) and (d) degraded $Sr_{1-x}O:Bi_{x=0.002}$ as indicated before and after sputtering.....**111**

Figure 7.1: XRD patterns of the SrO spin coating thin films with different number of layers annealed at 500 °C.....**119**

Figure 7.2: XRD patterns of the SrO:Bi powder and Si substrate with (a) spin coating thin films annealed at different annealing temperatures (2, 3, 4 and 5) of 800 °C, 900 °C , 1000 °C and 1100 °C respectively, and (b) PLD thin films obtained with different types of lasers (2,3,4 and 5); (2,3) KrF 248 nm and (4, 5) ArF 193 nm laser deposited in different O_2 pressures of (2,4) 1×10^{-3} and (3,5) 3×10^{-3} mbar, respectively.....**120**

Figure 7.3: PL spectra of $Sr_{1-x}O:Bi_{x=0.002}$ measured with a 325 nm He-Cd laser with slit widths 24 and 2000 nm, and PMT voltages 1000 and 1400 V, for powder and thin films respectively: (a) powder (b) PLD thin films with different types of lasers, (1, 2) KrF 248 nm and (3, 4) ArF 193 nm laser deposited in different O_2 pressures of (1, 3) 1×10^{-3} and (2, 4) 3×10^{-3} mbar, respectively. (c) spin coating thin films at different annealing temperatures and (d) the PL spin coating thin films intensity as a function of annealing temperature.....**122**

Figure 7.4: CIE coordinates for emission from the $Sr_{1-x}O:Bi_{x=0.002}$ powder annealed at 1100 °C, spin coating thin film annealed at 900 °C and PLD thin film obtained with the KrF 248 nm laser in 3×10^{-3} mBar O_2.....**125**

Figure 7.5: SEM images for the $Sr_{1-x}O:Bi_{x=0.002}$ thin films (a) by spin coating at 900 °C, b, c, d and e PLD thin films deposited in different O_2 pressure by different excimer laser energies ((b and c) KrF 248 nm and (d and e) ArF 193 nm) laser with O_2 pressures of 1×10^{-3} and 3×10^{-3} mbar, respectively **127**

Figure 7.6: 2D and 3D AFM images micrographs of the the $Sr_{1-x}O:Bi_{x=0.002}$ thin films

fabricated by (a) spin coating at 900 °C, (b), (c), (d) and (e) the PLD thin films deposited in different O_2 pressure by different excimer laser energies ((b and c) KrF 248 nm and (d and e) ArF 193 nm) laser with O_2 pressures of 1×10^{-3} and 3×10^{-3} mbar, respectively.....**131**

Figure 8.1: XRD patterns of the $Sr_{1-x}O:Bi_{x=0.002}$ powder and thin films with substrate temperatures of 50 °C, 100 °C, 200 °C, 350 °C and 500 °C, respectively, (a) in O_2 (b) in vacuum, with XRD pattern for SrO powder and XRD pattern database pattern for SrO.....**140**

Figure 8.2: (Color online) EDS spectra of the $Sr_{1-x}O:Bi_{x=0.002}$ films deposited at the different substrate temperatures of 50 °C, 100 °C, 200 °C, 350 °C and 500 °C, respectively, (a - e) in O_2 (f - j) in a vacuum.....**141**

Figure 8.3: SEM images of the $Sr_{1-x}O:Bi_{x=0.002}$ films deposited at the different substrate temperatures of 50 °C, 100 °C, 200 °C, 350 °C and 500 °C, respectively, (a - e) in O_2 (f - j) in a vacuum.....**143**

Figure 8.4: 3D AFM images of the $Sr_{1-x}O:Bi_{x=0.002}$ films deposited at the different substrate temperatures of 50 °C, 100 °C, 200 °C, 350 °C and 500 °C, respectively, (a - e) in O_2 (f - j) in a vacuum.....**146**

Figure 8.5: PL spectra of the $Sr_{1-x}O:Bi_{x=0.002}$ measured with a 325 nm He-Cd laser (a) powder (b and c) thin films deposited at the different substrate temperatures of 50 °C, 100 °C, 200 °C, 350 °C and 500 °C, in O_2 and a vacuum, respectively.....**149**

Figure 8.6: CL spectra of the $Sr_{1-x}O:Bi_{x=0.002}$ (a) powder (b and c) thin films deposited at the different substrate temperatures of 50 °C, 100 °C, 200 °C, 350 °C and 500 °C, in O_2 and a vacuum, respectively.....**151**

Figure 8.7: The calculated chromaticity coordinates for the $Sr_{1-x}O:Bi_{x=0.002}$ as powder and thin films with substrate temperatures of (a) 200 °C in O_2 and (b) 50 °C in vacuum, on the basis of their PL and CL data.....**152**

Figure 8.8: ToF-SIMS mass spectra of SrO:Bi phosphors for negative ions analysis of thin films with substrate temperatures of (a) 200 °C in O_2 and (b) 50 °C in vacuum.**154**

Figure 8.9: The negative mode ToF SIMS depth profiles of the $Sr_{1-x}O:Bi_{x=0.002}$ films deposited at the different substrate temperatures of 50 °C, 100 °C, 200 °C, 350 °C and 500 °C, respectively, (a - e) in O_2 (f - j) in a vacuum.....**156**

Figure 8.10: The negative mode Tof-SIMS depth profiles of the $Sr_{1-x}O:Bi_{x=0.002}$ films deposited at substrate temereture of 50 °C in O_2 with a different selected measured peak area of O^- **157**

Figure 8.11: ToF-SIMS 3D images for the overlay of the $Sr_{1-x}O:Bi_{x=0.002}$ films (Si^- (blue), SrO^- (green) and O^- (red)) deposited at the different substrate temperatures of 50 °C, 100 °C, 200 °C, 350 °C and 500 °C, respectively, (a - e) in O_2 (f - j) in a vacuum.....**158**

List of Tables

Table 2.1. Materials that emit different colors when doped with Bi^{3+}.....**23**

Table 3.1. Some materials prepared by sol-gel combustion and their application.....**31**

Table 3.2. Performance parameters: excimer versus Nd:YAG laser systems Source.....**42**

Table 6.1. The emission peak position, FWHM and CIE coordinates (X, Y) of $Sr_{1-x}O:Bi_{x=0.002}$.....**104**

Table 7.1. The CIE coordinates (X, Y) of $Sr_{1-x}O:Bi_{x=0.002}$ powder and thin films.....**124**

Table 7.2. Roughness parameters of the spin coating and PLD thin films.....**128**

Table 8.1. Roughness parameters of PLD thin films at the different substrate temperatures and atmospheres.....**145**

Table 8.2. The CIE coordinates (X, Y) of $Sr_{1-x}O:Bi_{x=0.002}$ powder and thin films.....**152**

Table 8.3. Atomic/molecular ions and their atomic mass units.....**153**

Chapter 1: Introduction

This chapter serves as the introductory chapter on a research study done on the synthesis and characterization of bismuth-doped strontium oxide powder and thin films. It also includes the motivation for the research aims and provides the layout of the thesis.

1.1 General overview

The research efforts to fabricate effective new phosphor materials for applications in next-generation displays and solid-state lighting have been the subject of intense research during the last decades. Recently, the study of the luminescence behavior of the oxide materials has attracted considerable attention owing to their unique optical, thermal, electrical and mechanical properties which can be exploited to fabricate promising phosphor materials [1]. In particular, the bismuth (Bi) ion doped simple oxide hosts is the subject of intensive investigations as materials suitable in optical applications [2]. The luminescence properties of Bi ion doped oxide hosts exhibit extraordinary luminescent properties due to the fact that Bi ions have a large number of valence states, with strong interaction with the surrounding host lattice [3]. The diversity in the Bi valence state (e.g. +3, +2, +1, 0, -2, etc), in addition to the easy conversion into each other or existence of many Bi valence states in a single component can be used as a candidate for different applications [3]. Therefore, there are many possibilities to study the optical properties of the Bi ions in simple oxide hosts. SrO phosphor is an important basic chemical raw material. Many properties of doped SrO have been demonstrated in the fields of optical, display and magnetic materials [4]. Although consumption requirements fluctuate from year to year, the overall consumption of strontium compounds and metals appears to be increasing [5]. In recent years, many researchers have been investigating the luminescence properties of SrO activated with Bi^{3+} ions, which was found to be a good alternative to the

rare earth ion doping, because it has good luminescence properties and is cheap compared with the rare earth ions [6].

The thin film is a layer of material ranging from nanometer fractions to several micrometers in thickness. Thin films luminescence is of great interest from both the scientific and technological point of view, where the research interest on it has been reflected by the rapid developments in a variety of thin films applications such as devices, including flat-panel displays, light sources, solar cells and integrated optics systems [7]. The luminescent material phosphors deposited in the form of thin films have several important advantages over powder phosphors of the same composition due to the higher lateral resolution from smaller grains, their good luminescence characteristics, better thermal stability and better adhesion to the substrate [8]. Thin films can be prepared by several deposition techniques such as spin coating, evaporation, the sputtering method, electron beam deposition, spray pyrolysis, chemical vapor deposition, anodic growth and pulsed laser deposition (PLD) [9].

In this research study, synthesis and characterization of SrO:Bi powder and thin films have been investigated for possible use in the efficient application in the fields of lighting and displays.

1.2 Motivation

The spectroscopic properties of Bi ions have been attracting much attention and become a hot research topic in the field of phosphor materials in which they are used either as sensitizer or activator ions. The investigations on the optical properties of Bi were done for both application and fundamental points of view [1]. Many interesting results have been reported. Yousif et al. [2] reported the elimination of the blue emission from the Bi ion's spectra by incorporation of La^{3+} ions in the Y_2O_3 lattice. An unusual behavior of Bi during heat treatment has been reported by many researchers. Xu et al. [10] reported the reviving behavior of the Bi-doped $MgO–Al_2O_3–GeO_2$ glasses, where the reversible reaction of Bi from a higher to a lower and back to a higher oxidation state is possible during heat treatment. The reviving behavior of the Bi in their case was responsible for the unusual luminescence properties of this component. Yousif et al. showed the post heat treatment

on CaO:Bi led to the enrichment of the Ca^{2+} site with multiple Bi centers [2]. These centers were responsible for the change in the ultra-broadband cathodoluminescence (CL) emission as a function of different electron beam currents/beam voltages. Yousif et al. [11] reported that the ultraviolet emission of Bi^{3+} can be shifted to longer wavelengths by adding more Ga^{3+} in the $Y_3Al_{5-X}Ga_xO_{12}$ matrix. Bi^{3+} activated alkaline-earth oxide SrO have many applications in different phosphor fields, such as light-emitting diodes and display devices. Oxides generally exhibit relatively high phonon energies larger than 500 cm^{-1} due to the stretching vibration of the host lattice, but SrO has, as experimentally determined, a phonon energy of about 30 meV (230 cm^{-1}) [6], suggesting that it may have an advantage compared to many other oxide hosts due to its smaller phonon energy. SrO:Bi^{3+},Eu^{3+} is a good candidate for light-emitting diodes [5]. SrO is a ceramic material with a wide range of applications: it is expected to be useful both in electronic devices and as a phosphor host. In recent years, there has been a growing focus on research in light emitting diodes (LEDs) because of their long operation lifetime, energy-saving features and high material stability. To see the possibility of using the phosphor in applications in fields of lighting and displays, especially for the use in a field emission display (FED), the stability of the luminescence under electron beam irradiation of the phosphor must be determined and for the use in photonic application it must be stable under photon irradiation as well.

For the systematic investigation, we firstly investigated the luminescent properties of the Bi^{3+} ion doped SrO as a powder synthesized by sol-gel combustion method and as thin films. In order to enhance the light output from the Bi^{3+} ions, we need a systematic investigation of the crystal structure and luminescent properties of our phosphor material. Different doping concentrations, annealing temperatures, then thin film fabrication techniques and different growth parameters were therefore investigated.

1.3 Research aims

The major aim of the research project is to study the synthesis and characterization of SrO:Bi powder and thin films. This aim consisted of different aims which were addressed below:

1- Prepare and characterize the SrO:Bi^{3+} phosphor powder by using the sol-gel combustion method.
2- Study the luminescent properties and investigate the effect of heat treatment of the SrO:Bi^{3+} phosphor powder.
3- Study the stability of the SrO:Bi^{3+} phosphor powder under electron beam irradiation.
4- Prepare SrO:Bi^{3+} thin films by the sol-gel spin coating technique.
5- Prepare SrO:Bi^{3+} thin films by the PLD technique.
6- Characterize the thin films prepared.

1.4 Thesis layout

This thesis is divided into nine chapters. Chapter 1 includes a general introduction to the work and aims of the study. Chapter 2 contains a brief background of phosphor materials, luminescence and its processes, the applications of the phosphors that were fabricated in this study, then a description of the phosphor materials as hosts and activators is presented. The alkaline-earth oxides as host with s^2 outer shell ions as luminescent centers are mentioned and special attention is given to the Bi^{3+} ions doped SrO. Chapter 3 gives a brief theoretical description of the experimental techniques that were used to synthesize the phosphors. Chapter 4 gives a brief theoretical description of the characterization techniques of the phosphors. In chapter 5 the luminescent properties from Bi doped SrO powders prepared by the sol-gel combustion method are reported. In chapter 6 the luminescence properties of the $Sr_{1-x}O:Bi_{x=0.002}$ were investigated by the different excitation sources. Also, the CL degradation of the phosphor was investigated. Chapter 7 gives the comparison and analysis of SrO:Bi phosphor thin films fabricated by the spin coating and PLD techniques. Chapter 8 presents the effect of the background atmosphere and different substrate temperature on SrO:Bi PLD thin films. Finally, a summary and suggestions for future work are given in chapter 9 and contains the publications and conference participation.

1.5 References

[1] G. Blasse and B. C. Grabmaier, Luminescent Materials, Springer, Berlin, Germany, 1994. ISBN: 978-3-540-58019-5.

[2] A. Yousif and H.C. Swart, La^{3+} eliminate the blue component from the emission of $Y_2O_3:Bi^{3+}$. *Mater. Lett.*. **171,** (2016) 171–173. DOI: 10.1016/j.matlet.2016.02.081.

[3] A. Yousif, R. M. Jafer, S. Som, M. M. Duvenhage, E. Coetsee and H. C. Swart, Ultra-broadband luminescent from a Bi-doped CaO matrix. *RSC Adv*. **5(67)** (2015) 54115–54122. DOI: 10.1039/c5ra09246a.

[4] Fu. Jipeng, Su. Zhang, Ma. Tengfei, Jia. Yonglei, P. Ran, J. Lihong, Li. Da, Li. Haifeng, S. Wenzhi and Li. Chengyu, A convenient and efficient synthesis method to improve the emission intensity of rare earth ion doped phosphors: the synthesis and luminescent properties of novel SrO:Ce^{3+} phosphor. *RSC Adv.* **5,** (2015) 93951–93956. DOI: 10.1039/c5ra15089b.

[5] Renping Cao, Fangteng Zhang, Chenxing Liao and Jianrong Qiu, Yellow-to-orange emission from Bi^{2+}-doped RF_2 (R = Ca and Sr) phosphors, *Opt. Express.* **21(13)** (2013) 15728-15733. DOI:10.1364/oe.21.015728.

[6] Fu. Jipeng, R. Pang, L. Jiang, Y. Jia, W. Sun, S. Zhang and C. Li, A novel dichromic self-referencing optical probe SrO:Bi^{3+},Eu^{3+} for temperature spatially and temporally imaging, *Dalton Trans.* **45(34)** (2016) 13317–13323. DOI: 10.1039/c6dt01552b.

[7] Y. Zhang, J. Hao.Metal-ion doped luminescent thin films for optoelectronic applications. *J. Mater. Chem.* **C1(36)** (2013) 5607. DOI:10.1039/c3tc31024h.

[8] J.S. Bae, K.S. Shim, B.K. Moon, B.C. Choi, J.H. Jeong, S. Yi and J.H. Kim. Photoluminescence characteristics of $ZnGa_2O_{4-x}M_x:Mn^{2+}$ (M=S, Se) thin film phosphors grown by pulsed laser ablation. *Thin Solid Films*. **479(1-2)** (2005) 238–244. DOI: 10.1016/j.tsf.2004.11.18.

[9] M.R. Byeon, E.H. Chung, J.P. Kim, T.E. Hong, J.S. Jin, E.D. Jeong, J.S. Bae, Y.D. Kim, S. Park, W.T. Oh, Y.S. Huh, S.J. Chang, S.B. Lee, I.H. Jung and J. Hwang. The effects for the deposition temperature onto the structural, compositional and optical properties of pulsed laser ablated Cu_2ZnSnS_4 thin films grown on soda lime glass substrates. *Thin Solid Films*. **546**, (2013) 387-392. DOI: 10.1016/j.tsf.2013.05.032.

[10] B. Xu, S. Zhou, M. Guan, D. Tan, Y. Teng, J. Zhou, Z. Ma, Z. Hong and J. Qiu. Unusual luminescence quenching and reviving behavior of Bi-doped germanate glasses. *Optics Express*, **19(23)** (2011) 23436. DOI: 10.1364/oe.19.023436.

[11] A. Yousif, Vinod Kumar, H.A.A. Seed Ahmed, S. Som, L.L. Noto, O.M. Ntwaeaborwa, H.C. Swart. Effect of Ga^{3+} Doping on the Photoluminescence Properties of $Y_3Al_{5-x}Ga_xO_{12}:Bi^{3+}$ Phosphor. *ECS Journal of Solid State Science and Technology*, **3(11)** (2014) R222–R227. DOI: 10.1149/2.0021412jss.

Chapter 2: Background information

This chapter presents a brief background of phosphor materials, luminescence and its processes and the applications of the phosphors that were fabricated in this study. Then a description of the phosphor materials as hosts and activators is presented. The alkaline-earth oxides as hosts for ions with s^2 outer shell as luminescent centers are mentioned and special attention is given to Bi^{3+} doped SrO.

2.1 Background of Phosphors

Luminescent materials, also known as phosphors, can be defined as any material that will emit light (red, green and blue) when an external electromagnetic radiation excitation source is applied (photons, heat etc.). The phosphors consist of one chemical compound referred to as a host lattice, and one or more activators (dopants), mostly rare earth ions or transition metals, in amounts from parts per million to a few mole percent. These impurities are introduced intentionally in a host lattice to serve as luminescent (light emitting) centers. The phosphor host or matrix is usually an insulator or a semiconductor [1]. In general, the host needs to be transparent to the radiation source with which it is excited, and the characteristic luminescence properties are obtained either directly from the host or activators introduced intentionally to the host material. If more than one activator is used during excitation, they are called co-activators or co-dopants, where one activator (sensitizer) tends to absorb energy from the primary excitation and transfers it to the other activator to enhance its luminescent intensity [2]. Phosphors may be either in the powder or a thin film form with specific requirements on particle size distribution and morphology [2].

2.2 Classification of phosphors

In general, the host material is regarded as the "home" of optically active ions and it should exhibit good optical, mechanical and thermal properties [4]. It can be classified into several main types based on the anions, e.g. simple oxides and sulfides. Examples of oxide phosphors are zinc oxide (ZnO), strontium oxide (SrO), yttrium oxide Y_2O_3 or cadmium oxide (CdO), while sulfides are zinc sulfide (ZnS), lead sulfide (PbS) and cadmium sulfide (CdS). There are many other types of more complex hosts such as aluminates, fluorides, silicates etc. Host materials can also be classified into three groups based on crystallinity: crystals, amorphous materials and hosts that incorporate the properties of both (glass ceramics) [5]. Host material generally requires close lattice matches, and the valence of the host cation should be the same or similar to those of the dopant ions in order to prevent the formation of crystal defects and lattice stresses arising from doping [4]. Usually, most of these phosphors are doped with rare-earth ions such as europium (Eu^{3+}), praseodymium (Pr^{3+}), terbium (Tb^{3+}), and cerium (Ce^{3+}) or with transition metals ions such as manganese (Mn^{2+}) or chromium (Cr^{2+}) or post-transition metals such as bismuth (Bi^{3+}) and lead (Pb^{2+}), to tune the color of their emissions. The activator is a foreign ion or a structural defect that forms the heart of the phosphor material and it has a characteristic absorption and it also emits light when absorbing energy [6]. The luminescent impurities are incorporated intentionally into a host lattice with the optimal concentration. The appropriate luminescent center can be selected according to the emission color, ionic valence, atomic radius and the light output efficiency. As mentioned earlier it can be classified by many types of lighting centers in the inorganic phosphors, such as:

- lanthanide elements: (e.g. europium (Eu^{3+}), praseodymium (Pr^{3+})
- the ions with an s^2 outer shell (e.g. lead (Pb^{2+}) and bismuth (Bi^{3+})
- the transition metal ions (e.g. manganese (Mn^{2+}) and chromium (Cr^{3+}))
- the structural defects.

Figure 1 is a schematic diagram showing the role of activator and sensitizer in the luminescence process [3]. In figure 1 (a), light emission is a result of direct excitation of

the activator atom represented by A (the absorber) surrounded by the host lattice atoms, represented by H, while figure 1(b) shows light emission from A as a result of excitation of an energy transfer from the co-activator atom (the sensitizer) represented by S.

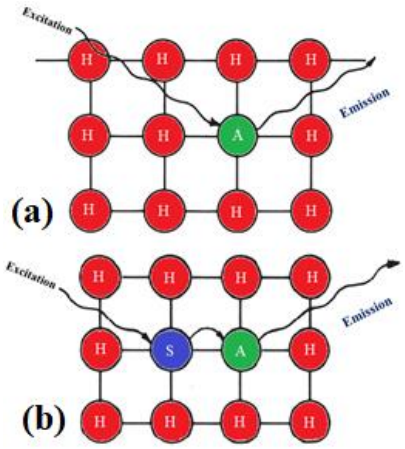

Figure 2.1: Representation of the luminescence process: (a) activator (A) in a host (H) and (b) sensitizer (S) and activator (A) in a host (H). (Reproduced from [3])

In addition, phosphors can be classified according to the method in which they emit light. For example, the emission of light can be caused by recombination of the charge carriers excited across the bandgap (not need to added doping) such as for ZnO where it is due to excitonic recombination, or the ionic transitions such as Y_2O_3: RE (RE = Eu^{3+}, Ce^{3+}, Tb^{3+}, etc) where the dopant is responsible for emission and can be classified as an ionic (dopant) transition phosphors because light emission in these phosphors is due to transitions taking place in the dopant [7].

2.3 Types of light emission

Light is a form of energy which is generated by another form of energy. There are two common ways for light to be emitted, incandescence and luminescence [8].

2.3.1 Incandescence

Incandescence is glow light coming from heat energy. When something was heated by high enough energy, it will begin to glow "red hot": that is incandescence [4]. There are different types of incandescence, classified by the source glow, where some materials that glow gives off both heat and light at the same time:

- The sun and stars glow by incandescence which gives off both heat and light as a result of nuclear reactions in its core [8].
- When the metal heated in a flame or an electric stoves heater or exposed to gas flames will glow with a reddish color, where the red-hot will change to orange and yellow under prolonged exposure.
- Light from the older type of light bulb, where the light production is from the heated tungsten filament, the heat being a result of an electrical current.

The different types of incandescence are shown in figure 2.2.

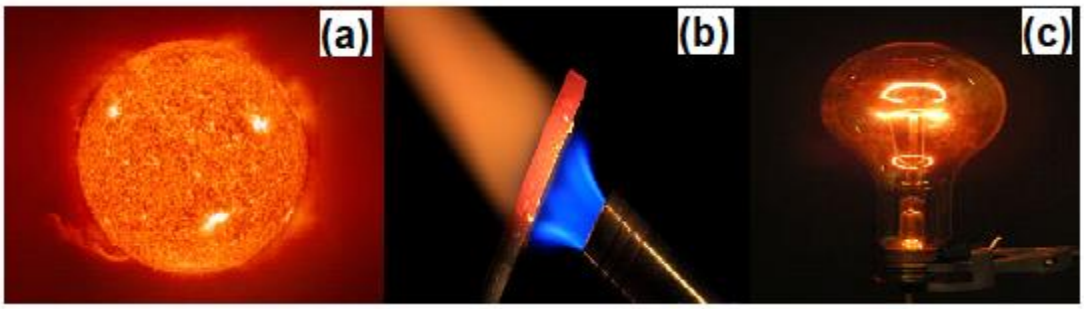

Figure 2.2: Different types of incandescence (a) the sun, (b) bar of iron that glows red under radiant heat from gas flames and (c) an ordinary bulb [9,10,11].

2.3.2 Luminescence

Luminescence is the so-called “cold light”, the process of emission of light from phosphor materials when applying other sources of energy to them. Generally optical radiation (from UV to IR light) may be used. In luminescence, an electron gets excited from its ground state (lowest energy level) by some energy source to an excited state (higher energy level). The electron then emits the energy in the form of light, so it can relaxes again to the ground state [2].

There are two forms of luminescence that can be identified regarding the lifetimes, namely fluorescence and phosphorescence [5]. Also, there are different luminesce types that depend on the type of excitation, such as photoluminescence, cathodoluminescence and others.

2.3.2.1 Fluorescence

It is the emission of light from the material when still subjected to the excitation source and luminescence stops immediately after removing the source of excitation. Fluorescence is the property of some materials to absorb light at a particular wavelength and emit light of longer wavelength almost immediately, in less than 10^{-7} s with the return of the molecule to the ground state [1].

2.3.2.2 Phosphorescence

It is the emission of light from materials exposed to radiation which continues as a dim light after the removal of the excitation radiation. The phosphorescence occurs in a manner similar to fluorescence: phosphorescence is the property of some materials to absorb light at a particular wavelength and emit light of a longer wavelength, but different from fluorescence materials the emission is delayed from 10^{-4} to 10 seconds or more, so these materials appear to glow in the dark [1].

A Jablonski diagram, figure 2.3, shows the processes of absorption, fluorescence and phosphorescence [12].

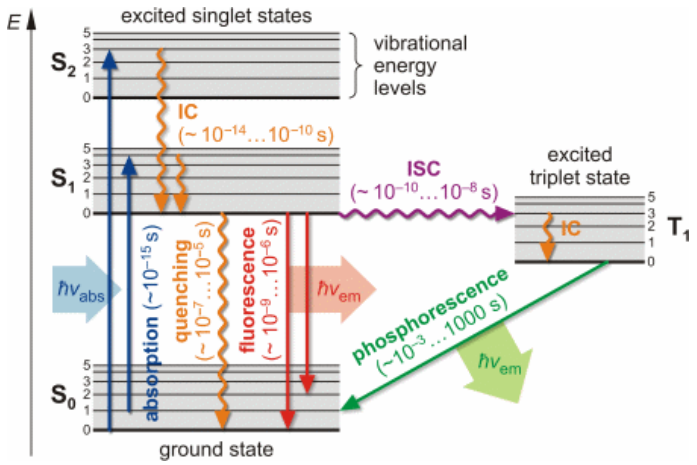

Figure 2.3: Jablonski energy diagram for absorption, fluorescence and phosphorescence [12].

The reason for delayed emission in the phosphorescence process is due to the electron spin orientation, where a spin-flip occurs. When the electron undergoes a spin-flip, a triplet state is created. The transition from a triplet state to the ground state is forbidden, which means that the reverse transition from triplet to the ground state with the emission of

phosphorescence takes more time. While in a fluorescence process, an electron does not change its spin orientation (excited singlet state) [13].

2.3.2.3 Photoluminescence (PL)

Photoluminescence is a process in which a substance absorbs electromagnetic radiation (i.e. photons, including ultraviolet light) and an electron is excited from ground state to a higher energy state and later returns to a lower energy state by emission of a photon. The period between absorption and emission is typically extremely short, in order of 10 ns and the difference in energy between the PL emission and the absorption is called the Stokes shift [14]. The emission spectrum is obtained by plotting an intensity against the wavelength of light emitted from the sample excited by an appropriate source of excitation for continuous energy. In chapters 5, 6 and 7, 8 some results for photoluminescence from powders and thin films samples are discussed, respectively.

2.3.2.4 Cathodoluminescence (CL)

Cathodoluminescence is a process where the luminescence results from excitation by high energy electrons, where a beam of electrons impacts on a luminescent material such as a phosphor causing the emission of photons. The CL emission spectrum is obtained by plotting an intensity against the wavelength of light emitted from the sample. Degradation of the CL intensity is defined as a reduction of cathodoluminescence efficiency of phosphors during electron beam bombardment. The rate of degradation of the CL intensity and development of an electron stimulated surface chemical reaction (ESSCR) model was described well by Pfahl's law [14]

$$I(N) = \frac{I_0}{(I+CN)} \qquad (2.1)$$

where I, I_0 are the aged and initial CL intensity, C is the burning parameter which is equal to the inverse of the number of electrons per unit area required to reduce the intensity to half of its original value and N is the number of electrons per unit area. The CL degradation depends on the type of gas remaining in the vacuum chamber, the gas pressure, the beam voltage and the electron (coulombic) dose during the process [2]. In chapter 6 some results for CL degradation are given.

2.3.2.5 Other types of luminescence

Other types of luminescence can occur e.g.

- Thermoluminescence: Absorbed light is re-emitted upon heating after pre-storage of energy.
- Electroluminescence: is a photoelectric and electric phenomenon where light will be produced in response to a strong current or an electric field that passed through it.
- Chemiluminescence: is the emission of light (luminescence) produced by chemical reactions.
- Bioluminescence: is the production and emission of light from chemi-luminescence where the energy is supplied by living organisms.
- Radioluminescence: luminescence produced in a material by the bombardment of nuclear ionizing radiation (X-rays, α, β, and γ and rays).
- Mechanoluminescence: emission resulting from any mechanical action on a solid.
- Sonoluminescence: imploding bubbles in a liquid when excited by ultrasound.

2.4 Applications of phosphors

The most recent phosphor research delivered promising results for several new applications. Constantly increasing technologies require further research efforts to develop these technologies and make them more efficient and inexpensive. Applications of phosphors can be classified into:

- Energy saving light sources e.g. fluorescent lamps, Light-emitting diodes (LED) [3].
- Display devices represented by cathode ray tubes (CRT), flat panel displays (FPDs) and field emission displays (FEDs) [8].
- Detector systems e.g. X-ray screen and scintillators [5].
- Solar energy converters.
- Other simple applications, such as luminous paint, persistent luminescence phosphors for signage, optical amplifiers, optical lasers, signs, light switches, etc. [5].

Among all these applications, our focus in this section will be on LEDs and FEDs, as these are potential applications of our phosphor.

2.4.1 Light emitting diodes

More than a century and a half since the introduction of incandescent lighting and the introduction of fluorescent lighting, solid-state light sources such as LEDs are revolutionizing an increasing number of applications. LEDs have emerged as some of the world's most efficient sources of visible light. The first LED lamps and displays were created in the late 1960s and early 1970s and were primarily used in direct-view applications, either as indicators or as part of a multi-element display, where LEDs are over ten times more efficient than filtered incandescent sources [15]. Today, the LED is considered as the most matured technology in modern lighting applications and may provide up to 50% of lighting by 2025 [16]. Significant cost reductions are expected mostly through the expansion of LED chips, lamps and packages. A LED is essentially a p- and n-type junction diode that permits the flow of current in one direction alone. When carriers are injected across a forward biased junction, it emits incoherent light. Generally, holes and electrons are the two types of charge carriers responsible for current in semiconductor materials. In N-type semiconductor material, electrons are the majority carriers and holes are the minority carriers. In P-type semiconductor material, the opposite is true. When the voltage is applied across a pn junction in a diode, the electrons and holes flow through the space charge region and become a minority carrier. These carriers are then deployed in the neutral semiconductor regions, with the re-combination of majority carriers. In a LED, this process is directly from the conduction band to the valence band [17]. Illustrated in figure 2.4.

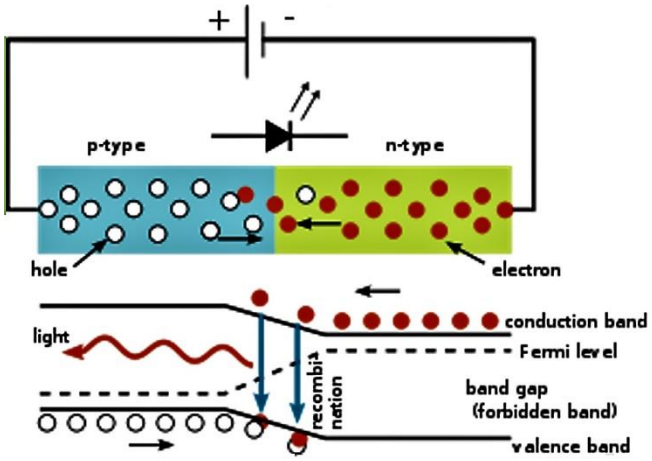

Figure 2.4: The basic process of photon generation [18].

An LED uses electrical energy to produce photons of a certain wavelength λ which depends on the band gap E_g of the material according to

$$\lambda = \frac{hc}{Eg} \qquad (2.2)$$

where h is the Planck constant and c is the speed of light in vacuum [19].

The wavelength of the LED, and its color, depends on the band gap energy of the materials forming the pn junction. Due to the materials available and the limited number of energy gaps, LEDs can only emit light of certain wavelengths; they do not emit white light naturally. Three different methods are used to generate white light [20]

- RGB system: Mix red, blue, and green LEDs together to create white light.
- Phosphor system: Coated LEDs in a phosphor that shifts the color into the white spectrum.
- A novel hybrid method, which combines the thermal modelling and temperature measurement, is proposed to estimate the junction temperature of high-power LEDs at the system level, and therefore predict the lifetime of LED luminaries based on the known LM-80 data.

2.4.1.1 LEDs efficiency

Compared to other lighting sources, LED lamps exhibit higher efficiency, e.g. between 2012 and 2014 the LED efficiency improved from 60 to 100 lumens per watt and is

expected to improve to 150 lumens per watt by 2020 [20]. A very important metric of an LED is the external quantum efficiency η_{EQE}. It quantifies the efficiency of the conversion of electrical energy into emitted light energy. External quantum efficiency (η_{EQE}) can be defined as the light output divided by the electrical input power.

A common metric of optoelectronic devices is their output power emitted externally to the device (P_{out}) measured in an integrating sphere. Thus from there, two quantities define the efficiency of the LEDs: the wall plug efficiency (WPE) η_{wp} i.e., the ratio of electrical input power to optical output power, and the external quantum efficiency (η_{EQE}), the ratio between the number of electrically injected carriers and externally observed photons [21]. Thus η_{EQE} also can be defined as the product of internal radiative efficiency and extraction efficiency [22]. η_{EQE} is easily assessed by

$$\eta_{EQE} = P_{out}(\text{optical}) / IV \qquad (2.3)$$

where P is the LED power output, I is the injected current and V the diode voltage [22]. For indirect bandgap semiconductors, η_{EQE} is generally less than 1% [23], whereas, for a direct bandgap material, it could be substantial.

2.4.1.2 LEDs Applications

At present, LEDs are the lighting solution for general lighting applications. They have demonstrated advantages such as low power consumption, durability, the possibility of direct mounting on circuit boards, mercury-free composition and brightness over other light sources [20]. Therefore, LEDs have found applications in every area of life [21] such as lighting, devices (medical applications, clothing and toys) and remote controls, indicators and signs, swimming pool lighting and optoisolators and optocouplers.

2.4.1.3 Advantages of using LEDs

- More efficient: More light per unit of energy than incandescent bulbs 80-100 lm/W for LED bulbs, compared to only 10-17 lm/W for incandescent; this is useful in battery powered or energy-saving devices.

- LEDs can emit light from the intended color without using the color filters required by traditional lighting methods. This is more efficient and can reduce initial costs.
- Cool: Incandescent light sources can burn very hot, but a LED light source gives off little thermal heat.
- Resistant to breakage: Rather than being made of glass and thin wires, LEDs are being solid state components and are far less fragile than an incandescent bulb or fluorescent.
- Long Lasting: 30,000-50,000 hours for an LED, compared to 1,000 for incandescent or 8,000 hours for fluorescent.
- LEDs can be very small and are easily populated onto printed circuit boards for use on devices.
- LEDs light up very quickly. A typical red indicator LED will achieve full brightness in microseconds; Philips Lumileds technical datasheet DS23 for the Luxeon Star states "less than 100 ns." LEDs used in communications devices can have even faster response times [21].

2.4.1.4 Disadvantages of using LEDs

- LEDs are currently more expensive, price per lumen, on an initial capital cost basis, than more conventional lighting technologies. The additional expense partially stems from the relatively low lumen output and the drive circuitry and power supplies needed, LEDs have higher upfront costs. In the same store, the cost an A19 9 LED light bulb is greater than the cost of a six pack of A19 incandescent bulbs. However, when considering the total cost of ownership (including energy and maintenance costs), LEDs far surpass incandescent or halogen sources and begin to threaten the future existence of compact fluorescent lamps.
- LEDs do not approximate a "point source" of light, so they cannot be used in applications that need a highly collimated beam. LEDs are not capable to provide deviation below a few degrees. This is contrasted with commercial ruby lasers with divergences of 0.2 degrees or less. However, this can be corrected by using lenses and other optical devices [22].

LEDs have come a long way and currently they are widely used in many applications. In the future, I believe research will continue for high-intensity and high quality LEDs. Normally in white LEDs, as introduced by Nichia [24], used existing phosphors such as cerium doped yttrium aluminium garnet (YAG:Ce), a yellow phosphor, which when combined with the blue LED (~455nm), such as strontium oxide doped with bismuth (SrO:Bi), produces white light (as the eye sees it).

2.4.2 Field emission displays (FEDs)

The displays are the devices through which we can view animated objects, where screens are manufactured according to their applications. One of the most important markets driving physics research is the demand for a perfect visual display. The first FED was conceived by the Stanford Research Institute (now called SRI International) team and patented by Crost, Shoulders and Zinn in 1970 (US Patent 3,500,102). The FED is a display technology that is incorporated in panel display technology that uses electron emission sources in a wide range to provide electrons that strike colored phosphors to produce a color image as an electronic visual display [25]. It has taken more than three decades for FEDs to go from an idea to commercial product. Now FEDs are a very promising substitute for conventional liquid crystal displays (LCDs). While having the best available image quality of CRT displays, FEDs also offer a superior viewing angle (160°) while it is keeping perfect focus since it is a fixed pixel display and it has a faster response time as compared to LCDs [26].

In FEDs electrons coming from millions of tiny microtips pass through gates and light up pixels on a screen. Generally, a FED consists of a matrix of cathode ray tubes, each tube producing a single sub-pixel, grouped in threes to form red-green-blue (RGB) pixels. FEDs combine the advantages of CRTs, namely their high contrast levels and very fast response times, with the packaging advantages of LCD and other flat-panel technologies. They also offer the possibility of requiring less power, about half that of an LCD system. A FED display operates as a traditional CRT with an electron gun that uses a high voltage (10 kV) to accelerate electrons, which in turn excite phosphorus, but instead of a single electron gun, a FED display contains a network of individual nanoscopic guns, as many as 500 million of them (microtips). A FED is illustrated in figure 2.5.

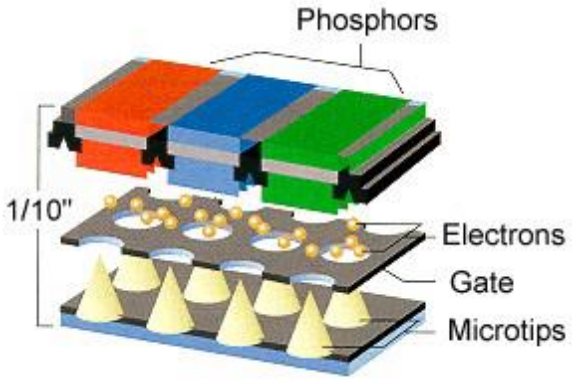

Figure 2.5: The basic components of a FED.

Figure 2.6 illustrates FED packaging, where the field emission display screens are comprised of a thin sandwich. In this the back is a sheet of glass or silicon that contains millions of tiny field emitters which is the cathode. The front is a sheet of glass coated with phosphor dots, which is the anode.

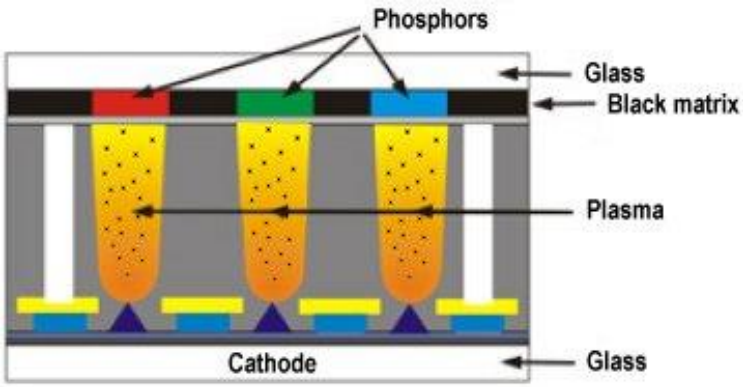

Figure 2.6: FED packaging.

2.5.2.1 Advantages and disadvantages of using FEDs

FEDs have advantages such as

- Brightness.
- Compact and lightweight.
- High speed.
- Different display sizes.
- It can work in wide temperature extremes.
- Low driving voltage.
- High-quality color.

However, FEDs also have some disadvantages such as

- FED display requires a vacuum to operate, so the display tube has to be sealed and mechanically robust and the phosphors must work well in the vacuum.
- The efficiency of the field emitters is based on the extremely small radii of the tips, but this small size renders the cathodes susceptible to damage by ion impact. The ions are produced by the high voltages interacting with residual gas molecules inside the device.
- Manufacturers are at present unable to compete with LCDs and plasma displays on a cost basis [15].

The FED devices are mainly composed of field emitter cathodes arrays and phosphor anodes. The luminescence properties of phosphors determine the display performance such as energy efficiency and images quality. Thus, phosphors for FEDs should possess high luminescence efficiency and good stability under such excitation conditions [27]. The blue emitting Bi-doped SrO powder was found to be stable under electron bombardment in both the base vacuum and back-filled O_2 environments (see chapter 6), which makes it an excellent candidate for application in field emission displays.

2.5 SrO host

SrO is a type of alkaline-earth oxide phosphors which is presently very important in a wide range of applications. The most extensive use of strontium oxide powder in the past was to solve problems in the cathode ray tubes industry. It was employed in the form of an aluminium alloy to help protect humans from X-ray emissions in the traditional color televisions. However, this long-lasting technology has now been replaced by the widespread use of flat displays (either liquid crystal or plasma displays). In recent years SrO powders have been essential in novel technological applications in the chemical and electronic industries, including the production of ferrite ceramic magnets and zinc refining, in addition, diverse strontium salts are currently consumed as pyrotechnic materials or paint additives [28]. Many properties of doped SrO have recently been demonstrated in the fields of optical, display and magnetic materials, which now it is expected to be useful both in electronic devices and as a phosphor material especially on LEDs applications [29]. It can be used in medical appliances, where it proved its efficiency as tissue or body member

replacements, restorative implant cement or filling compounds. Although consumption requirements fluctuate from year to year, the overall consumption of strontium compounds and metals appears to be increasing [30].

SrO is one of the most active catalysts among alkaline earth metal oxides, which can catalyze many chemical reactions, such as the oxidative coupling of methane, nitroaldol reactions, mixed Tishchenko reactions and selective oxidation of propane [31]. The melting and boiling points of SrO are about 2600 °C and 3200 °C, respectively. However, it will practically 'volatilize' if heated above 1400 °C in the air. This is probably due to SrO reacting with air at high temperatures because the thermodynamic parameters of SrO mentioned above are measured in an argon atmosphere [29]. SrO reacts with moisture and carbon dioxide present in the air and immediately forms strontium hydroxide $Sr(OH)_2$ and strontium carbonate $Sr(CO_3)$ if left in the air for a long time [32]. SrO has a small work function of 1.27 eV and it has an insulator direct band gap of 5.71 eV (217 nm) [33,34]. SrO crystals have a face-centered cubic symmetry with a two-atom basis. The first atom located at each lattice point and the second atom is located halfway between lattice points along the edge of the fcc unit cell. The coordination number of each atom in this structure is 6: each cation (Sr^{2+}) is coordinated to 6 anions (O^{2-}) at the vertices of an octahedron, and similarly, each anion is coordinated to 6 cations at the vertices of an octahedron, as illustrated in figure 2.6. The crystal structure of SrO is similar to NaCl or rock salt type with the space group of this structure called Fm3m (in Hermann-Mauguin notation) [35]. In this study it was drawn by using the Vesta program [36] as shown in figure 2.7.

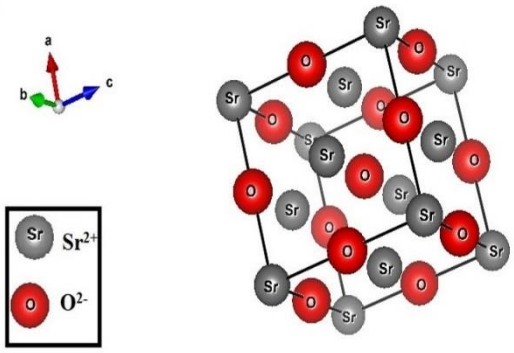

Figure 2.7: The crystal structure of SrO similar to NaCl or rock salt type with space group Fm3m (in Hermann-Mauguin notation).

Synthesis of SrO have been reported by various researchers because of the potential applications for these materials. For example, SrO materials have been applied as electron-inducing buffer layers in organic electroluminescence (EL) devices by Kim et al [37]. In 2003, SrO was also used as a buffer layer for the crystal growth of perovskite-type oxides such as $BaSrTiO_3$ (BST) and $SrTiO_3$ (STO) [38] (Kosola et al., 2003). BST and STO show high-temperature superconductivity and ferroelectricity, properties of interest for dynamic random access memory applications [39]. In (2011), Zhang et al. SrO films were obtained on a SiO_2/Si(100) substrate using an atomic layer deposition method, from bis (triisopropylcyclopentadienyl) strontium [40]. SrO has shown blue luminescence at 456 nm when Eu^{2+} ions are present, acting as emission centers, when phosphors were synthesized on a (110) single crystalline MgO substrate by the thermal treatment of SrO:Eu powders in a reducing atmosphere, reported by Komatsu et al. [33]. SrO phosphor containing Pb^{2+} as an activator was successfully prepared by the co-precipitation method using $(NH_4)_2CO_3$ followed by annealing at 1000 °C, were found to be stable and the efficient blue emission at 450 nm was observed, report by Taikar et al. [32]. In 2015, a convenient modified solid-state reaction method, interlayer solid-state reaction (ISSR) for obtaining Ce^{3+} doped SrO was reported, using the ISSR method, the investigations in this report indicated that ISSR may provide a new concept and strategy for conveniently synthesizing other ions doped functional materials, report by Jipeng et al. [29]. In 2016, a new red-blue dichromic phosphor, SrO:Bi^{3+}, Eu^{3+} was synthesized by solid-state reactions for the first time, and from the results acquired in that work a new way to achieve the temperature spatial and temporal images with temperature sensitive probes was achieved, report by Jipeng et al. [41]. In 2017, SrO nanoparticles (NPs), as well as SrO NPs coated on SiO_2 beads, have been successfully prepared using a nonaqueous reaction medium with benzyl alcohol. From that report, an active and reusable SrO based heterogeneous catalyst was designed that could be exploited in a continuous flow reactor for the large-scale production of biodiesel, report by Naor et al. [31]. With regards to this study, we discussed the synthesis and characterization of bismuth-doped strontium oxide powder and thin films.

2.6 Bismuth

Elemental bismuth (Bi) is a chemical element with an atomic number of 83. Bismuth is environmentally friendly since its toxicity is negligible as well as non-radioactive and the melting point of Bi is 271 °C [42]. Bi belongs to the fifth major group of the periodic table and is the heaviest element in this group with an atomic weight of 208.98 amu [43]. Bi atoms are the heaviest member of the group 15 (pnictogen) with an electronic configuration $[Xe]4f^{14}5d^{10}6s^2p^3$ and it has a large number of valence states (e.g. +3, +2, +1, 0, -2, etc.) in different materials [41]. Since the element of bismuth has an atomic number of 83, the Bi atom has 78 core electrons and 5 valence electrons, namely $6s^26p^3$ [44]. The luminescent properties of Bi ion doped materials exhibit wonderful luminescent properties due to a large number of valence states and strong interaction with the surrounding lattice. That is due to the fact that outer electron orbitals of Bi ions are not shielded from the surrounding environment, so it has the possibility of easy conversion of valence or existence of many valences states in a single component. In different valence states from the Bi ion, Bi^{3+} valence state is usually the most stable in most host materials [44]. In this study, the main focus of the investigation is the spectroscopic property of Bi^{3+} that either could act as an activator or a sensitizer in phosphor materials. The Bi^{3+} ion has 2 valence electrons. The $6s^2$ ground state has a single energy level $^1S_0$, while the $6s^16p^1$ excited configuration has energy levels $^3P_0$, $^3P_1$, $^3P_2$ and $^1P_1$ in order of increasing energy. According to dipole selection rules, excitations usually occur from the $^1S_0$ ground state to the $^1P_1$ and $^3P_1$ states, where electron transitions between the $^1S_0$ ground state and the ^3P_J levels are spin forbidden, but optical absorption can occur to the high energy $^1P_1$ level [46]. The emission from Bi^{3+} activated phosphors is usually ascribed to the $^3P_1 \rightarrow {}^1S_0$ transition. This is because of spin-orbit coupling between the $^1P_1$ and $^3P_1$ levels to make the lower energy transitions $^1S_0 \leftrightarrow {}^3P_1$ possible [41]. The fluorescent lifetime of Bi^{3+} is no longer than 5 µs in crystals or glasses [47]. Usually, the emission peaks of Bi^{3+} occur to cover a very broad spectral range, from the ultraviolet, blue, green, or even red wavelength regions with the variation of host materials. This depends on the composition and crystal structure of the host lattice, since the outer electron orbitals of Bi^{3+} that are not shielded, and the associated Stokes shifts also vary in large proportions e.g. some materials give different colors when doped with Bi^{3+} and are listed in Table 2.1.

Table 2.1. Materials that emit different colors when doped with Bi^{3+}.

Phosphor material	Emission	Ref.
$YBO_3 : Bi^{3+}$, $Y_3Al_{5x}Ga_xO_{12}:Bi^{3+}$ and $GaBO_3 : Bi^{3+}$	UV	[48,49,50]
$GdNbO4 :Bi^{3+}$, $Ca_{1-x}O:Bi_{x=0.5\%}$ and $LnNbO_4 :Bi^{3+}$	Blue	[51,52,53]
$Ca_3Al_2O_6 : Bi^{3+}$, $Ba_3Sc_4O_9:Bi^{3+}$ and $YVO_4:Bi^{3+}$	Green	[54,55,56]
$Zn_3V_2O_8: Bi^{3+}$, $CaTiO_3:Bi^{3+}$ and $Ca_2MgWO_6:Bi^{3+}$	Yellow	[57,58,59]
$Y_2WO_6:Bi^{3+}$ and $ScVO_4:Bi^{3+}$	Red	[60,61]

Many researchers have been investigating the luminescence properties of alkaline-earth oxides, especially SrO activated with Bi^{3+} ions, which were found to be an alternative to the rare earth ions because of their good luminescence properties. As an example, Ellervee [62] in 1977 reported about the spectral and polarization properties and the kinetics of luminescence. The impurities Bi^{3+} and Pb^{2+} were investigated as luminescent centers in alkali-earth sulphides (CaS and SrS) and oxides (CaO and SrO). Another report by Zavt et al. [63] in 1979 presented CaO and SrO containing Pb^{2+} or Bi^{3+} impurities and gave results of accurate low-temperature measurements of the emission spectra. After that, the theoretical model was discussed and compared with the experimental results [63]. In 1981 [64] Steen et al. gave a simple interpretation of the vibronic features in the emission and excitation spectra of the luminescence of the $6s^2$ ion activated alkaline-earth oxides (SrO and CaO as examples) and discussed theoretically treatments on the excited state of an ion in O_h symmetry sites. Nobuhiko [65] in 1987 reported details of the photoluminescence and excitation spectra that were obtained at various temperatures between 6 and 300 K. At low temperatures, the emission band originating from the $^3A_{1u}(sp) \rightarrow {}^1A_{1g}(s^2)$ transition in a Bi^{3+} ion shows a vibrational structure. In 2016 Jipeng Fu et al. [41] introduced a different application in SrO:Bi, when they reported about spatial and temporal temperature images on an aircraft surface which have been successfully realized under excitation of commercial 365 nm LED by painting on the $SrO:Bi^{3+},Eu^{3+}$ phosphor for a plane model,

and the thermal quenching mechanism revealed by Arrhenius theory is employed to interpret the temperature sensitive luminescence behavior [41].

2.7 References

[1] Ratnesh Tiwari, Vikas Dubey, Sanjay J. Dhoble, Emerging Synthesis Techniques for Luminescent Materials. Advances in Chemical and Materials Engineering (ACME). Publisher, IGI Global, Hershey PA. USA (2018). ISBN: 1522551719, 9781522551713.

[2] G. Blasse, B.C. Grabmaier. Luminescent Materials, Springer-Verlag, Berlin Heidelberg (1994), ISBN: 978-3-540-58019-5, 978-3-642-79017-1. DOI: 10.1007/978-3-642-79017-1.

[3] P.D. Nsimama, Characterization of $SrAl_2O_4Eu^{2+},Dy^{3+}$ Nano thin films prepared by pulsed laser deposition, PhD thesis, University of the Free State, (2010).

[4] M. William, Yen, Shigeo Shionoya, Hajime Yamamoto (Editors). PHOSPHOR HANDBOOK. Second Edition. CRC Press, Boca Raton (2007). ISBN: 0-8493-3564-7.

[5] H. A. A. Seed Ahmed, Luminescence from lanthanide ions and the effect of co-doping in silica and other hosts, PhD thesis, University of the Free State, (2012).

[6] K. N. Shinde, S. J. Dhoble, H. C. Swart, K. Park, Phosphate Phosphors for Solid-State Lighting. Springer-Verlag Berlin Heidelberg 174 (2012). ISBN: 978-3-642-34311-7. DOI: 10.1007/978-3-642-34312-4.

[7] M. A. Pulane, Cathodoluminescence Degradation and Surface, M.Sc. thesis, University of the Free State, (2011).

[8] M. -M. Biggs, Synthesis, characterization and luminescent mechanism of $ZnS:Mn^{2+}$ nanophosphor, Ph.D. thesis, University of the Free State, (2009).

[9] Internet: Sun-life [online], http://www.daviddarling.info/encyclopedia/S/Sunlife.html [Accessed 08 August 2018].

[10] Internet: https://fineartamerica.com/featured/heating-metal-2-of-3-ted-kinsman.html [Accessed 08 August 2018].

[11] Internet: https://en.wikibooks.org/wiki/Wikijunior:LightbulbGlow.jpg [Accessed 08 August 2018].

[12] Internet: fluorescence & phosphorescence http://home.uni-leipzig.de/pwm/web/?section=introduction&page=fluorescence [Accessed 08 August 2018].

[13] S. M. Khopkar, Basic Concepts of Analytical Chemistry. Second Edition. New Age International (New Delhi, 2004). ISBN 8122411592, 9788122411591.

[14] L. Ozawa, Cathodoluminescence and Photoluminescence - Theories and Practical Applications, Taylor & Francis Group (New York, 2007). ISBN 9781420052732.

[15] S. N. Ogugua, Tunable multicolor emission from dysprosium-doped mixed rare-earths oxyorthosilicate nanophosphors for application in ultraviolet-pumped multicolour and white light emitting diodes, MSc thesis, University of the Free State, (2015).

[16] Internet: https://www.lrc.rpi.edu/programs/solidstate/sslwhat.asp [Accessed 08 August 2018].

[17] F. M. Steranka, J. Bhat, D. Collins, L. Cook, M. G. Craford, R. Fletcher and J. J. Wierer. High power LEDs - Technology status and market applications. Physica Status Solidi (A) Applied Research. **194(2)** (2002) 380–388. DOI:10.1002/1521-396x(200212)194:2<380:aid-pssa380>3.0.co;2-n.

[18] S. D. Gupta. Artificial Lighting System for Plant Growth and Development: Chronological Advancement, Working Principles, and Comparative Assessment. Chapter 1.2.3 in: A. Agarwal (Editors). Light emitting diodes for agriculture: Smart lighting. Springer, Singapore (2017). ISBN: 978-981-10-5806 6.

[19] Donald A. Neamen. Semiconductor physics & devices: basic principle, fourth edition. The McGraw-Hill Companies, Inc. New York (2012). ISBN 978-0-07-352958-5.

[20] S. N. Ogugua, Preparation and characterization of powders and pulsed laser deposited thin films of rare-earths doped oxyorthosilicates, PhD thesis, University of the Free State, (2017).

[21] T. Seong, J. Han, H. Amano, H. Morkoç (eds. E. Matioli, and C. Weisbuch). III-Nitride Based Light Emitting Diodes and Applications, Springer Singapore (2017). ISBN 978-94-007-5862-9, 978-94-007-5863-6.

[22] R. Pode and B. Diouf. Light Emitting Diodes. *Solar Lighting*. **3**, (2011) 61–95. DOI:10.1007/978-1-4471-2134-3_3.

[23] K. V. S. Sreedhar. "Light Emitting Diodes (LEDs). IOSR- *J. Ece*. **9 (2)** (2014) 7–13. DOI: 10.9790/2834-09270713.

[24] A. Mills. Phosphors development for LED lighting. *III-Vs* Review. **18(3)** (2005) 32–34. DOI:10.1016/s0961-1290(05)01052-5.

[25] R. S. Liu, Phosphors, upconversion nanoparticles, quantum dots and their applications. Springer Science + Business Media Singapore 2016. ISBN 978-981-10-1589-2, 978-981-10-1590-8.

[26] N. Hirosaki, R. J. Xie, K. Inoue, T. Sekiguchi, B. Dierre, and K. Tamura, Blue-emitting AlN: Eu^{2+} nitride phosphor for field emission displays. *Phys. Lett.* **91(6)** (2007) 1–4.

[27] X. Wang, Z. Zhao, Q. Wu, Y. Li and Y. Wang. A Garnet-Based Ca2YZr2Al3O12:Eu3+ Red-Emitting Phosphor for n-UV Light Emitting Diodes and Field Emission Displays: Electronic Structure and Luminescence Properties. *Inorg. Chem.* **55(21)** (2016) 11072–11077. DOI:10.1021/acs.inorgchem.6b01711.

[28] J. Vu, H. Guo and B. Cheng, Shape evolution of $SrCO_3$ particles in the presence of poly-(styrene-alt-maleic acid). *J. Solid State Chem.* **179**, (2006) 800–803. DOI:10.1016/j.jssc.2005.12.001.

[29] Fu. Jipeng, Su. Zhang, Ma. Tengfei, Jia. Yonglei, P. Ran, J. Lihong, Li. Da, Li. Haifeng, S. Wenzhi and Li. Chengyu, A convenient and efficient synthesis method to improve the emission intensity of rare earth ion doped phosphors: the synthesis and luminescent properties of novel SrO:Ce^{3+} phosphor. *RSC Adv.* **5** (2015) 93951–93956. DOI: 10.1039/c5ra15089b.

[30] A. Joyce Ober, Strontium from Mineral Commodities Summaries. *U.S Bureau of Mines*. **(1)** (1992) 1323-1332.

[31] E. O. Naor, M. Koberg, and A. Gedanken. Nonaqueous synthesis of SrO nanopowder and SrO/SiO_2 composite and their application for biodiesel production via microwave irradiation. *Renewable Energy*. **101** (2017), 493–499. DOI:10.1016/j.renene.2016.09.007.

[32] K. Komatsu, T. Shirai, A. Nakamura, A. Kato, S. Ohshio, N. Nambu and H. Saitoh. Synthesis and luminescence properties of Eu^{2+}-doped 8-coordinated SrO phosphors. *Ceramics International*. **39(6)** (2013) 7115–7118. DOI:10.1016/j.ceramint.2013.02.053.

[33] K. Komatsu, M. Tanabe, I. Toda, S. Ohshio, H. Muramatsu and H. Saitoh, Synthesis of Strontium Oxide Whiskers with Preferential <111> Orientation by Atmospheric Chemical Vapor Deposition. *J. Mater. Sci*, **5(2)** (2016) 50. DOI:10.5539/jmsr.v5n2p50.

[34] F. Granados-Correa and J. Bonifacio-Martínez, Combustion synthesis process for the rapid preparation of high-purity SrO powders. *J. Mater. Sci.* **32(4)** (2014) 682–687. DOI:10.2478/s13536-014-0250-9.

[35] L. Liu and W. A. Bassett. Changes of the crystal structure and the lattice parameter of SrO at high pressure. *J. Geophys. Res*. **78(35)** (1973) 8470–8473. DOI:10.1029/jb078i035p08470.

[36] K. Momma and F. Izumi, VESTA 3 for three-dimensional visualization of crystal, volumetric and morphology data, *J. Appl. Crystallogr*. **44**, (2011) 1272-1276. DOI: 10.1107/s0021889811038970.

[37] R. Kim, Y. Kim, J. Cho and J.W. Park. Luminous efficiency and secondary electron emission characteristics of alternating current plasma display panels with MgO–SrO–CaO protective layers. *J. Vac. Sci. Technol.* **18(5)** (2000) 2493-2496. DOI:10.1116/1.1287151.

[38] T. Q. Ngo, A. B. Posadas, M. D. McDaniel, C. Hu, J. Bruley, E. T. Yu, A. A. Demkov and J. G. Ekerdt. Epitaxial c-axis oriented $BaTiO_3$ thin films on $SrTiO_3$-buffered Si (001) by atomic layer deposition. *J. Appl. Phys*. **104(8)** (2014) 082910. DOI:10.1063/1.4867469.

[39] A. Kosola, M. Putkonen, L.-S. Johansson and L. Niinisto. Effect of annealing in processing strontium titanate thin films by ALD. *Appl. Surf. Sc*. **211(1-4)** (2003) 102–112. DOI:10.1016/s0169-4332(03)00175-2.

[40] C. B. Zhang, L. Wielunski and B. G. Willis. Formation of strontium template on Si(1 0 0) by atomic layer deposition. *Appl. Surf. Sc*. **257(11)** (2011) 4826-4830. DOI:10.1016/j.apsusc.2010.12.098.

[41] Fu. Jipeng, R. Pang, L. Jiang, Y. Jia, W. Sun, S. Zhang and C. Li, A novel dichromic self-referencing optical probe SrO:Bi^{3+},Eu^{3+} for temperature spatially and temporally imaging, *Dalton Trans.* **45(34)** (2016) 13317–13323. DOI: 10.1039/c6dt01552b.

[42] A. Economou. Bismuth-film electrodes: Recent developments and potentialities for electroanalysis. *TrAC - Trends Anal. Chem*. **24(4)** (2005) 334–340. DOI:10.1016/j.trac.2004.11.006.

[43] K. Sam. The Disappearing Spoon (and other true tales of madness, love, and the history of the world from the Periodic Table of Elements). New York/Boston: Back Bay Books. 158–160 (2011). ISBN 978-0-316-051637.

[44] R. J. D. Tilley, Understanding solids: The Science of Materials, John Wiley & Sons, 2004. ISBNs: 0 470 85275 5 (Hbk).

[45] A. B. Gawande, R. P. Sonekar and S. K. Omanwar. Synthesis and Photoluminescence Study of Bi^{3+} and Pb^{2+} Activated $Ca_3(BO_3)_2$. *Int. J. Opt*. (**2014)** (2014) 1-6. DOI:10.1155/2014/418459.

[46] J. F. Liu. Luminescence properties of bismuth-doped SrO-B_2O_3 glasses with multiple valences state. *Optik – Optics*. **126(23)** (2015) 4115–4118. DOI:10.1016/j.ijleo.2015.07.207.

[47] M. Peng, B. Wu, N. Da, C. Wang, D. Chen, C. Zhu, and J. Qiu. Bismuth-activated luminescent materials for broadband optical amplifier in WDM system. *J. Non-Cryst. Solids*. **354(12–13)** (2008) 1221–1225. DOI:10.1016/j.jnoncrysol.2007.01.106.

[48] L. Chen, H. Zheng, J. Cheng, P. Song, G. Yang, G. Zhang and C. Wu, Site-selective luminescence of Bi^{3+} in the YBO_3 host under vacuum ultraviolet excitation at low temperature. *J. Lumin*. **128(12)** (2008) 2027–2030. DOI:10.1016/j.jlumin.2008.07.007.

[49] A. Yousif, V. Kumar, H. A. A. Seed Ahmed, S. Som, L. L. Noto, O. M. Ntwaeaborwa and H. C. Swart. Effect of Ga^{3+} Doping on the Photoluminescence Properties of $Y_3Al_{5-x}Ga_xO_{12}:Bi^{3+}$ Phosphor. *ECS J. Solid State Sci. Technol.* **3(11)** (2014) R222–R227. DOI:10.1149/2.0021412jss.

[50] F. Kellendonk, M. A. van Os, and G. Blasse, Luminescence of bismuth in yttrium aluminum borate. *Chem Phys Lett*. **61(2)** (1979) 239–241. DOI:10.1016/0009-2614(79)80634-x.

[51] X. Jing, C. Gibbons, D. Nicholas, J. Silver, A. Vecht and C. S. Frampton. Blue luminescence in yttrium and gadolinium niobates caused by bismuth. The importance of non-bonding ns^2 valence orbital electrons. *J. Mater. Chem*. **9(11)** (1999) 2913–2918. DOI:10.1039/a905724b.

[52] A. Yousif, R. E. Kroon, E. Coetsee, O. M. Ntwaeaborwa and H. C. Swart, Luminescence and electron degradation properties of $CaO:Bi^{3+}$ phosphor, *Appl. Surf. Sci.* **356,** (2015) 1064–1069. DOI:10.1016/j.apsusc.2015.08.210.

[53] X. Xiao and B. Yan, "Hybrid precursors synthesis and optical properties of $LnNbO_4:Bi^{3+}$ blue phosphors and Bi^{3+} sensitizing of on Dy^{3+}'s luminescence in $YNbO_4$ matrix,". *J Alloys Compd*. **421(1-2)** (2006) 252–257. DOI:10.1016/j.jallcom.2005.11.035.

[54] H. Ju, W. Deng, B. Wang, J. Liu, X. Tao, and S. Xu, The structure and luminescence properties of green $Ca_3Al_2O_6:Bi^{3+}$ phosphors. *J Alloys Compd*. **516**, (2015) 153– 156. DOI:10.1016/j.jallcom.2011.12.011.

[55] Y. Wang, J. Ding, and Y. Wang, Preparation and photoluminescence properties with the site-selected excitations of Bi^{3+}-activated $Ba_3Sc_4O_9$ phosphors, *J. Am. Ceram. Soc.* **100(6)** (2017) 2612–2620. DOI:10.1111/jace.14789.

[56] E. Cavalli, F. Angiuli, F. Mezzadri, M. Trevisani, M. Bettinelli, P. Boutinaud and M. G. Brik. Tunable luminescence of Bi^{3+}-doped $YP_xV_{1-x}O_4(0 \leq x \leq 1)$. *J. Phys. Condens. Matter*. **26(38)** (2014) 385503. DOI:10.1088/0953-8984/26/38/385503.

[57] X. Zhang, A. Guan, L. Zhou, and M. Gong, Synthesis and luminescence study of $Zn_3V_2O_8:Bi^{3+}$ yellow phosphor for solar spectral conversion, *Int J Appl Ceram Tec.* **14(3)** (2017) 392–398. DOI:10.1111/ijac.12663.

[58] T. Fu, H. Xu, W. Luo, D. Peng, Z. Chen and J. Fu. Synthesis and luminescence enhancement of $CaTiO_3:Bi^{3+}$ yellow phosphor by codoping Al^{3+}/B^{3+}ions, *J. Alloys Compd.* **674,** (2016) 51–55. DOI:10.1016/j.jallcom.2016.02.252.

[59] R. Cao, G. Quan, Z. Shi, Z. Luo, Q. Hu, and S. Guo. A double perovskite $Ca_2MgWO_6:Bi^{3+}$ yellow-emitting phosphor: Synthesis and luminescence properties, *J. Lumin.* **181**, (2017) 332–336. DOI:10.1016/j.jlumin.2016.09.046.

[60] G. Blasse and A. Bril, Investigations on Bi^{3+}-activated phosphors, *J. Chem. Phys.* **48(1)** (1968) 217–222. DOI:10.1063/1.1667905.

[61] F. Kang X. Yang, M. Peng, L. Wondraczek, Z. Ma, Q. Zhang and J. Qiu. Red Photoluminescence from Bi^{3+} and the Influence of the Oxygen-Vacancy Perturbation in $ScVO_4$: A Combined Experimental and Theoretical Study, *J. Phys. Chem. C*. **118(14)** (2014) 7515–7522. DOI:10.1021/jp4081965.

[62] A.F. Ellervee, Luminescence of Pb^{2+} and Bi^{3+} Centres in Alkali-Earth Sulphides and Oxides *Phys. Status Solidi (b).* **82(1)** (1977) 91–98. DOI: 10.1002/pssb.2220820107.

[63] G.S. Zavt and A.F. Ellervee, Pb^{2+} and Bi^{3+} impurity centres in alkali-earth oxides vibronic spectra, lattice dynamics, and electron-phonon interaction, *Phys. Status Solidi.* **94(2)** (1979) 757–768. DOI:10.1002/pssb.2220940249.

[64] A.C.V.D. Steen and L.T.F. Dijcks The Luminescence Properties of Alkaline-Earth Oxides Activated with $6s^2$ Ions, *Phys Status Solidi (b).* **283**, (1981) 283–292. DOI:10.1002/pssb.2221040130.

[65] N. Yamashita, S. Ikeda and S. Asano, Photoluminescence and excitation spectra of the $SrO:Bi^{3+}$ phosphor. *Physics Letters A.* **121(2)** (1987) 94–96. DOI: 10.1016/0375-9601(87)90272-6.

Chapter 3: Synthesis Techniques

In this chapter, a brief description of the experimental techniques used in this study is presented. These techniques include the combustion method used for the synthesis of the powder material, the PLD and the sol-gel spin coating used for the thin film preparation/deposition.

3.1 Combustion synthesis (CS)

The combustion synthesis method is a complex sequence of chemical reactions between a fuel and an oxidant accompanied by the production of heat or both heat and light in the form of either a flame or a glow. Interaction occurs in a redox (red-ox = reduction-oxidation) reaction electron transfer process in which the oxidizer gains an electron and increase in its oxidation state and the reducer lose an electron and reduce in its oxidation state to form a sample product. The combustion synthesis can be represented by a simple chemical equation of the model:

$$_{m}X + _{n}Y \rightarrow X_{m}Y_{n} \qquad (3.1)$$

where X is a fuel (metal) and Y is the oxidizers (nonmetal) [1]. The fuel must be able to achieve structural homogenization with other components and must be combusted at a low ignition temperature with the oxidizer [2]. The nature of the powder product after combustion heavily depends on the flaming temperature and gas evolution, and these parameters also depend on the salts in use such as nitrates or acetates (oxidizers) and type of fuel used like urea, carbohydrazide, glycine, etc. (reductant) and the ratio of the oxidant-to-fuel [3]. The combustion process is known for high reduction-oxidation activation energies, high exothermic reactions, and high reaction temperature (500 – 4000 K), that is dependent on the type of flame associated with the fuel used. Urea works more interactively

leading to the formation of a flare, than the presence of a solution in the compared to glycine characterized by smouldering [4]. The fuels accelerate the homogeneous mixing of the cations solution through the formation of complexes with the metal ions. They also produce C and H which form CO_2 and H_2O during combustion and also release heat [1].

3.1.1 Types of combustion synthesis

By depending on the adiabatic temperature and the state of the reactants (solid, liquid or gas), the combustion method can be classified into several types as [1]:

- Self-propagation high-temperature synthesis (SHS).
- Low-temperature combustion synthesis (LTCS).
- Volume combustion synthesis (VCS) (thermal explosion).
- Solid-state combustion (SSC).
- Solution combustion synthesis (SCS).
- Emulsion combustion synthesis.
- Sol-gel combustion synthesis.
- Gel-combustion synthesis, etc.

3.1.2 Sol-gel combustion technique

In the present work, all the powder samples were prepared using the sol-gel combustion technique. The sol-gel combustion method is a novel method that uses a unique combination of the chemical sol-gel process and combustion, where oxidizing metal salts and combustion agent (fuel) are very essential for the combustion process. The sol-gel combustion technique has been proved to be an extremely facile, time-saving and energy-efficient route for the synthesis of ultra-fine, high purity and good homogeneity SrO powders. The size of the sol particles depends on the pH, temperature and the solution composition.

3.1.2.1 The principle for sol-gel combustion

In a patent from 1967 (Pechini 1967), Pechini described a simple method in which a sol-gel was used to prepare metal oxide powders. Polymeric precursors were made from metal

salts, ethylene glycol, and citric acid. Marcilly et al. 1967; Marcilly et al. 1970 and Courty et al. 1973 proposed a similar method, but the polyol (ethylene glycol) was completely replaced with water, forming an amorphous gel-like matter instead of the polymer [5].

The sol-gel combustion method is based on the gelling and subsequent combustion of an aqueous solution containing salts of the desired metals such as metal alkoxide with an inorganic fuel (combustion agent) such as citric acid and it is hydrolyzed by water. It gives a voluminous and fluffy product with a large surface area [6]. Citric acid is considered appropriate to be used for obtaining precursors of transition metal oxides, due to its good capability of chelating metallic ions and low decomposition temperatures. It forms complexes with metal ions preventing the precipitation of hydroxylated compounds. The energy from the exothermic reaction in the combustion between the oxidant and reductant is high enough to form fine particles. Some examples of oxide materials where citric acid were used as fuel for their synthesis using the sol-gel combustion method and some applications are listed in Table 3.1.

Table 3.1: Some materials prepared by sol-gel combustion and their application.

Phosphor material	Application	Ref.
$Y_3Al_{5x}Ga_xO_{12}:Bi^{3+}$	UV-LED's	[7]
$CaWO_4:Eu^{3+}$	Fluorescent	[8]
$Ca_{1-x}O:Bi_{x=0.5\%}$	A variety of optical devices	[9]
$Y_2O_3:Eu^{3+}$	Red phosphor	[10]
$YAG:Ce^{3+}$	Blue LED	[11]

In our study, we used sol-gel combustion for synthesized all powder samples. Equation (3.2) is an example of a stoichiometric combustion reaction of strontium nitrate $Sr(NO_3)_2$ and citric acid ($C_6H_8O_7$) to form SrO:

$$Sr(NO_3)_2 + C_6H_8O_7 \rightarrow SrO + 6CO_2 + N_2 + 4H_2 \qquad (3.2)$$

When the complete reaction occurs, only the gaseous products CO_2, N_2 and H_2 are released and no residuals are left in the synthesized SrO material.

Figure 3.1 shows a schematic diagram for the preparation of nanocrystalline SrO:Bi powders by the sol-gel combustion process. Combustion reactions are initiated in a muffle furnace or on a hot plate preheated at 200-300 °C.

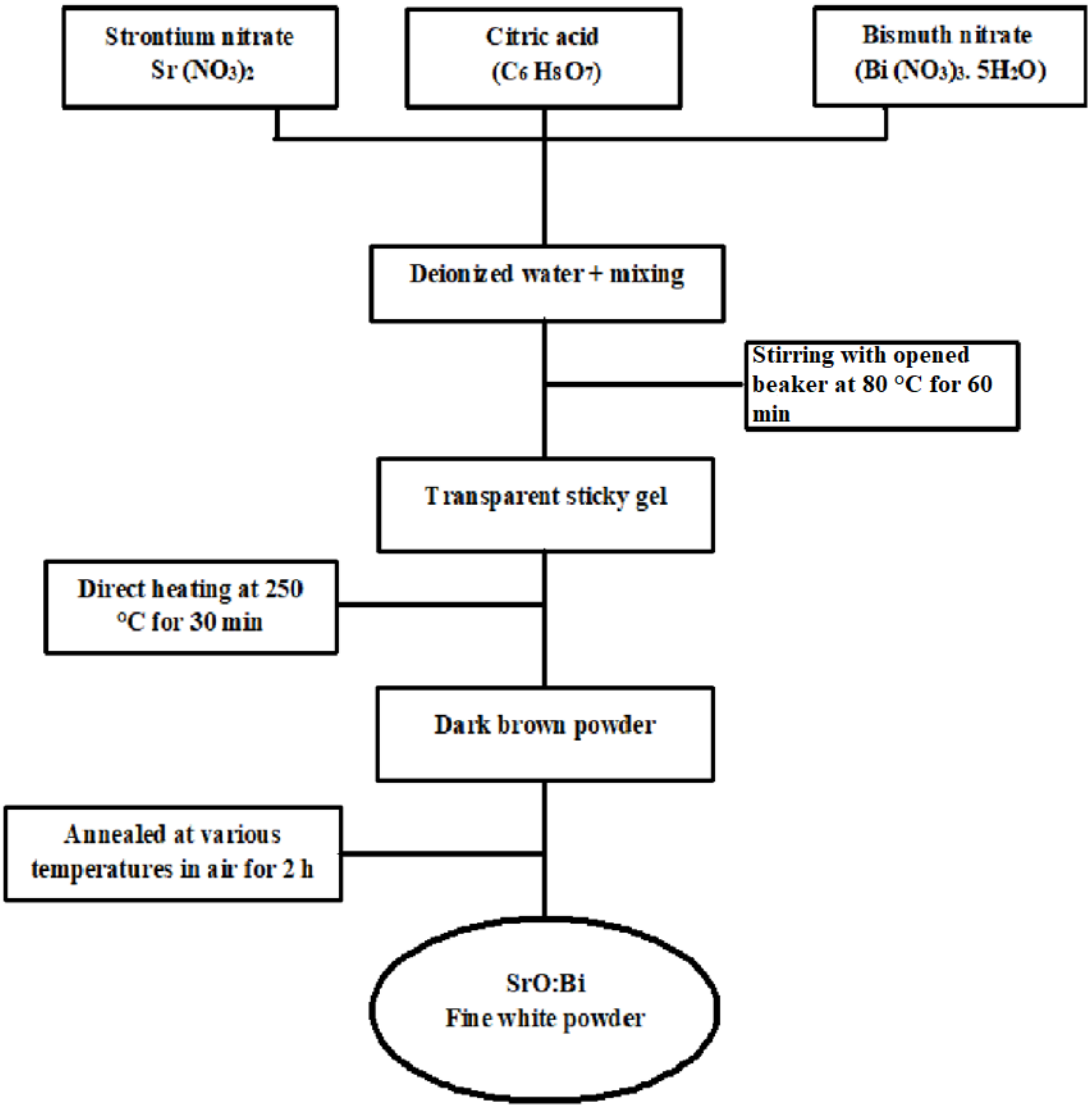

Figure 3.1: Schematic diagram of the preparation of nanocrystalline SrO powder by sol-gel combustion process.

In a typical reaction, see figure 3.2, the materials are dissolved in the deionized water during heating at 80 to 100 °C with continuous stirring using a magnetic agitator for

1 h. When the water evaporates, the solution is transferred into a viscous gel. The gel is dried by direct heating in an oven maintained at 250 °C for 30 min. After that, the powders are well crushed and then annealed in air at various temperatures in the furnace for 2 h with an increase rate of 5 °C/minute starting from 50 °C up to the required temperature. The temperature is set at a fix value. After two hours, after the temperature is established, the temperature is allowed to drop at the same rate until it reachs 50 °C again.

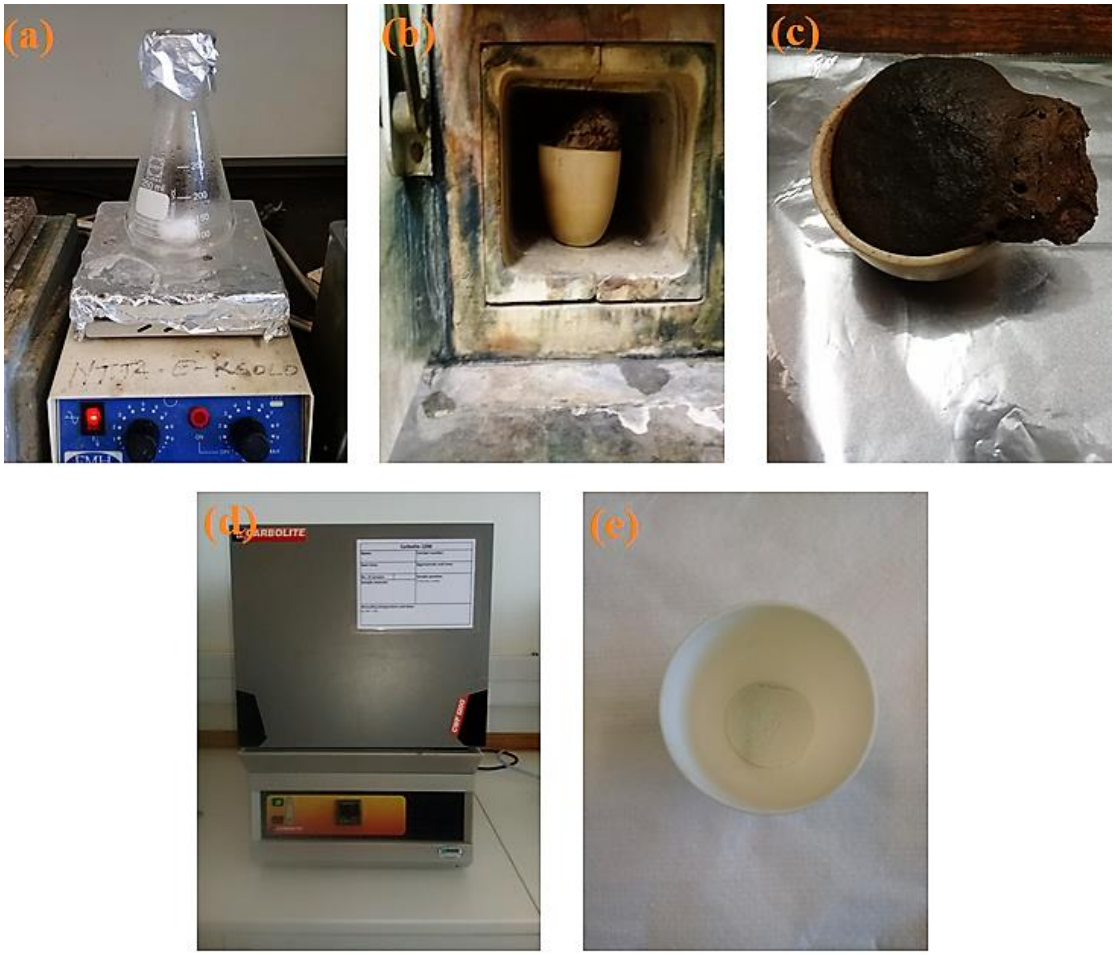

Figure 3.2: The equipment used for the combustion method: (a) stirring, (b) preheated to 250 °C for 30 min, (c) dark brown powder, (d) annealed at various temperatures, (e) fine white powder.

During the combustion, the flames extinguish within a few seconds, while the smoldering can last for several minutes. The type of combustion plays an important role in controlling the particle size in the combustion result.

3.1.2.2 Advantages of the Sol-gel combustion process

- Low cost and low-temperature process.
- High purity product and high-quality nano/microcrystal.
- Better control of stoichiometry.
- The exothermic reaction makes the product almost instantaneously.
- Does not require sophisticated equipment.
- The possibility of multicomponent oxides with single phase and high surface area.
- The product can be easily crushed and ground into a fine powder.

3.1.2.3 Limitations of the Sol-gel combustion process

- Many metal alkoxides are highly reactive and susceptible to hydrolysis thus causing a problem of their handling.
- Contamination due to carbonaceous residue, particle agglomeration, poor control on particle morphology.

3.2 Sol-gel process for thin film deposition

The sol-gel process has the capability to coat materials of various shapes and different surfaces, to control the composition easily for obtaining solutions with homogeneity and controlled concentration without using expensive equipment. Which makes it very useful for fabricating thin films [12]. The sol-gel synthesis has been developed in recent years as a potential alternative to the conventional hydrolytic route to inorganic oxides to get good thin films, because it has the ability to easily control viscosity, low cost and low fabricating temperature. Additionally, materials with high specific porosity and the specific surface area can be easily obtained by this method, which also allows the incorporation of substance components, other additives, such as the inhibitors [13]. The starting materials employed in the sol-gel process in most cases in the form of metal alkoxides, which readily undergo hydrolysis and condensation to form hydroxides

and oxides. However, mineral salts such as chlorides, acetates and nitrates are cheaper than metal alkoxides and are easier to deal with, so they are good substitutes if they are easily converted to oxides by thermal decomposition.

After selecting the chemical compounds that are combined forming, it is mixed in a deionized water-bath while mechanical stirring at pre-selected temperatures, to get the gel from precursors. The sol solution should be aged about 24 h before coating, to ensure that materials are not deposited before making films.

The different steps in the sol-gel thin film processing method, to prepare the thin films, are shown in figure 3.3:

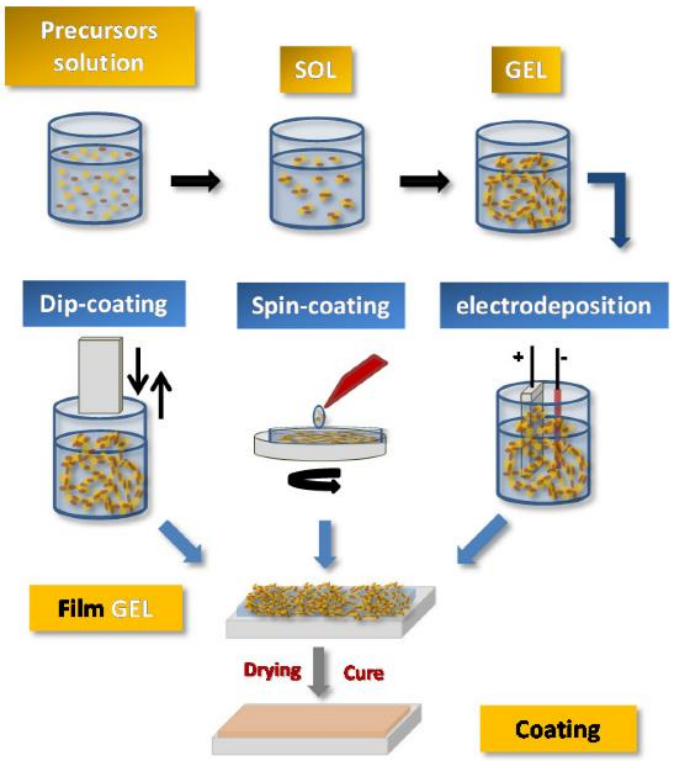

Figure 3.3: Steps involve in the processing routes to obtain coatings by sol-gel method. Adapted from [13].

In our study, the solution was prepared for spin coating by the sol-gel method. Strontium nitrate ($Sr(NO_3)_2$), bismuth nitrate ($Bi(NO_3)_3$. H_2O), citric acid (CA) and ethylene glycol (EG) were used as starting materials, dopant source, complexation agent and chelating agent, respectively. The molar ratio of metal ions to CA to EG was maintained at 1:1:4.

The schematic diagram to synthesize the $Sr_{-x}O:Bi_{x=0.002}$ phosphor by using the sol-gel method and to prepare the thin films are shown in figure 3.4.

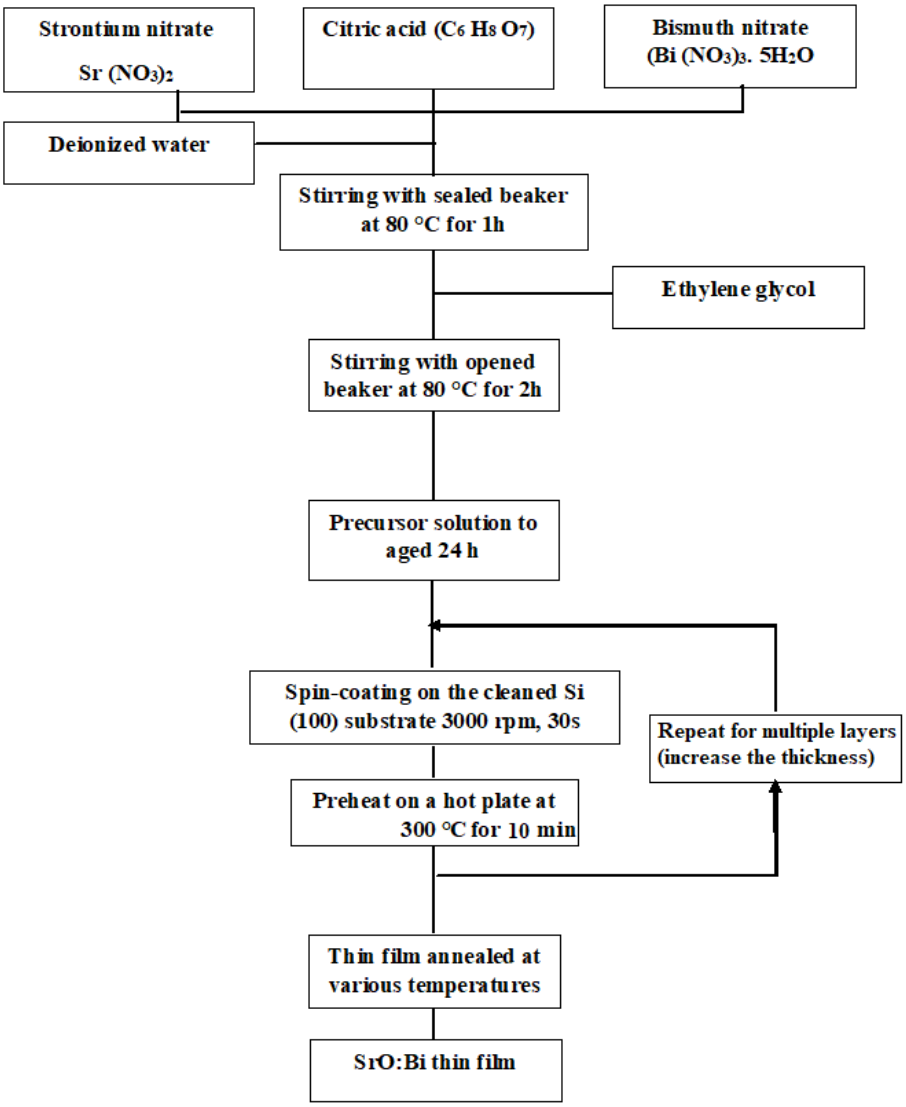

Figure 3.4: Schematic diagrams to synthesize the $Sr_{1-x}O:Bi_{x=0.002}$ phosphor by using the sol-gel method and to prepare the thin films by spin-coating.

3.3 Spin coating technique

Spin coating, also known as spin casting, is a simple process for depositing thin coatings quickly on relatively flat substrates. The substrate is placed on a rotary structure

(vacuum is often used to keep the substrate clamp in place) and the coating solution is added and spread out on the surface by spinning the substrate at high velocity speeds (typically around 1000 to 5000 rpm) depending on the properties of the liquid as well as the substrate. Spinning causes the solution to spread and leaves behind a very uniform layer of the selected material on the surface of the substrate and then the forms become solid films when dried [14]. For coating a special liquid precursor is used such as a sol-gel and deposited onto a smooth substrate such as Si, $LaAlO_3$, glass or fused silica, where deposition of a small quantity of the fluid solution is done onto the center of a substrate. Spin coating has been used to produce uniform thin films with the thickness of the order of micrometers and nanometers [15]. The perfect final film thickness will depend on the nature of the solution used in the spin process (viscosity, drying rate, percent solids, surface tension, etc.) and the parameters chosen for the spin process [16]. Accordingly, the final coating thickness can be predicted, h_f, in terms of several key solution parameters, according to equation (3.3):

$$h_f = x\left(\frac{e}{2(1-x)K}\right)^{1/3} \qquad (3.3)$$

where x is the effective solids content of the solution, e and K are the evaporation and flow constants, defined below, respectively, as:

$$e = C\sqrt{\omega} \qquad (3.4)$$

$$K = \frac{\rho\omega^2}{3\eta} \qquad (3.5)$$

where C is the proportionality constant that depends on whether the surface air flow is laminate or disturbed, and on the diffusion of dissolved solvents in the air (since it is mainly limited to the diffusion of evaporation particles through the aerodynamic boundary layer above the surface of the chip during rotation spinning), ω is the rotation rate, ρ is the solution's density, η is its viscosity [14].

The spin coating technique divided into different stages

- deposited coating the solution onto the substrate,
- spin-up the substrate is speeded to the ultimate desired spinning speed,

- the spin-of the substrate at a constant rate,
- The substrate keeps spinning at a constant rate and solvent evaporation dominates the coating thinning behavior. After evaporation of the whole solvent, a solid film is formed.

The stages are represented in figure 3.5:

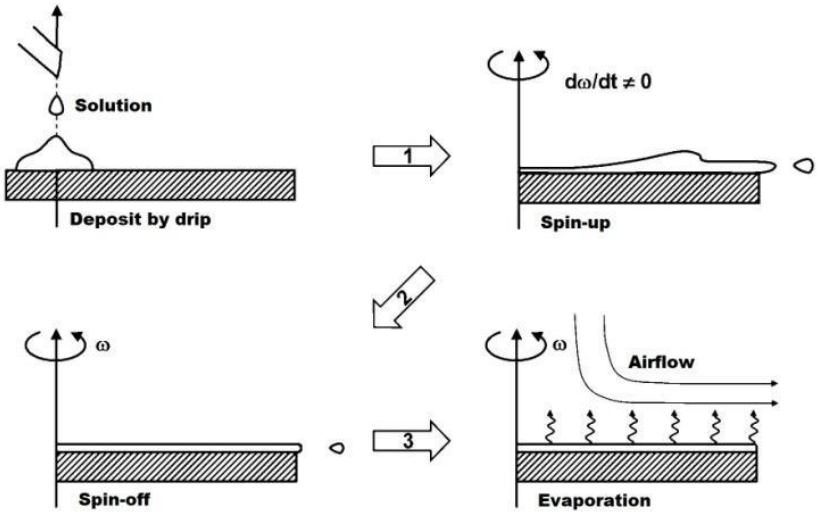

Figure 3.5: Stages of the spin coating technique. Adapted from [17].

Some advantages of fabricating films by this method are that it is a fast operating and low-cost system. The film thickness is easily controlled by different viscosity of the solution, changing spin speed and repeated depositions by a number of layers. Another advantage of spin coating is the ability of the film to be a good uniform films on flat substrates [18]. The biggest disadvantage of spin coating is its lack of material efficiency; which typical spin coating processes utilize only 2–5% of the material dispensed onto the substrate. Another disadvantage in the large substrates cannot be spun at a sufficiently high rate in order to allow the film to thin [19].

Spin coating thin films have been used in the manufacture of integrated circuits, solar cells, detectors, flat screen display coatings, color television screens, optical mirrors and

magnetic disks for data storage [12]. For the present research study, the model spin coater used is a SPEN 150 from Semiconductor Production System as shown in figure 3.6:

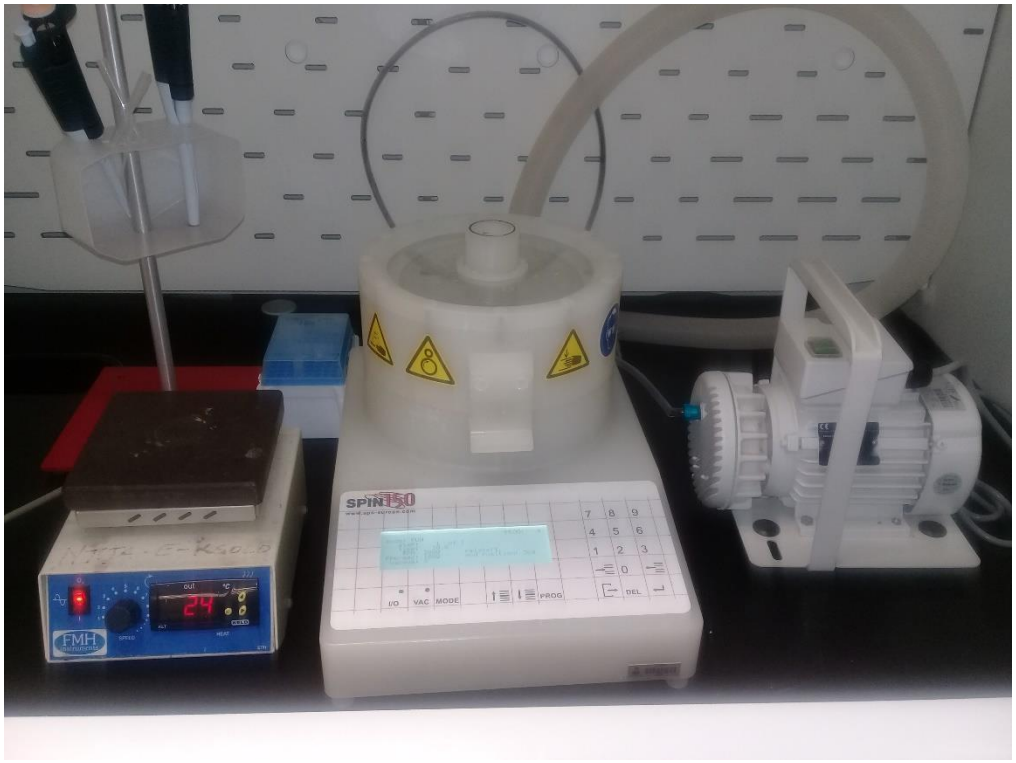

Figure 3.6: Spin coating SPEN 150 from Semiconductor Production System at the Department of Physics of the University of the Free State.

3.4 Pulsed laser deposition (PLD) technique

The PLD can be defined as a physical processes on condensed phase (solid or liquid) material in a coherent form mostly made as a solid target, and converted this material by the impact of a high power pulsed laser radiation on the solid target to the vapor form (atomic/molecular/ionic species), then compress it on substrate to form a solid and thin film [19]. The first laser deposition was by Smith and Turner in 1965, using a pulsed ruby laser to deposit thin films in vacuum [1]. In 1987, Dijkkamp et al. [20] recorded a big

breakthrough when they produced $YBa_2Cu_3O_7$ laser film with high-quality using alternative techniques, which was the first real start to the production of thin films using the laser.

Since its invention, the PLD technique offers many applications in Physics such as optoelectronics to micromechanics and integrated circuits and medical implants. Which are due to the high-quality film deposition ability from PLD. Especially at lower substrate temperatures a very wide range of materials, including complex oxides, semiconductors, nitrides, carbides, borides, metals and even polymers can be deposited [21].

3.4.1 The growth of thin films by PLD

The mechanism of PLD, in contrast to the simplicity of the set-up, is a very complex physical phenomenon. Which involves the physical process of the laser-material interaction of the impact of high-power pulsed radiation on a solid target and the formation of a plasma plume and the transfer of the ablated material through the plasma plume onto the heated substrate surface. PLD provides the best high controllability of the composition of the thin films and growth process with a controllable gas partial pressure, such as the ambient oxygen pressure and the control over the standards from other vacuum deposition techniques. It can also be deposited by controlling the fundamental criteria of the energy of the depositing flux (E), the substrate temperature (T), the relative and absolute arrival rates of atoms (Ri, where i could vary from 1 to 6). The majority of the materials used for PLD have strong absorption in the ranges between 200 nm and 400 nm laser wavelengths; which can easily achieve the energies required for a material to be transformed into a plasma [22]. Thus the thin film formation process in PLD generally can be divided into basically four stages:

1. Laser beam radiation interaction with the target.
2. Dynamics of ablation of materials and plume formation.
3. Deposition by evaporation of the ablation materials on the substrate.
4. The nucleation and growth of a thin film on the surface of the substrate.

These processes are displayed schematically in figure 3.7:

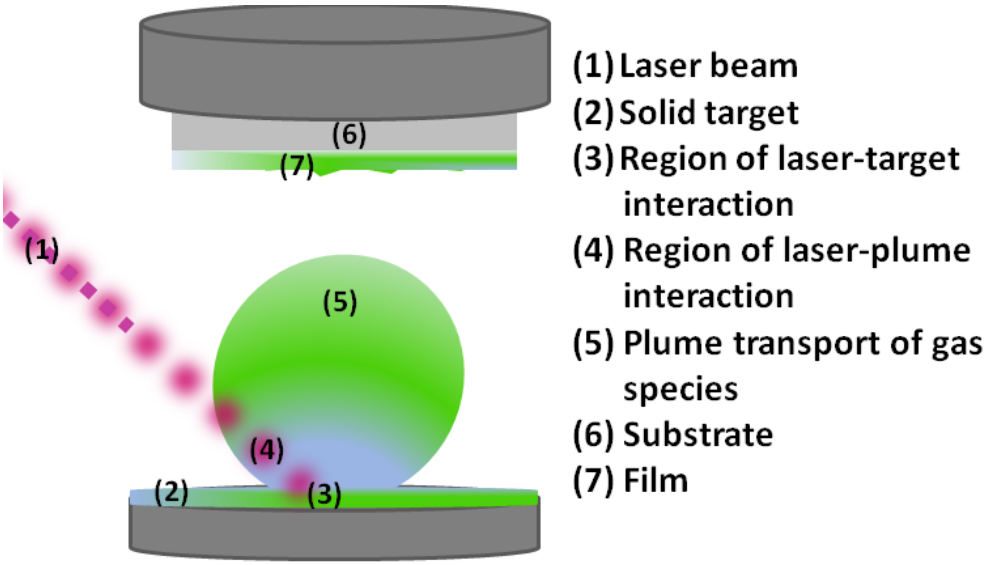

Figure 3.7: A schematic of the laser ablation process and its stages up to thin film formation [7].

When the laser beam radiation interacts with the target, the material is removed from the surface of an object by vaporization or other erosive processes called ablation. Where the laser beam is focused onto the surface of the target and all elements in the target are rapidly heated up to their evaporation temperature. The instantaneous ablation rate is dependent on the fluence of the laser hitting the target. The intensity of the laser light penetrating the surface of the target is [23]

$$I(x)=I(x_0)e^{-\alpha(x-x0)} \qquad (3.6)$$

where $I(x)$ is the reduced intensity at an ablated-layer of thickness x below the surface of the target, $I(x_0)$ is the intensity just before the incident laser light hit the target material, and α is the absorption coefficient of the target material. The Nd^{3+}:YAG laser and excimer lasers were used as the deposition sources in this project. It is useful to compare the advantages and disadvantages of Nd:YAG and excimer lasers. Nd:YAG lasers have a fundamental laser emission of 1064nm (from 1st to 5th harmonics) with respectively simple optical scheme and high power flux density. In order to achieve other wavelengths, nonlinear optics are used to frequency double to 532 nm. The 532 nm output is mixed with

residual 1064 nm or frequency doubled radiation to achieve the desired 3rd and 4th harmonics at the wavelength of 355 nm and 266 nm, most useable for PLD [7]. On the other hand, the excimer lasers have the flexibility in the repetition rate and high pulse energy in the ultraviolet range in contrast with 4th and 5th harmonics of Nd:YAG lasers. Table (3.2) displays the parameters of the Nd:YAG and excimer lasers.

Table 3.2: Performance parameters: excimer versus Nd:YAG laser systems. Sources: [25,26].

Laser type	**λ, nm**	**Pulse Energy, mJ**	**Photon Energy, eV**	**Repetition Rate, Hz**	**Pulse Duration, ns**
Excimer laser	193 (ArF)	50 - 600	6.42	Variable "1- 600"	4 - 34
	248 (KrF)	100 - 1200	5.0		
Nd:YAG laser	266 ($Nd:Y_3Al_5O_{12}$)	15 - 180	4.66	Fixed "0.1- 50"	4 - 18

Although visible or IR lasers have been used for PLD applications in the past, UV radiation is now most commonly employed. Among pulsed UV lasers, excimer lasers provide a variety of short wavelengths combined with energy levels that fit perfectly most PLD applications. In addition, it extends the range of possible target materials that can be used. It also enables a larger area on the target to be ablated with the desired fluence; in turn, this area enlargement increases the deposition rate and reduces the plume angle, resulting in higher deposition efficiency. Finally, higher pulse energy provides a larger process window, allowing a more consistent process [24].

During pulse duration time, the laser pulse is depositing energy on the target subsurface area, the energy is not dissipated. The heating is almost entirely localized at the irradiated area, lowering the threshold for ablation. Subsequently, less material is melted and re-fused, resulting in less recast, illustrated in figure 3.8.

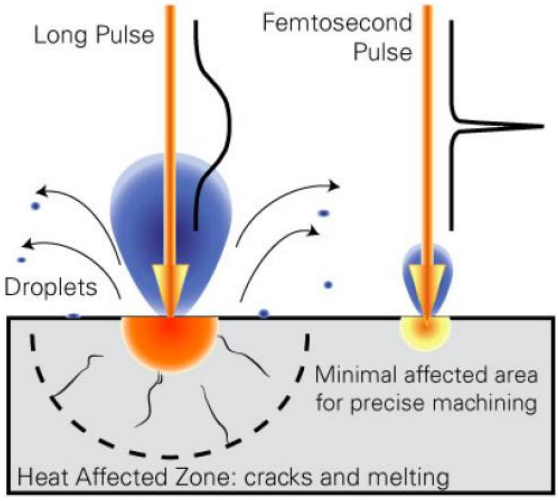

Figure 3.8: Difference between long (nanosecond) pulse and femtosecond pulse laser ablation.

The spot size of the laser and the plasma temperature has significant effects on the deposited film uniformity. The target-to-substrate distance is another parameter that governs the angular spread of the ablated materials.

Surface temperatures are observed to be dominated by pulse width effects for pulse times that are less than vaporization initiation times. Thus, for extremely short pulses the appearance of the vapor could be sufficiently delayed and decoupled from the initial pulse so that steep thermal-gradient-driven diffusion remains the only initially significant effect. For longer pulses, the normal latent heat and conventional vaporization process will control surface temperatures [27]. Once the ablation threshold of the target material is reached, the ionization of the target material induces plasma (plume) formation see figure 3.9, shown a schematic diagram of the typical PLD setup, a carousel capable of carrying up to six targets (25 mm in diameter) is situated inside a vacuum chamber connected to a turbo pump, target manipulation, substrate holder with heater, gas flow and vacuum gauging. A pulsed laser beam is focused onto a target of the material to be deposited, where the vapor (plume) is collected on a substrate place at a short distance from the target of typically 2-10 cm.

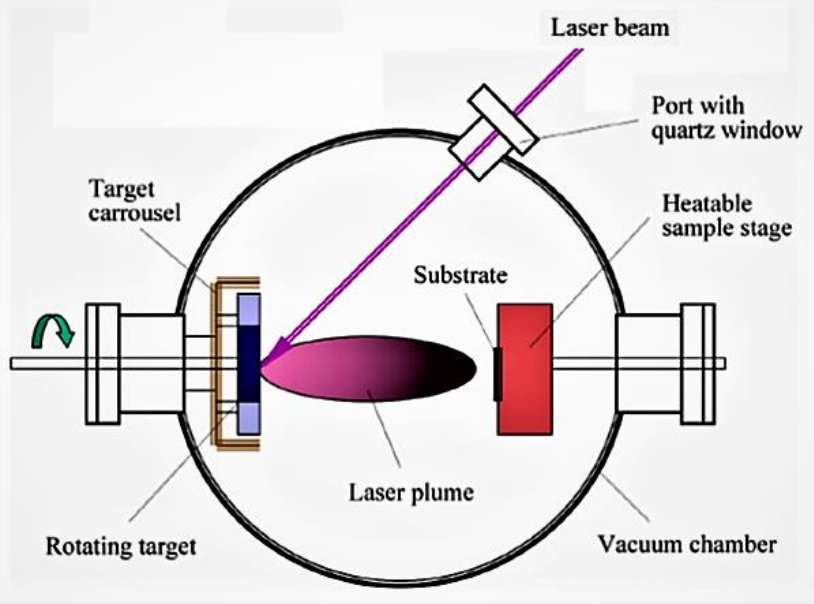

Figure 3.9: Schematic diagram of the PLD system, modified from [28].

In the ultrahigh vacuum (UHV) chamber, elementary or alloy targets are being struck at an angle of 45º by a pulsed and focused laser beam. Typical plasma temperature measured by emission spectroscopy during initial expansion is ≈ 10,000 K= 9,726.85 ºC), which is well above the maximum boiling point of most materials (≈ 3000 K =2,726.85 ºC) [28]. Heating of the plasma to these temperatures is thought to occur by inverse–Bremsstrahlung absorption of the laser light in a free – free transition of an electron-ion pair. This high temperature would evaporate the surface layer of the target thereby the atoms and ions ablated from the target are deposited on the substrates, which produces the exact composition in the thin films.

3.4.2 Advantages and disadvantages of PLD

Compared to many techniques used to prepare thin films deposition, such as magnetron sputtering, physical vapor deposition and chemical vapor deposition (CVD), metalorganic vapor phase epitaxy (MOVPE), sol-gel and spray pyrolysis, PLD has shown some outstanding advantages:

- PLD conceptually simplicity and flexibility in engineering design: a laser beam vaporizes a target surface, producing a film with the same composition as the target [29].
- High controllability of the composition of thin films and growth process with controllable gas partial pressure, such as ambient oxygen pressure [30].
- The rate of the film growth can be controlled by changing adjusting the laser parameters, deposition time, the substrate to target distance, etc [23].
- cost-effective: one laser can serve many vacuum systems and capable of producing multi-layers simply by switching between several different targets [28].
- Fast: high-quality sample can be grown reliably in 10 to 30 minutes [7].
- The biggest advantage is that it is versatile. A very wide range of materials, including oxides, metals, semiconductors and even polymers, can be grown by PLD. All that is required is a target of the desired composition. It differs from Molecular Beam Epitaxy (MBE) and (CVD) where a different source of precursors is required for each element of the compound [30].

On the other hand, it has some disadvantages

- The non-uniformity of the particulate size across the surface of the film. This non-uniform distribution of particulate size is due to the presence of molten material (up to ~ 10 μm) in the ablated material [23].
- There is an intrinsic "splashing" associated with laser ablation itself, which produces droplets or big particles of the target material on the substrate surface. From an industrial perspective, this is particularly serious as it will result in device failure [30].

Figure 3.10: shows photograph of the PLD system at the Department of Physics of the University of the Free State.

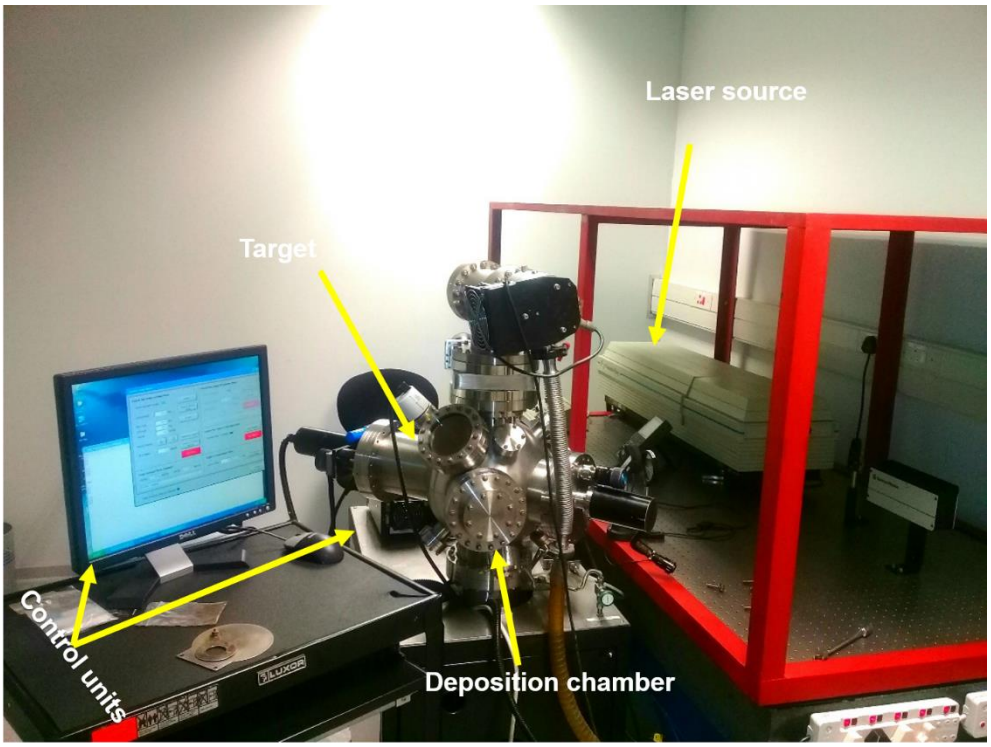

Figure 3.10: PLD system at the Department of Physics of the University of the Free State.

3.5 References

[1] S. N. Ogugua, Tunable multicolor emission from dysprosium-doped mixed rare-earths oxyorthosilicate nanophosphors for application in ultraviolet-pumped multicolour and white light emitting diodes, MSc. thesis, University of the Free State, (2015).

[2] R. D. Purohit and A. K. Tyagi. Auto-ignition synthesis of nanocrystalline $BaTi_4O_9$ powder. *J. Mater. Chem. A.* **12(2)** (2001) 312–316. DOI:10.1039/b103461h.

[3] S. V. Chavan and A. K. Tyagi, Preparation and characterization of $Sr_{0.09}Ce_{0.91}O_{1.91}$, $SrCeO_3$, and Sr_2CeO_4 by glycine–nitrate combustion: Crucial role of oxidant-to-fuel ratio. *J Mater Res.* **19(11)** (2004) 3181–3188. DOI:10.1557/jmr.2004.041.

[4] M. Lackner, Combustion synthesis: Novel routes to novel materials, Bentham Science Publishers, UAE (2009). ISBN: 978-1-60805-656-9.

[5] T. O. L. Sunde, T. Grande and M.-A. Einarsrud. Modified Pechini Synthesis of Oxide Powders and Thin Films. Handbook of Sol-Gel Science and Technology, 1–30 (2016). ISBN: 978-3-319-19454-7.

[6] H. Fang, B. Hu, L. Wang, R. Lu and C. Yang. Preparation of nanometer MgO by sol-gel auto-combustion. *Front Chem China.* **3(2)** (2008) 193–197. DOI:10.1007/s11458-008-0037-9.

[7] A. Yousif, V. Kumar, H. A. A. Seed Ahmed, S. Som, L. L. Noto, O. M. Ntwaeaborwa and H. C. Swart. Effect of Ga^{3+}Doping on the Photoluminescence Properties of $Y_3Al_{5-x}Ga_xO_{12}:Bi^{3+}$ Phosphor. *ECS J. Solid State Sci. Technol.* **3(11)** (2014) R222–R227. DOI:10.1149/2.0021412jss.

[8] S. T. Aruna and A. S. Mukasyan. Combustion synthesis and nanomaterials. *Curr. Opin. Solid St M*. **12(3-4)** (2008) 44–50. DOI:10.1016/j.cossms.2008.12.002.

[9] A. Yousif, R. M. Jafer, S. Som, M. M. Duvenhage, E. Coetsee and H. C. Swart, Ultra-broadband luminescent from a Bi-doped CaO matrix. *RSC Adv*, **5(67)** (2015) 54115–54122. DOI: 10.1039/c5ra09246a.

[10] S. Roy, W. Sigmund and F. Aldinger. Nanostructured Yttria Powders Via Gel Combustion. *J Mater Res*. **14(04)** (1999) 1524–1531. DOI:10.1557/jmr.1999.0204.

[11] G. Xia, S. Zhou, J. Zhang and J. Xu. Structural and optical properties of YAG:Ce^{3+} phosphors by sol–gel combustion method. *J. Cryst. Growth*. **279(3-4)** (2005) 357–362. DOI:10.1016/j.jcrysgro.2005.01.072.

[12] W. A. I. Tabaza, Synthesis, and characterization of $MgAl_2O_4$ and $(Mg_xZn_{1-x})Al_2O_4$ mixed spinel phosphors, Ph.D. thesis, University of the Free State, Bloemfontein, South Africa, (2014).

[13] R. Figueira, I. Fontinha, C. Silva and E. Pereira. Hybrid Sol-Gel Coatings: Smart and Green Materials for Corrosion Mitigation. *Coatings*. **6(1)** (2016) 12. DOI:10.3390/coatings6010012.

[14] D. P. Birnie. Spin Coating Technique. Sol-Gel Technologies for Glass Producers and Users, *Springer Science + Business Media New York* (2004) 49–55. ISBN: 978-1-4419-5455-8, 978-0-387-88953-5.

[15] S. Franssila. Introduction to Microfabrication, 2nd Ed., John Wiley & Sons (Chichester, 2010). ISBN 10: 0470851066.

[16] J. Tamarit-López, S. Morais, R. Puchades and Á. Maquieira. Use of polystyrene spin-coated compact discs for microimmunoassaying. *Anal. Chim. Acta*. **609(1)** (2008) 120–130. DOI:10.1016/j.aca.2007.12.028.

[17] P. Saravanan, G. V. Ramana, K. S. Rao, B. Sreedhar and A. Perumal. Thin magnetic films of Sm–Co nanocrystallites exploiting spin coating deposition. *Thin Solid Films*. **519(19)** (2011) 6290–6296. DOI:10.1016/j.tsf.2011.03.131.

[18] N. Sahu, B. Parija and S. Panigrahi. Fundamental understanding and modeling of spin coating process: A review. *Indian J. Phys.*, **83(4)** (2009) 493–502. DOI:10.1007/s12648-009-0009-z.

[19] A. Suzuki, T. Matsushita, Y. Sakamoto, N. Wada, T. Fukuda, H. Fujiwara and M. Okuda. Surface Flatness of Transparent Conducting ZnO:Ga Thin Films Grown by Pulsed Laser Deposition. *Jpn. J. Appl. Phys.* **35(Part 1, No. 10)** (1996)5457–5461. DOI:10.1143/jjap.35.5457.

[20] F. Ronci, P. Reale, B. Scrosati, S. Panero, V. Rossi Albertini Perfetti, P. Perfetti, V. Rossi Albertini, M. di Michiel and J. M. Merino. High-Resolution In-Situ Structural Measurements of the Li4/3Ti5/3O4"Zero-Strain" Insertion Material. *J Phys Cem B*. **106(12)** (2002) 3082–3086. DOI:10.1021/jp013240p.

[21] R. M. Jafer, Luminescence properties of $Y_2O_3:Bi^{3+}$ as powder and thin film phosphor for solar cell application, PhD thesis, University of the Free State, (2015).

[22] D. Bäuerle. Thin-Film Formation by Pulsed-Laser Deposition and Laser-Induced Evaporation. *Laser Processing and Chemistry*, (2011) 489–531. DOI:10.1007/978-3-642-17613-5_22.

[23] O. S. Nnalue. Preparation and characterization of powders and pulsed laser deposited thin films of rare-earths doped oxyorthosilicates. PHD thesis, University of the Free State, (2017).

[24] R. Delmdahl and R. Pätzel. Pulsed laser deposition with excimer lasers. *Phys. Status Solidi C*. **5(10)** (2008) 3276–3279. DOI:10.1002/pssc.200779515.

[25] R. E. Treece, J. S. Horwitz, J. H. Claassen and D. B. Chrisey. Pulsed laser deposition of high-quality NbN thin films. *Appl. Phys. Lett.* **65(22)** (1994) 2860–2862. DOI:10.1063/1.112516.

[26] R. Delmdahl and R. Pätzel. Pulsed laser deposition with excimer lasers. *Phys Status Solidi c*. **5(10)** (2008) 3276–3279. DOI:10.1002/pssc.200779515.

[27] P. P. Pronko, S. K. Dutta, D. Du and R. K. Singh. Thermophysical effects in laser processing of materials with picosecond and femtosecond pulses. *J. Appl. Phys*. **78(10)** (1995) 6233–6240. DOI:10.1063/1.36057.

[28] R. Manoj. Characterisation of Transparent Conducting Thin Films Grown by Pulsed Laser Deposition and RF Magnetron Sputtering. Department of Physics Cochin University of Science and Technology Cochin – 682 022, Kerala, India, (2006).

[29] T. Yoshitake, T. Hara and K. Nagayama. The influence of the repetition rate of laser pulses on the growth of diamond thin films by pulsed laser ablation of graphite. *Diam. Relat. Mater*. **12(3-7)** (2003) 306–309. DOI:10.1016/s0925-9635(02)00333-3.

[30] Y. Hsiu. Structure and properties of transparent conductive ZnO films grown by pulsed laser deposition (PLD). MS.c thesis The University of Birmingham, (2009).

Chapter 4: Characterization techniques

In this chapter, a brief description of the techniques that were used in the characterization of the powders and thin films is presented.

4.1 Introduction

This chapter gives a brief description of the theory behind the different research techniques used to characterize the phosphor materials. These include several surface, structural and optical techniques. The techniques include X-ray diffraction (XRD) which was used to determine the crystalline structure phases and quality of the phases; Scanning electron microscopy (SEM) was used to study the morphology; Energy dispersive spectroscopy (EDS) was used to acquiring elemental maps or spot chemical analyses; photoluminescence (PL) and cathodoluminescence (CL) were applied to investigate the luminescence characteristics; Ultraviolet-visible spectroscopy (UV-Vis spectroscopy) to detect the absorption positions and known band gap by reflectance; Auger electron spectroscopy (AES) was used to monitor changes in the surface chemical composition for the powders and thin films and to measure depth profiles of the thin films and detect degradation for elements under the electron beam irradiation; X-ray photoelectron spectroscopy (XPS) was used to explore the atoms in the sample surface and identify the oxidation state of the dopant ions; atomic force microscopy (AFM) was used for morphological and topographical analysis of the thin films; Time-of-flight Secondary Ion Mass Spectrometry (ToF SIMS) was used for spectral analysis to determine depth profiles, three-dimensional analysis and ion mapping. These techniques are discussed in detail in the following sections.

4.2 X-ray diffraction (XRD)

XRD is a technique that had been discovered in 1912 by Von Laue. It was used to determine the crystalline structure of solid materials of powders, thin films, sheets, fibers, metals, ceramics, organics, polymers and electronic materials. It can also be used for the identification of phases, lattice constants, determination of crystallite size and the degree of crystallinity in a mixture of amorphous and crystalline materials [1].

The general information about the structure of inorganic materials is available in the powder diffraction files (PDF) of the international center for diffraction data (ICDD) [2], which can be used as the database for phase and structure identification. The use of XRD to determine crystal structure was first suggested by Von Laue in 1912 and it was further developed by Bragg in 1913 and is now a well-developed technique [3].

The X-ray diffractometer consists of three basic elements: an X-ray tube (to generate monochromatic X-rays of a known wavelength), a sample holder and an X-ray detector, see (figure 4.1) [4].

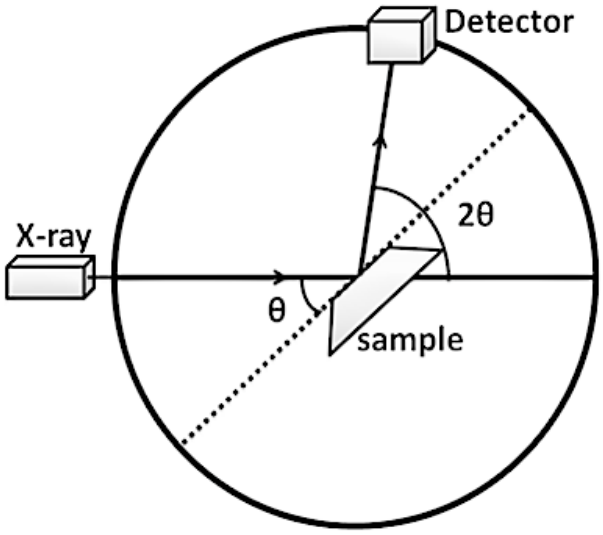

Figure 4.1: Schematic diagram of an X-ray diffractometer [4].

X-rays are electromagnetic radiation with a wavelength between 0.1 and 10.0 Å located in the region between ultraviolet and gamma rays [1]. It can be produced in a cathode ray tube when heating a filament to produce electrons which are accelerated to

produce a high-energy electron beam, which bombards a metal target with sufficient energy to dislodge the inner shell electrons of the target material, producing characteristic X-rays in the process [5].

The X-ray spectra consist of many components, and the most prevalent is the K_α and K_β. The target materials that are usually used in XRD are Cu, Fe, Mo, and Cr. Each of these has different specific characteristic wavelengths [6]. Cu is the most commonly target material used for single crystal diffraction with a wavelength of 1.5406 Å. A suitable metal filter, such as a Ni filter, is used to get monochromatic X-rays, which strongly absorbs the Kβ. λ = 1.3922 Å, radiation and provides monochromatic radiation (λ =1.5406 Å) for the experimental setup figure 4.2. The resulting X-rays after filtering are directed onto the rotated sample and the intensity of the diffracted X-rays is then recorded using a detector [6].

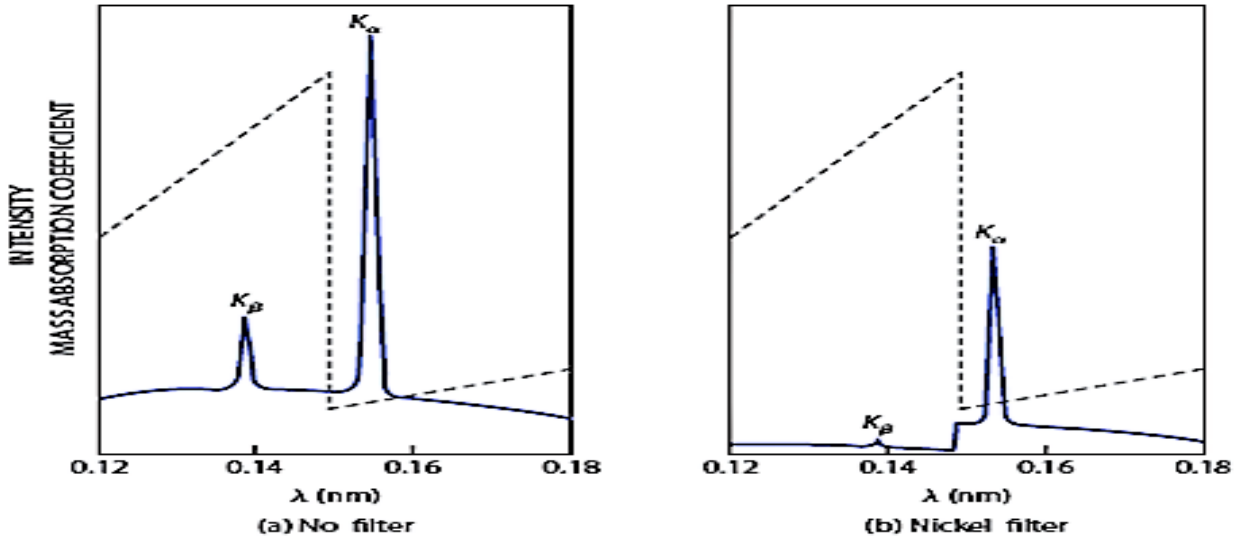

Figure 4.2: The characteristic X-ray emission obtained from a copper (Cu) target with a nickel (Ni) filter [1].

When the X-ray incident on a sample satisfies the equation of Bragg, constructive interference occurs, and the characteristic peak of the diffraction will be observed.

4.2.1 Bragg's law of diffraction

When an incident X-ray wave approach the material, it interact primarily with electrons in the atoms, the scattering will produce a diffraction pattern with sharp maximum (peaks) at certain angles which specify the description of the material. The peaks in the X-ray diffraction pattern are directly related to the interatomic distances [7].

The interaction of the incident rays with the sample produces constructive interference when the conditions satisfy Bragg's Law as expressed in the equation (4.1):

$$n\lambda = 2d\sin\theta \qquad (4.1)$$

This law is defined as Bragg's law, after W.L. Bragg, who first proposed it [8]. In equation 4.1, (λ) the wavelength of X-rays and θ is half of the scattering angle, which is the Bragg angle. Thus measuring the diffraction angles will allow for the inter-planar distance (d) to be calculated. n is an integer representing the order of the diffraction.

The angle between the transmitted and diffracted beams will be equal to 2θ because of the geometry of the Bragg's condition. It can be obtained readily in the experimental situations and the results of the X-ray diffraction are therefore given in terms of 2θ. The angle that is used in Bragg's equation must correspond to the angle between the incident radiation and the diffracting plane, i.e. θ [9].

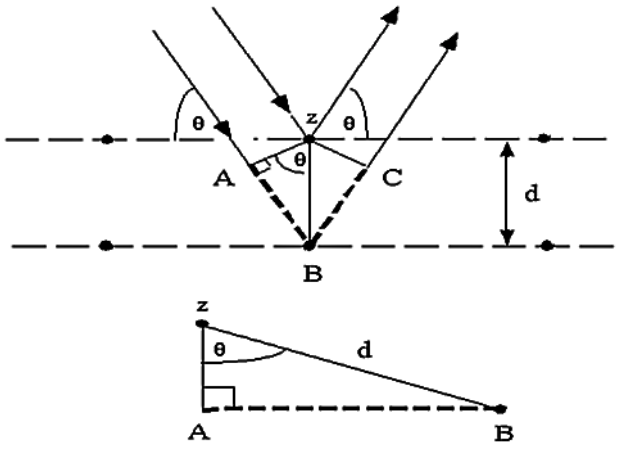

Figure 4.3: Schematic diagram of Bragg diffraction from a set of arrangements atoms.

The lattice parameters can be related to the Miller indexes *(hkl)* of each reflection plane and inter-planar distance d_{hkl}. For cubic structures (our samples are cubic) a lattice parameter *a* can be formulated as [10].

$$a = d_{hkl}\sqrt{h^2 + k^2 + l^2} \qquad (4.2)$$

Scherrer first observed in1918 that a small crystallite size could induce peak broadening of the XRD spectra. Scherrer's equation is given in eq 4.3 [1].

$$D = \frac{k\lambda}{\beta Cos\theta} \qquad (4.3)$$

where *D* is the mean size of the crystallites, *k* is the shape factor (in this work *k* is taken as 0.9 [11]), β is the full width at half maximum (FWHM) of a diffraction line located at an angle θ of on XRD *and* θ is the diffraction angle.

We calculated the strain (see chapter 5) induced in the powders due to crystal imperfection and distortion by using the formula:

$$\varepsilon = \frac{\beta}{4\tan\theta} \qquad (4.4)$$

For estimating crystallite size and lattice strain using the Williamson-Hall analysis, the Williamson-Hall equation 4.5 is

$$\beta \cos\theta = K\lambda / D + 4\varepsilon \sin\theta \qquad (4.5)$$

In the linear relation between 4sinθ along the x-axis and βcosθ along the y-axis, the crystalline size can be estimated from the y-intercept and the strain ε from the slope of the line [12].

In this study, the XRD data were obtained using a Bruker D8 Advance X-ray diffractometer equipped with a Cu anode X-ray tube figure 4.4. It was operated using a 40 mA filament

current and a generator voltage of 40 kV to accelerate the electrons. The scans were measured in the $\theta-2\theta$ configuration in the range of 20 – 70 ° in a step size of 0.0094°.

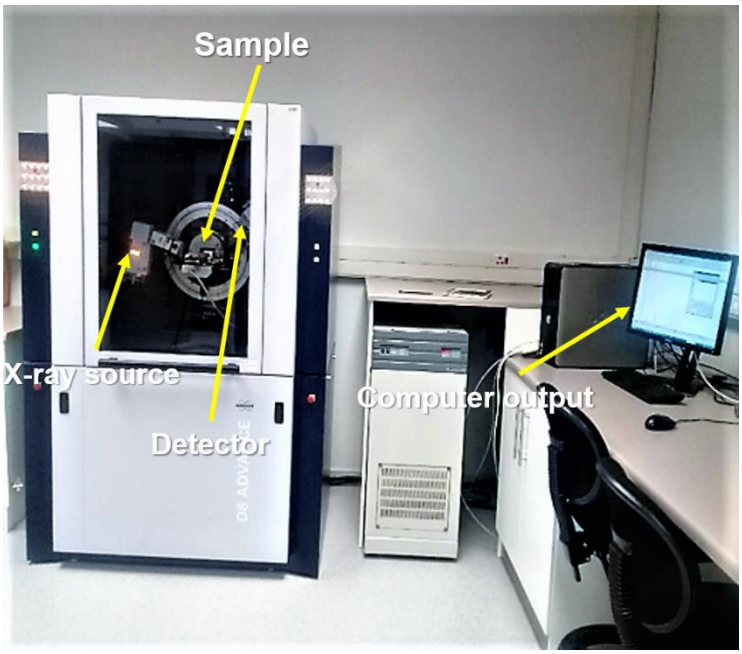

Figure 4.4: Bruker D8 Advance X-ray diffractometer at the Department of Physics, University of the Free State.

4.3 Scanning Electron Microscopy (SEM)

Scanning Electron Microscopy (SEM) is a technique that can be used to provide information about the sample including external morphology (texture), crystalline structure and orientation of materials making up the sample by producing images of the sample surface, in which SEM can also be used to perform energy-dispersive X-ray spectrometer (EDS) measurements to determine the chemical composition [13]. In most applications data is collected over a given area of the surface of the sample and a 2-dimensional image is generated that displays spatial variations in these properties.

Areas ranging from approximately 1 cm to 5 microns in width can be imaged in a scanning mode using the conventional SEM technique (magnification ranging from 20X to

approximately 30,000X, the spatial resolution of 50 to 100 nm) [14]. Figure (4.5) shows a simple schematic of SEM where the electrons are generated from an electron gun and then focused and accelerated onto the sample's surface. This electrons contain a significant amount of kinetic energy. This energy is dissipated by producing a variety of signals when the electrons in the solid sample slow down. These include secondary electrons, X-ray photons, Auger electrons, backscattered electrons, diffracted backscattered electrons, and heat. The backscattered electrons and secondary electrons are used to image the samples' surfaces. Secondary electrons provide information on the morphology and topography of the samples while backscattered electrons are used for illustrating contrasts in the compositions in multiphase samples (i.e. for rapid phase discrimination) [15].

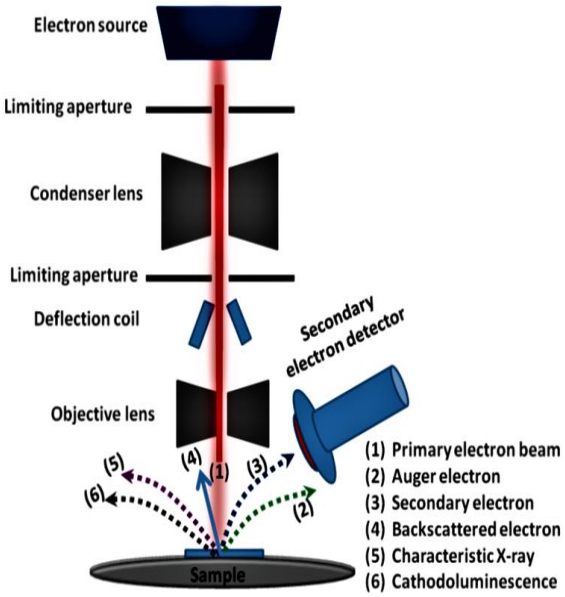

Figure 4.5: Schematic presentation of the field emission scanning electron microscopy [16].

Secondary electrons are emitted due to an inelastic scattering process close to the surface layers (100 nm) of a sample, hence, they are then detected, converted to a voltage and amplified to produce an image. Backscattered electrons are generated due to electron reflected from the sample through elastic scattering, hence, they have energy comparable to that of the incident electrons. The SEM images of this study were collected by using a

JEOL JSM-7800F high field emission scanning electron microscope (FE-SEM) equipped with an EDS, see figure (4.6).

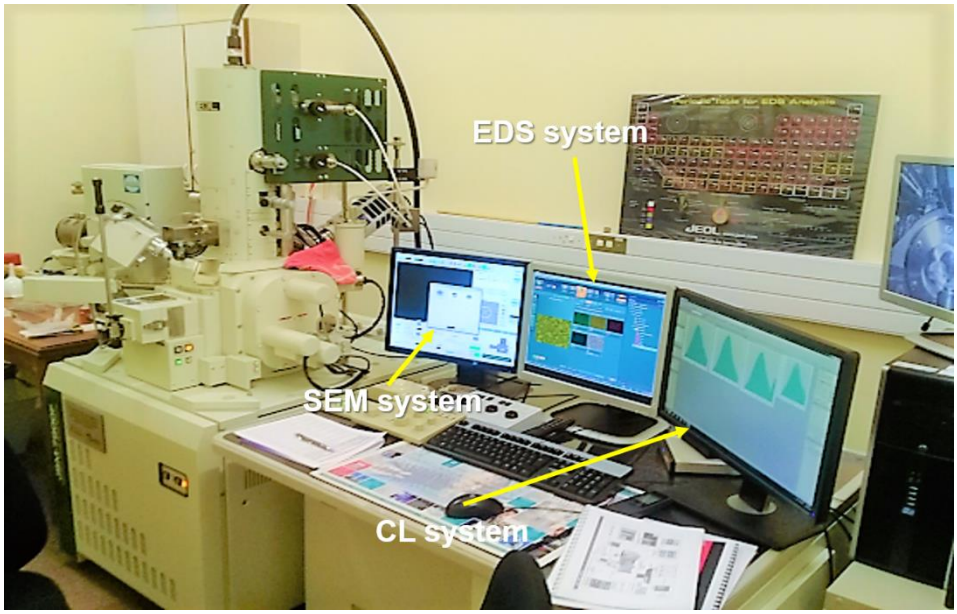

Figure 4.6: JEOL JSM-7800F system a typical SEM instrument, showing the electron column, sample chamber, EDS detector, electronics console, and visual display monitors, University of the Free State.

4.4 Energy dispersive X-rays spectroscopy

Energy Dispersive X-Ray Spectroscopy (EDS) is a chemical microanalysis technique used to determine the chemical composition of a sample. This technique can be used in conjunction with SEM. The EDS technique detects X-rays emitted from the sample during the bombardment by an electron beam to characterize the elemental composition of the analyzed volume. Features or phases as small as 1 μm or less can be analyzed [15]. When the sample is bombarded by an SEM-electron beam, electrons are expelled from the atoms that comprise the sample surface. Electrons from some higher state fill these electron vacancies and X-rays are emitted to balance the energy difference between the two states [15]. The atom within the sample contains ground state or “unexcited” electrons, situated in probability shells around the nucleus. Where the incident beam excites an electron in an

inner shell by the external energy source, prompting its ejection and resulting in the formation of a hole within the atom's electronic structure, then the excess energy is released in the form of an X-ray [9] see figure 4.7.

The EDS X-ray detector measures the relative abundance of X-rays emitted relative to their energy. The detector is usually a lithium-drifted silicon, solid-state device. When the X-ray device hits the detection detector, it creates a charge pulse proportional to the X-ray energy. The charge pulse is converted to the voltage pulse (which remains proportional to the X-ray energy) by the sensitive preamplifier of the charge [6]. The signal is then sent to a multi-channel analyzer where a potential is used to sort the pulses. The energy, as specified by the voltage measurement, is determined for each X-ray incident to a computer for viewing and further evaluation of the data. The spectrum of the X-ray energy is assessed against the charges to determine the elemental composition of the sample size [6].

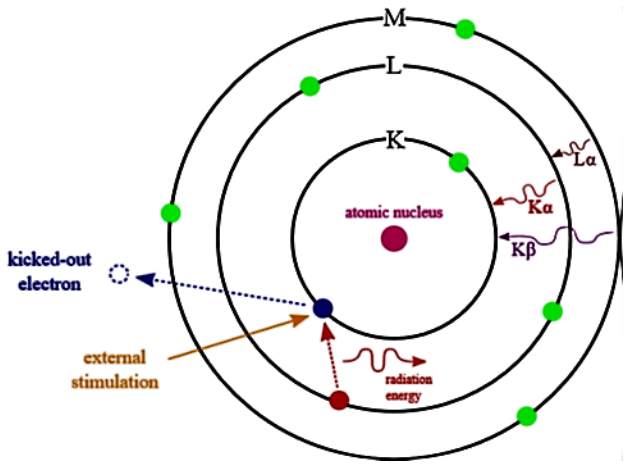

Figure 4.7: Schematic of emitted characteristic X-rays in an atom [6].

In this study the EDS data were collected by using Oxford Instruments X-Max^{N}-80 detector attached to the SEM, see figure 4.6.

4.5 UV-Vis spectroscopy

4.5.1 Absorption measurements

UV-Vis spectroscopy is used for the measurement of the absorption, reflection or transmission of light incident on a sample. When an ultraviolet or visible light beam is incident on the surface it either passes through the sample or reflects or is absorbed from a sample surface to the electronic transitions of the material. The simplest measurements can be done for liquid samples or transparent solid samples.

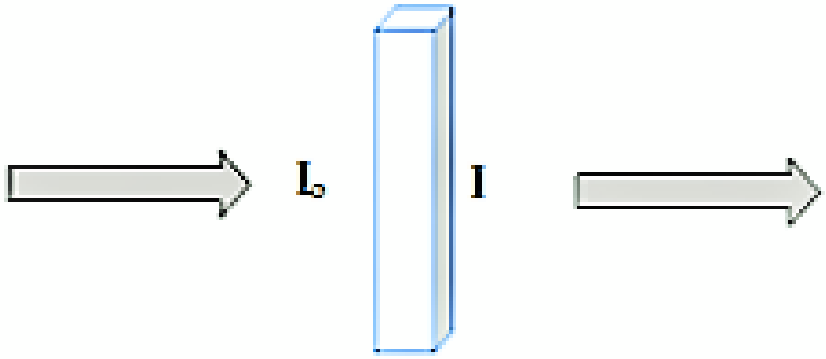

Figure 4.8: Incident and transmitted light.

The transmittance *(T)* is the ratio between the transmitted light *(I)* and the incident light *(I_o)*

$$T = \frac{I}{Io} \qquad (4.6)$$

and the absorbance *(A)* is the logarithmic ratio between the incident and the transmitted radiation intensities

$$A = \ log \frac{I_0}{II} = \epsilon lc = \ \alpha c. \qquad (4.7)$$

I_o and I can be measured experimentally and thus A can be determined. Beer's law states that the absorbance is proportional to concentration, hence the rest of the equation follows where ϵ is the molar absorptivity, l is the length of the sample, c is the sample concentration and α is the absorption coefficient. The absorption coefficient is wavelength dependent and a plot of α as a function of the wavelength is known as the absorption spectrum [17].

The basic parts of the UV spectrophotometer are light sources with a monochromator so that only the light of a single wavelength is emitted at one time. A machine often has two lamps, a deuterium lamp for the UV region and a tungsten lamp for the visible region [18], with the transition usually set near 330 nm and controlled by the software. A beamsplitter divides the light into two paths, either through the sample or a reference path, before it reaches the detector to give *I* and I_o, respectively, as presented in figure 4.9.

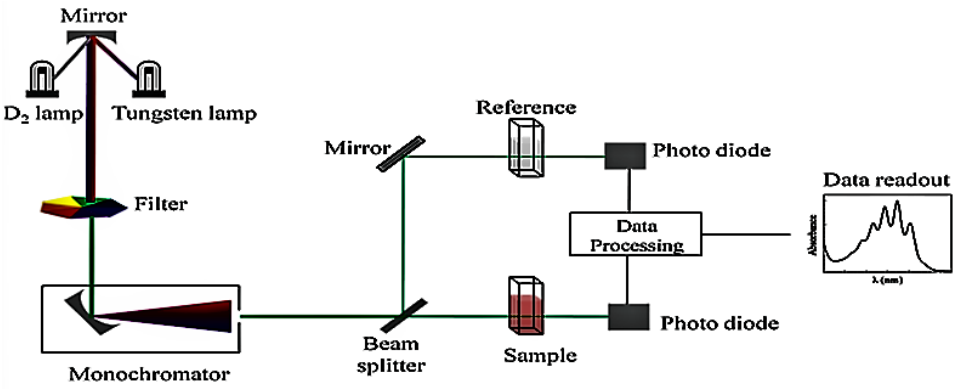

Figure 4.9: Schematic of a dual-beam UV-Visible spectrophotometer [12].

4.5.2 Determination of the energy band gap using reflection measurements

The optical band gap energy can be obtained from the UV-vis absorption edge using the well-known Tauc law relation [19].

$$\alpha h\upsilon = C_1(h\upsilon - E_g)^m \qquad (4.8)$$

where $h\upsilon$ is the incident photon energy, α is the absorption coefficient, C_1 is constant, E_g is the optical gap energy and *m* which depends on the type of electronic transition responsible for absorption. For direct band gap m equal 1/2 for allowed transition and 1/3 for forbidden transition, while for indirect bandgap *m* equal 2 for allowed transition and 3 for the forbidden transition. For example, in our materials SrO, it has a direct band gap, *Eg* can easily obtained by extrapolating the linear fitted regions to $[\alpha h\upsilon]^2 = 0$, By plotting $[\alpha h\upsilon]^2$ against $h\upsilon$ and fit the linear region with a line and extend it to the energy axis.

In the case of reflectance data when the material scatters in a perfectly diffuse manner the following Kubelka-Munk relation equation 4.9 can be used to obtain a quantity *F* which is proportional to the absorption coefficient

$$F(R_\infty) = (1 - R_\infty)^2/(2R_\infty) = 2\alpha/S \qquad (4.9)$$

where $R_\infty = R_{sample}/R_{reference}$ and *S* is scattering coefficient [19]. Assuming S is constant, using equations (4.8) and 4.9 can be combined as follows:

$$[F(R_\infty)*hv]^{0.5} = C_2\,(hv - E_g) \qquad (4.10)$$

To obtain *Eg* one can plot $[F(R\infty)*hv]^{0.5}$ against *hv* and fit the linear region with a line and extend it to the energy axis

Our diffuse reflectance spectra were recorded with a spectrophotometer with an integrating sphere that exhibits reflectance close to 100% reflectance in the wavelength range from near UV to the near IR. In this study, the Lambda 950 UV–Vis spectrophotometer, with an integrating sphere, was used to obtain the diffuse reflectance spectra, see figure 4.10.

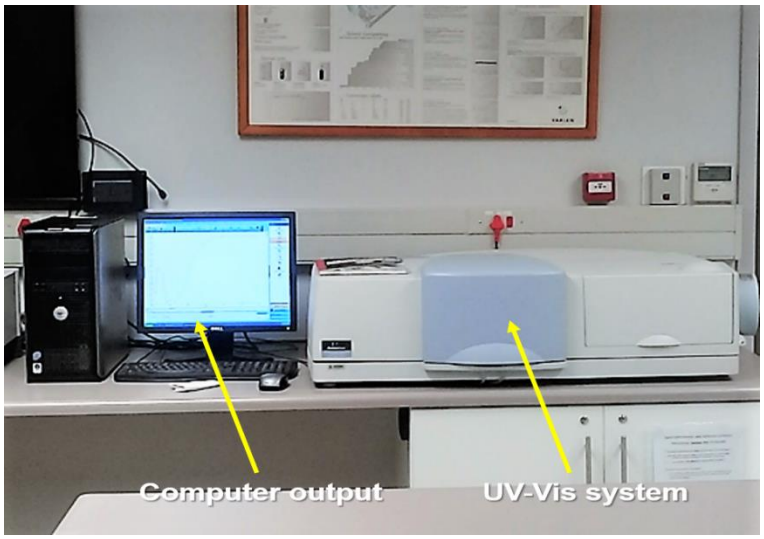

Figure 4.10: The Lambda 950 UV-Vis (Perkin Elmer Lamb) spectrophotometer at the Department of Physics, University of the Free State.

4.6 Photoluminescence spectroscopy

In photoluminescence (PL) spectroscopy light is directed onto a sample where it is absorbed and adds excess energy in the material in a process called photo-excitation (by absorbing a photon). Electrons get excited from the ground electronic state to one of the various vibrational excited states. This type of transition dependents on the photon's energy which will have different energies. Then drops to one of the vibrational levels of the ground electronic state emitting a photon during the process. A schematic diagram of the PL technique is presented as visualized with the Jablonski diagram shown in figure (4.11).

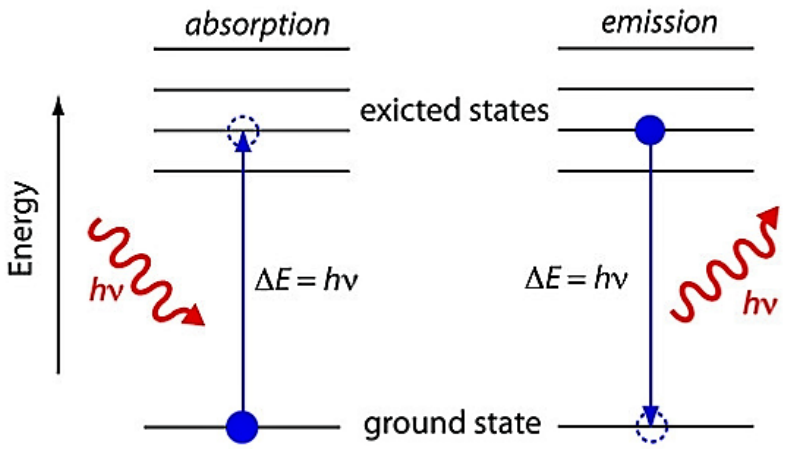

Figure 4.11: Simplified schematic energy diagram showing the excitation and emission involved in the photoluminescence process.

The excitation sources produce photons (Xenon lamp); this supplies excitation energy to the sample. The emitted luminescence is dispersed in a spectral device, the detector converts the optical signal to an electrical signal processed by electronic devices and finally by a controller computer. For an excitation scan the wavelength of the excitation light is varied while the emitted light intensity at a constant emission wavelength is monitored. Quite the opposite occurs for the emission spectrum which is a distribution of the emission intensity as a function of the wavelength measured at a fixed excitation wavelength. The excitation spectrum, to a good approximation, is assumed to be identical

to absorption if there is not any multiple overlapping of the excited states [17] and if all excitation leads to radiative recombination at the set emission wavelength.

In this study, a Cary Eclipse fluorescence spectrophotometer and a 325 nm He-Cd laser PL system were used for PL measurements. In figure 4.12 a schematic diagram of the process for the Cary Eclipse PL measurements is shown. The technique consists of a light source (xenon flash lamp) that produces photons. Xenon lamps are useful because of their high intensity at all wavelengths ranging upward from 250 nm [12]. In addition, it is equipped with PMT detector that exhibits a wide excitation spectrum range between 200 and 1200 nm. The output of the PMT signal is amplified and recorded. The measurements can be made by using both the fluorescence mode and the phosphorescence mode. The fluorescence emission was collected and measured when the lamp flashes, and in the phosphorescence mode is measured after the lamp has stopped flashing. All measurements were done in the fluorescence mode at room temperature.

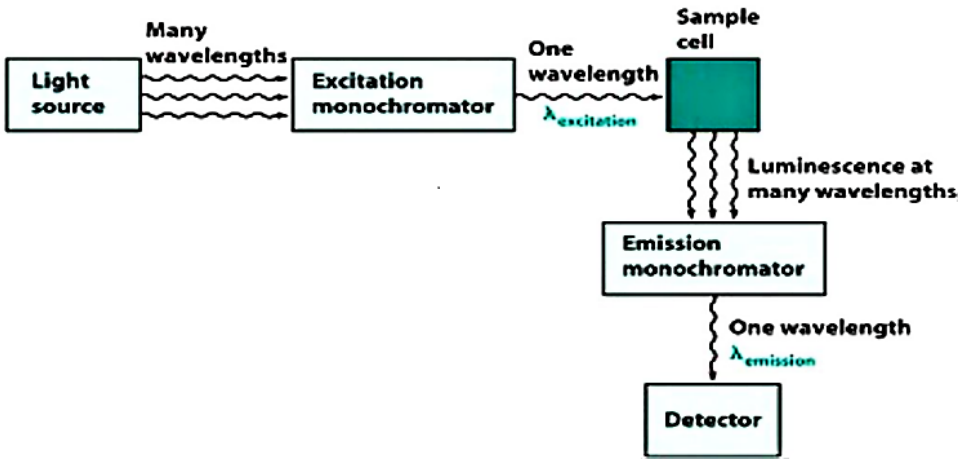

Figure 4.12: Schematic diagram of PL spectrometer, modified from [20].

On the other hand, the He-Cd laser system excites by using only a fixed wavelength of 325 nm. In figure 4.13 a schematic diagram for the typical structure system using a He-Cd laser is shown. The laser is composed of a tube, terminated by two Brewster's angle windows, with two laser mirrors mounted separately from the tube [21]. Inside the tube filled with helium also a reservoir containing the Cd and a heater to vaporize the metal.

The He-Cd lasers can give output powers of 50-100 mW and it can produce a high-quality beam at 442 nm (violet-blue) and/or 325 nm (UV) depending on the optics.
The monochromator has diffraction gratings, which serve as an engine of the entire optical measurement system where it is used to differentiate between emissions at different photon wavelengths, which are detected using a PMT [22].

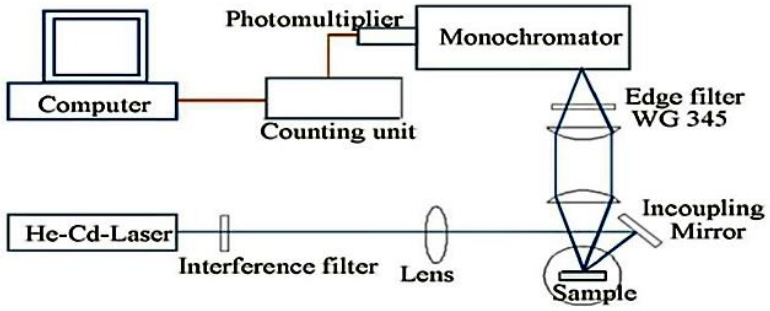

Figure 4.13: Schematic diagram of the PL system with a He-Cd laser with a fixed wavelength of 325 nm [23].

The emission and excitation spectra for the powder samples were measured using a Cary Eclipse fluorescence spectrophotometer as presented in figure 4.14.

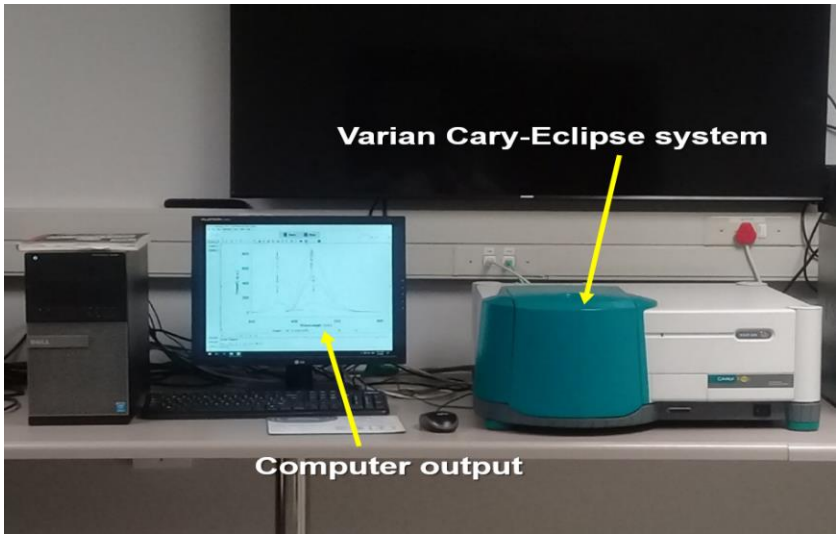

Figure 4.14: Varian Cary-Eclipse fluorescent spectroscopy at the Department of Physics, University of the Free State.

The emission spectra for the thin films samples were measured using the He-Cd laser spectrometer is presented in figure 4.15.

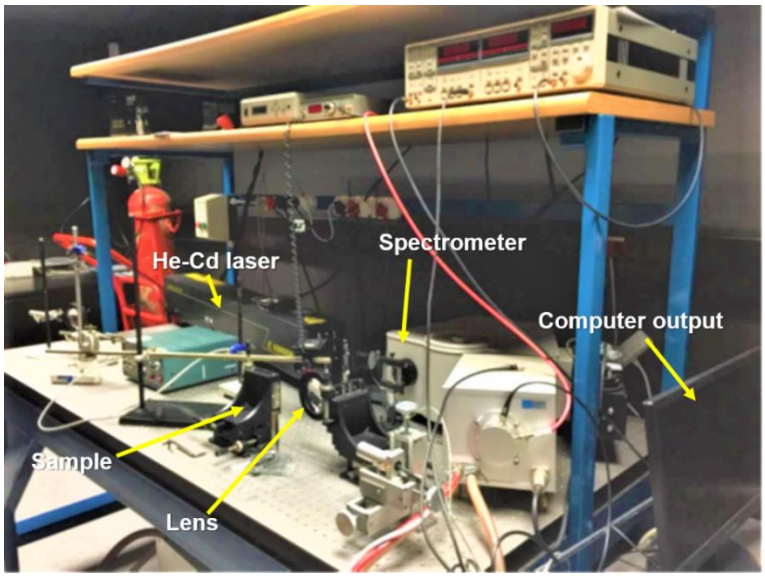

Figure 4.15: A typical PL laser system with an excitation wavelength of 325 nm at the Department of Physics, University of the Free State.

4.7 Cathodoluminescence spectroscopy (CL)

Cathodoluminescence is a process where the luminescence results from excitation by high energy electrons. Where a beam of electrons impacts on a luminescent material such as a phosphor, that results in the emission of photons. When a high energy electron beam impinges on materials, it will excite electrons from the valence band to the conduction band, leaving holes in the valence band. With electron-hole recombination, then a photon to be emitted [9]. CL can be used to investigate defects caused by impurities as well as other investigations in mineralogy, geology, and materials science [21]. In this study, the CL data were collected by two systems: a JEOL JSM-7800F high field emission scanning electron microscope (FE-SEM) equipped with EDS figure 4.6 and 549 Auger system with an S200 /PC2000 /USB2000 /HR2000 spectrometer type using OOI Base 32 computer software figure 4.17.

In the first system (JEOL JSM-7800F), the measurements can be done in two different modes, namely, monochromatic (by single wavelength) and panchromatic (all wavelengths of visible light). For the monochromatic mode, the focused e-beam is either scanned over the sample or positioned on the desired point. Thus the light emitting from the sample, passing through the monochromator, result in a spectrum. In the panchromatic mode, all light is directed at the detector where full wavelengths emitted from the sample contribute to a panchromatic photon map resulting spectrums [22].

The second system (the PHI 549 Auger), the powders were pressed into small holes of less than 1 mm that were drilled into a Cu sample holder. The holders and the Faraday cup were placed in the carousel. The Faraday cup function is to measure the electron beam size. The carousel was introduced into the vacuum chamber. After obtaining the desired vacuum, then will accelerated the electrons towards the sample. Then the CL emission spectrum is obtained by plotting an intensity against the wavelength of light emitted from the sample, collected using a spectrometer and recorded by a computer. In this system, the phosphor was subjected to an electron beam of the current density of 1.27 mA cm^{-2}, with a working beam voltage of 2 kV.

To determine the electron beam size was used in measurements, the beam current was measured while moving the edge of the Faraday cup perpendicular to the electron beam. The beam current as function of the distance moved by the edge of the Faraday cup was differentiated and plotted. The diameter of the electron beam is taken as the width at half-maximum. Figure (4.16) shows the beam current as a function moving distance of the edge of the Faraday cup. The electron beam size was found to be around 1.422 mm.

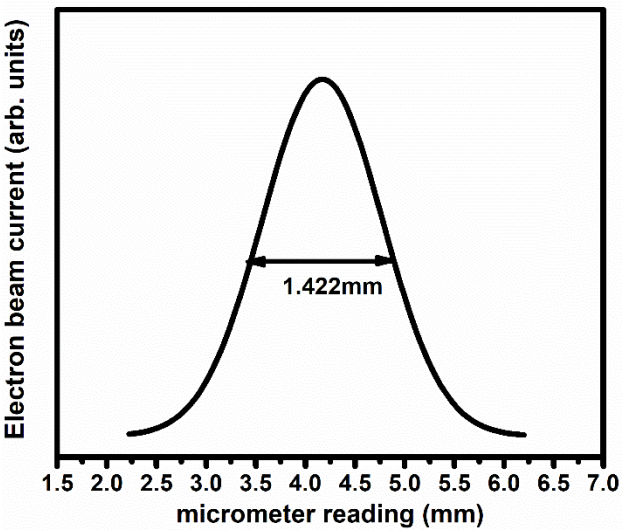

Figure 4.16: The beam current against moving distance of the edge of the Faraday cup.

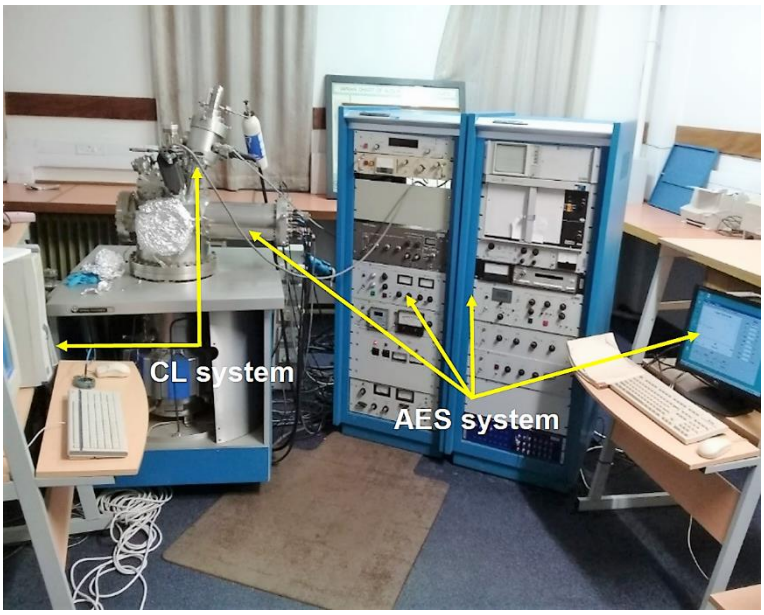

Figure 4.17: PHI, model 549, AES unit at the Department of Physics, University of the Free State.

4.8 Auger electron spectroscopy (AES) system

Auger electron spectroscopy (AES) was developed in the late 1960s, deriving its name from the effect first observed by Pierre Auger, a French physicist, in the mid-1920s

[23]. It is a surface analytical technique and it can determine the chemical composition of the surface layers of a sample with a shallow depth of about five monolayers from which data is taken [24]. All elements can be detected using this technique except H and He, because they do not have electrons occupying the L level (have less than three electrons) [24]. In the Auger process, a high-energy primary electron (2-10 keV) hits and release an electron from the core level (e.g. K level) thus ionizing the atom. The ionized atom that remains after the removal of the core hole-electron is in the highly excited state and will quickly relax back to a lower energy state. The electron from the higher level (L_1 level) will drop to the lower level to fill the void caused by the liberated electron, so that the atom will reorganize itself to a lower energy state. The energy released in the transition is either emitted as a photon or transferred to another electron in the higher level (L_2 level). So if the energy is sufficient, the electron can be ejected from the surface and detected as an Auger secondary electron. Auger electrons have relatively low kinetic energy, limiting the depth of escape. Thus, any Auger electrons emitted from an interaction below the surface will lose energy through additional scattering reactions along its path to the surface [25].

AES measurements must be performed under ultra-high vacuum conditions (pressures of 10^{-9} - 10^{-10} Torr) to prevent the effect of gases on the sample so that to prevent gasses from absorbing and scattering the very low energy Auger electrons, which make a thin "gas layer" on the surface of the specimen degrading analytical performance [16]. By using an incorporated ion gun into the vacuum system, the Auger can also be utilized for depth profiling. When the ion gun etches away the material, the electron probe that focuses on the same spot can give information about the changes in the concentration of the elements with sputter depth. So, depth profiling can be employed on the thin film phosphor to identify the elements into the bulk of the material. The changes in the chemical composition of the surface during degradation are also easily monitored with the Auger electron spectroscopy.

The PHI model 549 Auger spectrometer used in this study is shown in figure 4.17. It was used for the measurement of the AES spectrum, CL emission spectrum and also used for degradation of the elements and CL degradation. The phosphor was exposed to an electron beam voltage of energy 2 kV and beam current of 6.2 µA. The electron beam

irradiation was prolonged for 22 h at a vacuum pressure of 2.6×10^{-8} Torr and with O_2 to a pressure of 1.0×10^{-7} Torr.

4.9 X-ray photoelectron spectroscopy (XPS)

X-ray photoelectron spectroscopy (XPS), also known as electron spectroscopy for chemical analysis (ESCA), is a widely used surface technique to obtain chemical information at surfaces of different materials [20]. It was expanded and developed in the middle of 1960's as a practical technique by Siegbahn and his group in Sweden at University of Uppsala (Nobel Prize 1981) [26]. The XPS technique is routinely used to measure organic and inorganic compounds, elements, catalysts, ceramics, glasses, polymers, paints, papers, inks, woods, metal alloys, bio-materials, semiconductors and many others. When it is used to investigate the chemical composition the surface of the solid phosphor materials, provides quantitative information on all the elements in the periodic table (except hydrogen and helium) because they do not have electrons occupying the L level (have less than three electrons) [20]. The basic idea of the XPS mechanism is based on the photoelectric effect where photoelectrons released when the solid is excited with sufficient photon energy (hν), using monochromatic X-ray sources as a source of excitation [27]. Often the energy source for XPS are Mg Kα radiation (1253.6 eV) or Al Kα radiation (1486.6 eV) [20]. The basic components of an XPS spectrometer are an X-ray source, electron energy analyzer for the photoelectrons, and an electron detector. Figure 4.18 shows the schematic diagram of the XPS technique. The X-ray excitation ejects electrons from the core level of the atoms, which will be accelerated to the detector via the hemispherical analyzer as shown in the figure 4.18.

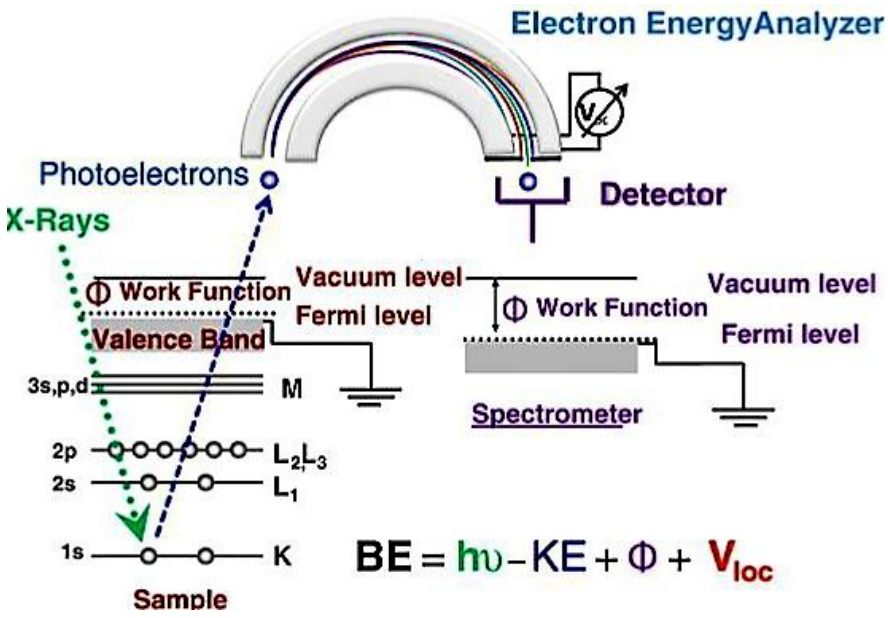

Figure 4.18: Schematic diagram of the XPS technique [28].

The kinetic energy of the ejected electrons is given by

$$KE = h\upsilon - E_B - \phi \qquad (4.12)$$

where KE is the kinetic energy of the ejected electron, $h\upsilon$ is the energy of the photon, E_B is the binding energy (BE) of the state from which the electron is ejected, and ϕ is the sample's work-function. Since the binding energies of the core electrons are characteristic of the elements in a particular chemical environment, the XPS allows the determination of the atomic structures of the sample. As we can obtain a depth profile of the sample in terms of XPS quantities by combining a sequence of ion gun etch cycles interleaved with XPS measurements from the current surface. The shifts in the binding energies also provide information regarding the chemical state of elements being analyzed. The characteristics of peaks detected by XPS correspond to the electron configuration of the electron within the atoms, e.g., 1s, 2s, 2p, 3s, 3p, 3d etc [6]. The sample analysis is conducted in an ultra-high vacuum (UHV) chamber, because electron counting detectors in XPS instruments are few meters away from the material irradiated with X-rays.

For collecting data in this study the PHI 5000 Scanning ESCA Microprobe system was used (figure 4.19). The VersaProbe PHI is operated by a patented high flux X-ray source providing a focused monochromatic x-ray beam that is scanned on the sample surface.

The X-ray source utilizes a focused electron beam scanned upon an Al anode for X-ray generation and a quartz crystal monochromator that focuses and scans the generated X-ray beam upon the sample surface. The monochromator is based on a 200 mm Rowland circle with quartz (100) crystals on an ellipsoidal substrate to generate a micro focused X-ray beam. The X-ray energy dispersion eliminates the $K\alpha_{3,4}$, $K\alpha_{5,6}$, and K_β X-ray lines and the Al Bremsstrahlung radiation background and narrows the Al $K_{\alpha 1,2}$ line to approximately 0.26 eV FWHM. This narrow line allows core and valence band spectra to be acquired with high energy resolution of the photoemission peaks and without X-ray satellite-induced photoemission peak overlaps. The removal of X-ray and Bremsstrahlung satellite radiation coupled with a narrow principle excitation line width results in significantly higher signal-to-background ratio data. The narrower X-ray line width also allows an electron energy analyzer to be observed with higher transmission, thereby reducing the observed damaged rate in monochromator-excited XPS spectra of X-ray sensitive sample. With the proper geometry configuration of X-ray source, crystal substrate and analysis target, the reflection beam yields a highly focused, monochromatic source of X-rays.

A 100 μm diameter monochromatic Al Kα X-ray beam ($h\nu$ = 1486.6 eV) generated by a 25 W, 15 kV electron beam was used to analyze the different binding energy peaks. A low energy Ar^+ ion gun and low energy neutralizer electron gun were used to minimize charging on the surface. Multipack version 9 software was utilized to analyse the spectra to identify the chemical compounds and their electronic states using Gaussian–Lorentz fits.

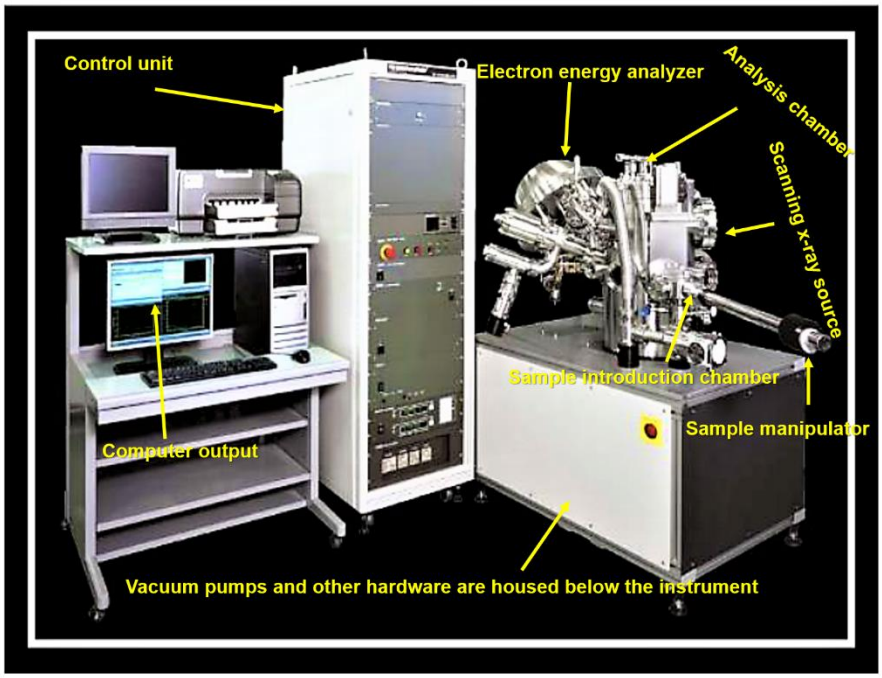

Figure 4.19: PHI 5000 Versaprobe II Scanning XPS Microprobe [29].

4.10 Atomic Force Microscopy (AFM)

Atomic Force Microscopy (AFM) is a form of scanning probe microscopy. A small probe is scanned across the sample to obtain information about the sample's surface including physical topography or measurements of the material's physical, magnetic, or chemical properties [30]. The AFM technique was invented in 1982 by Binning and Rohrer [31].

AFM has significantly influenced the development of the studies in the fields of materials science, biology, chemistry, physics and semiconductors [22]. AFM operates by measuring the force between a probe and the sample. During the scanning, the force between the tip and the sample is measured by monitoring the deflection of the cantilever. The deflection of the cantilever is controlled by using the optical lever technique. A beam from a laser diode is focused onto the end of the cantilever and the position of the reflected beam is monitored by a position sensitive detector [32]. By calculating the different signals in the photodiode quadrants, the amount of deflection can be correlated with height as presented schematically in figure 4.20.

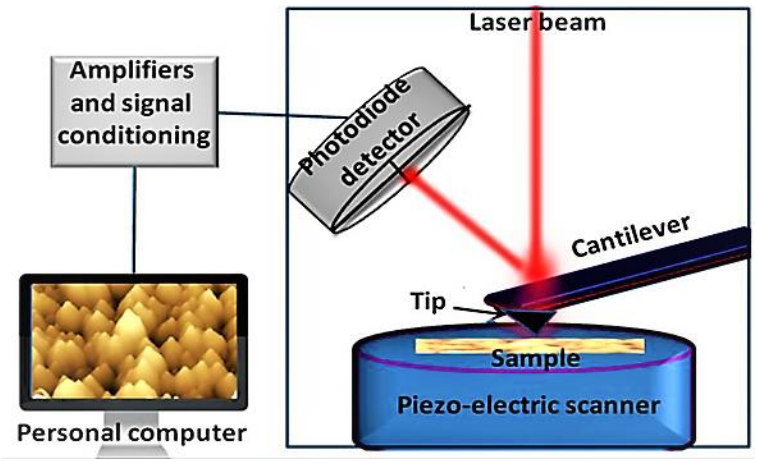

Figure 4.20: Schematic diagram of the setup of an AFM system [22].

It can present three-dimensional topography from AFM images of a sample surface. The resolution in the horizontal plane ranges from 0.1 to 1.0 nm and in the z-direction is 0.1 nm. The surface root-mean-square (RMS) roughness values were also estimated from the analysis of the AFM images of the films' surfaces. AFM can measure samples in three different modes, contact mode, tapping (intermittent contact) mode and non-contact mode. In contact mode the tip scan at a constant small height above the sample surface or under a constant force, where the tip is brought into soft mechanical contact with the surface of the sample [33]. The second mode, tapping (intermittent contact), where the tip contacts with the sample surface intermittently, which avoiding dragging the tip across the surface. This mode allows high-resolution tomographic imaging of the sample surface. In non-contact mode, the probe operates base on the attractive Van der Waals forces acting between the tip and the sample, where there is not any interaction between tip and sample that is why the image resolution is low [31].

In this study, the surface topography and roughness were examined from images captured in contact mode using a Shimadzu SPM-9600 AFM system as shown in figure (4.21).

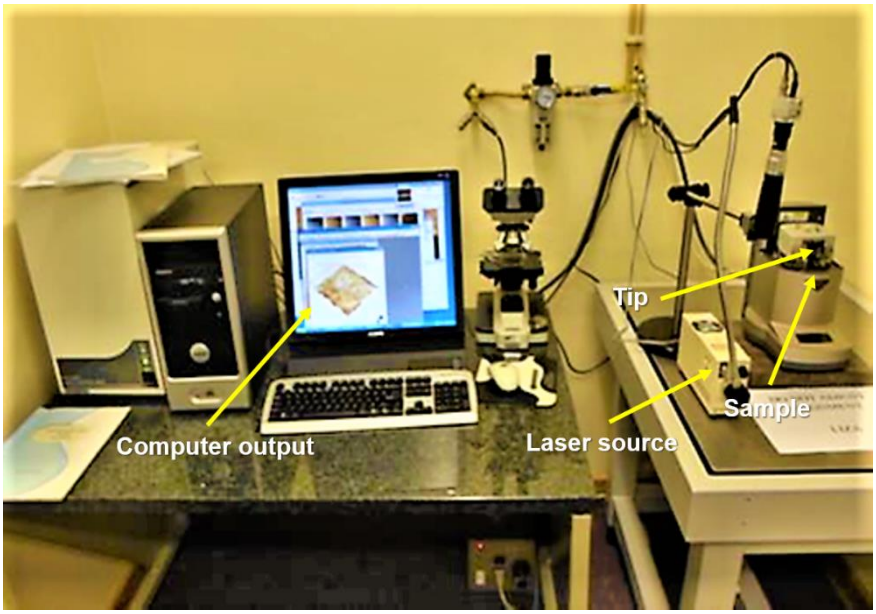

Figure 4.21: The Shimadzu SPM-9600 AFM system at the Department of Physics, University of the Free State.

4.11 Time-of-Flight Secondary Ion Mass Spectrometry (ToF SIMS)

The time-of-flight secondary ion mass spectroscopy (ToF SIMS) is an excellent characterization technique for thin film analyses. It can be useful to determine the distribution of low dopant concentrations in thin films or bulk materials [34]. It is a highly sensitive imaging technique for surface and volume characterization of organic and inorganic materials. ToF SIMS is essentially a surface survey with a highly energetic electrically focused primary ionic beam, which induces a collision cascade that led to the release of different mass charged molecules, which are secondary ion fragments [35]. The 3D imaging of thin films, however, is complicated by accentuated surface structures, which are transferred as artificial topographic features at the interfaces of the thin film images, which means that the properties of the samples which have features accentuated surface structures, the measurements are affected by surface topography [36]. In order to investigate the elemental distribution with depth across the film thickness and interfaces, the ToF SIMS technique was applied to the quantitative interpretation of the depth profiles done on the various features. The depth resolution is an important aspect of molecular depth profiling and is usually estimated by measuring the interface width between the organic

layer and the silicon substrate. A depth profile typically has three distinct sections, and its quality can be evaluated by measuring three parameters: the exponential decrease of the molecular signals in the initial transient region; the signal stability and the sputter/etching rate during the steady state region; and the depth resolution at the organic layer/Si substrate interface [35]. The basic idea of the ToF SIMs is the impact of a pulsed beam of primary ions onto a sample surface. The primary ions generate positively and negatively charged secondary ions from the surface of material after impact on the surface by Bi energy pulsed primary ion beam (Cs used as sputter gun) as presented in figure (4.22). The data acquisition is accomplished using the primary ion or a second ion gun operated in pulsed mode. Depth profiling by ToF SIMS allows monitoring of all species of interest simultaneously with a high-mass resolution to remove any interferences [31].

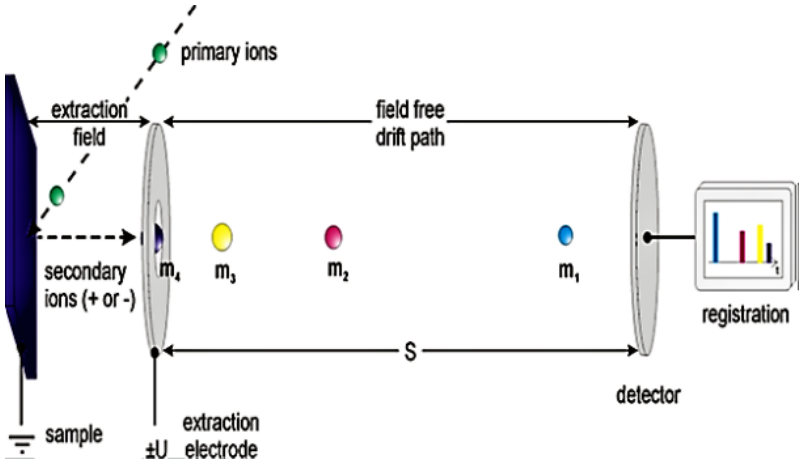

Figure 4.22: Schematic diagram of the principle of mass separation.

The basic equation governing the ToF separation can be derived as follows; the kinetic energy of the secondary ion is connected to its charge and the voltages are applied by:

$$KE = QV \qquad (4.14)$$

where $\frac{1}{2}\, mv^2 = QV$. *So*

$$v^2 = \frac{2QV}{m} \qquad (4.15)$$

where *KE* is the kinetic energy of the secondary ion, *Q* is the charge *V* the voltages, *v* is the

velocity, m is the mass. The measured time-of-flight (t) of the ion is given by d/v, where d is the length of the tube used. Henc

$$(\frac{t}{d})^2 = \frac{1}{v2} = \frac{m}{2QV}$$

Therefore: $$\frac{m}{Q} = 2V(\frac{t}{d})^2 \qquad (4.16)$$

But Q is related to the elementary particle e by $Q=ze$ where z is the number of the elementary charges. So equation (4.16) becomes:

$$\frac{m}{z} = 2eV(\frac{t}{d})^2 \qquad (4.17)$$

As the extraction pulse potential E is related to the applied voltage by $E = Vs$, where s is the length of the tube over which E is applied. So equation (4.17) becomes:

$$\frac{m}{z} = 2eEs(\frac{t}{d})^2 \qquad (4.18)$$

$\frac{m}{z}$ is the mass-to-charge ratio of the ions [37].

Figure 4.23 shows the schematic diagram for the ToF SIMS technique. The solid sample surface is bombarded with a pulsed primary ion beam during ToF SIMS depth profiling. Both atomic and molecular ions are emitted from the outer layers of the surface and extracted. Their mass is measured by their time of flight to the detector. The analysis cycle is repeated at high frequency to generate the complete mass spectrum with high dynamic range [38].

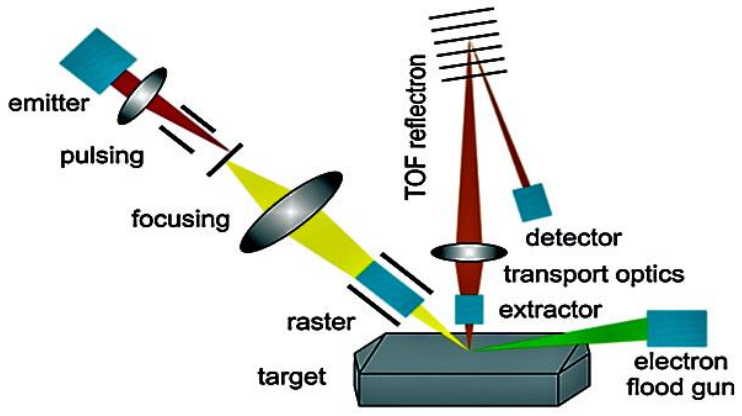

Figure 4.23: Schematic diagram for the ToF SIMS technique [39].

In this study work, the ToF SIMS measurements were performed with a ToF SIMS[5] instrument from ION-ToF figure 4.24.

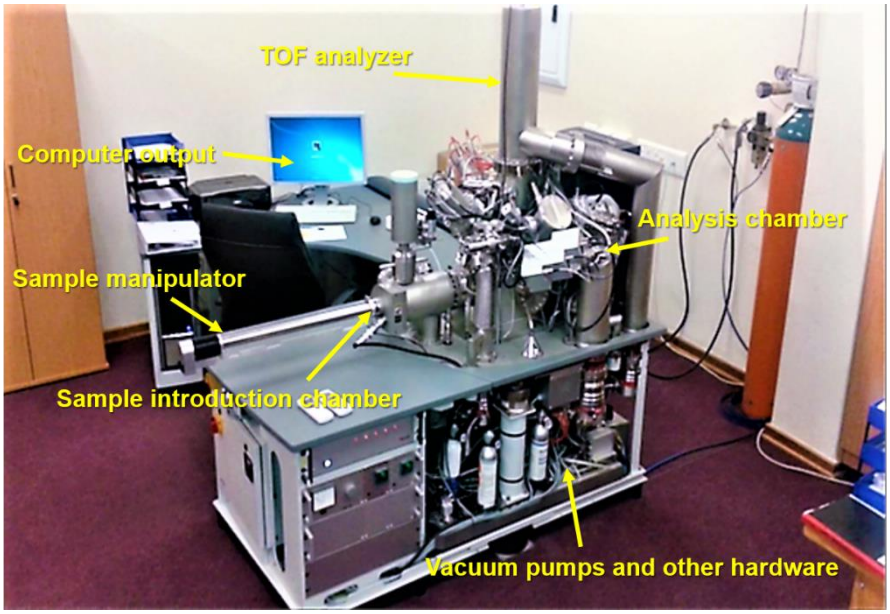

Figure 4.24: A photograph of the ToF SIMS5 at the Department of Physics, University of the Free State.

4.12 References

[1] B. D. Cullity, Element of x-ray direction, Addison-Wesley Publishing Company, Inc. 2nd Edition. Canada (1978) 77-73950. ISBN: 0-201-01174-3.

[2] V. Pecharsky and P. Zavalij, Fundamentals of Powder Diffraction and Structural Characterization of Materials. 2nd Edition, Springer Science & Business Media, LLC (2009). ISBN: 978-0-387-09578-3.

[3] G. Burns. Solid-state physics. Academic Press, Inc, Florida (1985). ISBN-10: 0121460703, ISBN-13: 978-0121460709.

[4] Internet: http://www.rigaku.com/en/products/xrd?gclid=CjwKCAjw39reBRBJEiwAO1m0OVrZgWHvc3afsHka8Cz8QvYdjlhNqZf3r2HOBO9euVOrhq6c04vz6xoCiykQAvD_BwE. (accessed 29 October 2018).

[5] R. Jenkins. Wavelength-Dispersive X-Ray Fluorescence Analysis. *Encyclopedia of Analytical Chemistry*. (2006). DOI:10.1002/9780470027318.a6807.

[6] Pulane. Mokoena, Study of the structure, particle morphology and optical properties of mixed metal oxides, MSc thesis, University of the Free State, (2017).

[7] D. M. Moore and R. C. Reynolds. X-ray Diffraction and the Identification and Analysis of Clay Minerals. Second edition. Oxford University, USA (1997). ISBN: 0195087135.

[8] W. H. Bragg and W. L. Bragg. The Reflection of X-rays by Crystals. Proceedings of the Royal Society A: Mathematical, *Phys Eng Sci*. **88(605)** (1913) 428–438. DOI:10.1098/rspa.1913.0040.

[9] M. M. Biggs. Synthesis, characterization and luminescent mechanism of ZnS:Mn^{2+} nanophosphor, MSc. thesis, University of the Free State, (2009).

[10] Harold P. Klug, Leroy E. Alexander. X-Ray Diffraction Procedures: For Polycrystalline and Amorphous Materials, 2nd Edition. John Wiley & Sons, New York, (1974) 960. ISBN: 978-0-471-49369-3.

[11] M. N. Rahaman, Ceramic Processing and Sintering, 2nd Ed. Marcel Dekker (New York, 2005). ISBN: 0824795733.

[12] W. A. I. Tabaza, Synthesis, and characterization of $MgAl_2O_4$ and $(MgxZn_{1-x})Al_2O_4$ mixed spinel phosphors, Ph.D. thesis, University of the Free State, (2014).

[13] D. K. Schroder. Semiconductor Material and Device Characterization, 3rd Edition, Wiley-VCH, Canada (2005) 840. ISBN 0-471-73906-5.

[14] G. D. Danilatos. Foundations of Environmental Scanning Electron Microscopy. *Advances in Electronics and Electron Physics*, (1988) 109–250. DOI: 10.1016/s0065-2539(08)60902-6.

[15] Internet: https://www.mee-inc.com/hamm/energy-dispersive-x-ray-spectroscopyeds/. [Accessed October 2018].

[16] A. Mohmmed, Luminescence properties of $Y_3(Al,Ga)_5O_{12}$:Tb thin films, Ph.D. thesis, University of the Free State, (2014).

[17] J. R. Meyer-Arendt, Introduction to Classical and Modern Optics, 4th Ed., Prentice-Hall (Englewood Cliffs, 1995). ISBN: 9780131243569.

[18] G. Blasse, B. C. Grabmaier. Luminescent materials. Springer-Verlag, Berlin Heidelberg, (1994). ISBN: 0387580190, 9780387580197.

[19] S. Som and S. K. Sharma. Eu^{3+}/Tb^{3+}-codoped Y_2O_3 nanophosphors: Rietveld refinement, bandgap and photoluminescence optimization. *J. Phys. D*. **45(41)** (2012) 415102. DOI:10.1088/0022-3727/45/41/415102.

[20] H. A. A. Seed Ahmed, Luminescence from lanthanide ions and the effect of co-doping in silica and other hosts. Ph.D. thesis, University of the Free State, (2012).

[21] M. A. Lephoto, Luminescent properties of combustion synthesized $BaAl_2O_4$:Eu^{2+} and $(Ba_{1-x}Sr_x)Al_2O_4$:Eu^{2+} phosphor co-doped with different rare earth ions, MSc Thesis, University of the Free State, (2011).

[22] R. M. Jafer, Luminescence properties of Y_2O_3:Bi^{3+} as powder and thin film phosphor for solar cell application, Ph.D. thesis, University of the Free State, (2015).

[23] P. J. Potts, A Handbook of Silicate Rock, Springer Science & Business Media, US (1992). ISBN 10: 0216932092, ISBN 13: 9780216932098.

[24] M. Thompson. Auger electron spectroscopy. Wiley, Chemical analysis, London, (1985) 74. ISBN:047104377X, 9780471043775.

[25] D. Briggs and M.P. Seah, 'Practical Surface Analysis. Volume 1 – Auger and X-ray Photoelectron Spectroscopy', Second Edition, John Wiley and Sons, Chichester, (1990). ISBN: 0471920819.

[26] John F. Moulder. Handbook of X-ray Photoelectron Spectroscopy: A Reference Book of Standard Spectra for Identification and Interpretation of XPS Data. Editors, Jill Chastain, Roger C. King. Physical Electronics, 1995. ISBN: 096481241X, 9780964812413.

[27] N. Zettili, Quantum Mechanics Concepts and Application, Wiley, Second Edition UK (2009). ISBN: 978-0-470-02679-3.

[28] H. ezen and S. Suzer. XPS for chemical- and charge-sensitive analyses. *Thin Solid Films.* **534**, (2013) 1–11. DOI:10.1016/j.tsf.2013.02.002.

[29] Internet: http://www.phi.com/surface-analysis-equipment/versaprobe.html [accessed January 2019].

[30] C. A. Evans, C. R. Brundle, S. Wihon, Encyclopedia of Materials Characterization Surfaces, Interfaces, Thin Films, Reed Publishing London (1992). ISBN-10: 0750691689, ISBN-13: 978-0750691680.

[31] J. H. Hopps. Atomic Force Microscopy/Scanning Tunneling Microscopy. 2nd Edition. Samuel H. Cohen, Mona T. Bray, Marcia L. Lightbody. Springer US (1994) 968656. ISBN: 978-1-4757-9324-6, 978-1-4757-9322-2.

[32] H. -J. Butt, B. Cappella and M. Kappl. Force measurements with the atomic force microscope: Technique, interpretation and applications. *Surf. Sci. Rep.* **59(1-6)** (2005) 1–152. DOI: 10.1016/j.surfrep.2005.08.003.

[33] G. Binnig, C. F. Quate and C. Gerber. Atomic Force Microscope. *Phys. Rev. Lett.* **56(9)** (1986) 930–933. DOI:10.1103/physrevlett.56.930.

[34] A. Yousif, R. M. Jafer, J. J. Terblans, O. M. Ntwaeaborwa, M. M. Duvenhage, V. Kumar and H. C. Swart. TOF SIMS induced artificial topographical effects on the $Y2(Al,Ga)_5O_{12}:Tb^{3+}$ thin films deposited on Si substrates by the pulsed laser deposition technique. *Appl. Surf. Sci*. **313**, (2014) 524–531. DOI: 10.1016/j.apsusc.2014.06.016.

[35] A. Balakrishna, M. M. Duvenhage, and H. C. Swart. Surface and chemical characterization of $ZnO:Eu^{3+}/Yb^{3+}$ spin coated thin films using SEM-CL and TOF-SIMS. *Vacuum.* **157**, (2018) 376-383. DOI: 10.1016/j.vacuum.2018.09.009.

[36] A. Yousif, R. M. Jafer, S. Som, M. M. Duvenhage, E. Coetsee and H. C. Swart. The effect of different annealing temperatures on the structure and luminescence properties of $Y_2O_3:Bi^{3+}$ thin films fabricated by spin coating. *Appl. Surf. Sci*. **365**, (2016) 93–98. DOI: 10.1016/j.apsusc.2016.01.013.

[37] W. C. Wiley and I. H. McLaren. Time-of-Flight Mass Spectrometer with Improved Resolution. *Rev. Sci. Instrum.* **26(12)** (1955) 1150–1157. DOI:10.1063/1.1715212.

[38] S. Chehreh Chelgani and B. Hart. TOF-SIMS studies of surface chemistry of minerals subjected to

flotation separation– A review. *Miner Eng*. **57**, (2014) 1–11. DOI: 10.1016/j.mineng.2013.12.001.

[39] S. N. Ogugua, Tunable multicolor emission from dysprosium-doped mixed rare-earths oxyorthosilicate nanophosphors for application in ultraviolet-pumped multicolour and white light emitting diodes, MSc. thesis, University of the Free State, (2015).

Chapter 5: Luminescence properties of Bi doped SrO powder

In this chapter, the photoluminescent and cathodoluminescent properties of Bi doped SrO powders were investigated for samples having different doping concentrations and different annealing temperatures.

5.1 Introduction

The old cathode ray tubes contained about 8% strontium oxide (SrO) by weight, which has been the major use of strontium since 1970 [1]. The United States required by law that strontium be used in the faceplate of color televisions and other devices containing color cathode ray tubes. The purpose of SrO was to block emitted X-rays. These X-ray emitting televisions are, however, no longer in production and are replaced by flat panel displays. Since 2007, no television faceplate plants were in operation in the United States, leading to the elimination of what was once a dominant end use and reconfiguring the entire strontium consumption scenario. SrO phosphor is an important basic chemical raw material. Many properties of doped SrO have been demonstrated in the fields of optical, display and magnetic materials [2]. It can be used in medical appliances, where it proved to be efficient to be used in tissue or body member replacements and restorative implant cement or filling compounds. Although consumption requirements fluctuate from year to year, the overall consumption of strontium compounds and metals appears to be increasing [3]. There is renewed interest in Bi doped phosphor which has become a hot research area [4]. Ellervee [5] observed an absorption band at 264 nm for a SrO:Bi^{3+} single crystal in 1977. Yamashita et al. [6] obtained the excitation and emission spectra of SrO:$Bi^{3\div}$ at different temperatures in 1987. The ions of central group metals such as Bi can be used to activate luminescent materials to emit useful broad emissions [7]. They may be considered environmentally friendly since the toxicity of Bi and its salts is negligible [8]. Therefore,

Bi represents an almost ideal substitute for other (often toxic) heavy metal ions, but it also inherently offers a wide range of useful optical properties [9]. Bi doped materials exhibit good luminescence properties due to the large number of possible Bi ion valence states and the strong interaction of these ions with the surrounding lattice. Bi^{3+} activated alkaline-earth oxides such as SrO have many applications in different phosphor fields, such as light-emitting diodes and display devices [10]. Oxides generally exhibit relatively high phonon energies larger than 500 cm^{-1} due to the stretching vibration of the host lattice, but SrO has, as experimentally determined, a phonon energy of about 30 meV (230 cm^{-1}) [10], suggesting that it may have an advantage compared to many other oxide hosts due to its smaller phonon energy. SrO:Bi^{3+},Eu^{3+} is a good candidate for light emitting diodes [11]. SrO is a ceramic material with a wide range of applications. It is expected to be useful both in electronic devices and as a phosphor host. For example, SrO has a small work function of 1.27 eV, which makes it possible to apply SrO materials as electron-injection buffer layers in organic electroluminescence (EL) devices [12]. Although the melting point of SrO is about 2600 °C, it will volatilize if heated above 1400 °C in air [2]. It has a direct band gap of 6.1 eV (203 nm) calculated using the oxygen K-edge [13] or estimated from UV–vis analysis of SrO quantum dots [14]. SrO has shown blue luminescence at 444 nm when Bi^{3+} ions are present, acting as emission centers in photoluminescence (PL) devices [11]. The weak absorption band near 250 nm was ascribed to the absorption of the SrO host defects. The radiative emission transition was identified as $^3P_1 \rightarrow {}^1S_0$ of the Bi^{3+} ions [11]. Many researchers have investigated the luminescence properties of SrO activated with Bi^{3+} ions [11], which was found to be a good alternative to the rare earth doping, because it has good luminescence properties and cheap compared with the rare earth ions.

In this study, we have reported the luminescence properties of SrO:Bi produced using a sol-gel combustion method in order to determine if the phosphor may have potential applications in fields of lighting and displays. These luminescence properties may also affect their different applications in some special fields, such as optical telecommunication. A wide range of temperatures (800 - 1200 °C) and concentrations of Bi (0.05 - 0.7 mol%) were used to determine the optimum sample annealing temperature and concentration. The relationship between temperature, concentration, and luminescence chromaticity was established.

5.2 Sample preparation

Pure host material (SrO) as well as doped $Sr_{1-x}O:Bi_x$ phosphors with different concentrations of Bi (x = 0.0005, 0.001, 0.002, 0.003 and 0.007) were synthesized by the sol-gel combustion method. The sol-gel process offers advantages such as better mixing of starting materials and chemical homogeneity. Furthermore, it requires only a low temperature furnace and simple equipment. Reasonable cost samples having high purity may be produced easily and safely. The powder samples of $Sr_{1-x}O:Bi_x$ with different concentrations of Bi were prepared by using strontium nitrate [$Sr(NO_3)_2$, Sigma-Aldrich, purity 99.95%] and bismuth nitrate [$Bi(NO_3)_3.5H_2O$, Sigma-Aldrich 99.999% pure] as precursors. Citric acid ($C_6H_8O_7$) was used as a fuel for combustion. The molar ratio of the metal ions to citrate was 1:1, as for the following reaction forming SrO and gaseous products:

$$Sr(NO_3)_2 + C_6H_8O_7 + 2O_2 \rightarrow SrO + 6CO_2 + N_2 + 4H_2O. \qquad (5.1)$$

The host was produced using 0.019 mol of both $Sr(NO_3)_2$ and $C_6H_8O_7$, while for doped samples different amounts of $Bi(NO_3)_3.5H_2O$ replaced some $Sr(NO_3)_2$. The precursors were dissolved in 50 ml of deionized water and heated at 100 °C with continuous stirring using a magnetic agitator for 1 h until the solution turned into a transparent sticky gel. The gel was dried by direct heating on a hot plate maintained at 250 ^oC for 30 min. The resulting product was a dark brown powder. It was well crushed and then annealed in air at 1200 °C in a ceramic tube furnace for 2 h with an initial increasing heating rate of 5 °C/min up to the required temperature. After obtaining the optimal Bi concentration (0.2 mol%), samples of this concentration were annealed at different annealing temperatures from 800 to 1200 °C for 2 h.

5.3 Characterization

The structural properties of the $Sr_{1-x}O:Bi_x$ powders were analyzed using a Bruker D8 Advance powder diffractometer with a Cu Kα radiation of wavelength 0.154 nm. The scanning electron microscopy (SEM) of the powder was performed using a JEOL JSM-7800F microscope for analysis of the morphology. The diffuse reflectance (DR) spectra measurements were recorded using a Lambda 950 UV-vis spectrophotometer with spectralon integrating sphere accessory. For the PL measurements of the phosphor powders

a Cary Eclipse spectrophotometer was used at room temperature with a monochromatized xenon flash lamp as the excitation source. The CL emission spectra were measured using a Gatan MonoCL4 accessory fitted to the JEOL JSM-7800F system in a vacuum of the order of 10^{-5} - 10^{-6} Torr and electron energy of 5 keV.

5.4 Results and discussion

5.4.1 Structure and morphology

Figure 5.1(a) shows the XRD patterns of $Sr_{1-x}O:Bi_x$ powders (between x = 0 and 0.007) annealed at 1200 °C for 2 h. The XRD patterns were in accordance with the JCPDS standard #06-0520 of the cubic phase of SrO, which means that there was no change in the structure with the addition of Bi in the SrO. No extra phases were observed. Figure 5.2 shows the crystal structure of SrO drawn using the Vesta program [15]. SrO has space group $Fm\bar{3}m$ [2] and forms crystals with face-centred cubic (fcc) symmetry with a two-atom basis. The first atom is located at each lattice point and the second atom is located halfway between lattice points along the fcc unit cell edge. The coordination number of each atom in this structure is 6: each cation (Sr^{2+} gray particles) is coordinated to six anions (O^{2-} red particles) at the vertices of an octahedron, and similarly each anion is coordinated to six cations at the vertices of an octahedron. The reason that there was no change in the structure with the addition of Bi in the SrO may be because the ionic radii of Bi^{3+} (0.110 nm) and Sr^{2+} (0.121 nm) [16] are similar. The ionic radius of Bi^{3+} is considered since blue luminescence (presented later in section 5.4.3) was observed consistent with this valence state.

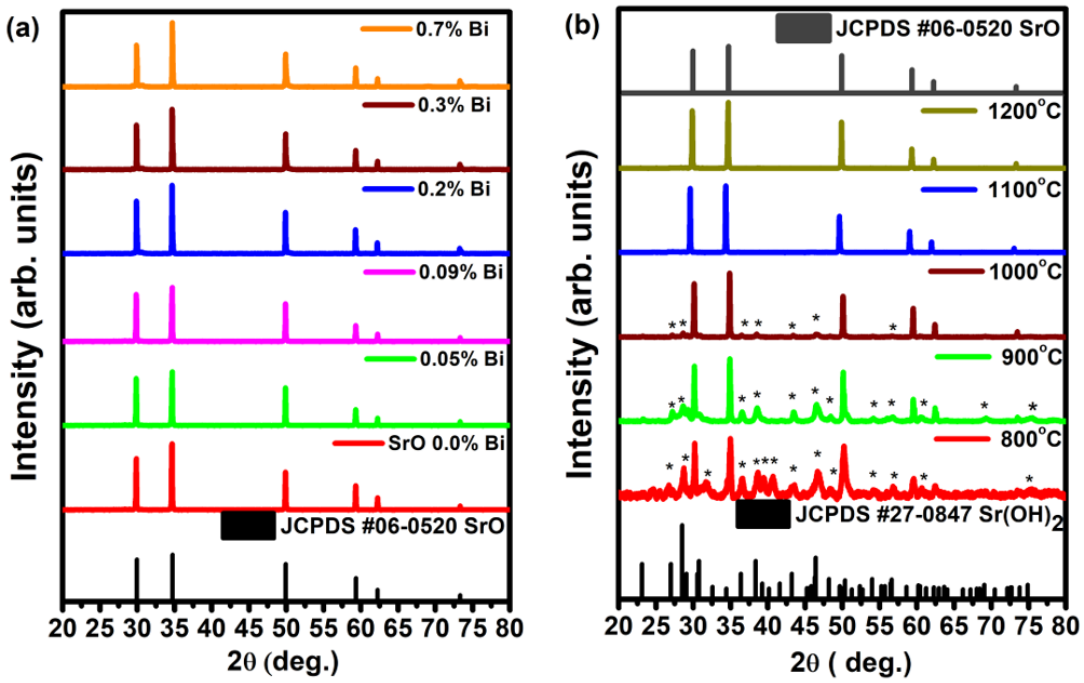

Figure 5.1: (a) XRD patterns of $Sr_{1-x}O:Bi_x$ for different concentration of Bi annealed at 1200 °C. (b) XRD patterns of $Sr_{1-x}O:Bi_x$ phosphor powder after different annealing temperatures for Bi concentration fixed at 0.2 mol%, (*) indicates $Sr(OH)_2$ peaks.

PL measurements (presented later in section 5.4.3) showed that the maximum luminescence emission occurred for the sample doped with 0.2 mol% Bi^{3+}, therefore figure 5.1(b) shows the XRD patterns of such optimally doped samples annealed at various temperatures for 2 h. When the sample was annealed at 800 °C, the XRD pattern indicated the presence of two well-defined crystalline phases [SrO, JCPDS #06 0520 and $Sr(OH)_2$, JCPDS #27 0847]. A decrease in the relative peak intensity of the $Sr(OH)_2$ was observed with increasing annealing temperatures of 900 °C and 1000 °C and it disappeared completely for samples annealed at 1100 and 1200 °C. It must be pointed out that the intervals of 100 °C between measurements might be too large to pinpoint the exact optimized temperature and a more detailed study with smaller temperature intervals between 1000 and 1200 °C is needed before commercialization.

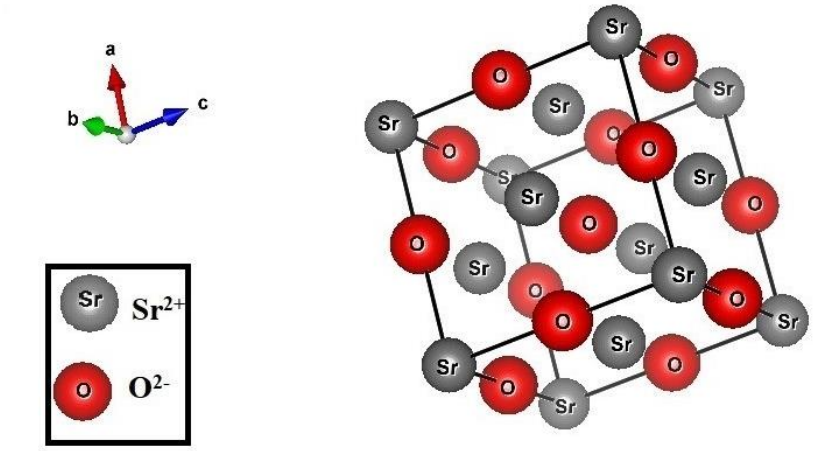

Figure 5.2: The unit cell of SrO.

Figure 5.3 shows the Williamson–Hall plots for the host and x = 0.002 optimally doped sample. Broadening of the XRD peaks may be attributed to both the crystallite size and microstrain according to:

$$\beta \cos \theta = K \lambda / D + 4\varepsilon \sin \theta \qquad (5.2)$$

where β is the 2θ-FWHM (in radians) for the diffraction peaks at the angle θ, K is the shape factor (generally assumed to be 0.9), λ is the x-ray wavelength (0.154 nm), D is the crystallite size and ε is the microstrain [17].

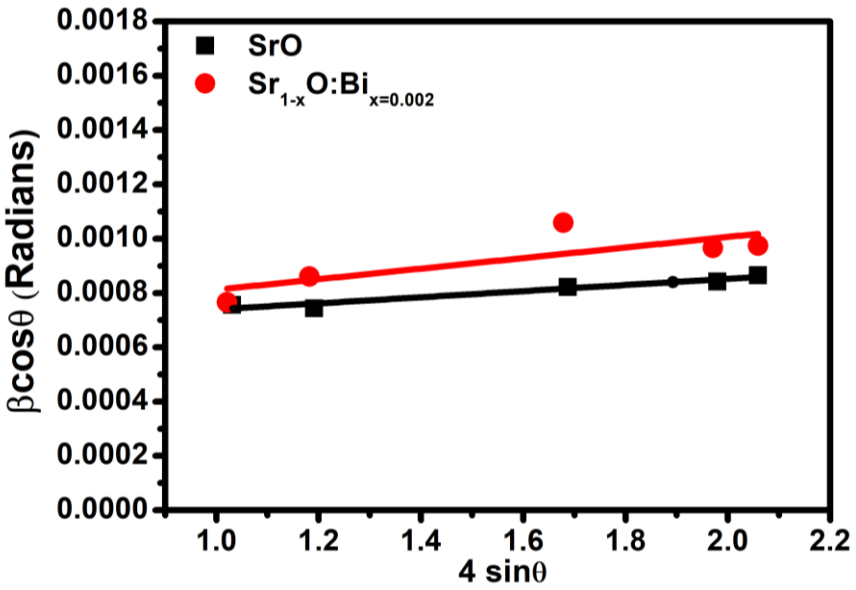

Figure 5.3: Williamson–Hall plots.

The crystallite size of the host, calculated by using the intercept of the Williamson–Hall linear fit, was 180 nm, while for the doped sample (x = 0.002) the crystallite size was 174 nm. The host and doped samples had slopes of (1.2 ± 0.2) x 10^{-4} and (1.9 ± 0.9) x 10^{-4}, respectively, indicating only a small amount of microstrain in this material produced with the sol-gel combustion method. The slight increase of the microstrain for the doped sample is readily attributed to the difference in ionic radii of the Sr^{2+} and Bi^{3+} ions as well as the introduction of the necessary charge compensating defects. Figure 5.4 shows the SEM images of the $Sr_{1-x}O:Bi_{x=0.002}$ phosphor for the samples annealed at 1100 and 1200 °C. The images clearly show a change in the surface morphology and in the shapes and sizes of the particles. The sample annealed at 1100 °C consisted of aggregated grains of size ~1 μm, and when annealed at 1200 °C, the grains grew much larger by coalescence. The grain size may play a role in the Bi activated PL emission. In the case of SrB_4O_7:Bi, NIR-emission could be observed from the polycrystalline material, but not from single crystals, suggesting that emission centers precipitate at grain boundaries [18].

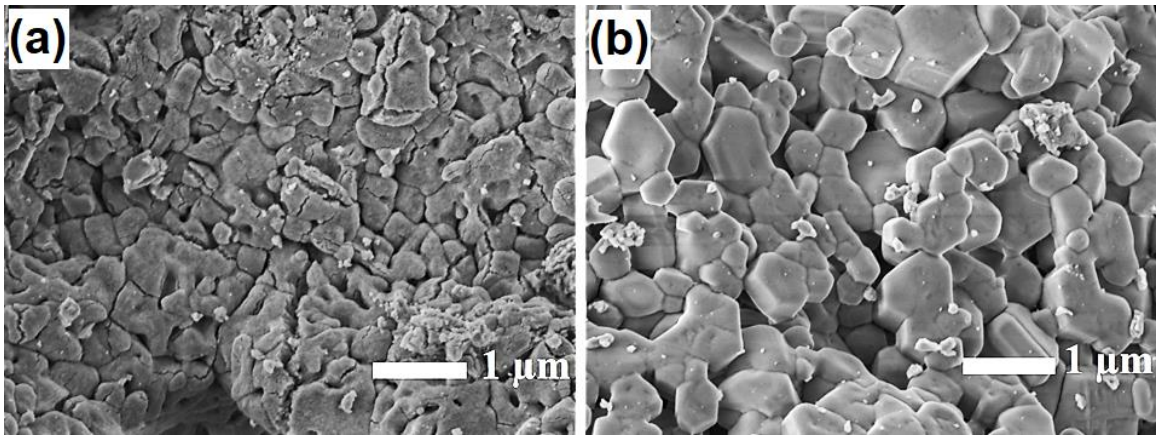

Figure 5.4: SEM images for the $Sr_{1-x}O:Bi_{x=0.002}$ samples annealed at (a) 1100 °C and (b) 1200 °C.

5.4.2 Diffuse reflection spectra and band gap calculations

Figure 5.5 shows the DR measurements for the host and various doped samples. The SrO host was strongly reflecting (~100%) down to a wavelength of about 230 nm, which was due to the wide band gap of SrO. For samples doped with Bi an absorption band at 275 nm was observed, which increased with Bi concentration. The DR data (R_∞) can be transformed to a value [$F(R_\infty)$] proportional to absorbance by using the Kubelka-Munk equation [19]:

$$F(R_\infty) = (1 - R_\infty)^2/2R_\infty. \qquad (5.3)$$

The optical band gap energy was then calculated using the well-known Tauc law relation [19]

$$\alpha h\nu = C(h\nu - E_g)^m \qquad (5.4)$$

where $F(R_\infty)$ was substituted by the absorption coefficient (α), $h\nu$ is the incident photon energy, C is a constant, E_g is the optical band gap energy and $m = ½$ for a direct band gap material like SrO [2]. Plotting $[F(R_\infty)h\nu]^2$ against $h\nu$ and extending a linear fit to the energy axis allowed the determination of E_g as 5.7 ± 0.1 eV, as shown in the inset of figure 5.5. The bandgap of SrO has been reported as 5.9 eV [2] and the small difference for our sample may be due to the defects introduced during synthesis of the samples. This reduction in the

band gap is due to defect structures formed due to the highly exothermic combustion reaction followed by quenching.

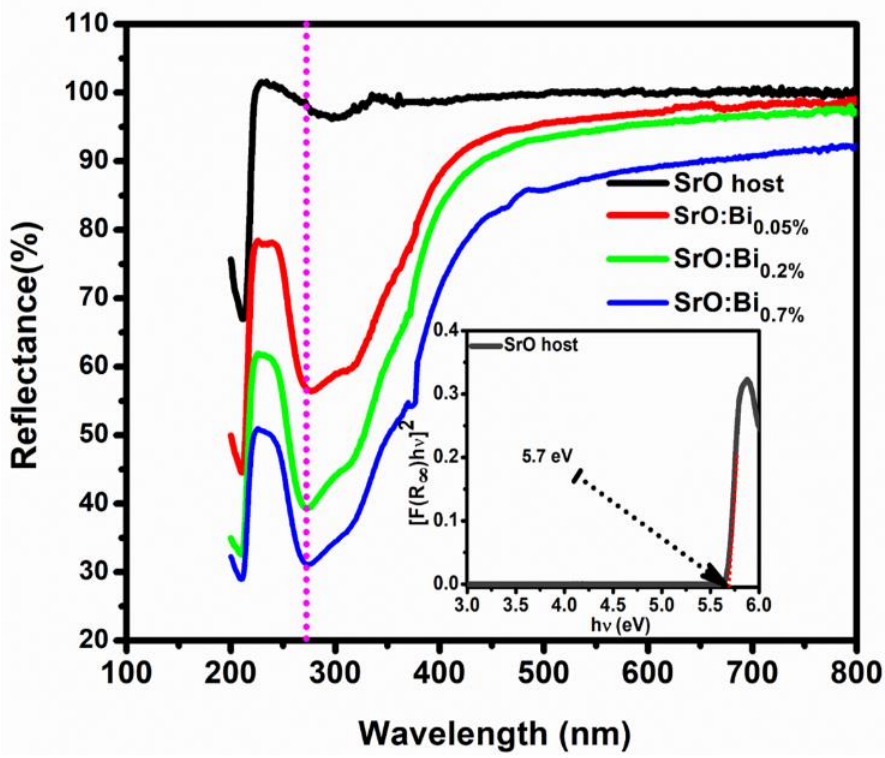

Figure 5.5: Diffuse reflection spectra of $Sr_{1-x}O:Bi_x$ samples annealed at 1200 °C. The inset shows a Tauc plot to determine the band gap.

5.4.3 Luminescence properties

5.4.3.1 Photoluminescence properties

The PL excitation as well as emission spectra of the $Sr_{1-x}O:Bi_x$ phosphors (x = 0.0005, 0.001, 0.002, 0.003 and 0.007) annealed at 1200 °C are shown in figure 5.6. The spectra show the luminescence with the emission in the blue range centered at 445 nm. The luminescence peak can be attributed to Bi^{3+} ions which are known for emitting blue light. The ground state of the Bi^{3+} electronic configuration $[Xe]4f^{14}5d^{10}6s^2$ is $^1S_0$, while the excited states from the 6s6p configuration are $^3P_0$, $^3P_1$, $^3P_2$, and $^1P_1$ in the sequence of increasing energy. Transitions from $^1S_0$ to $^3P_1$, $^3P_2$ and $^1P_1$ are usually denoted as A, B and C, respectively [19]. The transitions $^1S_0 \rightarrow {}^3P_0$ and $^1S_0 \rightarrow {}^3P_2$ are spin forbidden, while $^1S_0 \rightarrow {}^1P_1$ is spin allowed. Spin-orbit coupling of the $^1P_1$ and $^3P_1$ levels means that the $^1S_0 \rightarrow$

$^3P_1$ transition may also occur [11]. Therefore Bi^{3+} ions can be excited from the ground state to the $^3P_1$ (A band) or $^1P_1$ (C band) states with an appropriate wavelength of light in the UV range.

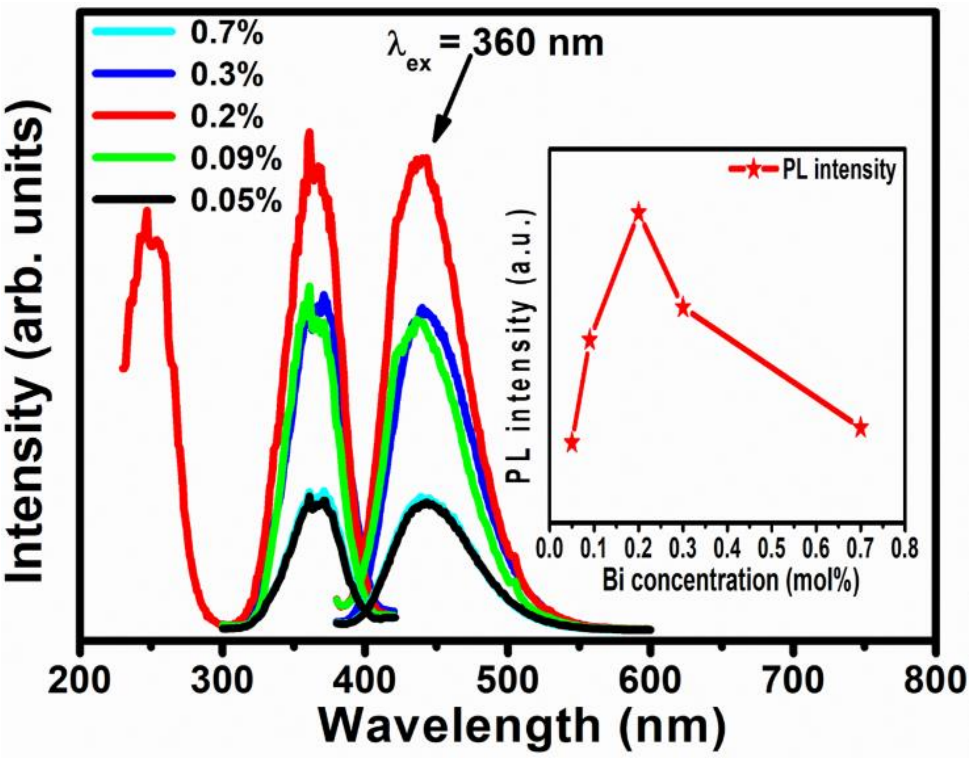

Figure 5.6: PL excitation and emission spectra of $Sr_{1-x}O:Bi_x$ phosphor for different concentrations of Bi^{3+} annealed at 1200 °C. The inset shows the maximum PL intensity (at 445 nm) as a function of Bi^{3+} concentration.

The excitation spectra showed a strong broad band centered at 360 nm, consistent with the $^1S_0 \rightarrow {}^3P_1$ (A band) transition. Som and Sharma [19] reported the existence of two excitation bands in $SrO:Bi^{3+}$, namely one at 365 nm and another much weaker one at 250 nm, which were, respectively attributed to the $^1S_0 \rightarrow {}^3P_1$ transition (A band) and absorption due to SrO host defects. They reported a broad band of blue fluorescence emission which extended from 400 to 520 nm centered at 444 nm, due to the $^3P_1 \rightarrow {}^1S_0$ transition of Bi^{3+}. The Stokes shift between excitation and emission is small due to relaxation in the $^3P_1$ band. In our samples, we had a broad band of blue fluorescence emission which extended from 400 to 500 nm, centered at 445 nm, which is similar to the luminescence reported by Jipeng

et al. [11]. Figure 5.6 shows that the PL intensity of the sample having a 0.2 mol% Bi^{3+}concentration was the maximum. The excitation spectrum of SrO:Bi^{3+} shows a strong broad band centered at 360 nm (3.4 eV), which corresponds to the $^1S_0 \rightarrow {}^3P_1$ transition and a second excitation band at 260 nm (4.7 eV). Three possibilities may be considered for the origin of the second excitation band: firstly, absorption of SrO host defects as reported by Som and Sharma [19]; secondly, metal-to-metal charge transfer (MMCT) between the Bi^{3+} ions at the Sr^{2+} cation of the host; thirdly the C band excitation of the Bi^{3+} ions. Awater and Dorenbos [20] reported that the MMCT transition energies may be used to locate the Bi^{3+} ground state relative to the conduction band bottom in various materials and attributed excitation in $Sr_{1-x}O:Bi_x$ at 4.7 eV to the MMCT transition. Ober and Polyak [1] reported a model to predict the energy of the MMCT transition of Bi^{3+} ions with an accuracy of 3 000 cm^{-1} in different hosts

$$\text{MMCT (cm}^{-1}) = k_{CN'} \left[\chi_{CN}\,(Bi^{3+}) - \alpha^{CN}_{CN'}\,\frac{\chi_{CN'}\,(M^{n+})}{d_{corr}}\right] \qquad (5.5)$$

where CN is the coordination of the Bi^{3+} ions, CN' is the coordination of the metal ion to which charge transfer occurs, χ represents the optical electronegativity, $k_{CN'}$ and $\alpha^{CN}_{CN'}$ are tabulated constants, and d_{corr} is the separation of the Bi^{3+} and M^{n+} ions given by the separation of their sites in the host lattice corrected for the difference of the Bi^{3+} and M^{n+} crystal ionic radii (r) according to $d_{corr} = d_{host} + \frac{1}{2}\left(r(Bi^{3+}) - r(M^{n+})\right)$. For $CN = 6$ and $CN' = 6$ appropriate for Bi doped SrO, k_6 = 39 285 cm^{-1} and α^6_6 = 1.16 [4]. Also $\chi_6\,(Bi^{3+})$ = 1.399 and $\chi_6\,(Sr^{2+})$ = 1.139 [23]. From figure 5.2 the separation of two Sr^{2+} ions in SrO is $\frac{a}{\sqrt{2}}$ where a = 5.16 Å is the lattice constant [24], so if Bi^{3+} substitutes Sr^{2+} then d_{corr} = 3.649 + ½(1.17 – 1.32) = 3.574 Å where the crystal radii are used from Shannon [9]. From these data, equation (5.5) gives the predicted MMCT energy as 5.0 ± 0.4 eV (i.e. in the range 230 – 267 nm). This validates the assignment of Awater and Dorenbos [20] since 4.7 eV does fall within this range. Alternatively, Wang *et al.* [23] and Yamashita *et al* [6] attributed the higher energy excitation to the C band. The energy values of the C band may be estimated from that of the C band using [23]

$$E_C = 3.236 + 2.290(E_A - 2.972)^{0.856}. \qquad (5.6)$$

Using the measured energy of the A band transition (360 nm, 3.444 eV), the predicted C band energy from this equation is 4.44 eV (279 nm), which is slightly lower than the predicted MMCT energy. Therefore, it was considered likely that the measured excitation band at 260 nm was a result of the C band absorption [as shown in figure 5.7(a)], or a combination of C-band and MMCT absorption. Figure 5.7(a) shows a schematic diagram of the energy levels in the Bi^{3+} doped SrO, using the bandgap value (5.7 eV) determined from the diffuse reflectance measurements and the PL measurements.

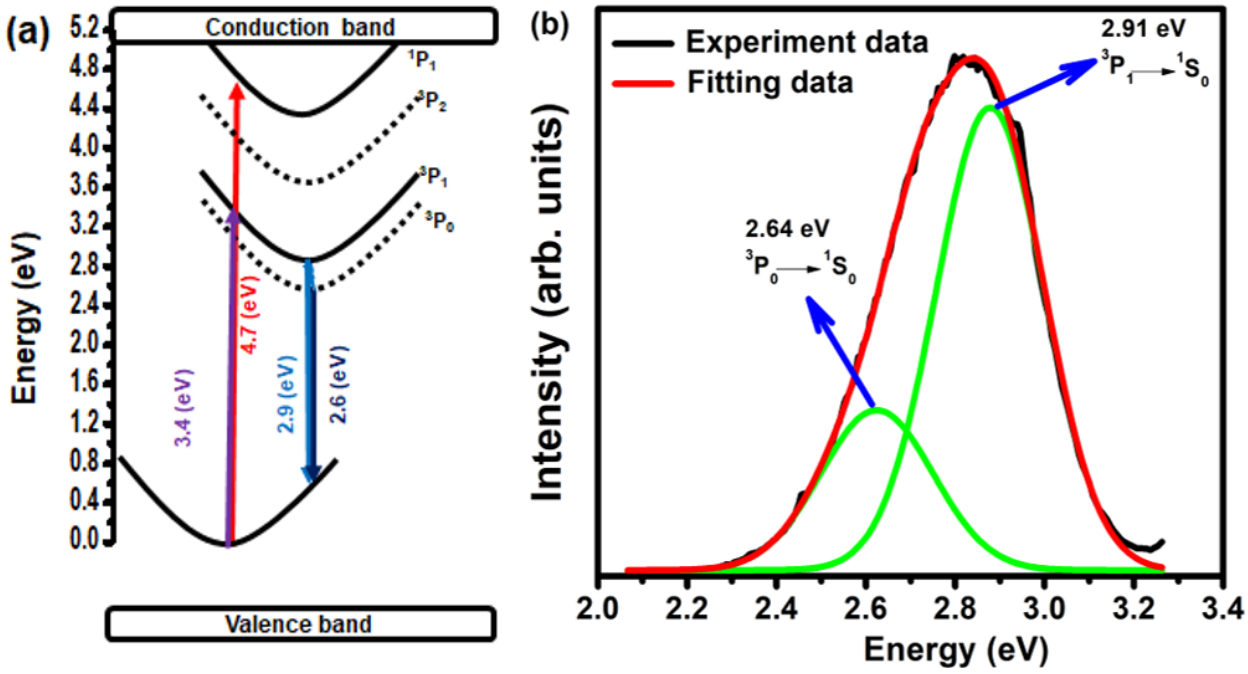

Figure 5.7: (a) Schematic diagram of the energy levels of the Bi^{3+} ion, and (b) Gaussian fitting of the emission band of $Sr_{1-x}O:Bi_{x=0.002}$.

Figure 5.7(b) shows the broad emission of the optimized sample, for which the asymmetry of the peak indicated towards more than one emission centre. Gaussian fitting was performed, giving peaks at 2.64 eV (469 nm) and 2.91 eV (426 nm). The more intense, higher energy peak is attributed to the $^3P_1 \rightarrow {}^1S_0$ transition [24]. Ellervee [5] reported that CaO, CaS, and SrO phosphors doped with Bi have an equidistant quasi-line structure in the spectra caused by $^3P_1 \rightarrow {}^1S_0$, and $^3P_0 \rightarrow {}^1S_0$ electronic transitions, while Zavt and Ellerveeet [25], Steen and Dijcks [26] and Yamashita *et al.* [6] reported that the second emission peak

in SrO:Bi was caused by the forbidden $^3P_0 \rightarrow {}^1S_0$ transition which is initiated by the mixing of $^3P_0$ and $^3P_1$ states by lattice vibrations. The existence of two peaks on the broad emission peak in figure 5.7(b) may therefore be ascribed to these two transitions.

In general, in order to obtain the best luminescence efficiency for a phosphor, the concentration of the activator in the host must be as low enough as possible. However, it is found that the luminescence efficiency decreases if the activator concentration exceeds the specific value known as critical concentration. This effect is called as concentration quenching. If the concentration of the dopant is low enough to obtain good luminescence the dopant ion can be considered as an isolated centre in the host system. However, with the increase of the dopant concentration the ion centres become close to each other for possible interaction. Strong interaction between two active ions is capable of transferring excitation energy from one to the other. Therefore, the probability for energy transfer is greater than that of emission and the energy of excitement is transmitted repeatedly from one activator to the other and eventually lost to the surface, disturbances or impurities. So it does not contribute to the luminescence. The emission efficiency therefore decreases despite the increase in the ion concentration of the activator [27]. The inset in figure 5.6 shows that the maximum luminescence occurred from the sample doped with 0.2 mol% Bi^{3+} and a further increase in the Bi^{3+}concentration resulted in concentration quenching.

There are mainly three ways the energy can be transferred from one ion to the other: (i) exchange interaction, (ii) radiation reabsorption, or (iii) multipolar interaction. The interaction mechanism responsible for the energy migration between the dopant ions can be identified by calculating the critical distance between the adjacent Bi^{3+} ions, which is equal to the average shortest distance between the nearest activator ions corresponding to the critical concentration [28]. If the critical distance is more than 5 Å the exchange interaction becomes inactive and only the multipole-multipole interaction is the major cause of concentration quenching [29]. The critical distance from concentration quenching data is given by

$$R_c \approx 2\left[\frac{3V}{4\pi N X_C}\right]^{1/3} \quad \ldots (5.7)$$

where $V = 137$ Å^3 is the volume of the unit cell (calculated from the lattice constant a = 5.16 Å mentioned earlier), $N = 4$ is the number of cations in the unit cell and $X_C = 0.002$ is the optimal concentration. These values give $R_c = 20.2$ Å, which means that the multipole-multipole interaction was the major cause of concentration quenching.

Figure 5.8 shows the effect of the annealing temperature on the fluorescence intensity of the 0.2 mol% doped samples. The PL intensity increased with the increase of the annealing temperature up to 1100 °C and then decreased with a further increase in temperature up to 1200 °C. Jipeng *et al*. [2] reported that the emission intensity of SrO:Ce^{3+} phosphor was strongly affected by the reaction temperatures because the temperature will affect the depth and impurity concentration of the doping due to diffusion of the dopants. In our results, the reason for the first enhanced and then reduced luminescence intensity with annealing as in figure 5.8 can possibly be due to a combination of the decrease of the $Sr(OH)_2$, as mentioned in the XRD discussion, and the segregation/diffusion of the Bi^{3+} ions from the bulk to populate the surfaces of the particles with a consequent loss in Bi^{3+} due to volatile species as a result of the increased annealing temperature [30]. The intensity increased up to 1100 °C due to a decrease on the hydroxyl concentration.

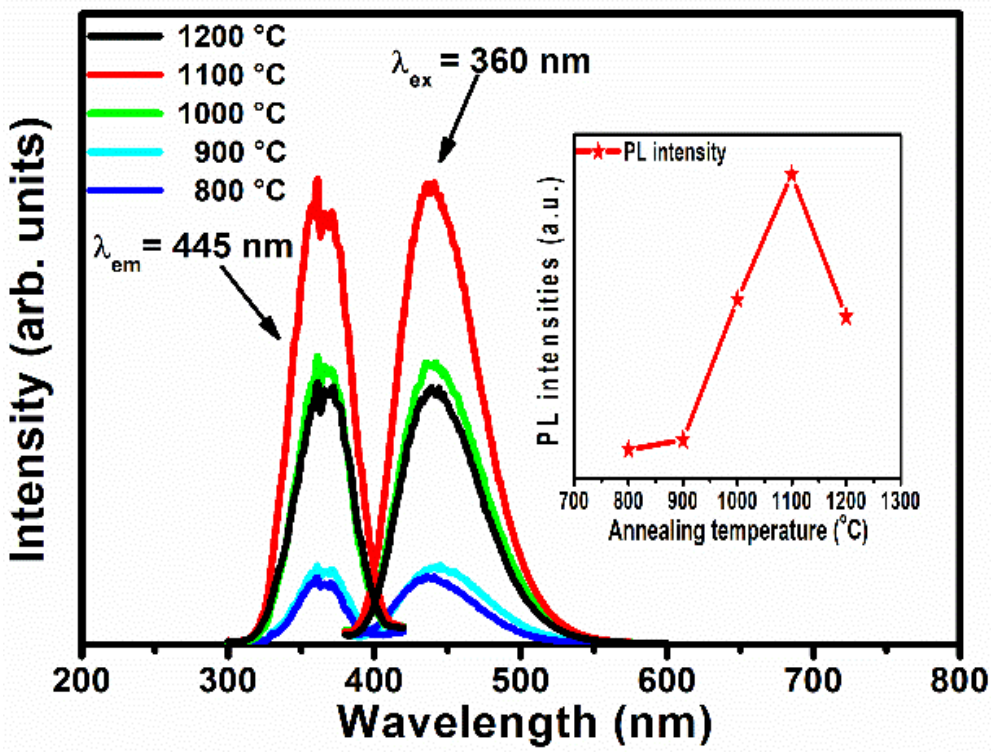

Figure 5.8: PL excitation and emission spectra of $Sr_{1-x}O:Bi_{x=0.002}$ after different annealing temperatures. The inset shows the maximum PL intensity of 445 nm as a function of annealing temperature.

5.4.3.2 Cathodoluminescence properties

Figure 5.9 shows the CL emission spectra for the samples measured with the Gatan system connected to the SEM. Similar to the PL, the emission intensity first increased for the samples annealed up to 1100 °C and then decreased for the sample annealed at 1200 °C. As in the case of the PL, that was first due to a decrease of the hydroxyl concentration and then to segregation of the Bi^{3+} ions from the bulk to the surface. The emission from the sample annealed at 1200 °C was much broader on the high wavelength side, which was probably caused by the presence of both Bi^{3+} and Bi^{2+} in the structure of the sample prepared at the higher temperature, which may have contributed to a broad emission peak ranging up to 700 nm. Yousif et al. [31] reported that CaO:Bi annealed at 1200 °C showed ultra-broadband CL emission as a function of different beam currents and voltages and attributed this to the presence of both Bi^{3+} and Bi^{2+} in the material.

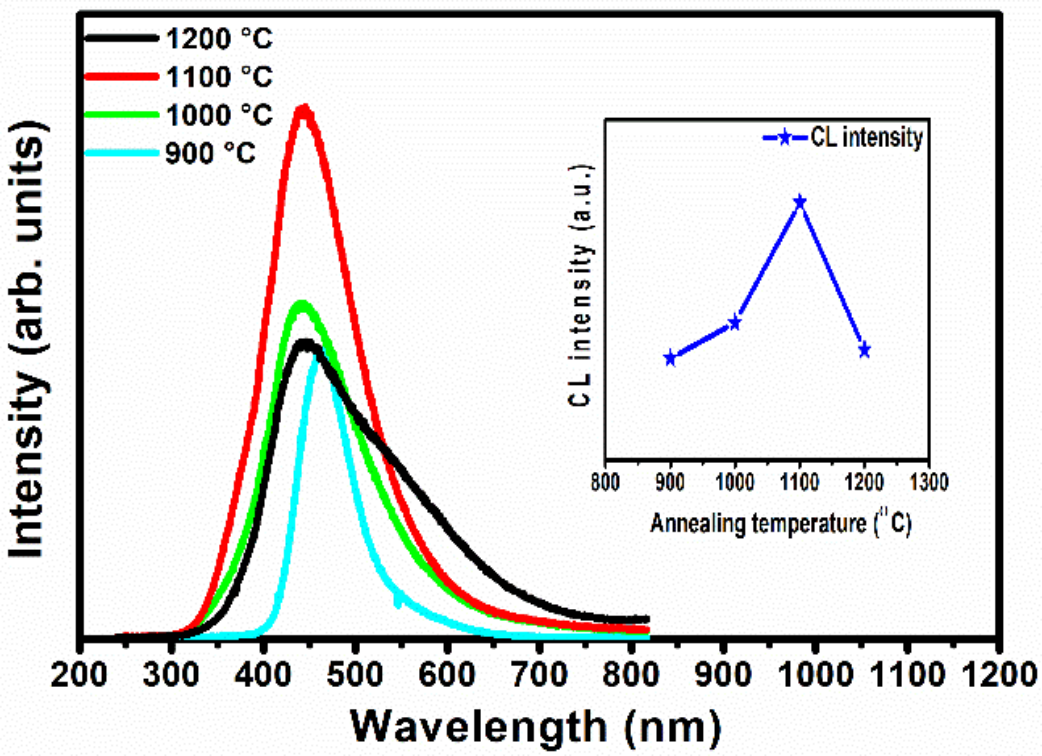

Figure 5.9: The CL emission intensities versus wavelength for the $Sr_{1-x}O:Bi_{x=0.002}$ obtained after annealing at the different temperatures. The inset shows the maximum CL intensity as a function of annealing temperatures.

5.5 Conclusion

The XRD results showed that the sol-gel combustion method produced a cubic phase structure of SrO after high temperature annealing that ranged between 1100 °C up to 1200 °C, although below 1100 °C strontium hydroxide peaks were also present. The band gap was determined from reflectance measurements to be 5.7 eV for the SrO host. The optimum Bi^{3+} concentration for the maximum PL intensity was found to be at 0.2 mol%, while for higher Bi^{3+} concentrations the PL intensity decreased due to concentration quenching. The optimum annealing temperature for maximum PL and CL intensity of the $Sr_{1-x}O:Bi_x$ was 1100 °C. The intensity first increased due to the removal of hydroxides with an increase in temperature up to 1100 °C and then decreased for the highest annealing temperature of 1200 °C. $Sr_{1-x}O:Bi_x$ exhibited broad blue PL and CL emission. The phosphor may have potential applications in fields of lighting and displays due to its broad blue emission.

5.6 References

[1] J. A. Ober, D.E. Polyak, *Mineral Yearbook 2007*:Strontium, U.S. Department of the Interior, U.S. Geological Survey, Washington, May 2010; 73.1-3.7.

[2] Fu. Jipeng, Su. Zhang, Ma. Tengfei, Jia. Yonglei, P. Ran, J. Lihong, Li. Da, Li. Haifeng, S. Wenzhi and Li. Chengyu, A convenient and efficient synthesis method to improve the emission intensity of rare earth ion doped phosphors: the synthesis and luminescent properties of novel SrO:Ce^{3+} phosphor. *RSC Adv.* **5,** (2015), 93951–93956. DOI: 10.1039/c5ra15089b.

[3] A. Joyce Ober; Strontium from Mineral Commodities Summaries, (U.S Bureau of Mines. Pittsburg, 1992) 1323-1332.

[4] P. Boutinaud, Revisiting the Spectroscopy of the Bi^{3+} Ion in Oxide Compounds. *Inorg Chem.* **52(10)** (2013) 6028–6038. DOI: 10.1021/ic400382k.

[5] A. F. Ellervee, Luminescence of Pb^{2+} and Bi^{3+} Centres in Alkali-Earth Sulphides and Oxides *Phys. Status Solidi (B).* **82(1)** (1977) 91–98. DOI: 10.1002/pssb.2220820107.

[6] N. Yamashita, S. Ikeda and S. Asano, Photoluminescence and excitation spectra of the SrO:Bi^{3+} phoshor, *Phys Lett A.* **121(2)** (1987) 94–96. DOI: 10.1016/0375-9601(87)90272-6.

[7] Renping Cao, Fangteng Zhang, Chenxing Liao and Jianrong Qiu, Yellow-to-orange emission from Bi^{2+}-doped RF_2 (R = Ca and Sr) phosphors, *Opt. Express.* **21(13)** (2013) 15728-15733. DOI:10.1364/oe.21.015728.

[8] A. Economou, Bismuth-film electrodes: Recent developments and potentialities for electroanalysis, *TrAC - Trends Anal. Chem*. **24(4)** (2005) 334–340. DOI: 10.1016/j.trac.2004.11.006.

[9] M. Peng, J. Lei, L. Li, L. Wondraczek, Q. Zhang and J. Qiu, Site-specific reduction of Bi^{3+} to Bi^{2+} in bismuth-doped over-stoichiometric barium phosphates, *Mater. Chem. C.* **1(34)** (2013) 5303–5308. DOI:10.1039/c3tc31069h.

[10] Fu. Jipeng, R. Pang, Y. Jia, W. Sun, J. Lihong, S. Zhang and C. Li, Intense red–green up-conversion emission and their mechanisms of SrO:Er^{3+}/Yb^{3+},Gd^{3+},Lu^{3+},Bi^{3+}, *J. Lumin.* **181,** (2017) 240–245. DOI: 10.1016/j.jlumin.2016.09.029.

[11] Fu. Jipeng, R. Pang, L. Jiang, Y. Jia, W. Sun, S. Zhang and C. Li, A novel dichromic self-referencing optical probe SrO:Bi^{3+},Eu^{3+} for temperature spatially and temporally imaging, *Dalton Trans.* **45(34)** (2016) 13317–13323. DOI: 10.1039/c6dt01552b.

[12] K. Komatsu, M. Tanabe, I. Toda, S. Ohshio, H. Muramatsu and H. Saitoh, Synthesis of Strontium Oxide Whiskers with Preferential <111> Orientation by Atmospheric Chemical Vapor Deposition. *J. Mater. Sci*. **5(2)** (2016) 5. DOI:10.5539/jmsr.v5n2p50.

[13] J. A. McLeod, R. G. Wilks, N. A. Skorikov, L. D. Finkelstein, M. Abu-Samak, E. Z. Kurmaev and A. Moewes, Band gaps and electronic structure of alkaline-earth and post-transition-metal oxides, *Phys. Rev. B.* **81(24)** (2010) 245123 (9 pages). DOI: 10.1103/physrevb.81.245123.

[14] K. R. Nemade and S. A. Waghuley, UV-VIS spectroscopic study of one pot synthesized strontium oxide quantum dots, *Results Phys.* **3,** (2013) 52–54. DOI: 10.1016/j.rinp.2013.03.001.

[15] K. Momma and F. Izumi, VESTA 3 for three-dimensional visualization of crystal, volumetric and morphology data, *J. Appl. Crystallogr.* **44,** (2011) 1272-1276. DOI: 10.1107/s0021889811038970.

[16] R. D. Shannon, Revised Effective Ionic Radii and Systematic Studies of Interatomic Distances in Halides and Chalcogenides, *Acta Cryst.* **A32,** (1976) 751-767. DOI: 10.1107/s0567739476001551.

[17] W. A. I. Tabaza, H. C. Swart and R. E. Kroon, Optical properties of Bi and energy transfer from Bi to Tb in $MgAl_2O_4$ phosphor. *J. Lumin.* **148,** (2014) 192–197. DOI: 10.1016/j.jlumin.2013.12.018.

[18] M. Peng, B. Sprenger, M. A. Schmidt, H. Schwefel, and L. Wondraczek. Broadband NIR photoluminescence from Bi-doped $Ba_2P_2O_7$ crystals: Insights into the nature of NIR-emitting Bismuth centers. *Opt. Express.* **18(12)** (2010)12852. DOI:10.1364/oe.18.012852.

[19] S. Som and S. K. Sharma. Eu^{3+}/Tb^{3+}-codoped Y_2O_3 nanophosphors: Rietveld refinement, bandgap and photoluminescence optimization. *J. Phys. D: Appl. Phys*. **45(41)** (2012) 415102. DOI:10.1088/0022-3727/45/41/415102.

[20] R. H. P. Awater and P. Dorenbos, The Bi^{3+} 6s and 6p electron binding energies in relation to the chemical environment of inorganic compounds, *J. Lumin.* **184,** (2017) 221–231. DOI: 10.1016/j.jlumin.2016.12.021.

[21] K. Li and D. Xue, Estimation of Electronegativity Values of Elements in Different Valence States, *J. Phys. Chem. A.* **110(39)** (2006) 11332–11337. DOI: 10.1021/jp062886k.

[22] L. Liu and W.A. Bassett, Changes of the crystal structure and the lattice parameter of SrO at high pressure. *J. Geophys. Res.* **78(35)** (1973) 8470–8473. DOI: 10.1029/jb078i035p08470.

[23] L. Wang, Q. Sun, Q. Liu and J. Shi, Investigation and application of quantitative relationship between sp energy levels of Bi^{3+} ion and host lattice, *J. Solid State Chem.* **191,** (2012)142–146. DOI: 10.1016/j.jssc.2012.03.015.

[24] L. Chen, H. Zheng, J. Cheng, P. Song, G. Yang, G. Zhang and C. Wu, Site-selective luminescence of Bi^{3+} in the YBO_3 host under vacuum ultraviolet excitation at low temperature, *J. Lumin.* **128(3)** (2008) 2027–2030. DOI: 10.1016/j.jlumin.2008.07.007.

[25] G. S. Zavt and A. F. Ellervee, Pb^{2+} and Bi^{3+} impurity centres in alkali-earth oxides vibronic spectra, lattice dynamics, and electron-phonon interaction, *Phys. Status Solidi.* **94(2)** (1979) 757–768. DOI: 10.1002/pssb.2220940249.

[26] A. C. V. D. Steen and L. T. F. Dijcks, The Luminescence Properties of Alkaline-Earth Oxides Activated with $6s^2$ Ions. *Phys. Status Solidi (b).* **104(1)** (1981) 283–292. DOI: 10.1002/pssb.2221040130.

[27] D. L. Dexter, and J. H. Schulman. A Theory of Sensitized Luminescence in Solids. *J. Chem. Phys.* **22(6)** (1954)1063–1070. DOI: 10.1063/1.1699044.

[28] G. Blasse. Energy transfer in oxidic phosphors. *Physics Letters A.* **28(6)** (1968) 444–445. DOI:10.1016/0375-9601(68)90486-6.

[29] Vinay Kumar, M. Manhas, A.K. Bedyal and H.C. Swart, Synthesis, spectral and surface investigation of novel $CaMgB_2O_5:Dy^{3+}$ nanophosphor for UV based white LEDs. Materials Research Bulletin. *Materials*

Res. Bulletin. **91**, (2017) 140–147. DOI: 10.1016/j.materresbull.2017.03.037.

[30] R.M. Jafer, A. Yousif, Vinod Kumar, H.C. Swart and E. Coetsee The effect of annealing temperature on the luminescence properties of Y_2O_3 phosphor powders doped with a high concentration of Bi^{3+}, *J. Lumin.* **180,** (2016) 198–203. DOI: 10.1016/j.jlumin.2016.08.042.

[31] A. Yousif, R. M. Jafer, S. Som, M. M. Duvenhage, E. Coetsee and H. C. Swart, Ultra-broadband luminescent from a Bi-doped CaO matrix. *RSC Adv*. **5(67)** (2015) 54115–54122. DOI: 10.1039/c5ra09246a.

Chapter 6: Surface analysis and cathodoluminescence degradation of Bi doped SrO powder

In this chapter the luminescence properties of $Sr_{1-x}O:Bi_{x=0.002}$ were investigated by using different excitation sources. The cathodoluminescence degradation and the surface elemental composition of the phosphor was also explored.

6.1 Introduction

The luminescence from Bi ions can be useful in obtaining blue to red emitting phosphors using different hosts when excited by ultraviolet light due to efficient conversion to longer wavelengths [1]. Many studies in literature that show absorption bands of Bi^{3+} are usually attributed to $^1S_0 - {}^1P_1$ and $^1S_0 - {}^3P_1$ transitions that are allowed due to a spin-orbit coupling that is depending on the Bi content in the host matrix [2]. The alkali-earth oxide phosphor offers a potential low-cost alternative to lanthanide-based blue phosphors and it have many applications in different phosphor fields, such as light-emitting diodes and display devices [3]. SrO is one of the alkaline-earth oxides groups, which exhibits properties typical of an insulator, with a wide direct band gap of 6.1 eV (203 nm**)** [4]. In recent years, there has been a growing focus on research in light emitting diodes (LEDs) because of their long operation lifetime, energy-saving features and high material stability. To consider the possibility of using the phosphor in applications in fields of lighting and displays, or especially for the use as a field emission display (FED) phosphor, the stability of the luminescence must be determined [5].

Electron degradation studies have been reported for Sr containing $Sr_3(PO_4)_2$:Tb and $LiSrBO_3:Sm^{3+}$ phosphors by Pitale *et al.* [6] and Nagpure *et al*. [7], demonstrating that during prolonged electron bombardment in both vacuum and oxygen atmosphere, some SrO species were formed on the surface. The new surface chemical species formed during electron beam bombardment may have been responsible for the stability of the

cathodoluminescence (CL) after their formation, giving a good reason to study the CL stability of SrO:Bi itself.

In this study, we have reported the luminescence properties of SrO:Bi produced using a sol-gel combustion method in order to determine if the phosphor may have potential applications in fields of lighting and displays. The powder $Sr_{1-x}O:Bi_{x=0.002}$ was synthesized by the sol-gel combustion method. Structural, photoluminescence (PL), cathodoluminescence (CL) properties and the chemical stability of the powder during electron beam irradiation were investigated. The high-resolution X-ray photoelectron spectroscopy (XPS) spectra of the O 1s and Sr 3d peaks, for the undegraded and electron beam degraded $Sr_{1-x}O:Bi_{x=0.002}$ phosphor samples have also been measured and analyzed.

6.2 Sample preparation

Pure host material (SrO) as well as doped $Sr_{1-x}O:Bi_{x=0.002}$ phosphor was synthesized by the sol-gel combustion method. The sol-gel process offers advantages such as better mixing of starting materials and chemical homogeneity. Furthermore, it needs only a low temperature furnace and simple equipment. Reasonable cost samples having high purity may be produced easily and safely. The powder samples of $Sr_{1-x}O:Bi_{x=0.002}$ were prepared by using strontium nitrate ($Sr(NO_3)_2$, Sigma-Aldrich, purity 99.95%) and bismuth nitrate ($Bi(NO_3)_3.5H_2O$, Sigma-Aldrich 99.999% pure) as precursors. Citric acid ($C_6H_8O_7$) was used as a fuel for combustion. The molar ratio of the metal ions to citrate was 1:1, as for the following reaction forming SrO and gaseous products as mention in chapter 5 equation 5.1.

The host was produced using 0.019 mol of both $Sr(NO_3)_2$ and $C_6H_8O_7$, while for doped samples different amounts of $Bi(NO_3)_3.5H_2O$ replaced some $Sr(NO_3)_2$. The precursors were dissolved in 50 ml of deionized water and heated at 100 °C with continuous stirring using a magnetic agitator for 1 h until the solution turned into a transparent sticky gel. The gel was dried by direct heating on a hot plate maintained at 250 °C for 30 min. The resulting product was a dark brown powder. It was well crushed and then annealed in air at 1100 °C in a ceramic tube furnace for 2 h with an initial increasing heating rate of 5 °C/min up to the required temperature.

6.3 Characterization

The structural properties of the $Sr_{1-x}O:Bi_x$ powders were analyzed using a Bruker D8 Advance powder diffractometer with a Cu Kα radiation of wavelength 0.154 nm. The scanning electron microscopy (SEM) of the powder was performed using a JEOL JSM-7800F microscope for analysis of the morphology. The CL emission spectra were measured using a Gatan MonoCL4 accessory fitted to the JEOL JSM-7800F system in a vacuum of the order of 10^{-5}–10^{-6} Torr and electron energy of 5 keV.The powders were exposed to an electron beam in an Auger system (PHI Model 549) with a beam current of 6.2 µA (current density of 1.27 $mA.cm^{-2}$) and beam energy of 2 keV. The CL degradation and Auger electron spectroscopy (AES) were monitored simultaneously in order to determine if there was any relation between the degradation and surface compositional changes during prolonged electron bombardment. An Ocean Optics PC2000 spectrometer attached to the vacuum chamber of the PHI 549 Auger electron spectrometer was used for the CL data collection by using OOI Base 32 computer software. The experiments were carried out in a vacuum base pressure of 2.6×10^{-8} Torr and an O_2 partial pressure of 1.0×10^{-7} Torr during electron bombardment for around 22 h. High-resolution X-ray photoelectron spectroscopy (XPS) spectra of the surface of the freshly annealed and degradation sample as well as in the bulk of these samples after sputtering were obtained. A PHI 5000 Versaprobe-Scanning ESCA Microprobe was used. The x-ray beam used was a 100 µm diameter monochromatic Al Kα X-ray beam (hν = 1486.6 eV) generated by a 25 W, 15 keV electron beam. The pass energy of the hemispherical analyzer was maintained at 11 eV. An Ar ion gun (2 kV energy ions) at the rate of 14 nm/min was used to clean/sputter the powder samples.

6.4 Results and discussion

6.4.1 Structure and morphology

The XRD pattern of the $Sr_{1-x}O:Bi_{x=0.002}$ powder phosphor plus the profile of the JCPDS data file are shown in figure 6.1(a). The patterns clearly indicate that all diffraction peaks can be assigned to the face-centred cubic (fcc) crystalline phase of strontium oxide that matches well with the standard data of SrO (#06-0520 of the cubic phase) with the

space group of Fm3m [8] and forms crystals with face-centred cubic (fcc) symmetry with a two-atom basis. The first atom is located at each lattice point and the second atom is located halfway between lattice points along the fcc unit cell edge as shown in figure 6.1(b), were drawn using the Vesta program [9]. The coordination number of each atom in this structure is 6: each cation (Sr^{2+} grey particles) is coordinated to 6 anions (O^{2-} red particles) at the vertices of an octahedron, and similarly each anion is coordinated to 6 cations at the vertices of an octahedron. No extra phases were observed in XRD pattern. Figure 6.1(c) exhibits the SEM image of the $Sr_{1-x}O:Bi_{x=0.002}$. The image shows aggregated particles that consist of elongated and spherical particles with an average size of ~1 μm. In addition, an aggregation of irregular lumps that consisted of irregular particles was also observed.

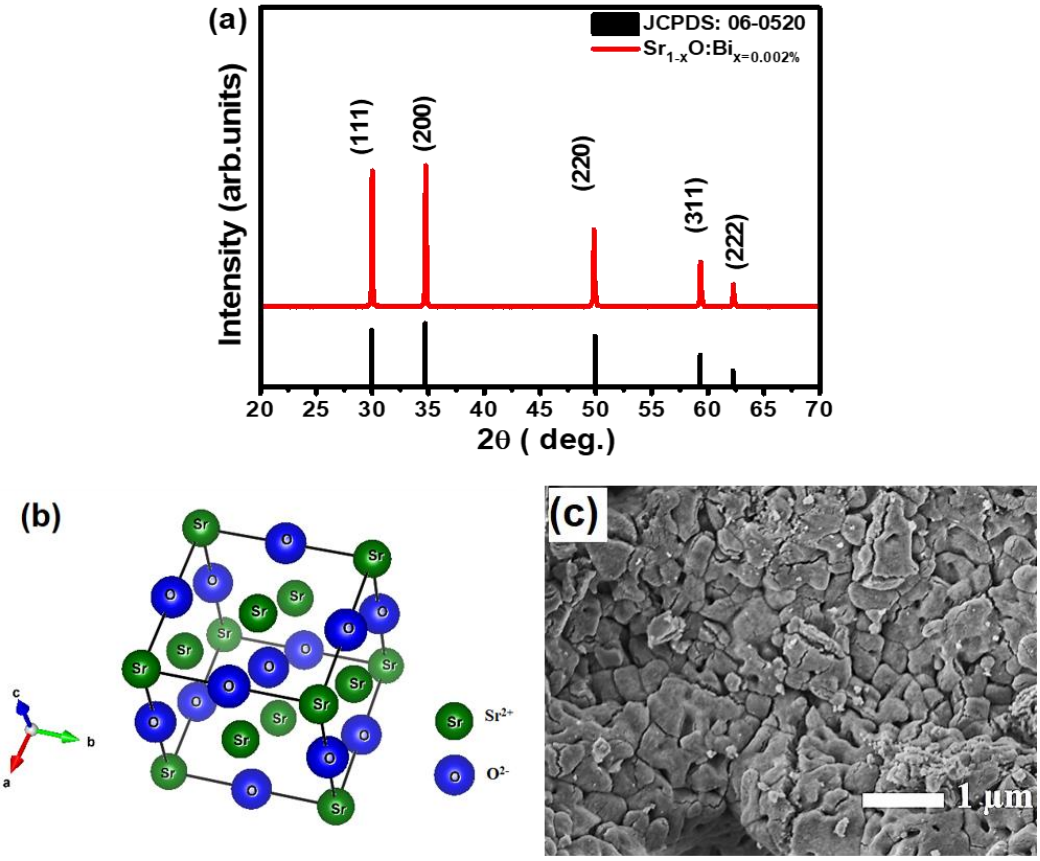

Figure 6.1: (a) Shows the XRD pattern of $Sr_{1-x}O:Bi_{x=0.002}$ powder annealed at 1100 °C and standard JCPDS data file no. 06-0520, (b) the unit cell of SrO and (c) represent the SEM micrograph of the $Sr_{1-x}O:Bi_{x=0.002}$ powder annealed at 1100 °C.

6.4.2 Luminescence properties

The luminescence properties of the Bi^{3+} were examined by using different excitation sources in our study, namely the xenon lamp with an excitation wavelength of 360 nm for the PL and electron beams with energies 5 keV (in the SEM) and 2.5 keV (in the Auger system). All the results are presented in figure 6.2. To obtain the emission spectra by using the xenon lamp the excitation spectrum was recorded under the excitation band of 360 nm. The full width at half-maximum (FWHM) of the emission band is 68 nm and range from 380 to 520 nm. The ground state of the Bi^{3+} electronic configuration $[Xe]4f^{14}5d^{10}6s^2$ is $^1S_0$, while the excited states from the 6s6p configuration are $^3P_0$, $^3P_1$, $^3P_2$ and $^1P_1$ in sequence of increasing energy. Transitions from $^1S_0$ to $^3P_1$, $^3P_2$ and $^1P_1$ are usually denoted as A, B and C, respectively [10]. The transitions $^1S_0 \rightarrow {}^3P_0$ and $^1S_0 \rightarrow {}^3P_2$ are spin forbidden, while $^1S_0 \rightarrow {}^1P_1$ is spin allowed. Spin-orbit coupling of the $^1P_1$ and $^3P_1$ levels means that the $^1S_0 \rightarrow {}^3P_1$ transition may also occur [11]. Therefore, Bi^{3+} ions can be excited from the ground state to $^3P_1$ (A band) or $^1P_1$ (C band) states with an appropriate wavelength of light in the UV range. Thus, the observed excitation and emission can be attributed to the $^1S_0 \rightarrow {}^3P_1$ and $^3P_1 \rightarrow {}^1S_0$ transitions, respectively. There was a small shift in the peak position from 445 nm to 452 nm between the PL and CL maximum intensity positions, respectively. The full width at half-maximum (FWHM) of the PL emission band was 68 nm, while much broader emission bands were observed when using an electron beam as the excitation source (FWHMs of 70 nm and 102 nm with the 2.5 and 5 keV electron beams, respectively). This data is summarized in Table 6.1. The difference between PL and CL may be due to the large energy difference as well as the different mechanisms for the excitation. For PL 360 nm light was used to excite and the energy of these photons was only 3.444 eV. Luminescent centres were directly excited by the UV photons. The 360 nm photons were absorbed by the Bi^{3+} ions directly, exciting electrons from the $^1S_0$ to the $^3P_1$ level. However, under the much higher energy electron-beam irradiation during CL, luminescent centers in the phosphors may be excited by either direct or indirect excitation. When an electron penetrates the surface of a phosphor, it causes ionization of the host lattice atoms, freeing many secondary electrons which can also cause ionization and create further secondary electrons [12]. When lower energy secondary electrons reach the luminescent centres, they may directly excite the luminescent centres. Also, these

secondary electrons generate many electron-hole (EH) pairs by collision with lattice ions. Generated EHs pairs may act as mobile carriers in the material and recombine at luminescent centres or may decay nonradiatively through energy transfer to the $6s^2$ shell of Bi^{3+} ions and induce its characteristic emission [13]. The high energy of the electron sources have the ability to excite the Bi^{3+} ions as well as the host lattice. Excitation with the photons from the source with less energy compared with the others has a higher probability of exciting the lower energy emission in the specific excitation band (360 nm). The formation of new emissive species due to damage induced by high energy electrons bombardment might also cause an increase in the FWHM in the case of the CL. PL emission has also been measured by using the higher energy 260 nm wavelength as an excitation source. The results are compared to the 360 nm excitation in figure 6.2 (b). The emission spectrum excited by a 260 nm radiation shows a broader emission band centred at 450 nm with FWHM 76 nm that was slightly shifted with respect to the 445 nm emission when excited by 360 nm radiation. The CL excitation sources [14] have the abilities to excite the Bi^{3+} ions at both excitation wavelengths. Thus, the excitation with the PL photons from the source with less energy compared with the CL has a higher probability of exciting the lower energy emission in the specific excitation band (360 nm) and is therefore partially responsible for the smaller FWHM and the shift in the emission spectrum. Yousif et al. [15] also reported peak shifts and broadening of the emission on the high wavelength side for $CaO:Bi^{3+}$ when excited with different photon wavelengths and with an electron beam. A similar shift in the emission band was reported for La_2O_3:Bi thin films when observing PL and EL. The red-shift of the EL band compared to PL was attributed to relaxation of the selection rule forbidding the lowest energy $^3P_1 \rightarrow {}^1S_0$ transition of Bi^{3+} ions as a result of the high electric field [16]. Figure 6.2 (c) represents the chromaticity co-ordinates of the PL (excited at 360 nm), AES-CL (2.5 keV) and SEM-CL (5 keV) spectra for $Sr_{1-x}O:Bi_{x=0.002}$, which were determined using the Commission Internationale de I'Eclairage (CIE) coordinate system [17]. The calculated chromaticity coordinates are tabulated in Table 6.1 The coordinates are reasonably good for different optical applications for blue emission. It can be seen that the color coordinates traverse a range from the light blue to deep blue region on varying the excitation source from CL to PL.

Table 6.1: The emission peak position, FWHM and CIE coordinates (X, Y) of $Sr_{1-x}O:Bi_{x=0.002}$.

Excitation source	Peak position (nm)	FWHM (nm)	CIE coordinates	
			X	Y
PL (Ex. 360 nm, 3.44 eV)	445	68	0.15	0.06
PL (Ex. 260 nm, 4.77 eV)	450	76	0.15	0.08
AES-CL (2.5 keV)	452	70	0.15	0.13
SEM-CL (5 keV)	452	102	0.19	0.17

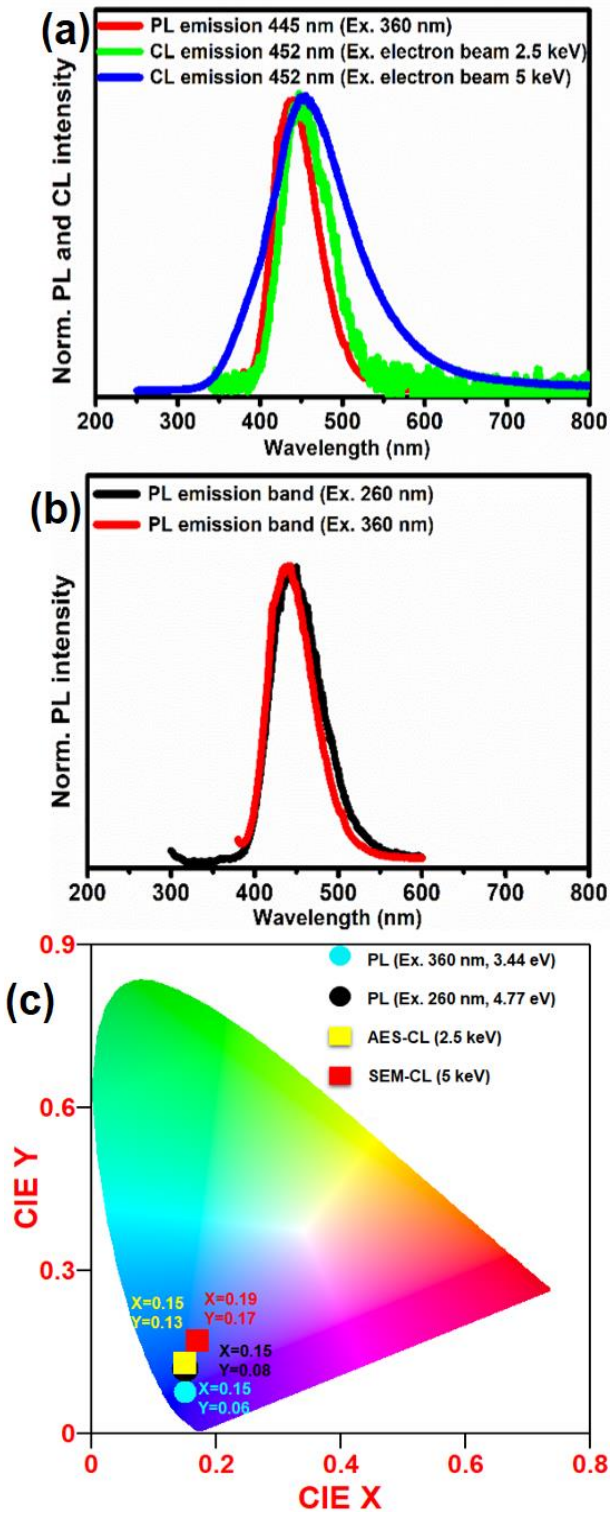

Figure 6.2: (a) Emission spectra of $Sr_{1-x}O:Bi_{x=0.002}$ annealed at 1100 °C obtained by using the xenon lamp at 360 nm and electron beams with beam voltages of 2.5 keV and 5 keV. (b) PL excitation and emission by using 260 nm and 360 nm and (c) CIE coordinates for emission.

6.4.3 Surface analysis and CL degradation

Figure 6.3 shows the Auger spectra before and after electron beam exposure of the $Sr_{1-x}O:Bi_{x=0.002}$ sample annealed for 2 h at 1100 °C. The experiments were performed in (a) a vacuum with base pressure of 2.6×10^{-8} Torr and (b) an oxygen partial pressure of 1.0×10^{-7} Torr. The presence of all major elements of SrO, namely Sr at the lower energy range 61 - 130 eV and O at 510 eV [18] were confirmed, but Bi was not observed in the spectra where it is expected to be detected at 101 keV, due to its low concentration [18].

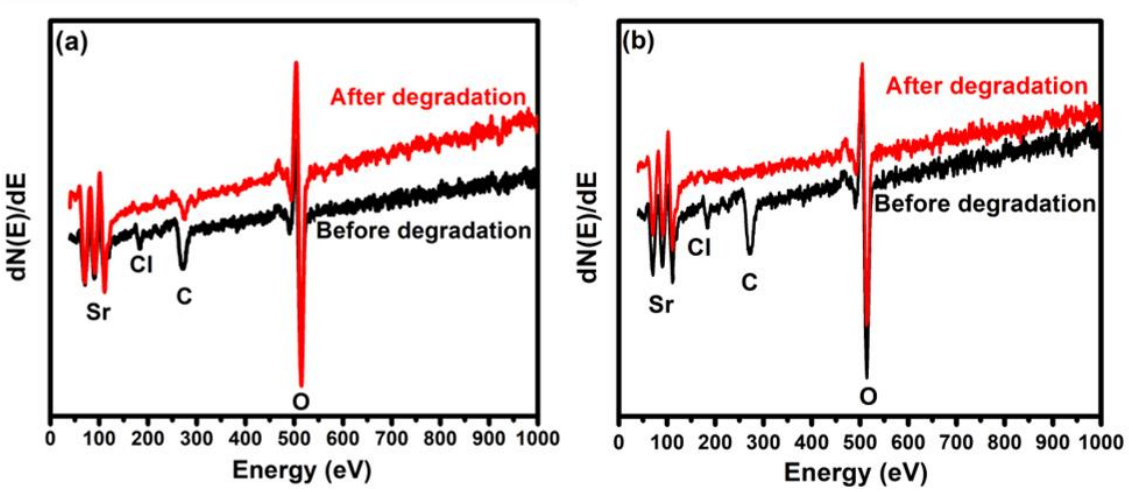

Figure 6.3: AES spectra of the $Sr_{1-x}O:Bi_{x=0.002}$ powder before and after electron-beam bombardment in (a) a vacuum base pressure of 2.6×10^{-8} Torr, and (b) backfilled with oxygen up to a pressure of 1.0×10^{-7} Torr.

Cl and C were also detected before degradation and were attributed to adventitious impurity species on the surface due to handling and exposure to atmospheric pressure. During degradation the C and Cl decreased or were eliminated as volatile species (such as CO and CO_2) [19], which indicated that the contaminants were only present on the surface. Figure 6.4 shows the Auger peak-to-peak heights (APPHs) as a function of electron dose for $Sr_{1-x}O:Bi_{x=0.002}$ powder during degradation of the sample in (a) vacuum base pressure and (b) in an oxygen partial pressure. The C reduced at a faster rate in the O_2 atmosphere compared to the vacuum base pressure due to the reaction of O_2 with the adventitious C at a higher rate to form volatile compounds on the surface for the irradiated sample [20]. The reduction

and removal of the carbon from the surface of the materials during degradation is well explained by the electron stimulated surface chemical reaction (ESSCR) model as reported by Swart *et al*. [20,21]. Generally, in the ESSCR process, the changes in the sample occur due to the electron beam dissociation of the molecular O_2 and other residual gases adsorbed on the surface from molecular species to atomic/ionic species. For example, water vapor may dissociate according to $H_2O \rightarrow 2H^+ + O^{2-}$ and the products subsequently react with C to form volatile compounds (CO_x, CH_4, etc.) [22]. The ESSCR mechanism for the removal of the Cl and C was again confirmed as indicated in figures (6.3 and 6.4).

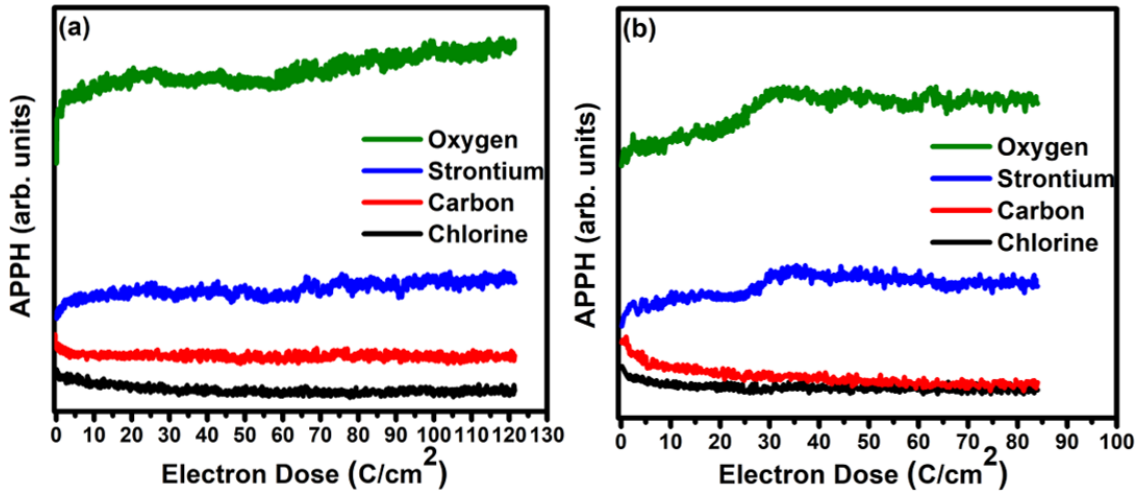

Figure 6.4: APPHs as a function of electron beam dose in (a) a vacuum base pressure of 2.6×10^{-8} Torr, and (b) backfilled with oxygen up to a pressure of 3.5×10^{-7} Torr.

Figure 6.5 shows the CL intensity maximum at 450 nm as a function of electron dose in (a) vacuum and (b) backfilled with oxygen. The CL spectra are shown as insets before and after the degradation process. By simultaneous monitoring of the CL and AES peak to peak heights over time for 22 h, the CL degradation and surface chemical changes of the phosphor were investigated. For vacuum (figure 6.5(a)) the CL intensity has slightly reduced after irradiation of about 50 C/cm^2 and stabilized thereafter. With O_2 [figure 6.5(b)] it is clear that the degradation was slightly higher and after a dose of about 35 C/cm^2 the CL intensity had stabilized.

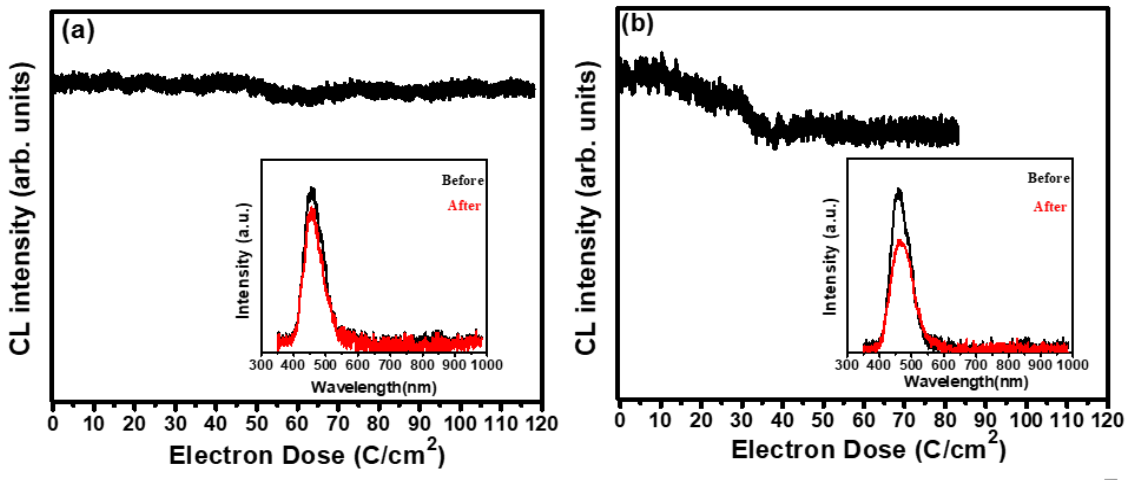

Figure 6.5: CL Intensity as a function of electron dose exposure at (a) a vacuum base pressure of 2.6×10^{-8} Torr, and (b) backfilled with oxygen until a pressure of 3.5×10^{-7} Torr. The insets represent the CL spectra before and after degradation.

The degradation of the CL intensity was correlated with the presence of the C on the surface, where most of the C was removed from the surface during this process over time for 22 h as shown in figure 6.4. The slight decrease of the CL intensity (less than 20%) can also be explained by ESSCRs. The peak position and shape of the CL spectra remained the same before and after degradation for both conditions (vacuum and oxygen) with only a small decrease in the intensity. Hasabeldaim *et al.* [23] found that changes in the surface character and the presence of defects played a crucial role in the degradation and emission process of ZnO. The presence of the surface contamination such as C and Cl affected the CL degradation initially. In our results the CL intensity reduced slightly more and at a higher rate in the presence of O_2, due to the reaction of O_2 with the adventitious C at a higher rate. This suggests that some dead non-luminescent surface layer which formed due to the ESSCR as C is removed from the surface was responsible for the CL degradation. This dead layer has been primarily attributed to surface recombination, which has been modelled to sophisticated levels. Due to dangling bonds at the surface, some researchers believe that it is covered by a layer of surface recombination (SR) centres [24]. During the CL process, the charging of a surface will cause the electrons that are excited to the conduction band in the depletion layer to experience a repulsive force near the surface and the probability is greater than the electron-hole pair will be swept apart before radiative

recombination takes place, resulting in a loss in CL intensity. The surface charging will also directly alter the CL efficiency if the surface potential becomes large enough to alter the arrival energy of the exciting electrons. This occurred less in vacuum than with O_2, which caused the CL intensity to correspondingly decrease slightly less. It was quite evident that the SrO:Bi powder sample was stable after C and Cl removal under electron bombardment, making it an excellent candidate for application in field emission displays.

The elemental composition and the oxidation state of the cations were analysed using the analytical XPS technique. XPS analysis was performed for the $Sr_{1-x}O:Bi_{x=0.002}$ sample before and after degradation in vacuum in order to evaluate the differences and changes of their surface chemical composition. The measurements were made before and after 120 s of Ar^+ sputtering of which the purpose was to clean the surface. Figure 6.6 shows the XPS survey spectra. The survey indicates that as mentioned Sr and O are the major components on the surface of these materials, but Bi was not observed due to its low concentration. C was also detected, which was significantly removed after 120 s sputtering and completely removed after degradation as mentioned earlier. This indicates that the adventitious C atoms were only on the surface due to handling and exposure to the atmospheric environment. All binding energies were corrected by considering the charge shift using the C 1s peak (C–C) bond of graphitic carbon (binding energy 284.5 eV) as a reference [25]. Strontium oxide and mixed oxides containing strontium are expected to strongly chemisorb carbon dioxide and water. These processes may lead to the formation of surface carbonates and surface hydroxides [8].

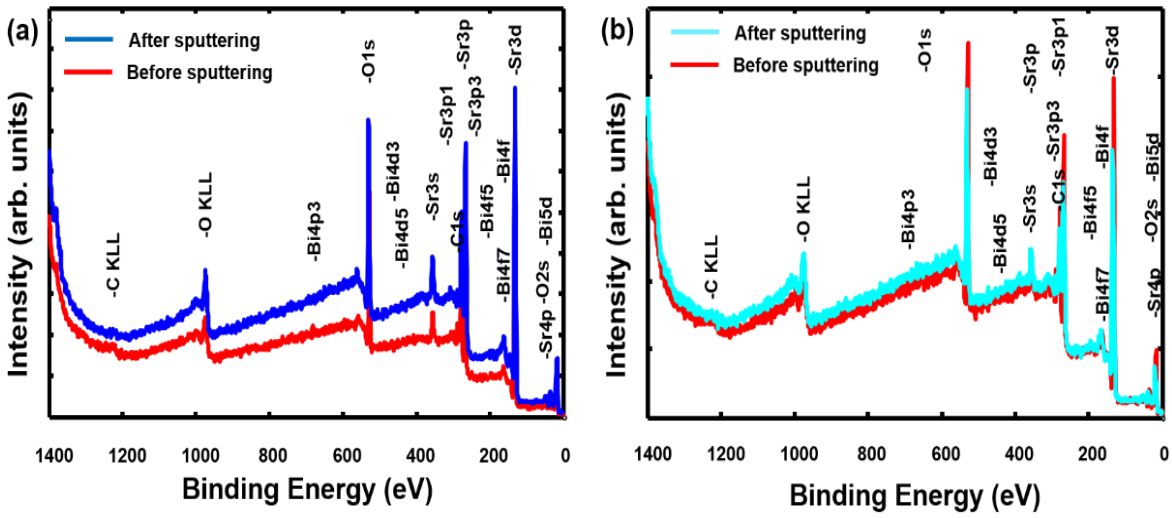

Figure 6.6: XPS survey spectra of SrO:Bi before sputtering and after 120 s of Ar^{+} sputtering (a) un degradation and (b) after degradation.

Figure 6.7 shows the high-resolution XPS spectra of the Sr 3d measured before and after 120 s Ar^{+} sputtering that were deconvoluted using the MULTIPACK software as shown in figure 6.7 (a and b) respectively. The un-degraded spectrum exhibits four characteristic peaks at binding energies of 131.5 and 133.4 eV and 132.6 and 134.2 eV, originating from the $3d_{5/2}$ and $3d_{3/2}$ shells of the atom. Peaks that were assigned to SrO and $SrCO_3$, respectively [26]. Tabah [27] reported that the Sr peaks are also visible in the SrO/C catalyst with reduced intensity and a slight shift compared to the pristine SrO. Figure 6.7 (c and d) show the high-resolution XPS spectra of the Sr^{2+} from $Sr_{1-x}O:Bi_{x=0.002}$ after 22 h of degradation, before and after 120 s of Ar^{+} sputtering. The two characteristic peaks at binding energies of 131.5 and 133.4 eV originating from the $3d_{5/2}$ and $3d_{3/2}$ shells of the atom were assigned to SrO. The Sr^{2+} peaks in figure 6.7 (a and b) that were assigned to $SrCO_3$ were significantly removed after 120 s sputtering as well as completely removed after degradation, figure 6.7 (c and d). The results are in accordance with the expectation that SrO, a basic oxide, will strongly chemisorb carbon dioxide and water vapor from its environment and appear on the surface as contamination.

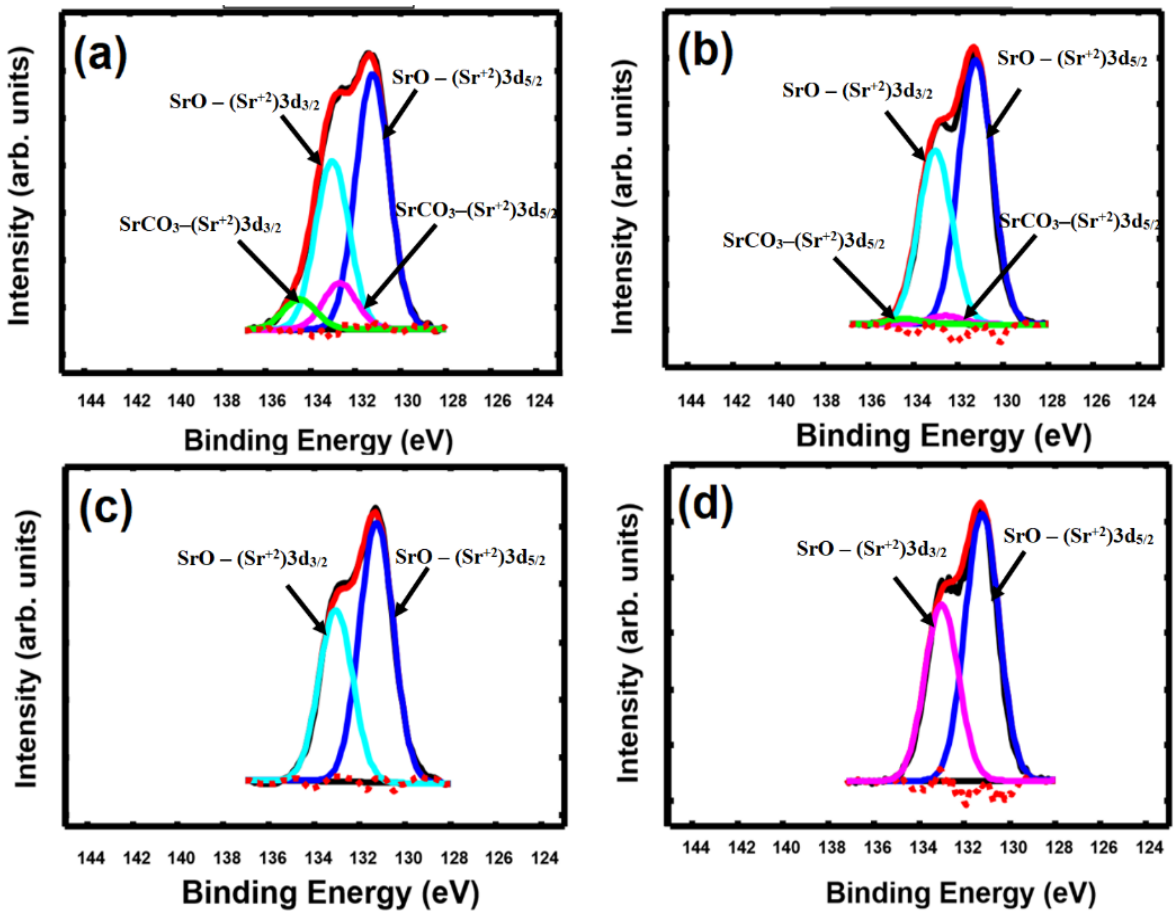

Figure 6.7: Deconvolution of the Sr^{2+} XPS peak of $Sr_{1-x}O:Bi_{x=0.002}$ (a) and (b) un-degradated, (c) and (d) degraded $Sr_{1-x}O:Bi_{x=0.002}$ as indicated before and after sputtering.

The O 1s XPS spectra of the un-degraded $Sr_{1-x}O:Bi_{x=0.002}$ and degraded $Sr_{1-x}O:Bi_{x=0.002}$, measured before and after 120 s Ar^+ sputtering were deconvoluted as shown in figure 6.8. In figure 6.8 (a and b) the O 1s peak of the un-degradation samples before and after sputtering can be deconvoluted into two components, namely, O1 and O2. The O1 component is attributed to O^{2-} ions on the cubic structure of the Sr^{2+} ion group [25], O2 was ascribed to the loosely bonded species from the atmosphere such as CO_3, H_2O, and O_2.The intensity of the O2 peak has decreased after 120 s sputtering and was also completely removed after 22 h electron degradation figure 6.8 (c and d), which was due to the removal of the surface contaminants as mentioned and discuss before as part of figure 6.5 (a and b).

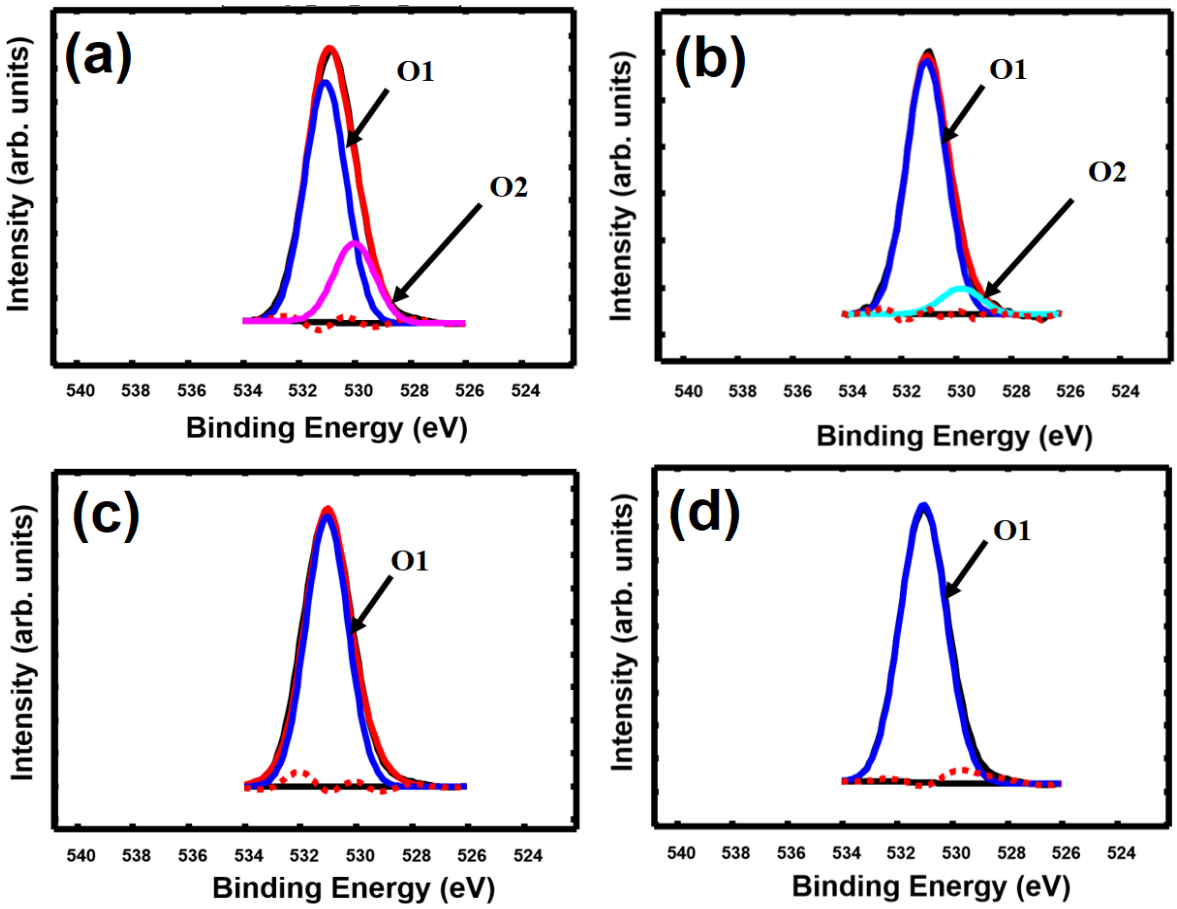

Figure 6.8: Deconvolution of O 1s XPS peak of $Sr_{1-x}O:Bi_{x=0.002}$ (a) and (b) un-degradation, (c) and (d) degraded $Sr_{1-x}O:Bi_{x=0.002}$ as indicated before and after sputtering.

6.5 Conclusion

Blue emitting $Sr_{1-x}O:Bi_{x=0.002}$ phosphor powder was successfully prepared by the sol-gel combustion method. The luminescence properties of the $Sr_{1-x}O:Bi_{x=0.002}$ were investigated by using different excitation sources. The high energy of the electron sources have the ability to excite the Bi^{3+} ions as well as the host lattice. The CL of the $Sr_{1-x}O:Bi_{x=0.002}$ has been investigated as a function of the accelerating voltage. $Sr_{1-x}O:Bi_x$ exhibited broad blue PL and CL emission. The stability of the $Sr_{1-x}O:Bi_x$ was also tested in vacuum and O_2 environment during prolonged electron bombardment. The CL intensity reduced slightly more and at a higher rate in the O_2 back-filled environment than in vacuum during the degradation studies, due to the reaction of O_2 with the adventitious C at a higher rate to form volatile compounds on the surface of the irradiated sample. A new non-

luminescent surface layer formed after the removal of C, which caused the CL intensity to decrease slightly more than in the case of the vacuum. The degradation, however, was only in the order of around 20%. Except for the initial degradation, the blue emitting Bi doped SrO powder was found to be stable under electron bombardment in both the base vacuum and back-filled O_2 environments. The high-resolution XPS results for the $Sr_{1-x}O:Bi_{x=0.002}$ sample indicated the presence of the major components Sr and O of this material. The results indicated the SrO, a basic oxide, strongly chemisorb carbon dioxide and water vapor from its environment and appear on the surface as contamination. All surface contaminated elements were completely removed after degradation. The results of these emissions make it an excellent candidate for application in FEDs.

6.6 References

[1] Renping Cao, Fangteng Zhang, Chenxing Liao and Jianrong Qiu, Yellow-to-orange emission from Bi^{2+}-doped RF_2 (R = Ca and Sr) phosphors, *Opt. Express.* **21(13)** (2013) 15728-15733. DOI: 10.1364/oe.21.015728.

[2] L. Wang, Q. Sun, Q. Liu and J. Shi, Investigation and application of quantitative relationship between sp energy levels of Bi^{3+} ion and host lattice, *J. Solid State Chem.* **191,** (2012)142–146. DOI: 10.1016/j.jssc.2012.03.015.

[3] Fu. Jipeng, R. Pang, Y. Jia, W. Sun, J. Lihong, S. Zhang and C. Li, Intense red–green up-conversion emission and their mechanisms of SrO:Er^{3+}/Yb^{3+},Gd^{3+},Lu^{3+},Bi^{3+}, *J. Lumin.* **181,** (2017) 240–245. DOI: 10.1016/j.jlumin.2016.09.029.

[4] J. A. McLeod, R. G. Wilks, N. A. Skorikov, L. D. Finkelstein, M. Abu-Samak, E. Z. Kurmaev and A. Moewes, Band gaps and electronic structure of alkaline-earth and post-transition-metal oxides, *Phys. Rev. B* **81(24)** (2010) 245123 (9 pages). DOI: 10.1103/physrevb.81.245123.

[5] A. Yousif, R.E. Kroon, E. Coetsee, O.M. Ntwaeaborwa and H.C. Swart, Luminescence and electron degradation properties of CaO:Bi^{3+} phosphor, *Appl. Surf. Sci.* **356,** (2015) 1064–1069. DOI: 10.1016/j.apsusc.2015.08.210.

[6] I.M. Nagpure, Shreyas S. Pitale, E. Coetsee, O.M. Ntwaeaborwa, J.J. Terblans and H.C. Swart, Cathodoluminescence properties and surface characterization of $Sr_3(PO_4)_2$:Tb phosphor. *Appl. Surf. Sci.* **257,** (2011) 10147– 10155. DOI: 10.1016/j.apsusc.2011.07.008.

[7] Shreyas S. Pitale, I.M. Nagpure, Vinay Kumar, O.M. Ntwaeaborwa, J.J. Terblans and H.C. Swart, Investigations on the low voltage cathodoluminescence stability and surface chemical behaviour using Auger and X-ray photoelectron spectroscopy on $LiSrBO_3:Sm^{3+}$ phosphor, *Mater. Res. Bull.* **46,** (2011) 987-994. DOI: 10.1016/j.materresbull.2011.03.022.

[8] Fu. Jipeng, Su. Zhang, Ma. Tengfei, Jia. Yonglei, P. Ran, J. Lihong, Li. Da, Li. Haifeng, S. Wenzhi and Li. Chengyu, A convenient and efficient synthesis method to improve the emission intensity of rare earth ion doped phosphors: the synthesis and luminescent properties of novel SrO:Ce^{3+} phosphor, *RSC Adv.* **5,** (2015) 93951–93956. DOI: 10.1039/c5ra15089b.

[9] K. Momma and F. Izumi, VESTA 3 for three-dimensional visualization of crystal, volumetric and morphology data, *J. Appl. Crystallogr.* **44,** (2011) 1272-1276. DOI: 10.1107/s0021889811038970.

[10] R. H. P. Awater and P. Dorenbos, The Bi^{3+} 6s and 6p electron binding energies in relation to the chemical environment of inorganic compounds, *J. Lumin.* **184,** (2017) 221–231. DOI: 10.1016/j.jlumin.2016.12.021.

[11] Fu. Jipeng, R. Pang, L. Jiang, Y. Jia, W. Sun, S. Zhang and C. Li, A novel dichromic self-referencing optical probe SrO:Bi^{3+},Eu^{3+} for temperature spatially and temporally imaging, *Dalton Trans.* **45(34)** (2016) 13317–13323. DOI: 10.1039/c6dt01552b.

[12] R.M. Jafer, A. Yousif, Vinod Kumar, H.C. Swart and E. Coetsee, The effect of annealing temperature on the luminescence properties of Y_2O_3 phosphor powders doped with a high concentration of Bi^{3+}, *J. Lumin.* **180** (2016) 198–203. DOI: 10.1016/j.jlumin.2016.08.042.

[13] A. Yousif, R. M. Jafer, S. Som, M. M. Duvenhage, E. Coetsee and H. C. Swart, Ultra-broadband luminescent from a Bi-doped CaO matrix. *RSC Adv*. **5(67),** (2015) 54115–54122. DOI: 10.1039/c5ra09246a.

[14] L. J. Brillson, Applications of Depth-Resolved Cathodoluminescence Spectroscopy, *J. Phys. D.* **45,** (2012) 183001. DOI: 10.1088/0022-3727/45/18/183001.

[15] A. Yousif, R.E. Kroon, E. Coetsee, O.M. Ntwaeaborwa and H.C. Swart, Luminescence and electron degradation properties of CaO:Bi^{3+} phosphor, *Appl. Surf. Sci.* **356,** (2015) 1064–1069. DOI: 10.1016/j.apsusc.2015.08.210.

[16] T. Minami, T. Miyata, K. Ueda, S. Matsui, and H. Fukada. PL and EL Characteristics in New Blue Emitting La_2O_3:Bi Phosphor Thin Films. *ECS Trans*. **16(30)** 39-45 (2009). DOI:10.1149/1.3106670.

[17] A. D. Broadbent. A critical review of the development of the CIE1931 RGB color-matching functions. *Color Res Appl*. **29(4)** (2004)267–272. DOI:10.1002/col.20020.

[18] R. M. Jafer, A. Yousif, Vinod Kumar, Trilok Kumar Pathak, L.P. Purohit, H.C. Swart and E. Coetsee, Comparison of Y_2O_3:Bi^{3+} phosphor thin films fabricated by the spin coating and radio frequency magnetron techniques, *Phys. B Condens. Matter.* **497,** (2016) 39–44. DOI: 10.1016/j.physb.2016.06.007.

[19] Lawrence E. Davis, Noel C. Mac Donald, Paul W. Palmberg, Gerald E. Riach and Roland E. Weber. Handbook of Auger Electron Spectroscopy. 2nd Edition. Published by Physical Electronics Division of Perkin-Elmer. Minnesota (1976). ISBN: 9788578110796.

[20] H. C. Swart, J. S. Sebastian, T. A. Trottier, S. L. Jones and P. H. Holloway, Degradation of zinc sulfide phosphors under electron bombardment. *J. Vacuum Sci. Technol. A* **14(3)** (1996) 1697–1703. DOI: 10.1116/1.580322.

[21] H. C. Swart, J. J. Terblans, O. M. Ntwaeaborwa, R. E. Kroon and B. M. Mothudi, PL and CL degradation and characteristics of $SrAl_2O_4$: Eu^{2+},Dy^{3+} phosphors. *Physica B: Condensed Matter.* **407(10)** (2012) 1664–1667. DOI: 10.1016/j.physb.2011.09.112.

[22] A. Yousif, H. C. Swart and O. M. Ntwaeaborwa, Surface state of $Y_3(Al,Ga)_5O_{12}$:Tb phosphor under electron beam bombardment, *Appl. Surf. Sci.* **258(17)** (2012) 6495–6503. DOI: 10.1016/j.apsusc.2012.03.066.

[23] E. Hasabeldaim, O. M. Ntwaeaborwa, R. E. Kroon and H. C. Swart, Surface analysis and cathodoluminescence degradation of undoped ZnO and ZnO:Zn phosphors. *J. Vacuum Sci. Technol.* **B34(4)** (2016) 8. DOI: 10.1116/1.4953561.

[24] B. L. Abrams and P. H. Holloway. Role of the Surface in Luminescent Processes. *Chem. Rev*, **104(12)** (2004) 5783–5802. DOI:10.1021/cr020351r.

[25] J.F. Moulder, Handbook of X-ray Photoelectron Spectroscopy: a Reference Book of Standard Spectra for Identification and Interpretation of XPS Data, Physical Electronics, Chicago, 1995. ISBN: 096481241X 9780964812413.

[26] V. Young and T. Otagawa. XPS studies on strontium compounds. *Appl. Sci. Res.* **20(3)**, (1985) 228–248. DOI:10.1016/0378-5963(85)90083-2.

[27] B. Tabah, A. P. Nagvenkar, N. Perkas and A. Gedanken. Solar-Heated Sustainable Biodiesel Production from Waste Cooking Oil Using a Sonochemically Deposited SrO Catalyst on Microporous Activated Carbon. *Energy & Fuels*, **31(6)** (2017) 6228–6239. DOI: 10.1021/acs.energyfuels.7b00932.

Chapter 7: Comparison of SrO:Bi phosphor thin films fabricated by spin coating and pulsed laser deposition

In this chapter, the structural, morphological and optical properties of SrO:Bi thin films prepared by spin coating and pulsed laser deposition were investigated and compared to each other.

7.1 Introduction

Many studies have been conducted to develop new oxide phosphors in the thin films form to improve the luminescent performance, including color purity, emission intensity and quantum efficiency. The alkaline-earth oxides form a chemically interesting series of metal oxides [1]. Accordingly, some light emitting diodes (LEDs) that have been fabricated to use a near ultraviolet source, coupled with blue, green and red phosphors and have attracted much attention. For that reason it is important to develop new blue phosphors that could be effectively excited in the near ultraviolet (n-UV) range [2]. Strontium oxide (SrO) is one of the alkaline-earth oxides which exhibits optical properties typical of an insulator, with a wide band gap of 6.14 eV [3]. SrO is a ceramic material and if doped with different metal ions it has a wide range of applications in luminescent materials. Despite the wide potential application of doped SrO, simple and convenient methods of directly synthesizing different types of ion doped SrO are still rare, except for some matrices of SrO doped with ions of rare-earth elements, such as SrO:Ce^{3+} [4] and SrO:Eu^{2+} [5] that were investigated in the LEDs field. The SrO activated by another group of important activators, the so-called mercury-like ions such as Bi^{3+}, however, has not been well studied in this field. On the other hand, Bi ions can be useful in obtaining blue to red emitting phosphors by using different hosts when excited by UV light due to an efficient conversion to longer wavelengths. Therefore, the emission of Bi^{3+} ions can be used as a candidate for n-UV LED applications, using an appropriate matrix. In most hosts, an absorption band of the Bi^{3+} ion lies in the UV region and a C band in the vacuum UV (VUV) region [6].

Absorption bands of Bi^{3+} are usually attributed to two transitions where $^1S_0 - {}^3P_1$ transition is allowed and $^1S_0 - {}^1P_1$ transition becomes allowed due to a spin-orbit coupling. The $^3P_1$ excited state is lower than that of the $^1P_1$ excited state, and gives emission usually in a single broadband due to the $^3P_1 - {}^1S_0$ transition [7]. For over 20 years there is a broad technological and scientific interest in the epitaxial growth of oxides on semiconductors. Frequently, thin interfacial layers are required to achieve growth of oxides on semiconductors with sufficient structural perfection and device performance [8]. Highly oriented strontium oxide (SrO) whiskers were obtained using a chemical vapor deposition technique at atmospheric pressure which were synthesized on a single-crystalline Si(100) substrate from strontium bis-dipivaloylmethanate, $Sr(C_{11}H_{19}O_2)_2$ [9]. Careful ex-situ investigations of molecular beam epitaxy growth of films of SrO were not performed, partially due to the fact that SrO is unstable in air. Thus, the structural properties and crystalline quality and luminescence of SrO films are not well understood [10]. Various techniques can be used to fabricate SrO thin films such as radio frequency magnetron sputtering, spin coating, pulsed laser deposition (PLD), chemical vapor deposition and spray pyrolysis. The sol-gel spin coating method is considered one of the most important research and industrial processes because of its ease and low cost, capable of providing homogeneous films at the molecular level, excellent control of film composition and low crystallization temperature. This is due to the mixing of the liquid precursors. Post-annealing treatments may be used to improve the film's structure and morphology in order to obtain the desired characteristics [11]. PLD is a widely used technique to grow thin films for a variety of applications. The major advantage of the PLD is the ability to transfer the material stoichiometry from a multi-component ablation target to a growing film [12]. In this work, SrO films were successfully deposited by using the sol-gel spin coating and PLD techniques. The structural, optical and morphological properties were studied by X-ray diffraction (XRD), photoluminescence spectroscopy (PL) with a 325 nm He-Cd laser, scanning electron microscope (SEM) and atomic force microscope (AFM).

7.2 Experimental procedure

7.2.1 Sample preparation

The experimental part consists of two sections. Firstly, $Sr_{-x}O:Bi_{x=0.002}$ thin films were prepared by the sol-gel spin coating method and secondly the powder was synthesized by the sol-gel combustion method and it was used as a target for the PLD technique to fabricate the $SrO:Bi_{0.002}$ thin films. In the first part strontium nitrate ($Sr(NO_3)_2$, Sigma-Aldrich, purity 99.95%), bismuth nitrate ($Bi(NO_3)_3$. H_2O, Sigma-Aldrich 99.999% pure) and citric acid CA ($C_6H_8O_7$) were used as a starting material, dopant source, complexation agent, respectively. These chemicals were mixed together and dissolved into 50 ml of distilled water and then chelated in a sealed beaker in a water-bath with mechanical stirring at 80 °C. After 1 h, the beaker was opened and ethylene glycol (EG) was added as polymerization agent. The molar ratio of the metal ions to CA to EG was maintained at 1:1:4. The resulting solution was continuously heated and kept under stirring to promote the esterification and polymerization reactions. Then the sealed beaker was kept at 80 °C for 2 h in a water bath. The sol solution was aged for 24 h at room temperature ranging between 25 and 32 °C, before the spin coating process. Two parts of the solution were synthesized, the first without any dopants and used as host and the other with the Bi dopant. The Si wafers and glass slides that were used as substrates were cleaned ultrasonically for 30 min using acetone to remove the organic contaminations and then rinsed with methanol and deionized water, after which they were then dried by N_2 gas. The solution without dopant was dropped onto the glass substrates which were spun at 3000 rpm for 30 s by using a spin coater. After deposition, the wet thin films were dried at 300 °C for 10 min to remove any residual water and also to remove the organic residuals. Sequentially deposition of 7, 12, 20 and 30 layers was performed as shown in figure (3.4). The total thickness of the spin-coated layers was not determined. The thin films were then annealed at 500 °C for 2 h in the ambient atmosphere in a Carbolite furnace. The solution doped with Bi 0.2 mol% was deposited on Si (100) substrates of 12 layers in a similar way. Finally, the thin films were annealed at various temperatures for 2 h in the ambient atmosphere in the Carbolite furnace.

Secondly, the starting materials used in the first part without EG were used to prepare SrO:Bi powder synthesized by the sol-gel combustion method and it was used as a target for the PLD technique. The molar ratio of the nitrate to citrate was 1:1. The starting materials were dissolved in deionized water under stirring and heating to obtain a homogenous precursor solution gel. The solution was placed in a furnace preheated at 250 °C. When the combustion process was completed a solid foamy brown powder was obtained. It was well crushed and then annealed in air at 1100 °C in a ceramic tube furnace for 2 h with an initial increasing heating rate of 5 °C/min up to the required temperature. The ground powder was pressed with ethanol as the binder and was used as an ablation target. The target was annealed at 200 °C for 2 h in air to remove all adventitious water containing species that might be present and then placed inside the chamber of the PLD system on a rotating target holder that can also move linearly (forward and backward). The deposition chamber was evacuated to a base pressure of 5×10^{-5} mbar and then backfilled with O_2 to a pressure of 1×10^{-3} or 3×10^{-3} mbar. The target was ablated using different types of excimer lasers in the lab of laser department, national institute for laser, plasma and radiation physics, Bucharest-Magurele, Romania. The first one was a KrF laser (248 nm) with energy 300 mJ/pulse while the second one was a ArF laser (193 nm) with energy 150 mJ/pulse. In both cases the substrate temperatures was 300 °C, the laser pulse frequency was 10 Hz and 4200 pulses were used during a deposition time of 7 min.

7.2.2 Characterization technique

The structure of the thin films was characterized by XRD measurements using a Bruker D8 Advance diffractometer (40 kV, 40 mA) with Cu Kα X-rays (0.154 nm). The optical properties of the thin films were measured using a Horiba iHR320 monochromator attached with a photomultiplier tube (PMT), by exciting with a 325 nm wavelength He-Cd laser. The surface morphology was recorded using a JEOL JSM-7800F SEM. The surface topography and roughness were examined from images captured in contact mode using a Shimadzu SPM-9600 AFM instrument. The root means square (RMS) roughnesses were estimated by analyzing the topography scans of the film surfaces using commercial software installed in the AFM host computer.

7.3 Results and discussion

7.3.1 XRD Analysis

Figure 7.1. shows the XRD patterns of the 7, 12, 20 and 30 number of layers of undoped SrO thin films annealed at 1100 °C that were deposited on the amorphous glass substrates. In the 7, 12 and 20 layer thin films, only one peak of SrO having a cubic phase, with 111 index was observed according to the PDF card number 06-0520. The 222 reflection was also visible for the thicker 30-layer sample. Furthermore, the intensity of the XRD peaks increased with the increase in number of layers. This result indicated a high degree of (111) textured growth of the thin films. This may be due to the fact that the (111) oriented surface is the lower energy surface for face-centered-cubic (fcc) structure as is the case for most (fcc) metal films [13]. No secondary phases were found in the X-ray patterns.

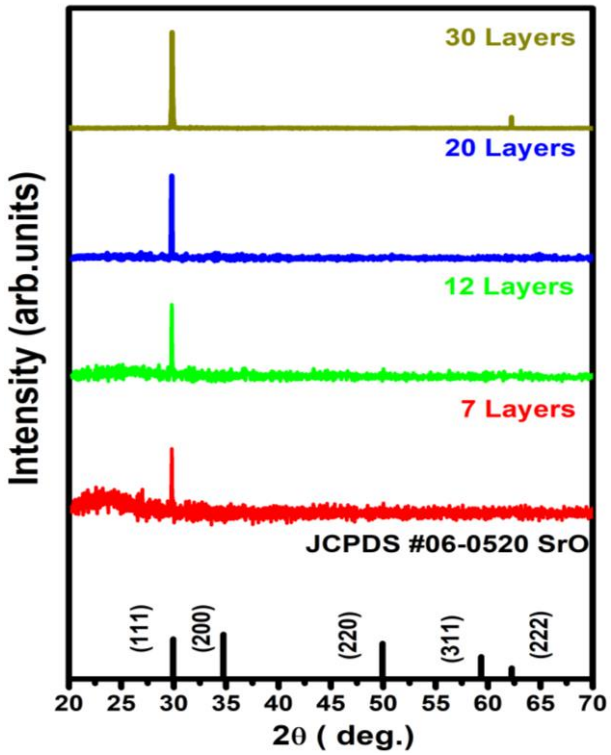

Figure 7.1: XRD patterns of the SrO spin coating thin films with different number of layers annealed at 500 °C.

Figure 7.2 shows the comparison of the XRD patterns of the $Sr_{1-x}O:Bi_{x=0.002}$ powder produced by the sol-gel combustion method and the doped thin films deposited on the Si(100) substrates produced by different methods. Figure 7.2 (a) the sol-gel spin coating method deposited on Si (100) substrates of 12 layers in a similar way, post-annealed at various temperatures between 800 °C and 1100 °C for 2 h and (b) corresponds to PLD thin films produced by using different energy lasers at various O_2 pressures. All peaks of the XRD patterns of the powder were consistent with the cubic structure of the SrO (JPCDS 06-0520). For all thin films samples produced by the sol-gel spin coating method, XRD showed the thin film had a strong (111) preferential orientation on the cubic phase and peaks which are labeled with an asterisk (*) can be associated with diffraction from the Si(100) substrate. The substrate peaks have been obtained in several other measurements in the past [14,15].

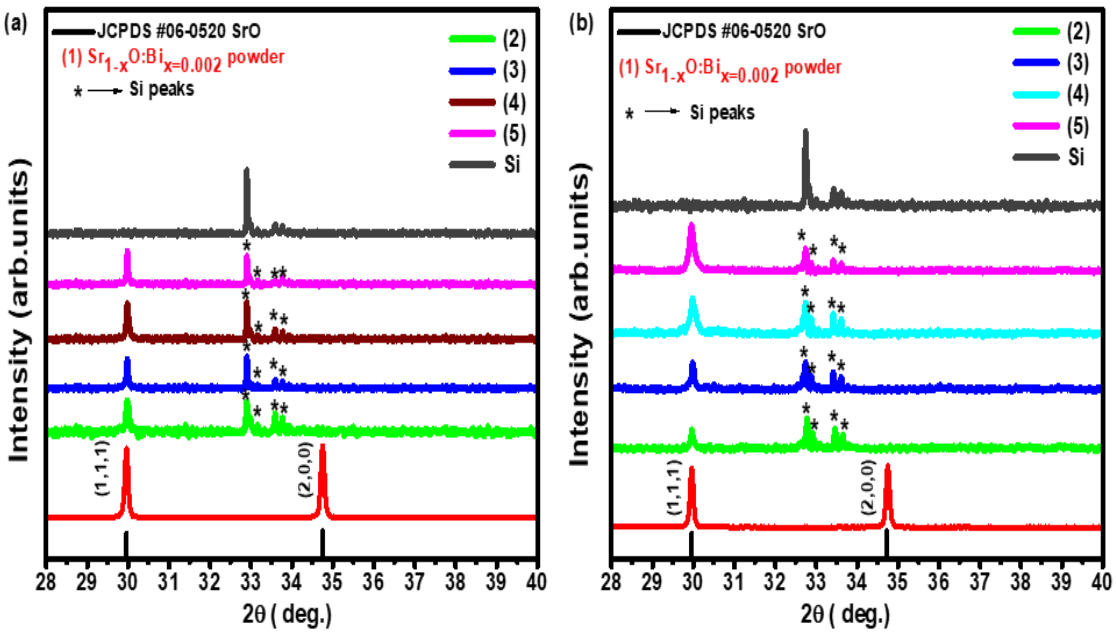

Figure 7.2: XRD patterns of the SrO:Bi powder and Si substrate with (a) spin coating thin films annealed at different annealing temperatures (2, 3, 4 and 5) of 800 °C, 900 °C , 1000 °C and 1100 °C respectively, and (b) PLD thin films obtained with different types of lasers (2,3,4 and 5); (2,3) KrF 248 nm and (4, 5) ArF 193 nm laser deposited in different O_2 pressures of (2,4) 1×10^{-3} and (3,5) 3×10^{-3} mbar, respectively.

The crystallite sizes of the $Sr_{1-x}O:Bi_{x=0.002}$ thin films were calculated using the full width at half maxima (FWHM) of the 111 peak after the contribution of the XRD machine was removed using Scherrer's formula [16]

$$D = \frac{K\lambda}{\beta \cos\theta} \qquad (7.1)$$

where D is the size of the crystallites, K is a correlation factor (taken as 0.94), λ is the wavelength of Cu Kα radiation (0.154 nm), β is the FWHM of the 111 peak and θ is the Bragg diffraction angle. The calculated crystallite size of the thin films produced by the sol-gel spin coating annealed at 800, 900, 1000 and 1100 °C were 68, 69, 72 and 73 nm, respectively. The results imply that the crystallite size of the sol–gel-derived films increased slightly with the increasing annealing temperatures, which can be understood by considering the merging process induced by thermal treatment. This may be due to the improvement in the crystallinity of the film grown at the higher substrate temperature [17]. The crystallite size of samples produced by PLD using the KrF 248 nm laser with O_2 at pressures of 1×10^{-3} and 3×10^{-3} mbar were 75 and 77 nm, respectively, while the crystallite size of the samples produced using the ArF 193 nm laser with O_2 pressures of 1×10^{-3} and 3×10^{-3} mbar were 44 and 45 nm. The results imply that the crystallite size of the PLD films were not much affected by the O_2 pressure, but showed a significant increase with the increase of photons energy of the excimer laser.

7.3.2 Photoluminescence (PL) study

Figure 7.3(a) shows the emission spectrum when the $Sr_{1-x}O:Bi_{x=0.002}$ powder sample was excited with the 325 nm He-Cd laser at room temperature. The spectrum shows the main PL peak position of the powder with a broad band of blue fluorescence emission which extends from 400 to 520 nm and is centered at 445 nm. This luminescence peak was attributed to the Bi^{3+} ions, which are known for emitting blue light. The phosphor synthesized by the sol-gel combustion method has already been reported previously, when excited by using the Cary Eclipse system at 260 and 360 nm, and gave the same broad blue emission spectrum centered at 445 nm. The Bi^{3+} ion has a $[Xe]4f^{14}5d^{10}6s^2$ electronic configuration. Emission and absorption spectra are therefore expected to be broad bands and strongly dependent on the host's structure by the covalence and coordination numbers [18]. The ground state of the Bi^{3+} is $^1S_0$, whereas the excited states from the 6s6p

configuration are $^3P_0$, $^3P_1$, $^3P_2$ and $^1P_1$ in the sequence of increasing energy. Transitions from $^1S_0$ to $^3P_1$, $^3P_2$ and $^1P_1$ are usually denoted as A, B and C, respectively. The transitions $^1S_0 \rightarrow {}^3P_0$ and $^1S_0 \rightarrow {}^3P_2$ are spin forbidden, while $^1S_0 \rightarrow {}^1P_1$ is spin allowed. Spin-orbit coupling of the $^1P_1$ and $^3P_1$ levels means that the $^1S_0 \rightarrow {}^3P_1$ transition may occur. Bi^{3+} ions may be excited from the ground state to $^3P_1$ (A band) or $^1P_1$ (C band) states with an appropriate wavelength of light in the UV range [19]. The SrO phosphors doped with Bi have a quasi-line structure in the spectra caused by $^3P_1 \rightarrow {}^1S_0$, and $^3P_0 \rightarrow {}^1S_0$ electronic transitions, while Zavt *et al.* [20], Steen [21] and Yamashita *et al.* [22] reported that the second emission peak in SrO:Bi was due to the forbidden $^3P_0 \rightarrow {}^1S_0$ transition which is initiated by the mixing of $^3P_0$ and $^3P_1$ states by lattice vibrations. The existence of two peaks on the broad emission peak may therefore be ascribed to these states.

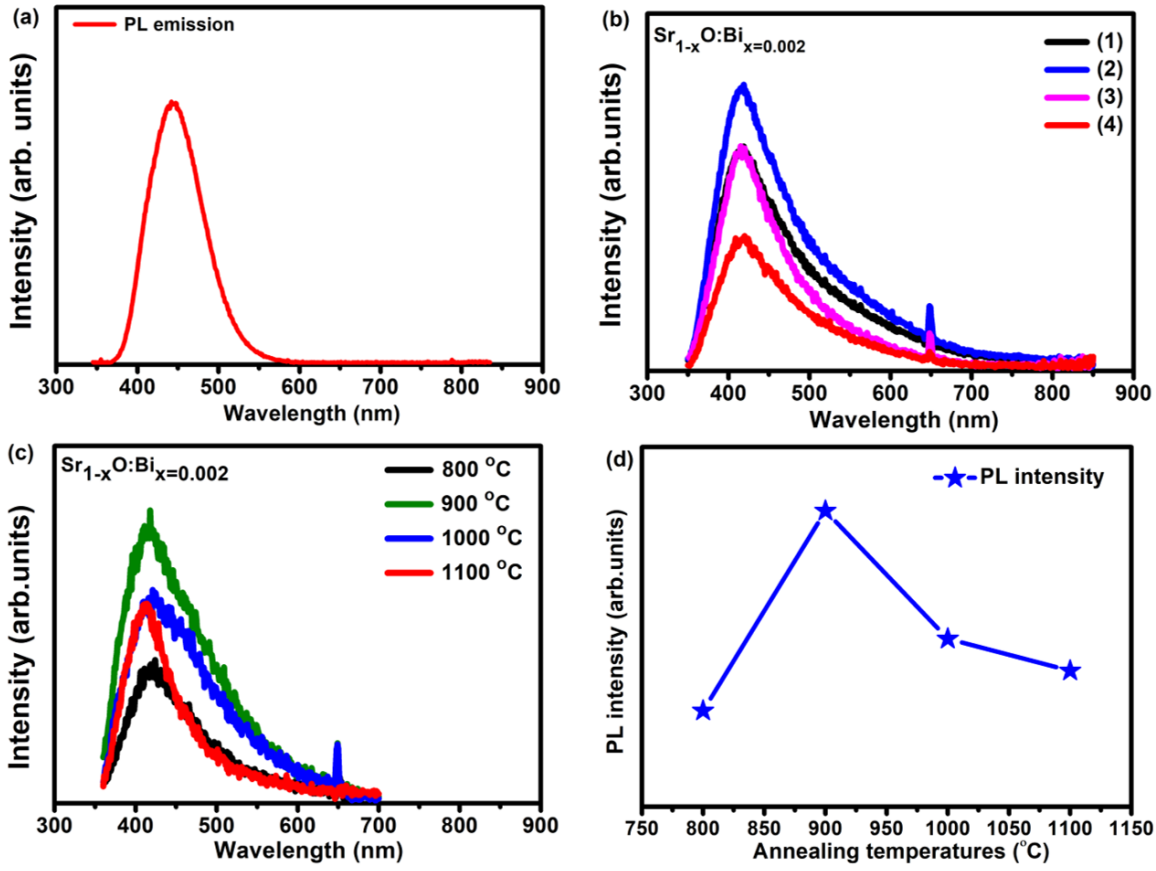

Figure 7.3: PL spectra of $Sr_{1-x}O:Bi_{x=0.002}$ measured with a 325 nm He-Cd laser with slit widths 24 and 2000 nm, and PMT voltages 1000 and 1400 V, for powder and thin films respectively: (a) powder (b) PLD thin films with different types of lasers, (1, 2) KrF 248 nm and (3, 4) ArF 193 nm laser deposited in different O_2

pressures of (1, 3) 1 × 10^{-3} and (2, 4) 3 × 10^{-3} mbar, respectively. (c) spin coating thin films at different annealing temperatures and (d) the PL spin coating thin films intensity as a function of annealing temperature.

Figure 7.3(b) shows the PL of the $Sr_{1-x}O:Bi_{x=0.002}$ thin films fabricated by the PLD technique, the numbers 1, 2, 3 and 4 indicate the spectra of the thin films deposited by using different excimer type lasers, (1, 2) KrF 248 nm and (3, 4) ArF 193 nm laser deposited in different O_2 pressures of (1, 3) 1 × 10^{-3} and (2, 4) 3 × 10^{-3} mbar, respectively. The emissions of all PLD films were almost similar to the emission of the spin coating film. The film that was grown in the high O_2 pressure may be enriched in oxygen with respect to the films grown at the lower O_2 pressure. Jones et al. [23] reported that when they studied $Eu:Y_2O_3$ thin films at different oxygen pressures that the increase in oxygen pressure resulted in an increase in surface roughness, which in turn increased the PL intensity of the films, whereas the improvement in PL performance was probably brought about by reduced internal reflections caused by the rougher surfaces. Figure 7.3(c) shows the PL of the $Sr_{1-x}O:Bi_{x=0.002}$ phosphor 12 layer spin coating thin films that were annealed at 800 °C, 900 °C, 1000 °C and 1100 °C, respectively. The PLD and spin coating thin films samples showed a broad emission, although still a double peak like for the powder. The main PL emission peak position of the thin films showed a shift to shorter wavelengths at 427 nm, when compared to the powder (445 nm), which extends from 380 to 520 nm and centered at 427 nm. This shift of the main peak position can be attributed to the change in the surrounding structure of the Bi^{3+} ions, due to a change in the crystal field, where the binding energy of the atoms and molecules in the thin film forms on average, much less compared to that in bulk powder. Yousif et al. [24] reported that all the phosphor hosts activated with Bi^{3+} ions showed large changes in their luminescence properties due to their outer electrons which are not shielded from the surrounding environment. Also, Dlamini et al. [25] have measured a slight shift in the wavelength of the PL spectra for the $Y_3(Al,Ga)_5O_{12}:Ce^{3+}$ thin films due to a change in the crystal field. Yousif et al. [26] reported the shift of the PL emission of the $Y_2O_3:Bi^{3+}$ thin films fabricated by spin coating at high temperatures due to the Si diffusion, which was responsible for the change in the Bi^{3+} doped Y_2O_3 phosphor material structure to a structure of Bi^{3+} doped yttrium silicate phosphor. Figure 7.3(d), shows the PL spin coating thin films intensity as a function of

annealing temperature. The optimum annealing temperatures for the samples for the maximum PL intensity was found to be at 900 °C. The intensity first increased up to 900 °C, and then decreased in the higher temperature at 1000 °C and 1100 °C. Hu et al. [27] reported that a low substrate temperature is responsible for a low PL intensity due to the defects in the film's structure and nonstoichiometry of the film's composition. Then the reduced luminescence intensity in samples at 1000 °C and 1100 °C may be due to a consequent loss in Bi^{3+} due to volatile species as a result of the increased annealing temperature. There was a blue shift in the sample annealing at 1100 °C which may be due to the large quantities of volatilized Bi^{3+}. On the other hand, maybe due was diffusion of Si and the formation of a new host material.

In figure 7.3 (b) and (c) a peak at 650 nm was detected which is attributed to the second order peak of the 325 nm He-Cd laser excitation source.

The chromaticity coordinates of the PL for the $Sr_{1-x}O:Bi_{x=0.002}$ powder that was used as the target to fabricate the PLD thin film, together with the optimum samples from the spin coating and PLD films, are shown in figure 7.4, which were determined using the Commission Internationale de I'Eclairage (CIE) coordinate system [28]. The calculated chromaticity coordinates for the $Sr_{1-x}O:Bi_{x=0.002}$ to get the blue PL for the powder and thin films are tabulated in Table 7.1.

Table 7.1: The CIE coordinates (X, Y) of $Sr_{1-x}O:Bi_{x=0.002}$ powder and thin films.

Sample	**CIE coordinates**	
	X	Y
Powder	0.150	0.056
Spin coating at 900 °C	0.190	0.059
PLD 248 nm at 3×10^{-3} mbar	0.020	0.060

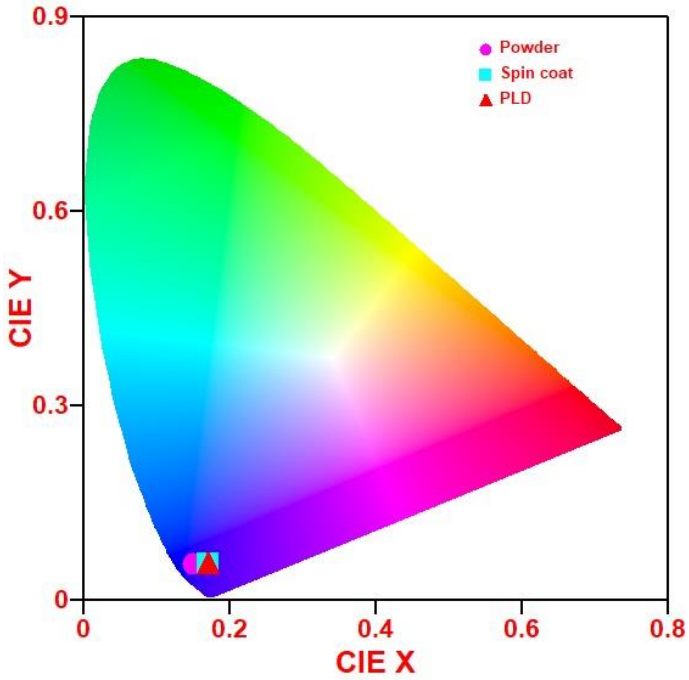

Figure 7.4: CIE coordinates for emission from the $Sr_{1-x}O:Bi_{x=0.002}$ powder annealed at 1100 °C, spin coating thin film annealed at 900 °C and PLD thin film obtained with the KrF 248 nm laser in 3×10^{-3} mbar O_2.

7.3.3 Surface morphology

7.3.3.1 Scanning electron microscopy

Figure 7.5 shows surface morphology SEM micrographs of the thin films (a) deposited by spin coating at 900 °C, (b), (c), (d) and (e) PLD thin films deposited in different O_2 pressures by different excimer laser energies (KrF 248 nm and ArF 193 nm) with O_2 a pressures of 1×10^{-3} and $3 \times 10^{-3.}$ It is clearly seen that their surface morphology differs depending on the technique in which they were deposited. The film deposited by spin coating figure 7.5 (a) has a smoother surface compare with the PLD samples that were totally different. The surface seemed to be smooth with agglomerated particles in some areas. These features can be attributed to the physics behind the spin coating process [29], wherein the sol material flow due to centrifugal forces which impose a shear stress within the film during deposition. Where the rapid shrinkage due to the removal of solvent and continuous condensation creates a tensile stress within the film and changes the rheological properties of the film [19]. All the SEM images for PLD samples show a rough thin film

surface that contains rounded particles of different sizes and shapes which seem to be independent of the effect of O_2 pressure. The alternative laser pulse energies appear to produce particles different in shape (examples are mentioned by the red circles), which are observed in figure 7.5 (b, c, d and e) and it appeared more clearly in 3D AFM images in figure 7.6. Some of the big particles consist of an agglomeration of smaller particles, where the deposition process of the film on the substrate involves different stages, one of them being the particle agglomeration in which the formed particles start to coalesce to each other to form bigger particles [30]. The particulates are transferred by the ablation plume to the substrate and are incorporated in the growing film [31]. The laser ablation process produces the atomization of the target material and has an explosive-like character and is accompanied by the formation of particulates that are transferred by the ablation plume to the substrate and incorporated in the growing film [32].

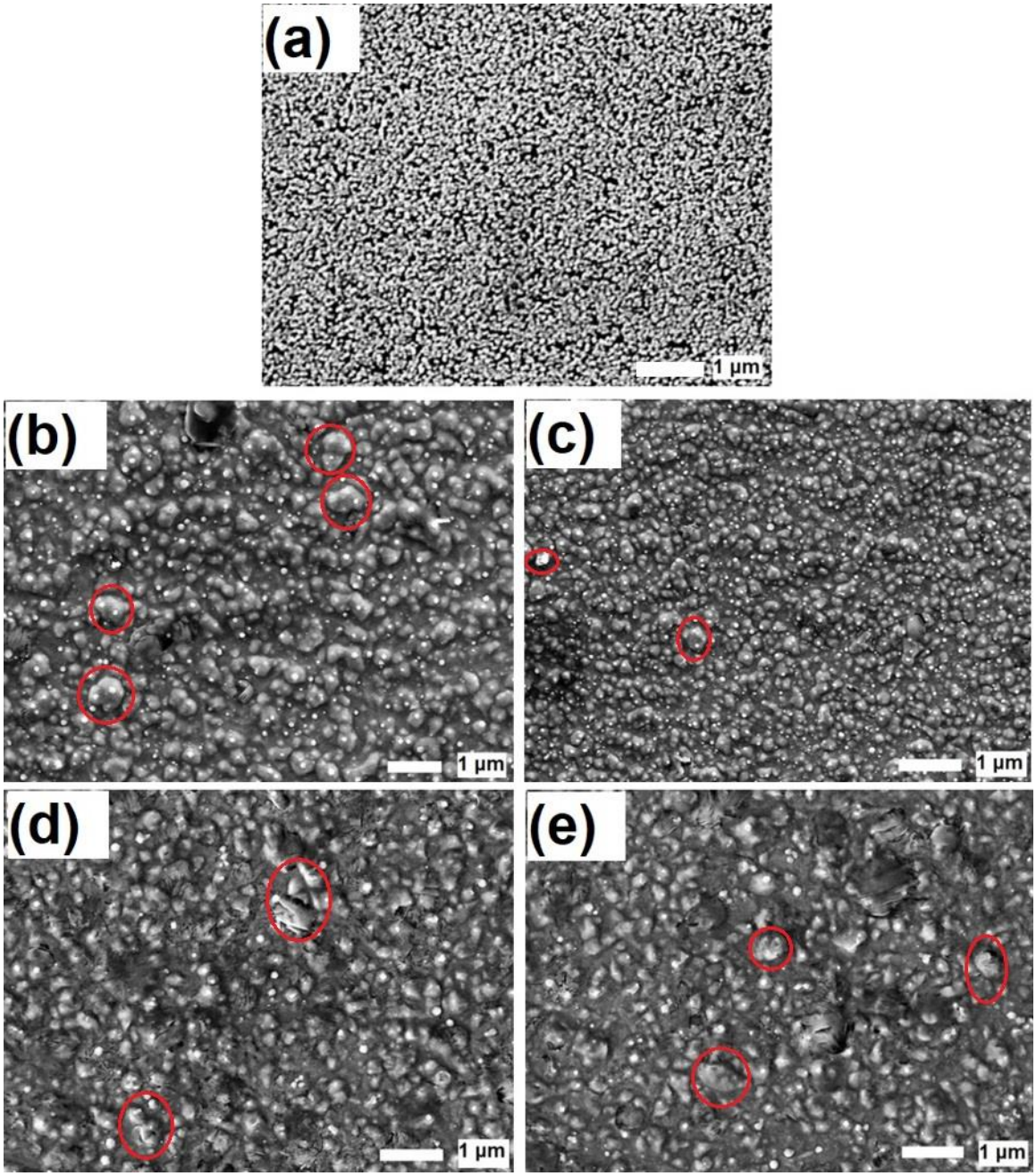

Figure 7.5: SEM images for the $Sr_{1-x}O:Bi_{x=0.002}$ thin films (a) by spin coating at 900 °C, b, c, d and e PLD thin films deposited in different O_2 pressure by different excimer laser energies ((b and c) KrF 248 nm and (d and e) ArF 193 nm) laser with O_2 pressures of 1×10^{-3} and 3×10^{-3} mbar, respectively.

7.3.3.2 Atomic force microscope

Figure 7.6 shows 2D and 3D AFM images for a region of 3×3 µm^2 for the same samples as used for SEM. In figure 7.6 (a) it can be seen that the films fabricated by the spin coating

technique were covered with small cubic shaped particles of about 100 nm in size. These particles have well-defined boundaries and are homogeneously distributed on the substrate surface with uniform particle sizes. Whilst all samples fabricated by the PLD technique (figure 7.6 (b,c,d and e)) show that the substrates were well covered with rounded irregular particles of different sizes. The change in the surface morphologies was associated with the plasma plume dynamics by the different O_2 pressure and different laser energy, where the PLD process involves laser beam and target material interaction. Consequently, the plasma plume will be released from the target surface in a perpendicular direction heading toward a substrate. The plasma plume contains ions, electrons, atoms, molecules and clusters. Their kinetic energy are high because of the high energy of the laser pulse [33]. The roughnesses of the films weres studied and are included in Table 7.2. Where the average roughness (R_a), the mean of the measured heights over the entire area/length, describes the roughness of mechanical surfaces. R_a provides a general idea about the characteristic of the overall profile heights variation and monitoring the manufacturing process. Whilst the root mean square roughness (R_q), is the square root of the surface heights distribution and is more precise than the average roughness for the area with a large deviation from the mean height. Therefore, it determines the ultimate optical surface. The ten-point mean height roughness (R_z), is the difference between the average of five highest heights and five lowest valleys for the evaluated surface: it is more responsive to occasional deep valley and highest height. The surface roughness R_q for all thin films deposited by PLD were higher compared to the thin film prepared by the spin coating technique. It can be concluded that the two different thin films fabricating techniques have an effect on the surface morphology and surface roughness.

Table 7.2: Roughness parameters of the spin coating and PLD thin films.

Sample name	R_a (nm)	R_q (nm)	R_z (nm)	R_q/R_a
Spin coating 900 °C	2.5	3.1	23.8	1.24
PLD 248 nm at 1 × 10^{-3} mbar	30.2	34.1	266.9	1.12
PLD 248 nm at 3 × 10^{-3} mbar	18.1	23.7	238.0	1.30
PLD 193 nm at 1 × 10^{-3} mbar	30.1	38.0	241.3	1.18
PLD 193 nm at 3 × 10^{-3} mbar	34.4	33.4	276.3	1.26

The different measures of films roughness (R_a, R_q and R_z) increased relative to one other. Hasabeldaim et al [11] reported that for a Gaussian distribution of asperity height, the statistical theory yields that the ratio of R_q to R_a should be 1.25. Some authors note that the asperity height distribution of most engineering surfaces (tribology) may be approximated by a Gaussian distribution with R_q/R_a values of up to 1.31. Therefore, for our samples the values R_q/R_a were calculated from the AFM images (see Table 7.2) and found to be reasonably close to the value that was predicted by the theory, meaning that the films having a Gaussian distribution for their asperity height, which indicate that the statistical relationships for surface roughness are applicable.

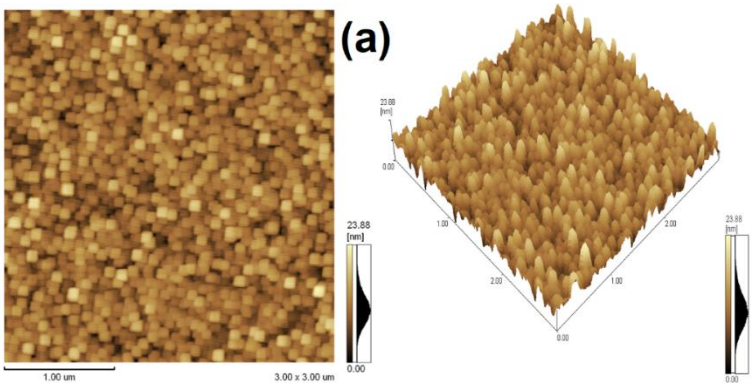

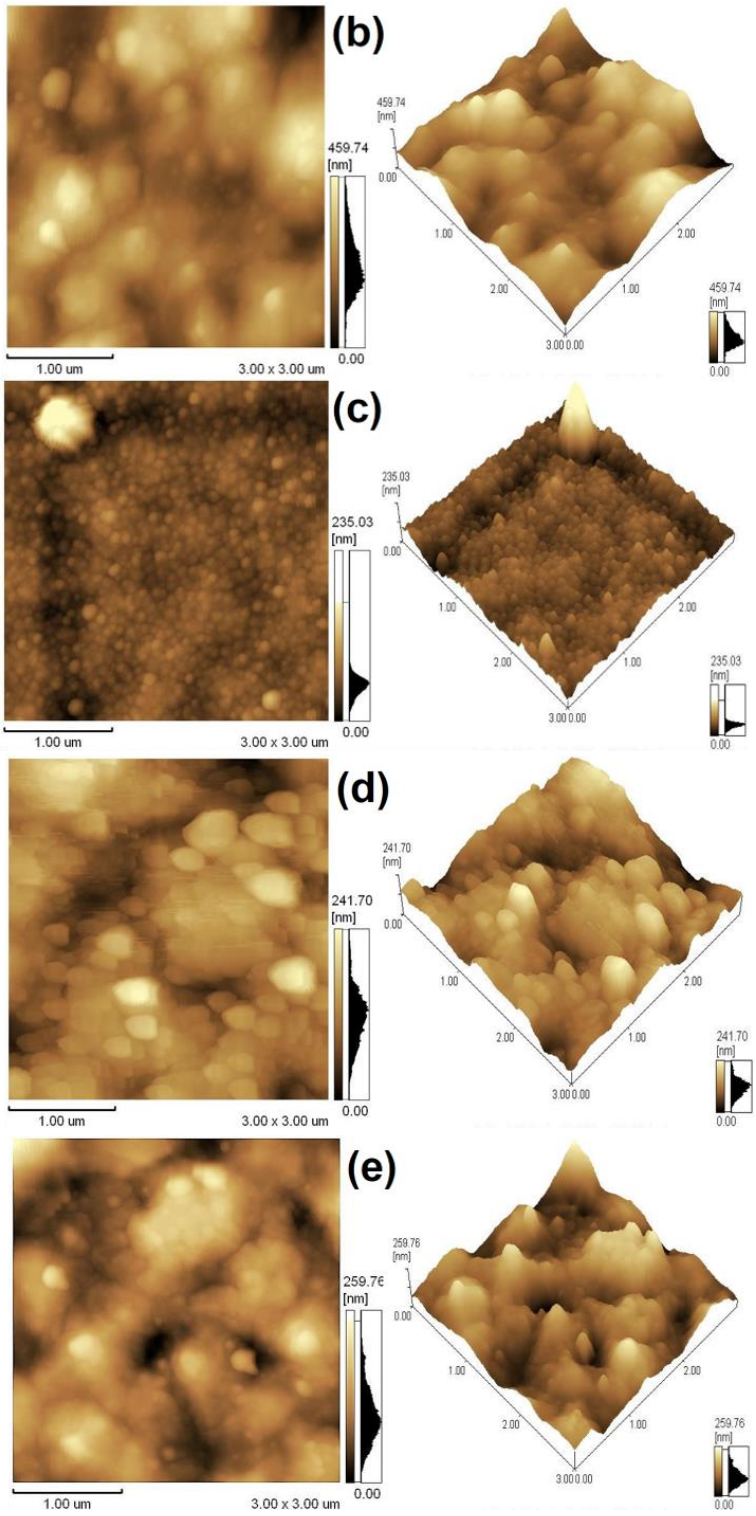

Figure 7.6: 2D and 3D AFM images micrographs of the the $Sr_{1-x}O:Bi_{x=0.002}$ thin films fabricated by (a) spin coating at 900 °C, (b), (c), (d) and (e) the PLD thin films deposited in different O_2 pressure by different excimer laser energies ((b and c) KrF 248 nm and (d and e) ArF 193 nm) laser with O_2 pressures of 1×10^{-3} and 3×10^{-3} mbar, respectively. .

7.4 Conclusion

$Sr_{1-x}O:Bi_{x=0.02}$ thin films were successfully fabricated by using the spin coating and PLD techniques. For all the thin films samples, XRD showed the thin films had a strong (111) preferential orientation on the cubic phase. The crystallite size for the spin coating sample increased with increasing annealing temperatures. PL spectra showed blue emissions at 427 nm with a small blue shift compared with the powder which was attributed to Si diffusion in the structure. Deposition by spin coating gives a smoother surface roughness compared with deposition by PLD. All surface roughness results indicate their good optical surfaces and that the statistical relationships for the surface roughness are applicable.

7.5 References

[1] M. A. Bolorizadeh, V. A. Sashin, A. S. Kheifets and M. J. Ford. Electronic band structure of calcium oxide. *J Electron Spectros Relat Phenomena*, **141(1)** (2004) 27–38. DOI:10.1016/j.elspec.2004.04.004.

[2] Y. Chiu, W. Liu, C. Chang, C. Liao, Y. Yeh, S. Janga and T. Chen, $Ca_2PO_4Cl : Eu^{2+}$: an intense near-ultraviolet converting blue phosphor for white light-emitting diodes. *J. Mater. Chem.* **20,** (2010) 1755. **DOI:** 10.1039/B920610H.

[3] J. A. McLeod, R. G. Wilks, N. A. Skorikov, L. D. Finkelstein, M. Abu-Samak, E. Z. Kurmaev and A. Moewes. Band gaps and electronic structure of alkaline-earth and post-transition-metal oxides, *B - Condens. Mater. Phys.* **81(24)** (2010) 1–9. DOI:10.1103/physrevb.81.245123.

[4] Jipeng Fu, Su Zhang, Tengfei Ma, Yonglei Jia, Ran Pang, Lihong Jiang, Da Li, Haifeng Li, Wenzhi Sunab and Chengyu Li, A convenient and efficient synthesis method to improve the emission intensity of rare earth ion doped phosphors: the synthesis and luminescent properties of novel $SrO:Ce^{3+}$ phosphor, *RSC Adv*. **5**, (2015) 93951–93956. DOI: 10.1039/c5ra15089b.

[5] K. Komatsu, T. Shirai, A. Nakamura, A. Kato, S. Ohshio, N. Nambu, I. Toda, H. Muramatsu and H. Saitoh. Synthesis and luminescence properties of Eu^{2+}-doped 8-coordinated SrO phosphors. Ceram. *Int.* **39**, (2013) 7 115–7118. DOI: 10.1016/j.ceramint.2013.02.053.

[6] A. Yousif, Vinod Kumar, H.A.A. Seed Ahmed, S. Som, L.L. Noto, O.M. Ntwaeaborwa and H.C. Swart, Effect of Ga^{3+} Doping on the Photoluminescence Properties of $Y_3Al_{5-x}Ga_xO_{12}:Bi^{3+}$ Phosphor. *ECS J. Solid State Sci. Technol*. **3 (11)** (2014) 222. DOI: 10.1149/2.0021412jss.

[7] R. H. P. Awater and P. Dorenbos. The Bi^{3+}6s and 6p electron binding energies in relation to the chemical environment of inorganic compounds. *J. Lumin*. **184** (2017) 221–231. DOI: 10.1016/j.jlumin.2016.12.021.

[8] J. Letteri, V. Vaithyanathan, S. K. Eah, J. Stephens, V. Sih, D. D. Awschalom, J. Levy, and D. G. Schlom, Epitaxial growth and magnetic properties of EuO on (001)Si by molecular-beam epitaxy, *Appl. Phys. Lett.* **83** (2003) 975. DOI:10.1063/1.1593832.

[9] K. Komatsu, M. Tanabe, I. Toda, S. Ohshio, H. Muramatsu, and H. Saitoh, "Synthesis of Strontium Oxide Whiskers with Preferential <111> Orientation by Atmospheric Chemical Vapor Deposition," *J. Mater. Sci. Res*. **5(2)** (2016) 50-55 DOI: 10.5539/jmsr.v5n2p50.

[10] O. Maksimov, V. D. Heydemann, P. Fisher, M. Skowronski, and P. a. Salvador, "Structural properties of SrO thin films grown by molecular beam epitaxy on $LaAlO_3$ substrates," *Appl. Phys. Lett.* **89(26)** (2006) 4–7. DOI:10.1063/1.2424440.

[11] E. Hasabeldaim, O. M. Ntwaeaborwa, R. E. Kroon, V. Craciun, E. Coetsee, and H. C. Swart, "Surface characterization and cathodoluminescence degradation of ZnO thin films," *Appl. Surf. Sci.* **424**, (2017) 412–420. DOI:10.1016/j.apsusc.2016.11.178.

[12] G. A. Hirata, O. A. Lopez, L. E. Shea, J. Y. Yi, T. Cheeks, J. McKittrick, J. Siqueiros, M. Avalos-Borja, A. Esparza, and C. Falcony, "Pulsed laser deposition of $Y_3A_{l5}O_{12}$:Tb photoluminescent thin films". *J. Vac. Sci. Technol A*. **14(3)** (1996), 1694-1696. DOI:10.1116/1.580321.

[13] J.-E. Lim, J. K. Jeong, K. H. Ahn, H. J. Kim, C. S. Hwang, D.-Y. Park and D.-S. Lee. Microstructural characterization of sputter-deposited Pt thin film electrode. *J. Mater. Res. Technol*. **19(02)** (2004) 460–468. DOI:10.1557/jmr.2004.0055.

[14] A. Raidou, F. Benmalek, T. Sall, M. Aggour, A. Qachaou, L. Laanab, M. Fahoume. Characterization of ZnO thin films grown by SILAR method. *O A Lib J*. **1(588)** (2014) 1-9. DOI:10.4236/oalib.1100588.

[15] A. Yousif, H. C. Swart, and O. M. Ntwaeaborwa, "Improved luminescence properties of pulsed laser deposited $Y_3(Al,Ga)_5O_{12}$:Tb thin films by post deposition annealing," *J. Lumin*. **143,** (2013) 201–206. DOI:10.1016/j.jlumin.2013.04.042.

[16] P. Kumar, H.K. Malik, A. Ghosh, R. Thangavel and K. Asokan' Doped zinc oxide window layers for dye sensitized solar cells' *Appl. Phys. Lett.* **102,** (2013) 221903–5. DOI:10.1063/1.4824363.

[17] A. Kennedy, K. Viswanathan and K. Pradeev raj. Study of the influence of substrate temperature on structural, optical, and electrical properties of Zn-doped $MnIn_2S_4$ thin films prepared by chemical spray pyrolysis. *Phys Letts A*. **380(36)** (2016) 2842–2848. DOI:10.1016/j.physleta.2016.06.043.

[18] R. M. Jafer, A. Yousif, V. Kumar, T.K. Pathak, L.P. Purohit, H.C. Swart and E. Coetsee. Comparison of Y_2O_3:Bi^{3+} phosphor thin films fabricated by the spin coating and radio frequency magnetron techniques. *Phys B: Condens Matt.* **497**, (2016) 39–44. DOI:10.1016/j.physb.2016.06.007.

[19] Fu. Jipeng, R. Pang, L. Jiang, Y. Jia, W. Sun, S. Zhang, and C. Li, A novel dichromic self-referencing optical probe SrO:Bi^{3+}, Eu^{3+} for temperature spatially and temporally imaging. *Dalton Trans*. **45(34)** (2016) 13317–13323. DOI: 10.1039/c6dt01552b.

[20] G. S. Zavt and A. F. Ellervee, Pb^{2+} and Bi^{3+} impurity centres in alkali-earth oxides vibronic spectra, lattice dynamics, and electron-phonon interaction, *Phys. Status Solidi*. **94(2)** (1979) 757–768. DOI:10.1002/pssb.2220940249.

[21] A. C. V. D. Steen and L. T. F. Dijcks The Luminescence Properties of Alkaline-Earth Oxides Activated with $6s^2$ Ions, *Phys Status Solidi (b).* **283**, (1981) 283–292. DOI:10.1002/pssb.2221040130.

[22] N. Yamashita, S. Ikeda and S. Asano, Photoluminescence and excitation spectra of the SrO:Bi^{3+} phosphor. *Phys Lett A*. **121(2)** (1987) 94–96. DOI: 10.1016/0375-9601(87)90272-6.

[23] S.L. Jones, D. Kumar, Rajiv K. Singh and P.H. Holloway. Luminescence of pulsed laser deposited Eu doped yttrium oxide films . *Appl. Phys. Lett*. **71**, (1998) 404. DOI:10.1063/1.11955.

[24] A. Yousif, R. M. Jafer, S. Som, M. M. Duvenhage, E. Coetsee, and H. C. Swart, Ultra-broadband luminescent from a Bi-doped CaO matrix. *RSC Adv*. **5(67)** (2015) 54115–54122. DOI: 10.1039/c5ra09246a.

[25] S. T. S. Dlamini, H. C. Swart, J. J. Terblans and O. M. Ntwaeaborwa. The effect of different gas atmospheres on the structure, morphology and photoluminescence properties of pulsed laser deposited $Y_3(Al,Ga)_5O_{12}:Ce^{3+}$ nano thin films. *Solid State Sci*. **23**, (2013) 65–71. DOI:10.1016/j.solidstatesciences.2013.06.009.

[26] A. Yousif, R. M. Jafer, S. Som, M. M. Duvenhage, E. Coetsee, and H. C. Swart, Applied Surface Science The effect of different annealing temperatures on the structure and luminescence properties of $Y_2O_3:Bi^{3+}$ thin films fabricated by spin coating, *Appl. Surf. Sci*. **365**, (2016) 93–98. DOI:10.1016/j.apsusc.2016.01.013.

[27] Y. Hu, X. Diao, C. Wang, W. Hao and T. Wang. Effects of heat treatment on properties of ITO films prepared by rf magnetron sputtering. *Vacuum.* **75(2)** (2004) 183-188. DOI:10.1016/s0042-207x(04)00151-4.

[28] L. T. Troland. Report of Committee on Colorimetry for 1920–21. *J. Opt. Soc. Am.* **6 (6)** (1922) 527–596. DOI:10.1364/JOSA.6.000527.

[29] N. Sahu, B. Parija and S. Panigrahi, Fundamental understanding and modeling of spin coating process, *Indian J. Phys*. **83(4)** (2009) 493-502. DOI:10.1007/s12648-009-0009-z.

[30] E. Hasabeldaim, O. M. Ntwaeaborwa, R. E. Kroon, E. Coetsee, and H. C. Swart, Effect of substrate temperature and post annealing temperature on ZnO:Zn PLD thin film properties, *Opt. Mater. (Amst).* **(74)**, (2017) 139–149. DOI:10.1016/j.optmat.2017.03.027.

[31] A. Yousif, J.J. Terblans, R.M. Jafer, Vinod Kumar, R.E. Kroon, O.M. Ntwaeaborwa, M.M. Duvenhage and H.C. Swart. Structural and morphology analysis of annealed $Y_3(Al,Ga)_5O_{12}$:Tb thin films synthesized by pulsed laser deposition *Appl. Surf. Sci.* **305,** (2014) 732-739. DOi:10.1016/j.apsusc.2014.03.185.

[32] R. Eason (Ed.), Pulsed Laser Deposition of Thin Films: Applications-Led Growth of Functional Materials, John Wiley & Sons (Hoboken, 2007). ISBN:9780470052129, DOI:10.1002/0470052120.

[33] K. Siraj, Y. Sohail and A. Tabassum, Metals and metal oxides particles produced by pulsed laser ablation under high vacuum'. *Turk J. Phys.* **35** (2011) 179-183. DOI:10.3906/fiz-1004-13.

Chapter 8: Effect of background atmosphere and substrate temperature on SrO:Bi thin films produced using pulsed laser deposition

In this chapter, SrO:Bi phosphor thin films were prepared by pulsed laser deposition (PLD) in the presence of a base pressure or after back-filling with oxygen (O_2) gas. The microstructures and the optimizing of the substrate temperature to improve the photoluminescence (PL) and cathodoluminescence (CL) emissions of the phosphor thin films were also investigated.

8.1 Introduction

The spectroscopic properties of alkaline-earth oxides activated with Bi^{3+} ions have been attracting much attention and become a hot research topic in the field of phosphor materials in the recent literature due to the following reasons [1]: firstly, the Bi^{3+} ion occupies a lattice site with cubic symmetry, and secondly, the luminescence bands show vibrational structure [2]. Among these hosts, the SrO has been extensively reported in the powder form due to its properties and applicability in several types of optoelectronic devices in different phosphor fields, such as light-emitting diodes and display devices [3]. The Bi^{3+} ions in this host showed a blue color as the result of the substitution by the Bi^{3+} ions of the Sr^{2+} ions in the SrO cubic structure [4]. SrO:Bi^{3+} has a vibrational structure in the PL spectrum as has been reported by some investigators [5]. There is a wide range of technological applications where thin film technologies are based on luminescent materials [6]. For example, Komatsu et al. [7] reported that randomly oriented SrO films and highly oriented SrO whiskers were synthesized using an atmospheric Chemical Vapor Deposition technique. Zhang et al. [8] reported that SrO films were obtained on a SiO_2/Si(100) substrate using an Atomic Layer Deposition method, from bis (triisopropyl cyclopentadienyl) strontium. Also, Maksimov et al. [9] reported on the structural properties of SrO thin films that were grown by Molecular Beam Epitaxy on $LaAlO_3$ substrates. It is clear that SrO thin films can be prepared by different preparation methods. It is well

documented that thin phosphor films have several important advantages compared to powders such as high thermal stability, structural density, better adhesion to the underlying substrates and efficient dissipation of heat for high power operation [10]. We could not find reports in the literature about the conversion of SrO:Bi powders to thin films. It is therefore important to develop a better understanding of the kinetics of the film formation, as this may be different for various growth conditions. Among these methods, the Pulsed Laser Deposition (PLD) method is an attractive technique to grow thin films for a variety of applications. PLD is known to be a flexible and cost-effective method for the formation of superconducting thin films. The major advantage of PLD is the ability to transfer the material stoichiometry from a multi-component ablation target to a growing film of practically any material [11]. Although it is well known that the PLD technique is a reliable method to fabricate oxide thin films, these favorable results do not occur under all experimental conditions [12]. Various parameters have to be optimized to produce thin films with the appropriate properties for each kind of material. PLD films have their individual advantages in terms of processing parameters where the degree of orientation is influenced by the growth mechanisms and the deposition conditions. Parameters that may play an important role in the fabrication of the films are temperature, target-substrate distance, the kinetic energy of the plume particles and inert background gas composition and pressure, which allows a sufficient control of the film composition and properties [13].

In this study $Sr_{1-x}O:Bi_{x=0.002}$ phosphor powder was converted to thin films by using the PLD technique. All the deposition parameters were kept constant except for the working atmosphere and substrate temperature. The working atmospheres used were base pressure and an oxygen pressure. The optimizing of the substrate temperature to improve the PL emission of the phosphor thin film was also investigated. A variety of techniques were employed to characterize the structural, morphological, chemical composition and optical properties of the films.

8.2 Experiment

$Sr_{1-x}O:Bi_{x=0.002}$ powder was prepared by the metal nitrate sol-gel combustion synthesis technique. The chemicals strontium nitrate ($Sr(NO_3)_2$ 99% pure), citric acid ($C_6H_8O_7$) and bismuth nitrate ($Bi(NO_3)_3.5H_2O$, 99.999% pure), all purchased from Sigma

Aldrich, were used as the starting materials. They were dissolved in distilled water under stirring and heating to obtain a homogenous precursor solution gel. The gel was placed in a furnace preheated at 250 °C. When the combustion process was completed a solid foamy brown powder was obtained. After that the powders were well crushed, then annealed in air. The furnace temperature was increased from 50 °C at a rate of 5 °C/min up to the required 1100 °C temperature, which was maintained for 2 h, and then decreased at the same rate. The ground powder was mixed with ethanol as a binder and pressed using an in-house built sample holder to create an ablation target. The target was annealed at 200 °C for 2 h in air to remove all adventitious water containing species that might be present and then placed inside the chamber of the PLD system on a rotating target holder that can also move linearly (forward and backward). Si (100) wafers were used as a substrate. They were cleaned in an ultrasonically bath using acetone, then ethanol and finally distilled water for 15 min, and then dried with N_2 gas. The deposition chamber was evacuated to a base pressure of 3.4×10^{-5} mbar and then backfilled with O_2 to a pressure of 0.027 mbar. The $Sr_{1-x}O:Bi_{x=0.002}$ target was ablated in the vacuum or O_2 working atmosphere using the fourth harmonic (266 nm) of a Nd:YAG (33.3 mJ/pulse) laser. The laser pulse frequency, number of pulses, fluency and target-to-substrate distance were fixed at 10 Hz, 10 000, 0.77 J/cm^2, and 4.5 cm, respectively. Laser deposition time was 60 min and the number of pulses was 36 000 for all samples. The substrate temperature was varied from 50, 100, 200, 350 and 500 °C. The structure of the thin films was characterized by X-ray diffraction (XRD) measurements using a Bruker D8 Advance diffractometer (40 kV, 40 mA) with Cu Kα X-rays (0.154 nm). Atomic force microscopy (AFM) using a Shimadzu SPM-9600 instrument was used to study the surface and roughness morphology. The sample morphology was characterized using a JEOL JSM-7800F scanning electron microscopy (SEM) equipped with an Energy Dispersive X-ray Spectrometer (EDS) for chemical compositions. PL spectra were collected with a He-Cd laser PL system with a 325 nm excitation wavelength. The CL emission spectra were measured using a Gatan MonoCL4 accessory fitted to the JEOL JSM-7800F system in a vacuum of the order of 10^{-5} - 10^{-6} Torr and an electron energy of 5 keV. ToF SIMS measurements were performed with an Ion of ToF SIMS. A pulsed 30 keV Bi^+ primary ion beam with a target current of 1 pA (30 nA DC) and the analytical field-of-view was 100 x 100 μm^2. The analysis was performed in saw tooth rastering mode

with 512×512 pixels^2 with a binning of 4 pixels. For depth profiling, the Cs^+ sputter gun operated at 1 kV and ~75 nA were used for both spectroscopy and imaging in the negative mode. Sputter area was 300×300 µm.

8.3 Results and discussion

8.3.1 Structural analysis

The PLD thin film crystallinity can be highly dependent on the deposition conditions and many material parameters, for example: the ambient gas pressure, the post-annealing conditions and density, kinetic and potential energies type of the condensing particles, as well as the temperature and physicochemical properties of the substrate [12]. Figure 8.1. (a) and (b) show the XRD patterns for the as-prepared $Sr_{1-x}O:Bi_{x=0.002}$ phosphor powder used as a target and SrO JCPDS file, as well as the thin films deposited on the Si substrates in different chamber atmospheres, namely (a) in O_2 (b) in vacuum and prepared at different substrate temperatures of 50 °C, 100 °C, 200 °C, 350 °C and 500 °C, respectively. In figure 8.1 (a) the XRD patterns of the films prepared in O_2 at different substrate temperatures show that the films prepared at 50 °C and 100 °C exhibited an amorphous state. The thin films prepared at 200 °C, 350 °C and 500 °C substrate temperatures showed some diffraction peaks attributed to the SrO cubic phase. A crystalline film with preferential growth in the [111] direction was observed and growth in the [200], which orientation occurred during increasing substrate temperature and continued growing at the higher temperatures. In the sample at 500 °C, the 111 and 200 SrO peaks are almost the same height, as in the powder, but for 350 °C and 200 °C, the 200 peak is much smaller which indicates some preferential orientation at lower temperatures. The peaks, which are labeled with an asterisk (*) are associated with diffraction from the Si substrate. Hu et al. [14] and Yousif et al. [11] reported that the amorphous films may be considered as having many defects and their compositions are sometimes nonstoichiometric, but the adatom mobility is expected to be higher at the higher temperatures, resulting in a higher probability for finding active nucleation sites on the substrate. As reported by Sato et al. [15], an increase of substrate temperature contributes to chemical reactions, leading to an increase of nucleation density on the

substrate. On the other hand, the characteristics of the thin films depend on the pressure of the background gas during PLD, since the surrounding particles interact with the particles in the plume. Thus, the collision between the ambient gas atoms and the particles in the plume will decrease the kinetic energies of the particles and hence increases the amount of time the particles stay in the plume [16], giving the particles enough time to form, so that agglomeration and growth into larger particles before reaching the substrate. The stoichiometric composition can easily occur during the deposition in O_2. When deposited, the atoms of the material can rearrange with the free oxygen in the O_2 ambient which may also react with the films grown with high substrate temperatures. As a result, the structure can become more crystalline, as seen in the XRD peak intensities of the films at 200 °C, 350 °C and 500 °C. These results indicate that the high growth temperature can improve the crystallinity of the SrO PLD thin film in the O_2 atmosphere, due to small crystallite coalescing together to form larger crystallites in the SrO films. Figure 8.1. (b) shows the XRD patterns of the film prepared at base pressure, indicating an amorphous phase due to the absence of any SrO diffraction peaks. The particles ejected in vacuum move freely and are expected to have the higher mean free path. Thus they do not have enough time to nucleate [17]. This may explain why better films were obtained in O_2 when compared to vacuum.

The crystallite size for samples at 200 °C, 350 °C and 500 °C in O_2 was estimated using Scherrer's equation by using the FWHM of the 111 peak [18]

$$D = \frac{K\lambda}{\beta \cos\theta} \qquad (8.1)$$

where D is the size of the crystallites, K is a correlation factor (0.94), λ is the X-ray wavelength, β is the FWHM and θ is Bragg's diffraction angle of the 111 peak. The calculated crystallite size of $Sr_{1-x}O{:}Bi_{x=0.002}$ thin films for substrate temperatures at 200 °C, 350 °C and 500 °C in O_2 were 48, 74 and 88 nm, respectively. The crystallite sizes increased with increasing the substrate temperature. This can be explained in terms of the high adatom mobility. As discussed by Vrakatseli et al. [19], when deposition occurs at high temperature the adatom mobility is expected to be higher, resulting in a higher probability for finding active nucleation sites on the substrate.

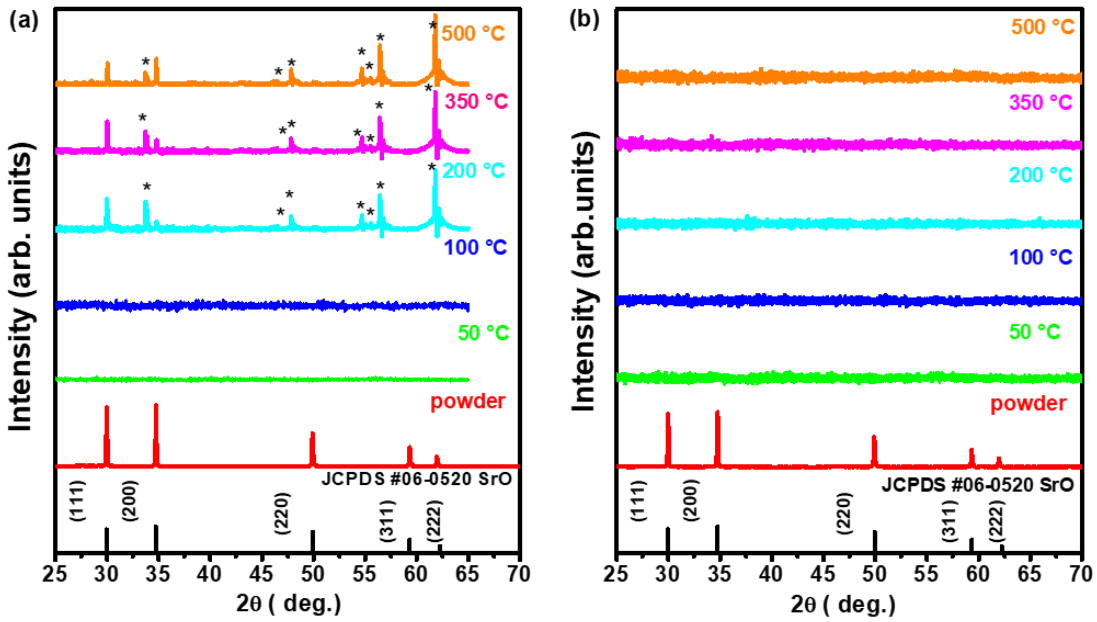

Figure 8.1: XRD patterns of the $Sr_{1-x}O:Bi_{x=0.002}$ powder and thin films with substrate temperatures of 50 °C, 100 °C, 200 °C, 350 °C and 500 °C, respectively, (a) in O_2 (b) in vacuum, with XRD pattern for SrO powder and XRD pattern database pattern for SrO.

8.3.2 Elemental composition analysis (EDS)

The elemental composition of the SrO:Bi thin films were investigated using EDS. Figure 8.2 show EDS spectra of $Sr_{1-x}O:Bi_{x=0.002}$ thin films at the different substrate temperatures of 50 °C, 100 °C, 200 °C, 350 °C and 500 °C, respectively, (a - e) in O_2 and (f - j) in vacuum. The intense peaks reveal the presence of various elements. Carbon (C) was probably coming from the atmospheric hydrocarbons or the organic citric acid used during synthesis. Sr and O were observed in the samples as expected. No Bi peaks was observed in the spectra where it is expected to be detected at 2.4, 2.7 and 3.4 keV [20], probably due to its low concentration in the samples. The insets in figure 8.2(a,b and c) are the respective elemental maps. It can be seen from the maps that all the elements were fairly evenly distributed on the surface of the films. Also, note that the intensity peaks of the elements are almost consistent for all samples, which means that the distribution of the elements are similar.

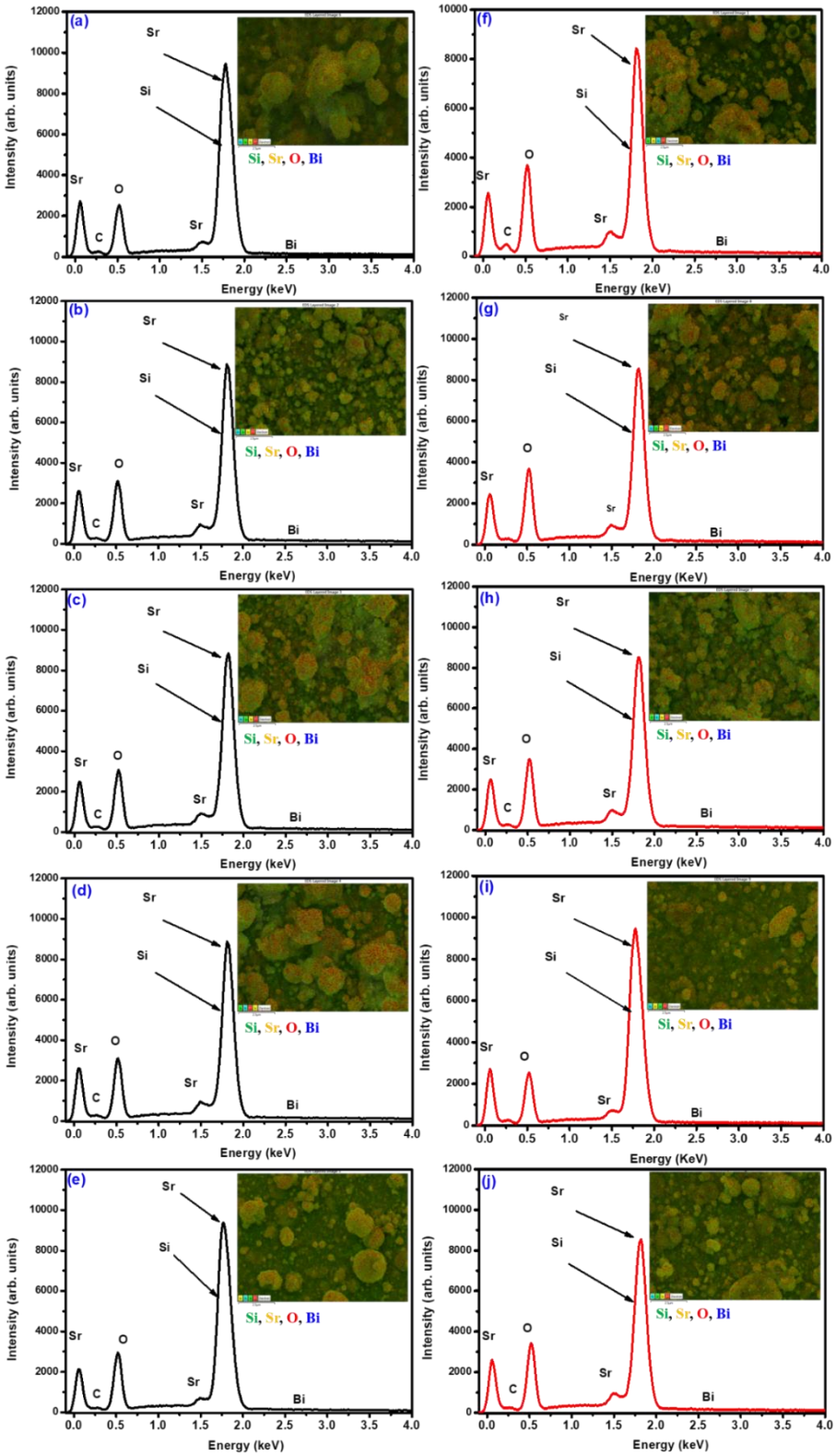

Figure 8.2: (Color online) EDS spectra of the $Sr_{-x}O:Bi_{x=0.002}$ films deposited at the different substrate temperatures of 50 °C, 100 °C, 200 °C, 350 °C and 500 °C, respectively, (a - e) in O_2 (f - j) in vacuum.

8.3.3 Surface morphology

8.3.3.1 Scanning electron microscopy

Figure 8.3. shows SEM micrographs of the $Sr_{1-x}O:Bi_{x=0.002}$ films deposited at the different substrate temperatures of 50 °C, 100 °C, 200 °C, 350 °C and 500 °C, respectively, (a - e) in O_2 and (f - j) in vacuum. All the SEM images show a very rough thin film surface that comprises of rounded irregular particles of different sizes and shapes, which were not uniformly distributed and which do not seem to be highly dependent on the substrate temperature. The large particulates formed on the film surface originated from small droplets blasted from the molten target, which solidify to spherical balls by the time they reach the substrate. In the deposition process the atomization of the target material has an explosive-like character, where these big particles form by starting from agglomeration during deposition from small particles coalesce to each other [21]. The rounded particles could be formed from local melting and ejected from the target to the substrates, which are typically found in laser ablation experiments where some of the big particles consist from a conglomeration of smaller particles [12]. The particulates are then transferred by the ablation plume to the substrate and insert in the growing film by incorporating it into the substrate [1]. In figure 8.3 (a – e) for the thin films deposited in O_2, the films prepared with the low substrate temperatures of 50 °C and 100 °C in O_2 (a and b), shows molten large droplets compared to the samples prepared at high substrate temperatures in O_2 (c, d and e). In figure 8.3 (f – j) thin films deposited in vacuum prepared with different substrate temperatures consisted of large agglomerated grains with different grain boundaries. All SEM images of the samples deposited in the vacuum are similar.

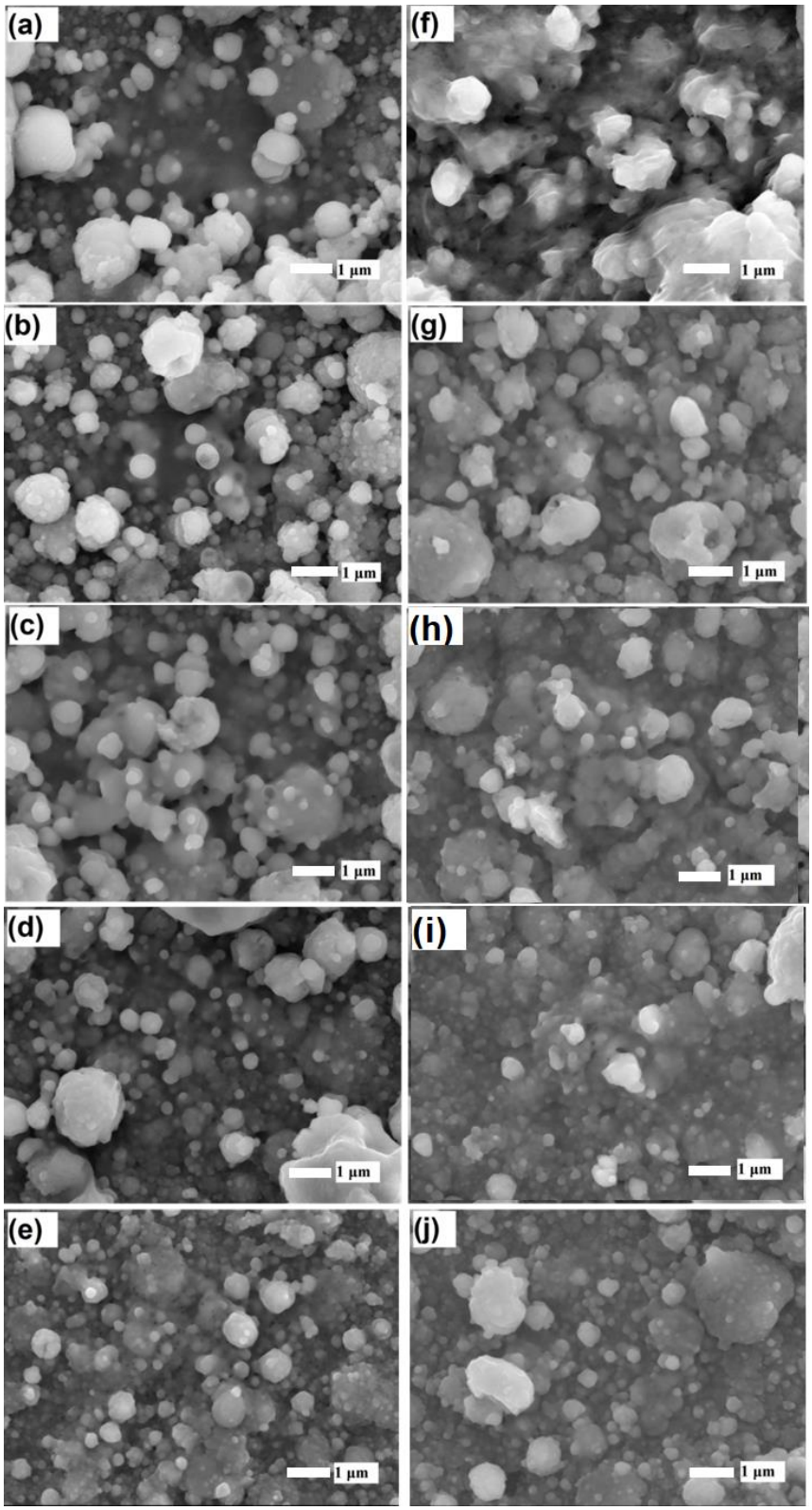

Figure 8.3. SEM images of the $Sr_{-x}O:Bi_{x=0.002}$ films deposited at the different substrate temperatures of 50 °C, 100 °C, 200 °C, 350 °C and 500 °C, respectively, (a - e) in O_2 (f - j) in a vacuum.

8.3.3.2 Atomic force microscopy

Figure 8.4 shows 3D AFM images for a region of 5 × 5 μm^2 of the $Sr_{1-x}O:Bi_{x=0.002}$ films deposited at the different substrate temperatures of 50 °C, 100 °C, 200 °C, 350 °C and 500 °C, respectively, (a - e) in O_2 and (f - j) in vacuum. Comparison of this series of images with the images made on SEM shows that the general trends are almost the same. It is known that AFM is a powerful analysis instrument that has been successfully applied to study the surface structure of various materials [22]. The AFM images show that the surface of the film consists of spherical and irregular particles of varying size. The roughness of the films was examined and included in Table 8.1. The average roughness (R_a), the mean of the measured heights over the entire area/length, describes the roughness of mechanical surfaces. It provides a general idea about the characteristic of the overall profile heights variation and monitoring the manufacturing process, while the root mean square roughness (R_q) is the square root of the surface heights distribution and is more precise than the average roughness for an area with a large deviation from the mean height. The ten-point mean height roughness (R_z), the difference between the average of five highest heights and five lowest valleys for the evaluated surface, is more responsive to occasional large variations in height [21]. These parameters for the $Sr_{1-x}O:Bi_{x=0.002}$ thin films surfaces were determined from their AFM images and are listed in Table 8.1, which indicates that the thin film roughness decreased with the increase of substrate temperature. This could indicate that the surfaces were denser at the higher substrate temperatures [23]. The increased substrate temperatures maybe led to an increase in atom mobility, where the high substrate temperature increases atom mobility and atoms move faster and arrive easier at equilibrium positions. Yang et al.[24] reported that the substrate temperature effect in $Zn_{1-x}Co_xO$ thin films caused a decrease of the R_q value when the temperature was increased. Some authors, Jafer [12], Coetsee et al. [25] and McKittrick et al. [26], reported that the morphology and the surface roughness (achieved when substrate temperature was increased) strongly influence the optical properties of the thin films studied. Raoufi et al. [27] and Hasabeldaim et al. [28] reported that some films having a Gaussian distribution for their asperity height, according to the statistical theory, which indicate to their good optical surfaces thin films.. Thus, according to the statistical theory, for a Gaussian

distribution of coarseness height, the ratio of R_q to R_a should be 1.25. Gündüz [29] reported that the asperity heigh t distribution of most engineering surfaces according to this relation may be approximated by a Gaussian distribution with R_q/R_a values up to 1.3. In our results it can be seen from Table 8.1 that the R_q/R_a values, which were estimated from the AFM data are reasonably close to the 1.25 value predicted by the statistical theory. This indicates that these are good optical surfaces and that the statistical relationships for the surface roughness are applicable.

Table 8.1. Roughness parameters of PLD thin films at the different substrate temperatures and atmospheres.

Sample name	R_a (nm)	R_q (nm)	R_z (nm)	R_q/R_a
50 °C in O_2	153.8	201.7	1.26	1.32
100 °C in O_2	181.7	198.6	2.46	1.09
200 °C in O_2	150.5	188.5	1.06	1.25
350 °C in O_2	168.8	180.4	2.24	1.06
500 °C in O_2	164.14	176.3	1.30	1.07
50 °C in Vacuum	183.13	243.7	1.39	1.33
100 °C in Vacuum	219.6	238.7	1.71	1.08
200 °C in Vacuum	181.8	235.3	2.02	1.29
350 °C in Vacuum	259.7	213.6	1.67	0.82
500 °C in Vacuum	212.07	208.9	1.75	0.98

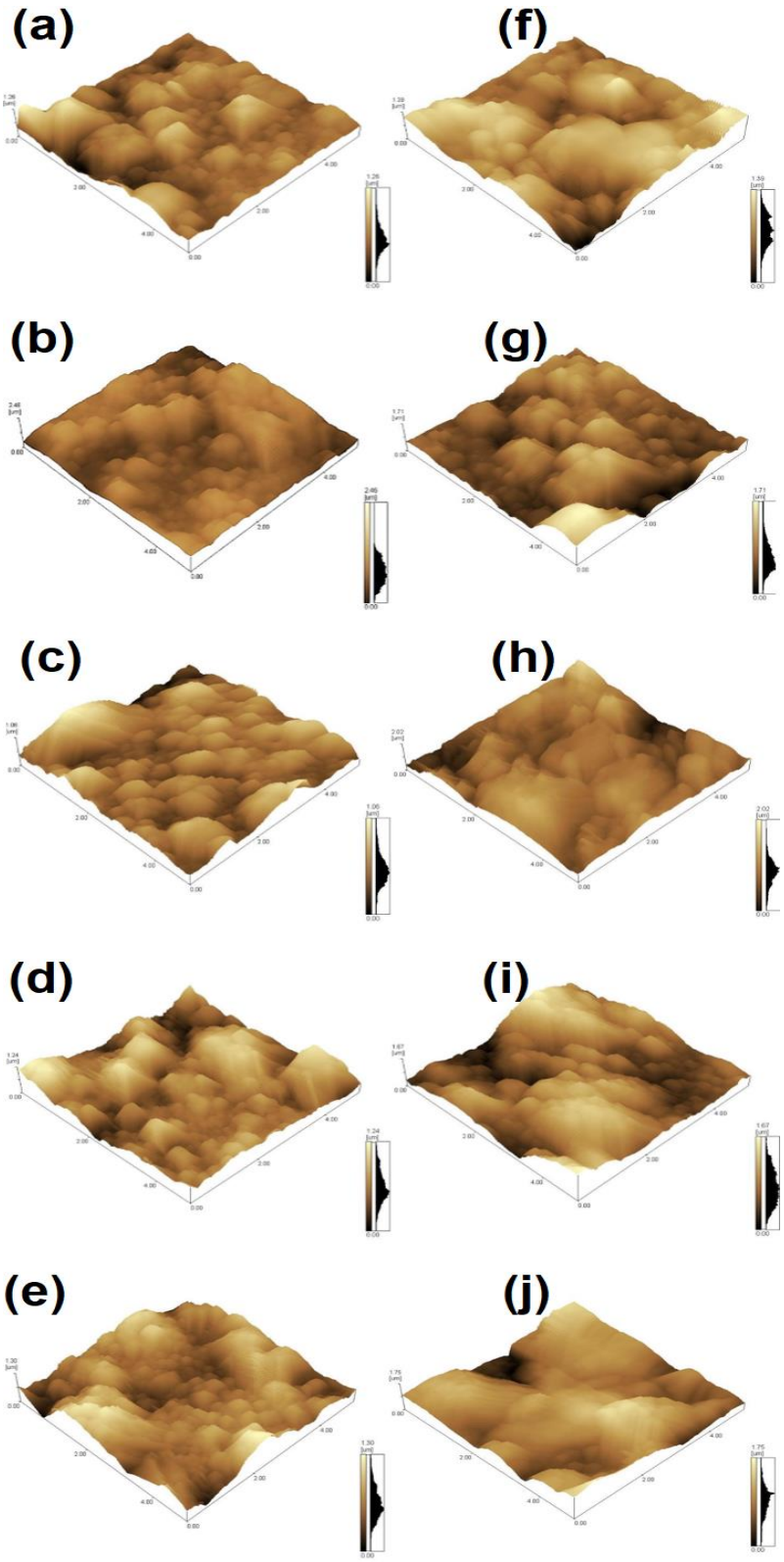

Figure 8.4. 3D AFM images of the $Sr_{-x}O:Bi_{x=0.002}$ films deposited at the different substrate temperatures of 50 °C, 100 °C, 200 °C, 350 °C and 500 °C, respectively, (a - e) in O_2 (f - j) in vacuum.

8.3.4 Photoluminescence (PL) properties

Figure 8.5(a) shows the emission spectrum when the $Sr_{1-x}O:Bi_{x=0.002}$ powder sample synthesized by the sol-gel combustion method was excited with the 325 nm He-Cd laser at room temperature. The spectrum shows the luminescence with the emission in the blue range centered at 445 nm. The luminescence peak was attributed to Bi^{3+} ions, which are known for emitting blue light. The ground state of the Bi^{3+} electronic configuration $[Xe]4f^{14}5d^{10}6s^2$ is $^1S_0$, while the excited states from the 6s6p configuration are $^3P_0$, $^3P_1$, $^3P_2$ and $^1P_1$ in the sequence of increasing energy. Transitions from $^1S_0$ to $^3P_1$, $^3P_2$ and $^1P_1$ are usually referred to as A, B and C, respectively [30]. The transitions $^1S_0 \rightarrow {}^3P_0$ and $^1S_0 \rightarrow {}^3P_2$ are spin forbidden, while $^1S_0 \rightarrow {}^1P_1$ is spin allowed. Spin-orbit coupling of the $^1P_1$ and $^3P_1$ levels means that the $^1S_0 \rightarrow {}^3P_1$ transition may also occur. Therefore Bi^{3+} ions can be excited from the ground state to $^3P_1$ (A band) or $^1P_1$ (C band) states with an appropriate wavelength of light in the UV range [31]. The broad emission peak was attributed to more than one emission center, namely $^3P_1 \rightarrow {}^1S_0$, and the second emission peak in SrO:Bi was caused by the forbidden $^3P_0 \rightarrow {}^lS_0$ transition which is initiated by the mixing of $^3P_0$ and $^3P_1$ states by lattice vibrations.

Figure 8.5 shows the room temperature PL emission spectra of the $Sr_{1-x}O:Bi_{x=0.002}$ thin films prepared at different substrate temperatures of 50 °C, 100 °C, 200 °C, 350 °C and 500 °C, deposited in (b) O_2 and (c) vacuum, respectively, excited by the 325 nm He-Cd laser. They show a broad band of blue fluorescence emission, which extended from 380 to 500 nm, centered at 427 nm. There was a small blue shift in the peak position from 445 nm to 427 nm between the PL for the powder and thin films maximum intensity positions. This shift of the main peak position is attributed to the change in the surrounding structure of the Bi^{3+} ions, due to a change in the crystal field, which has an effect on the ^3P_J levels of the Bi^{3+} ion. Many phosphor hosts activated with Bi^{3+} ions showed large changes in their luminescence properties due to their outer electrons which are not shielded from the surrounding environment [32]. It has been reported that the wavelength of the peak intensity and the FWHM in the wavelength region of the observable emissions from Bi^{3+}-activated oxide phosphors are considerably affected because the relative positions of the configuration coordinate curves of the excited states are very sensitive to the surrounding

ligands [33]. Dlamini et al. [35] measured a slight shift in the wavelength of the PL spectra for $Y_3(Al,Ga)_5O_{12}:Ce^{3+}$ thin films due to a change in the crystal field. The samples prepared at a substrate temperature of 500 °C in both O_2 and vacuum showed a significant blue shift to 380 nm, which may be due to volatility of the Bi from the thin film surface, which may possibly result in less optimal lattice order in the particles. On the other hand Si diffusion may have been responsible for the change in the PL emission position peak due to a change in the crystal field. Yousif et al. [6] reported such a shift of the PL emission of $Y_2O_3:Bi^{3+}$ thin films fabricated by spin coating at high temperatures due to the Si diffusion, which was responsible for the change in the Bi^{3+} doped Y_2O_3 phosphor material structure to a structure of Bi^{3+} doped yttrium silicate phosphor. Figure 8.5(b) shows that for the thin films deposited in O_2 the PL intensity increased with the increase of the substrate temperatures up to 200 °C and then decreased with further increase temperatures at 350 °C and 500 °C. Hu *et al*. [14] reported that a low substrate temperature is responsible for a low PL intensity due to the defects in the film's structure and nonstoichiometry of the film's composition. As reported by Jafer *et al*. [12] when studying $Y_2O_3:Bi^{3+}$ phosphor thin films prepared by PLD in the presence of oxygen (O_2) gas, the increased PL intensities were due to the increased crystallinity and associated with the decrease in surface roughness of thin films. In our samples, the increase of the PL intensities at higher substrate temperatures might be attributed to the improvement of the films' crystallinity, where samples at 50 °C and 100 °C exhibited an amorphous state (see figure 8.1(a)). The reduced luminescence intensity in samples prepared at 350 °C and 500 °C may be due to a consequent loss in Bi^{3+} due to volatile species as a result of the increased substrate temperature, which may be volatilized in large quantities in the sample at 500 °C, which caused the blue shift in this sample.

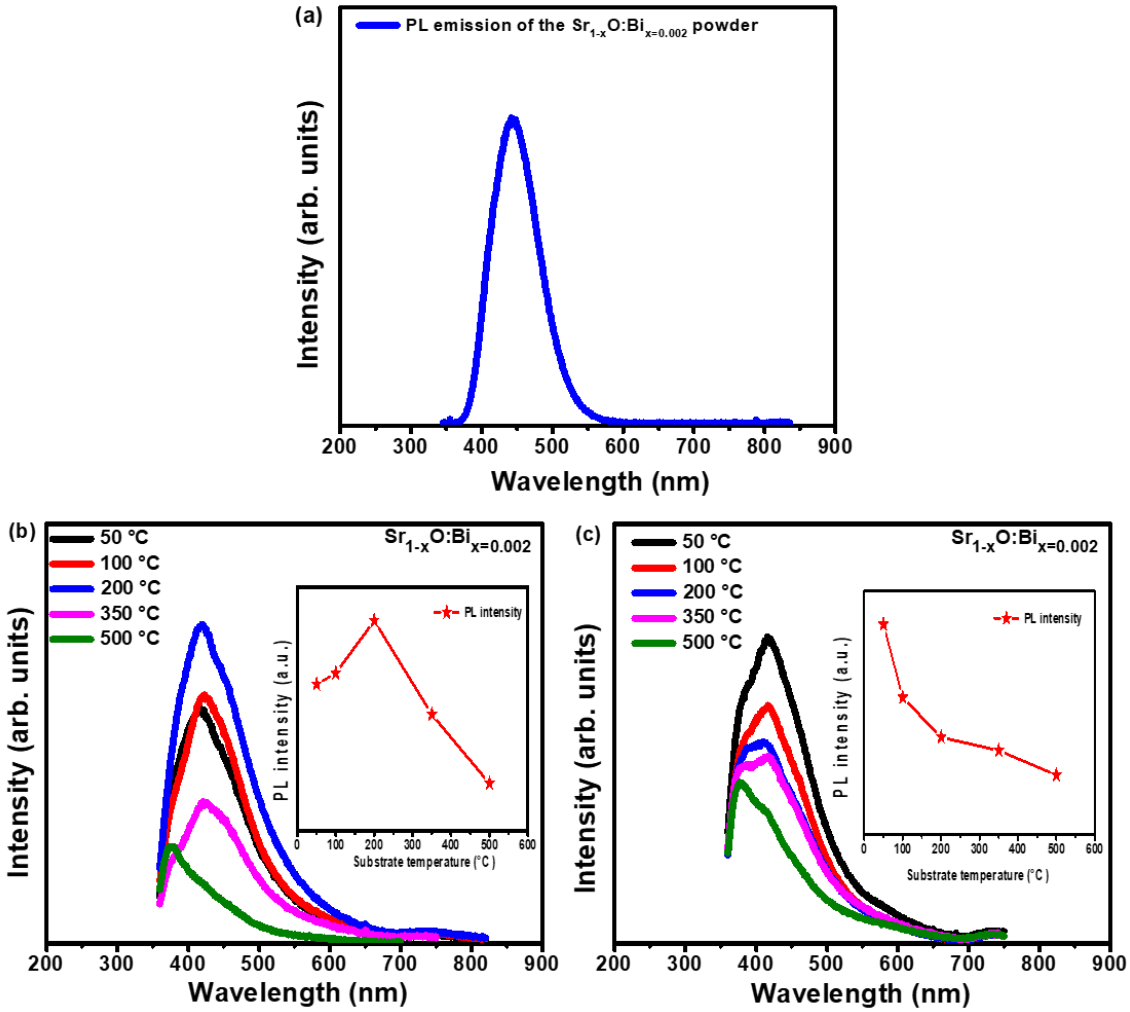

Figure 8.5. PL spectra of the $Sr_{1-x}O:Bi_{x=0.002}$ measured with a 325 nm He-Cd laser (a) powder (b and c) thin films deposited at the different substrate temperatures of 50 °C, 100 °C, 200 °C, 350 °C and 500 °C, in O_2 and a vacuum, respectively.

Figure 8.5(c) shows that for the thin films deposited in vacuum the PL intensity decreased with the increase of the substrate temperature. The amorphous films may be considered to have many defects in their structure and are sometimes nonstoichiometric in composition [35]. When the structure of the films is amorphous, some electrons are bound in a small range by the net non-uniform structure. A wide range of compositions is possible in amorphous films beyond those allowed for crystals, where incompatible crystal structures may inhibit the formation of regular diffusion of the materials with the substrate. In this case, maybe when increasing the substrate temperature, it led to an increase in diffusion of Si from the substrate and more volatility of the Bi at the higher temperatures.

8.3.5 Cathodoluminescence properties

Figure 8.6 shows the CL emission spectra for the $Sr_{1-x}O:Bi_{x=0.002}$ powder and thin films samples measured with the Gatan system connected to the SEM. Figure 8.6(a) shows the CL emission spectra for the powder which can also be attributed to the $6s^2$-6s6p transitions in Bi^{3+} ions due to the $^1S_0 \rightarrow {}^3P_1$ and $^3P_1 \rightarrow {}^1S_0$ transitions of Bi^{3+}, respectively as mentioned in previous chapters. Figure 8.6(b) shows the thin films deposited in O_2. Similar to the PL, the emission intensity first increased for the samples with an increase of the substrate temperatures up to 200 °C and then decreased with further increase in temperatures at 350 °C and 500 °C. As in the case of the PL, that was first due to the improvement of the films' crystallinity and then the reduced luminescence intensity may be due to a consequent loss in Bi^{3+} due to volatile species as a result of the increased substrate temperature. Figure 8.6(c) shows the CL of thin films deposited in vacuum. Similar to the PL, the emission intensity decreased with the increase of the substrate temperatures except for the sample with the substrate temperature at 500 °C, where the CL intensity increased again. This may be due to the high energy of the excitation since the electrons have the ability to excite the Bi^{3+} ions as well as the host lattice and Si substrate as well, where the energy of the electron beam allows probing the structure over various depths [38]. In samples prepared with substrate temperatures of 50 °C and 100 °C a new peak on the high wavelength side around 600 nm was observed, which may be caused by the presence of both Bi^{3+} and Bi^{2+} in the structure. Yousif et al. [32] reported that CaO:Bi showed ultra-broadband CL emission as a function of different beam current and voltage and attributed this to the presence of both Bi^{3+} and Bi^{2+} in the material.

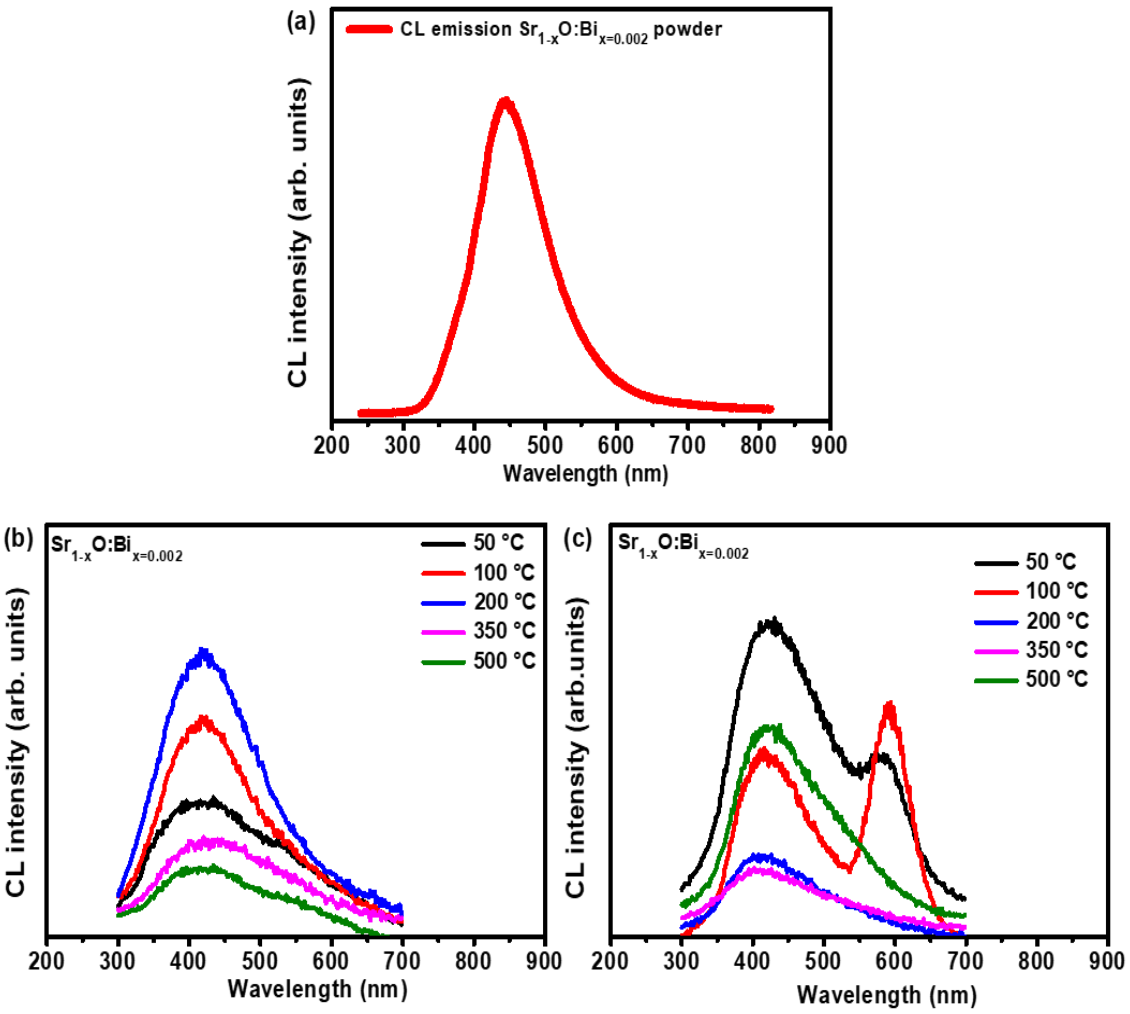

Figure 8.6. CL spectra of the $Sr_{1-x}O:Bi_{x=0.002}$ (a) powder (b and c) thin films deposited at the different substrate temperatures of 50 °C, 100 °C, 200 °C, 350 °C and 500 °C, in O_2 and a vacuum, respectively.

The FWHM when using an electron beam as the excitation source was observed as almost the same for powder and thin films, of about 102 nm, which was a much broader emission band if compared with the PL emission band of about 68 nm. This difference between PL and CL may be due to the large energy difference as well as the different mechanisms for the excitation. When using electron-beam irradiation during CL the energy was much higher than the PL source as mentioned and explained in section 7.4.2.

Figure 8.7 (a and b) represent the chromaticity coordinates of the PL and CL (5 keV) spectra for the $Sr_{1-x}O:Bi_{x=0.002}$ powder and thin films, which were determined using the Commission Internationale de I'Eclairage (CIE) coordinate system [39]. The calculated

chromaticity coordinates for powder and the optimum sample deposited in O_2 and vacuum, respectively, are tabulated in Table 8.2. The PL emission color coordinates for the films grown at a substrate temperature of 200 °C in O_2 and 50 °C in a vacuum seem to be close to the color coordinates of the powder. The CL emission color coordinates for the films grown at a substrate temperature of 200 °C in O_2 also seem to be close to the color coordinates of the powder, but there was the shifting toward the orange color in the CL emission band in the sample grown at a substrate temperature at 50 °C in vacuum, which was attributed to the formation of Bi^{2+} when excited by an electron beam.

Table 8.2. The CIE coordinates (X, Y) of $Sr_{1-x}O:Bi_{x=0.002}$ powder and thin films.

Excitation source	**PL CIE coordinates**		**CL CIE coordinates**	
	X	**Y**	**X**	**Y**
Powder	0.15	0.06	0.19	0.17
Thin film at 200 °C in O_2	0.16	0.06	0.17	0.18
Thin film at 50 °C in vacuum	0.16	0.06	0.29	0.29

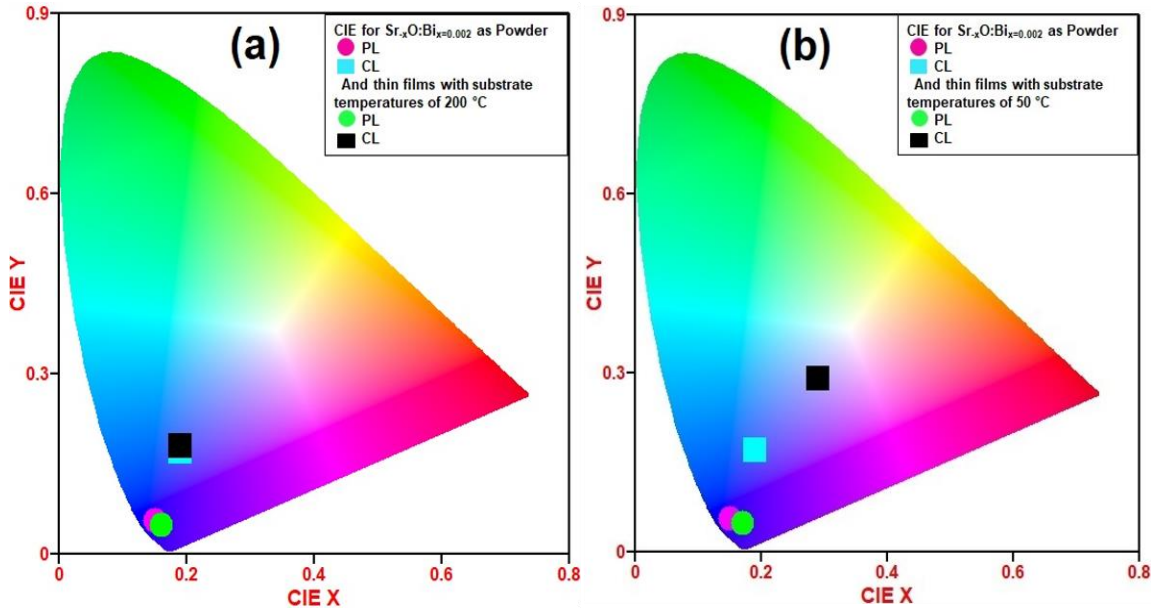

Figure 8.7. The calculated chromaticity coordinates for the $Sr_{1-x}O:Bi_{x=0.002}$ as powder and thin films with substrate temperatures of (a) 200 °C in O_2 and (b) 50 °C in vacuum, on the basis of their PL and CL data.

8.3.6 ToF SIMS analysis

In order to investigate the elemental distribution with depth across the film thickness and interfaces, the ToF-SIMS technique was applied. A depth profile of a thin film on a substrate typically has three distinct sections: the initial transient region; the steady state region of the film; and the layer/Si substrate interface [40].

Figure.8.8(a and b) show the negative mode secondary ions ToF-SIMS mass spectra of the optimum sample deposited in O_2 and vacuum, respectively. All the ionic and molecular species contained in the materials were present, including C^- and Cl^-, which were ascribed to contaminants from the atmosphere and sample holders. Only a small amount of Bi (not shown) was observed in the background of the spectra, where it is expected to be detected at 209 amu [41]. Bi might also come from the primary ion beam and are therefore not shown. All the atomic and molecules species detected in the negative mode were similar in both samples and are shown in table 8.3.

Table 8.3: Atomic/molecular ions and their atomic mass units

Atomic/molecular ions	**Mass/u**
C^-	12
O^-	16
OH^-	17
Si^-	28
Cl^-	35.4
SiO^-	43
$SiOH^-$	45
SrO^-	103.6

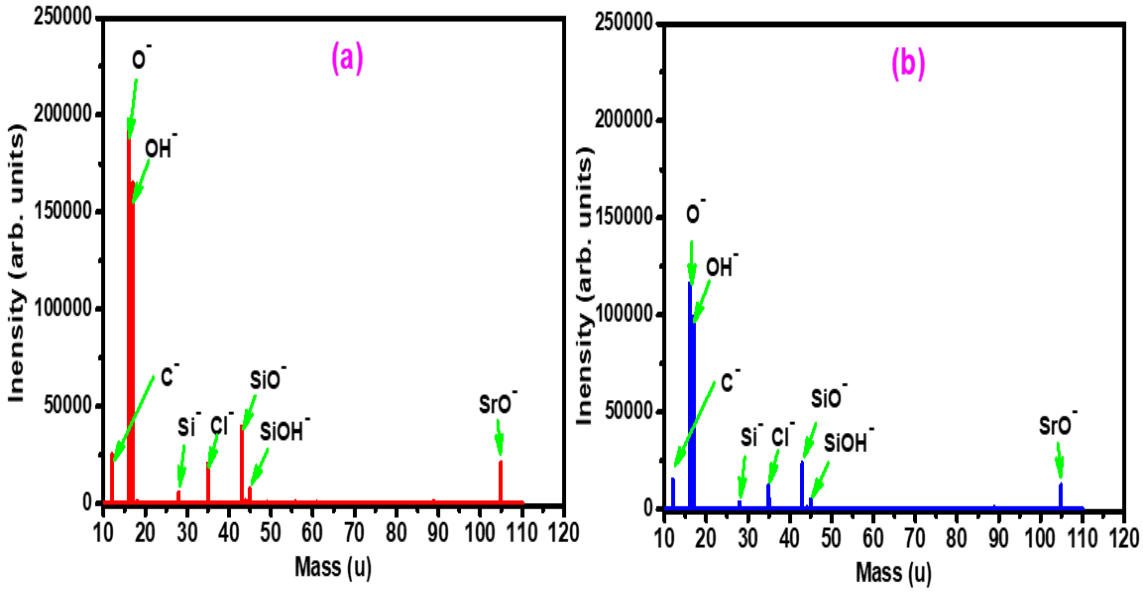

Figure 8.8. ToF-SIMS mass spectra of SrO:Bi phosphors for negative ions analysis of thin films with substrate temperatures of (a) 200 °C in O_2 and (b) 50 °C in vacuum.

The ToF-SIMS depth profiles for the SrO:Bi was established by etching a selected area on the thin film, which was subjected to continuous Cs^+ ion sputtering for the negative modes, as shown in figure. 8.9(a – j). The resulting depth profiles represent the distribution of the C^-, O^-, Si^-, Cl^- and SrO^- ions with sputtering depth. The rest of the profiles look similar, except for a slight thickness variation in the profiles. The thickness of the layers deposited in O_2 figure 8.9(a and b) at 50 and 100 °C, are thinner than the other samples deposited at higher temperatures. As the sample was sputtered deeper into the thin film, the elements concentration reduced significantly, after reaching the silicon substrate at 400 s. In the 200 and 350 °C samples, figure 8.8(c and d), the SrO layer remained relatively stable up to around 650 s, then reduced after reaching the silicon substrate. The sample at 500 °C, figure 8.9(e), seems to be slightly thicker than the others.

From these results, the samples deposited in O_2 became thicker when increasing the substrate temperature. These results are consistent with the XRD, in which the crystallinity increased with an increase in the substrate temperature see figure 8.1(a). In the samples deposited in vacuum figure 8.9(f - j) at different substrate temperatures, the profiles look similar, except for again some thickness variations on the different parts. The difference in

films depth profiling can be attributed to the high degree of diffusion of elements present in the phosphor material and also due to interdiffusion of the substrate and the phosphor material, leaving uneven films that varied in thickness and concentration.

Strangely and un-expectedly O^- was still present during sputtering into the Si substrate. The O^- intensity remained relatively stable during the sputtering for all samples. In order to test the reason why the O^- remained relatively stable during the sputtering, a closer look was given to the O^- peak. It was observed that the O^- peak consisted of a double peak due to surface topographical features [42] on the surface as seen in the SEM images. Different heights on the surface will led to different peak shifts when simultaneously measured. This make the data interpretation very difficult and a much more in depth study is needed, which will be done in the future. Quantitative chemical characterization of surfaces with topography by ToF-SIMS remains a significant challenge due to the lack of systematic and validated measurement methods. This was, however, not the purpose of this study. As a start the width of the peak area used to subtract the O^- from the data and measuring the OH^- peak, the depth profile of the 50 °C in O_2 was constructed, as presented in figure 8.10. Clearly, the oxygen was only present in the SrO layer and not in the Si. A further solution to the problem would also be looking at certain regions of the selected areas of sputtering to prevent surface topographical effects. Clearly a study on its own for future reference.

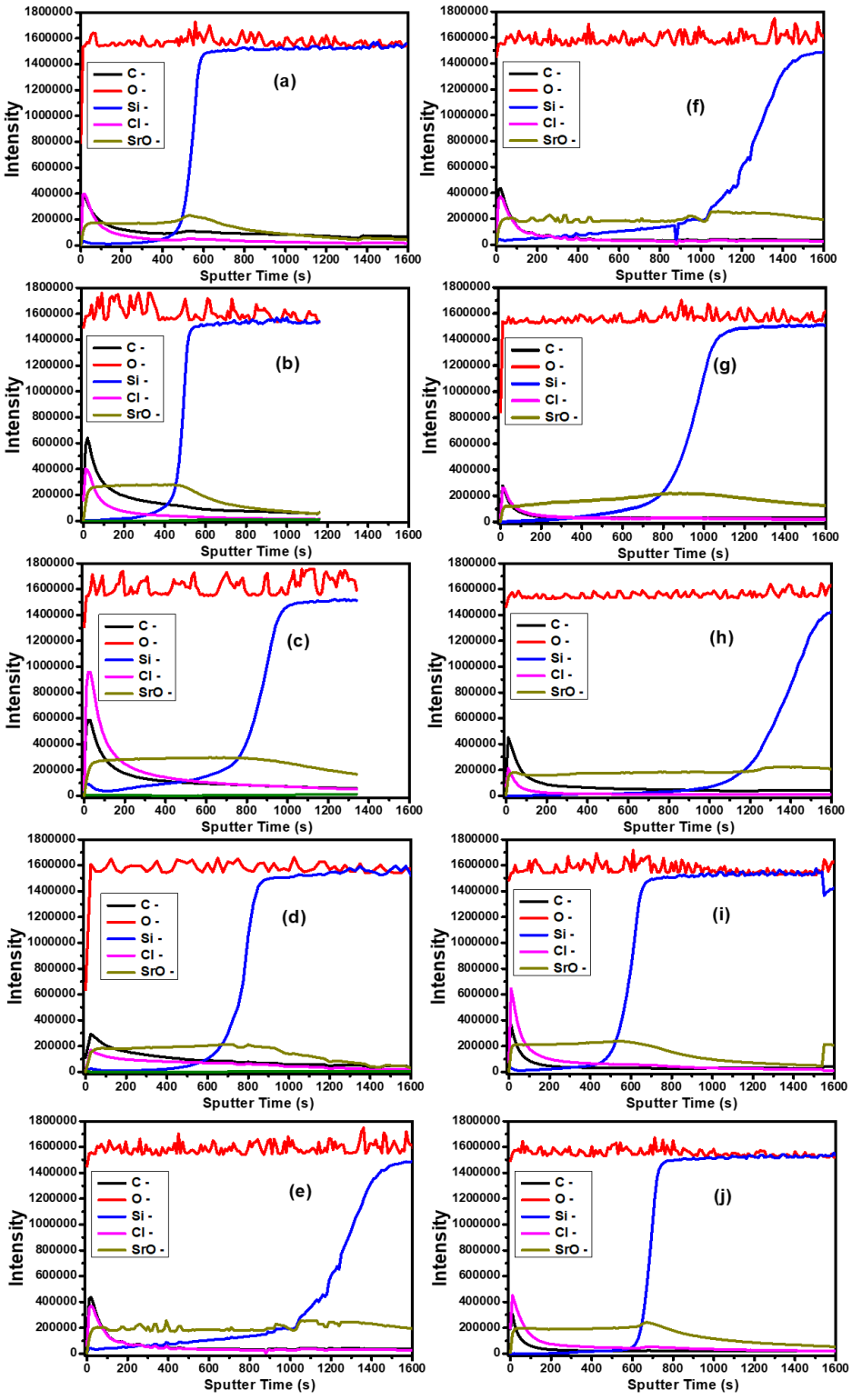

Figure 8.9. The negative mode ToF-SIMS depth profiles of the $Sr_{-x}O:Bi_{x=0.002}$ films deposited at the different substrate temperatures of 50 °C, 100 °C, 200 °C, 350 °C and 500 °C, respectively, (a - e) in O_2 (f - j) in a vacuum.

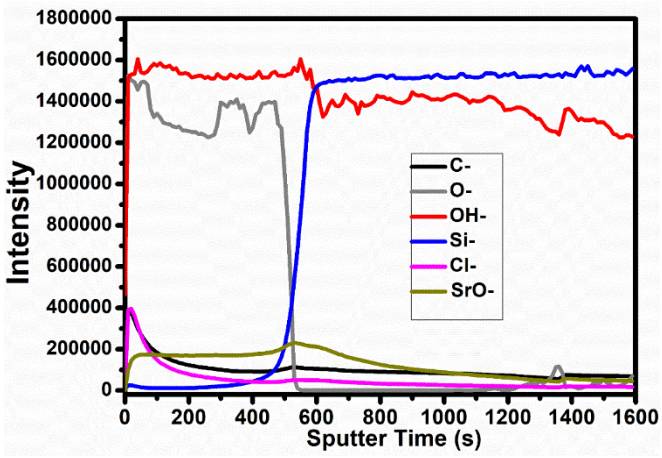

Figure 8.10. The negative mode ToF-SIMS depth profiles of the $Sr_{-x}O:Bi_{x=0.002}$ films deposited at substrate temperature of 50 °C in O_2 with a different selected measured peak area of O^- .

In the ToF-SIMS a 100×100 μm^2 area was analyzed, while a 300×300 μm^2 area was rastered with Cs^+. These 3D chemical images for the thin films were generated by sputtering layer by layer through the thin film while measuring the emitted fragments. Figure 8.11(a - e) in O_2 and (f - j) in vacuum show the ToF-SIMS 3D images for the overlay of the measured Si^- (blue), SrO^- (green) and O^- (red) of the SrO:Bi^{3+} samples. Please note that the depth profiles in figure 8.11 are the average profiles of the same volumes as used in the 3D images. The Si present in the SrO layer points towards Si diffusion during deposition. These images show evidence that the SrO:Bi samples deposited by PLD in O_2 and vacuum contained Si, which diffused from the Si substrate into the thin film layer, especially at the higher temperatures. ToF-SIMS provided artificial topographic features in the 3D depth profiles of the SrO:Bi films due to the agglomerated particles on the Si substrate's surface. Yousif et al. [42] showed that the presence of various types of particles on the surface of the PLD thin films as well as the differences in the film structure, played an important role to induce artificial topographical effects on $Y_3(Al,Ga)_5O_{12}:Tb^{3+}$ PLD thin films deposited on Si substrates measured by ToF-SIMS. Analysis of the 3D images shows big agglomerated particles on the surface of the Si substrate that appear embedded in the substrate and the substrate appears to be on the same level as the particles. This phenomenon is due to the artificial topographic effects, which are attributed to the experimental setup of the ToF-SIMS system.

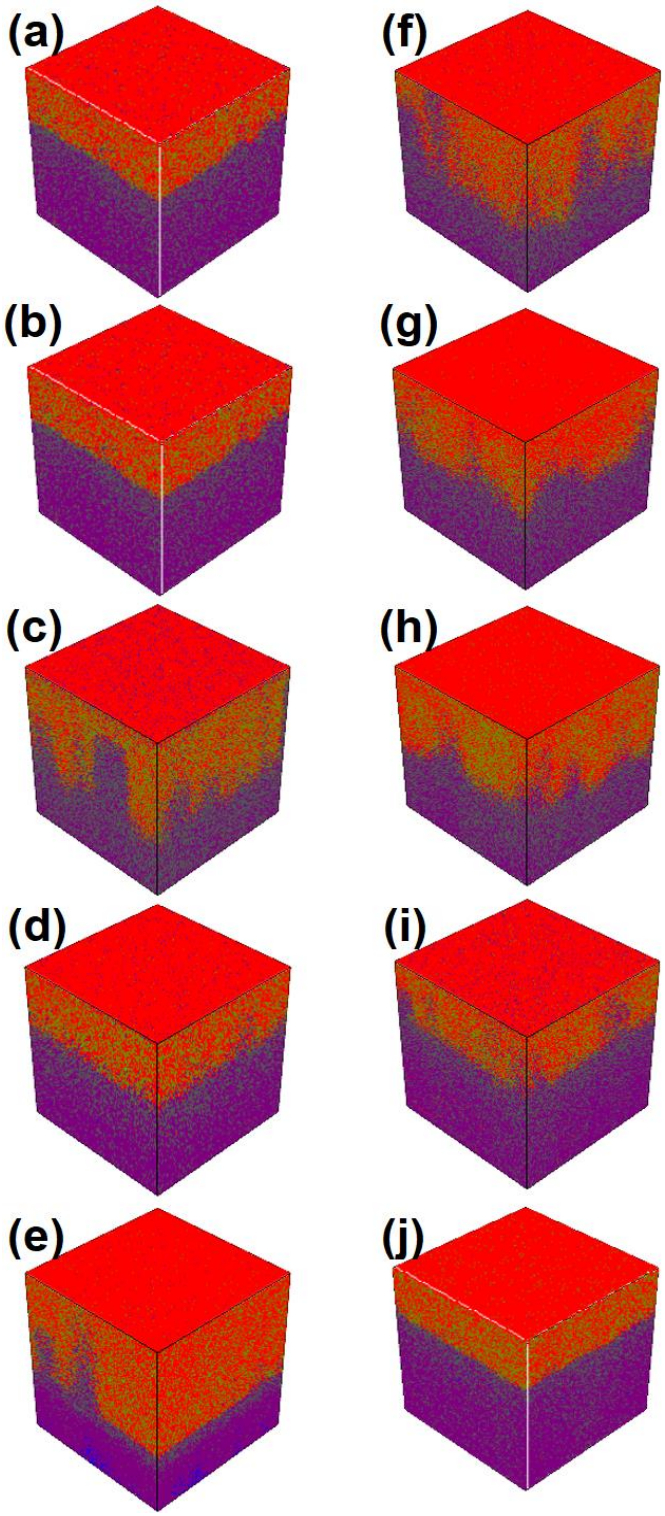

Figure 8.11. ToF-SIMS 3D images for the overlay of the $Sr_{1-x}O:Bi_{x=0.002}$ films (Si^- (blue), SrO^- (green) and O^- (red)) deposited at the different substrate temperatures of 50 °C, 100 °C, 200 °C, 350 °C and 500 °C, respectively, (a - e) in O_2 (f - j) in a vacuum.

8.4 Conclusion

$Sr_{1-x}O:Bi_{x=0.002}$ phosphor thin films were successfully fabricated in an O_2 and vacuum working atmosphere on Si (100) substrates by the PLD method. The films were deposited at different substrate temperatures. The structure, composition, morphology, PL and CL properties were investigated. The XRD of the films deposited in O_2 showed that the crystallinity increased with an increase in the substrate temperature, changing from an amorphous to a cubic structure. All films deposited in vacuum showed the amorphous structure. There was a small blue shift in the maximum peak position of the PL for the powder and the thin films. Si was responsible for a change in the surrounding structure of the Bi^{3+} ions. The increased crystallinity of the films deposited in O_2 resulted first in an increase in PL emission intensities, and then a decrease for the highest substrate temperatures due to a loss in Bi^{3+} due to volatile species. The PL intensity decreased with the increase of the substrate temperatures for the films deposited in vacuum due to defects in the film's structure and nonstoichiometry of the film's composition has became more as the substrate temperature increased. The optimum substrate temperature for maximum PL and CL intensity of the thin films deposited in O_2 and vacuum were 200 °C and 50 °C, respectively. From the XRD results, the films deposited at the substrate temperature of 500 °C in O_2 have the best crystallinity, but the film deposited at a substrate temperature of 200 °C has good emission intensity and good morphology. Therefore, in our case, the balance between the substrate temperature and the background gas pressure was obtained at the substrate temperature of 200 °C in O_2. The depth profiles for the samples deposited in the O_2 and vacuum at the different substrate temperatures, look similar, except for a slight thickness variation in the profiles and an increase in Si diffusion into the thin films at the higher substrate temperatures. ToF-SIMS provided artificial topographic features in the 3D depth profiles of the $SrO:Bi^{3+}$ films due to the agglomerated particles on the Si substrate's surface.

8.5 References

[1] A. C. V. D. Steen and L. T. F. Dijcks. The Luminescence Properties of Alkaline-Earth Oxides Activated with $6s^2$ Ions. *Phys. Status Solidi (b).* **104(1)** (1981) 283–292. DOI: 10.1002/pssb.2221040130.

[2] N. Yamashita, S. Ikeda and S. Asano. Photoluminescence and excitation spectra of the SrO:Bi^{3+} phosphor. *Phys Lett A.* **121(2)** (1987) 94–96. DOI: 10.1016/0375-9601(87)90272-6.

[3] Fu. Jipeng, R. Pang, Y. Jia, W. Sun, J. Lihong, S. Zhang and C. Li. Intense red–green up-conversion emission and their mechanisms of SrO:Er^{3+}/Yb^{3+},Gd^{3+},Lu^{3+},Bi^{3+}. *J. Lumin.* **181,** (2017) 240–245. DOI: 10.1016/j.jlumin.2016.09.029.

[4] A. F. Ellervee. Luminescence of Pb^{2+} and Bi^{3+} Centres in Alkali-Earth Sulphides and Oxides. *Phys. Status Solidi (b).* **82(1)** (1977) 91–98. DOI: 10.1002/pssb.2220820107.

[5] G. S. Zavt and A. F. Ellervee. Pb^{2+} and Bi^{3+} impurity centres in alkali-earth oxides vibronic spectra, lattice dynamics, and electron-phonon interaction. *Phys. Status Solidi.* **94(2)** (1979) 757–768. DOI: 10.1002/pssb.2220940249.

[6] A. Yousif, R. M. Jafer, S. Som, M. M. Duvenhage, E. Coetsee and H. C. Swart. The effect of different annealing temperatures on the structure and luminescence properties of Y_2O_3:Bi^{3+} thin films fabricated by spin coating. *Appl Surf Sc*, **365**, (2016) 93–98. DOI:10.1016/j.apsusc.2016.01.013.

[7] K. Komatsu, M. Tanabe, I. Toda, S. Ohshio, H. Muramatsu and H. Saitoh. Synthesis of Strontium Oxide Whiskers with Preferential <111> Orientation by Atmospheric Chemical Vapor Deposition. *J. Mater. Sci.*, **5(2)** (2016) 50-55. DOI:10.5539/jmsr.v5n2p50.

[8] C. B. Zhang, L. Wielunski and B. G. Willis, Formation of strontium template on Si(1 0 0) by atomic layer deposition. *Appl Surf Sc.* **257**, (2011) 4826-4830. DOI:10.1016/j.apsusc.2010.12.098.

[9] O. Maksimov, V. D. Heydemann, P. Fisher, M. Skowronski and P. A. Salvador. Structural properties of SrO thin films grown by molecular beam epitaxy on $LaAlO_3$ substrates. *Appl Phys Lett*, **89(26)** (2006) 262903(1-3). DOI:10.1063/1.2424440.

[10] A. Yousif, H. C. Swart, O. M. Ntwaeaborwa and E. Coetsee. Conversion of $Y_3(Al,Ga)_5O_{12}$:Tb^{3+} to $Y_2Si_2O_7$:Tb^{3+} thin film by annealing at higher temperatures. *Appl Surf Sc*, **270**, (2013) 331–339. DOI:10.1016/j.apsusc.2013.01.025.

[11] A. Yousif, H. C. Swart and O. M. Ntwaeaborwa. Improved luminescence properties of pulsed laser deposited $Y_3(Al,Ga)_5O_{12}$:Tb thin films by post deposition annealing. *J. Lumin*, **143**, (2013) 201–206. DOI:10.1016/j.jlumin.2013.04.042.

[12] R. M. Jafer, H. C. Swart, A. Yousif and E. Coetsee. The effect of different substrate temperatures on the structure and luminescence properties of Y_2O_3:Bi^{3+} thin films. *Solid State Sci*, **53**, (2016) 30–36. DOI:10.1016/j.solidstatesciences.2016.01.005.

[13] V. Kumar, H. C. Swart, S. Som, V. Kumar, A. Yousif, A. Pandey and O. M. Ntwaeaborwa. The role of growth atmosphere on the structural and optical quality of defect-free ZnO films for strong ultraviolet emission. *Laser Phys.* **24(10)** (2014) 105704 (1-9). DOI:10.1088/1054-660x/24/10/105704.

[14] Y. Hu, X. Diao, C. Wang, W. Hao and T. Wang. Effects of heat treatment on properties of ITO films prepared by rf magnetron sputtering. *Vacuum.* **75(2)** (2004)183-188. DOI:10.1016/s0042-207x(04)00151-4.

[15] Y. Sato, M. Taketomo, N. Ito and Y. Shigesato. Study on early stages of film growth for Sn doped In_2O_3 films deposited at various substrate temperatures. *Thin Solid Films*, **516(17)** (2008) 5868–5871. DOI:10.1016/j.tsf.2007.10.044.

[16] M. Liu, B. Y. Man, C. S. Xue, H. Z. Zhuang, H. C. Zhu, X. Q. Wei and C. S. Chen. The effect of nitrogen pressure on the two-step method deposition of GaN films. *Appl Phys A*. **85(1)** (2006) 83–86. DOI:10.1007/s00339-006-3656-3.

[17] S. N. Ogugua, R. L. Nyenge, P. T. Sechogela, H. C. Swart and O. M. Ntwaeaborwa. Influence of deposition atmosphere and substrate temperature on the structure, morphology, and photoluminescence of pulsed laser deposited $La_{0.5}Gd_{1.5}SiO_5:Dy^{3+}$. *J. Vac. Sci. Technol.* **34(2)** (2016) 021520 (1-12). DOI:10.1116/1.4942502.

[18] R. E. (Ted) Kroon. Nanoscience and the Scherrer equation versus the "Scherrer–Gottingen equation." *South African Journal of Science*. **109(5/6)**, (2013) Art. #a0019 (2 pages). DOI:10.1590/sajs.2013/a0019.

[19] V. Vrakatseli, A. Kalarakis, A. Kalampounias, E. Amanatides and D. Mataras. Glancing Angle Deposition Effect on Structure and Light-Induced Wettability of RF-Sputtered TiO_2 Thin Films. *Micromachines*. **9(8)** (2018) 389 (3-14). DOI:10.3390/mi9080389.

[20] P. Ju, P. Wang, B. Li, H. Fan, S. Ai, D. Zhang and Y. Wang. A novel calcined $Bi_2WO_6/BiVO_4$ heterojunction photocatalyst with highly enhanced photocatalytic activity. *Chem Eng J*. **236**, (2014) 430–437. DOI:10.1016/j.cej.2013.10.001.

[21] E. Hasabeldaim, O. M. Ntwaeaborwa, R. E. Kroon, E. Coetsee and H. C. Swart. Effect of substrate temperature and post annealing temperature on ZnO:Zn PLD thin film properties. *Opt. Mater. (Amst)*. **74**, (2017) 139–149. DOI: 10.1016/j.optmat.2017.03.027.

[22] A. Yousif, H. C. Swart, J. J. Terblans, R. M. Jafer, V. Kumar, R. E. Kroon and M. M. Duvenhage. Structural and morphology analysis of annealed $Y_3(Al,Ga)_5O_{12}$:Tb thin films synthesized by pulsed laser deposition. *Appl Surf Sc*. **305**, (2014) 732–739. DOI:10.1016/j.apsusc.2014.03.185.

[23] H. Malkas, S. Kaya and E. Yilmaz. Effects of Substrate Temperature on the Microstructure and Morphology of CdZnTe Thin Films. *J. Electron. Mater.*. **43(11)** (2014) 4011–4017. DOI:10.1007/s11664-014-3371-3.

[24] S.Y. Yang, B.Y. Man, M. Liu, C.S. Chen, X.G. Gao, C.C. Wang and B. Hu. Effect of substrate temperature on the morphology, structural and optical properties of $Zn_{1-x}Co_xO$ thin films. *Appl Surf Sc*. **257(9)** (2011) 3856–3860. DOI:10.1016/j.apsusc.2010.11.057.

[25] E. Coetsee, J. J. Terblans, H. C. Swart, J. M. Fitz-Gerald and J. R. Botha. Luminescence of Y_2SiO_5:Ce Nanocrystalline Thin Films. *E-j. surf. sci. nanotechnol.* **7**, (2009) 369–374. DOI:10.1380/ejssnt.2009.369.

[26] J. McKittrick, C. F. Bacalski, G. A. Hirata, K. M. Hubbard, S. G. Pattillo, K. V. Salazar and M. Trkula. Characterization of Photoluminescent $(Y_{1-x}Eu_x)_2O_3$ Thin Films Prepared by Metallorganic Chemical Vapor Deposition. *J. Am. Ceram. Soc.*. **83(5)** (2004) 1241–1246. DOI:10.1111/j.1151-2916.2000.tb01361.x.

[27] D. Raoufi and L. Eftekhari. Crystallography and morphology dependence of In_2O_3:Sn thin films on deposition rate. *Surf Coat Tech*. **274**, (2015) 44–50. DOI:10.1016/j.surfcoat.2015.04.034.

[28] E. Hasabeldaim, O. M. Ntwaeaborwa, R. E. Kroon, V. Craciun, E. Coetsee and H. C. Swart, Surface characterization and cathodoluminescence degradation of ZnO thin films, *Appl. Surf. Sci.* **(424)** (2017) 412–420. DOI:10.1016/j.apsusc.2016.11.178.

[29] B. Gündüz. Effects of molarity and solvents on the optical properties of the solutions of tris[4-(5-dicyanomethylidenemethyl-2-thienyl)phenyl]amine (TDCV-TPA) and structural properties of its film. *Optic Mat*. **36(2)** (2013) 425–436. DOI:10.1016/j.optmat.2013.10.005.

[30] R. H. P. Awater and P. Dorenbos. The Bi^{3+} 6s and 6p electron binding energies in relation to the chemical environment of inorganic compounds. *J. Lumin.* **184,** (2017) 221–231. DOI: 10.1016/j.jlumin.2016.12.021.

[31] Fu. Jipeng, R. Pang, L. Jiang, Y. Jia, W. Sun, S. Zhang and C. Li. A novel dichromic self-referencing optical probe SrO:Bi^{3+},Eu^{3+} for temperature spatially and temporally imaging. *Dalton Trans.* **45(34)** (2016) 13317–13323. DOI: 10.1039/c6dt01552b.

[32] A. Yousif, R. M. Jafer, S. Som, M. M. Duvenhage, E. Coetsee and H. C. Swart. Ultra-broadband luminescent from a Bi-doped CaO matrix. *RSC Adv*. **5(67)** (2015) 54115–54122. DOI: 10.1039/c5ra09246a.

[33] T. Minami, T. Miyata, K. Ueda, S. Matsui and H. Fukada. PL and EL Characteristics in New Blue Emitting La_2O_3:Bi Phosphor Thin Films. *ECS Transactions*. **16 (30)** (2009) 39-45. DOI:10.1149/1.3106670.

[34] M. J. Simpson, B. Doughty, B. Yang, K. Xiao, and Y.-Z. Ma. Imaging Electronic Trap States in Perovskite Thin Films with Combined Fluorescence and Femtosecond Transient Absorption Microscopy. *J Phys Chem Lett*. **7(9)** (2016) 1725–1731. DOI:10.1021/acs.jpclett.6b00715.

[35] S. T. S. Dlamini, H. C. Swart, J. J. Terblans and O. M. Ntwaeaborwa. The effect of different gas atmospheres on the structure, morphology and photoluminescence properties of pulsed laser deposited $Y_3(Al,Ga)_5O_{12}$:Ce^{3+} nano thin films. *Solid State Sc*. **23**, (2013) 65–71. DOI:10.1016/j.solidstatesciences.2013.06.009.

[36] M. Stock and P. Molian. Femtosecond pulsed laser deposition of amorphous, ultrahard boride thin films. *JVST A: J. Vac, Surf Films*. **22(3)** (2004) 670-675. DOI:10.1116/1.1722714.

[37] C. Guillén and J. Herrero. Structure. Optical and electrical properties of indium tin oxide thin films prepared by sputtering at room temperature and annealed in air or nitrogen. *J Appl Phy*. **101(7)** (2007) 073514. DOI:10.1063/1.2715539.

[38] X. Li, S. Sundaram, P. Disseix, G. Le Gac, S. Bouchoule, G. Patriarche and A. Ougazzaden. AlGaN-based MQWs grown on a thick relaxed AlGaN buffer on AlN templates emitting at 285 nm. *Optic M Exp*. **5(2)** (2015) 380. DOI:10.1364/ome.5.000380.

[39] R. M. Jafer, A. Yousif, Vinod Kumar, Trilok Kumar Pathak, L.P. Purohit, H.C. Swart and E. Coetsee. Comparison of Y_2O_3:Bi^{3+} phosphor thin films fabricated by the spin coating and radio frequency magnetron techniques. *Phys. B Condens. Matter.* **497,** (2016) 39–44. DOI: 10.1016/j.physb.2016.06.007.

[40] A. Balakrishna, M. M. Duvenhage, and H. C. Swart. Surface and chemical characterization of ZnO:Eu^{3+}/Yb^{3+} spin coated thin films using SEM-CL and TOF-SIMS. *Vacuum*, **157** (2018) 376–383. DOI:10.1016/j.vacuum.2018.09.009.

[41] J. R. De Laeter, J. K. Böhlke, P. De Bièvre, H. Hidaka, H. S. Peiser, K. J. R. Rosman and P. D. P. Taylor. Atomic Weights of the Elements: Review 2000, *Pure Appl. Chem*. **75**, (2003) 683. DOI:10.1351/pac200375060683.

[42] A. Yousif, R. M. Jafer, J. J. Terblans, O. M. Ntwaeaborwa, M. M. Duvenhage, Vinod Kumar, H. C. Swart, TOF SIMS induced artificial topographical effects on the $Y_2(Al,Ga)_5O_{12}:Tb^{3+}$ thin films deposited on Si substrates by the pulsed laser deposition technique, *Appl Surf Sc*, **313** (2014) 524–531. :DOI: 10.1016/j.apsusc.2014.06.016

Chapter 9: Conclusion

The general conclusion of this research study is summarized in this chapter. Some future research suggestions are included as well.

9.1 Summary

Synthesis and characterization of bismuth-doped strontium oxide powder and thin films were successfully investigated for possible use of efficient applications in the fields of lighting and displays.

The SrO:Bi powder was successfully synthesized by the sol-gel combustion method with different bismuth concentration and various annealing temperatures. The XRD patterns showed that the sol-gel combustion method produced a cubic phase structure of SrO after high temperature annealing that ranged between 1100 °C up to 1200 °C, although below 1100 °C strontium hydroxide peaks were also present. The band gap was determined from reflectance measurements to be 5.7 eV for the SrO host. The PL and CL results showed that the phosphor had a broad band of blue fluorescence emission which extended from 400 to 500 nm, centered at 445 nm due to $^3P_1 \rightarrow {}^1S_0$, and $^3P_0 \rightarrow {}^1S_0$ electronic transitions. The excitation spectrum of SrO:Bi^{3+} shows a strong broad band centered at 360 nm (3.4 eV), which corresponds to the $^1S_0 \rightarrow {}^3P_1$ transition and a second excitation band at 260 nm (4.7 eV), it was considered a result of the C band absorption, or a combination of C-band and MMCT absorption.

The optimum Bi^{3+} concentration for the maximum PL intensity was found to be at 0.2 mol%, while for higher Bi^{3+} concentrations the PL intensity decreased due to concentration quenching. The optimum annealing temperature for maximum PL and CL intensity of the $Sr_{1-x}O:Bi_x$ was 1100 °C. The intensity first increased due to the removal of hydroxides with an increase in temperature up to 1100 °C and then decreased for the

highest annealing temperature of 1200 °C. $Sr_{1-x}O:Bi_x$ exhibited broad blue PL and CL emission.

The luminescence properties of the optimum sample $Sr_{1-x}O:Bi_{x=0.002}$ annealed at 1100 °C were investigated by the different excitation source. The CL of the $Sr_{1-x}O:Bi_{x=0.002}$ has been investigated as a function of the accelerating voltage and beam current. $Sr_{1-x}O:Bi_x$ exhibited broad blue PL and CL emission. The CL intensity reduced slightly more and at a higher rate in the O_2 back-filled environment than in vacuum during the degradation studies, due to the reaction of O_2 with the adventitious C at a higher rate to form volatile compounds on the surface of the irradiated sample. A new non-luminescent surface layer formed after the removal of C, which caused the CL intensity to decrease slightly more than in the case of the vacuum. The degradation, however, was only in the order of around 20%. Except for the initial degradation, the blue emitting Bi doped SrO powder was found to be stable under electron bombardment in both the base vacuum and back-filled O_2 environments. The high-resolution XPS results for the $Sr_{1-x}O:Bi_{x=0.002}$ sample indicated the presence of the major components Sr and O of this material. The results indicated the SrO, a basic oxide, strongly chemisorb carbon dioxide and water vapor from its environment and appear on the surface as contamination. All surface contaminated elements were completely removed after degradation.

$Sr_{1-x}O:Bi_{x=0.002}$ thin films phosphors were prepared on Si(100) substrates by using sol-gel spin-coating and PLD techniques. All spin coating thin films samples, XRD showed the thin film had a strong (111) preferential orientation on the cubic phase and (222) peak appear in spin coating sample with increasing the number of layers after deposited 30 layers. The crystallite size increase with increasing annealing temperatures. Thin films were then successfully fabricated by PLD in vacuum or an O_2 working atmosphere on Si (100) substrates using different types of laser. Firstly, the films were deposited in O_2 at 300 °C substrate temperature using different types of excimer lasers i.e. a KrF laser (248 nm) with energy 300 mJ/pulse or a ArF laser (193 nm) with energy 150 mJ/pulse. XRD showed the thin films had a strong (111) preferential orientation on the cubic phase.

Other thin films growth by PLD technique deposition in the presence of a base pressure and oxygen (O_2) gas on Si (100) substrates at different substrate temperatures using a

Nd:YAG laser (266 nm) with energy 33.3 mJ/pulse. The structure, composition, morphology, the PL and CL properties and depth profiling were investigated. The XRD of the films deposited in O_2 showed that the crystallinity increased with an increase in the substrate temperature, changing from amorphous to a cubic structure. At the highest temperature of 500 °C, the 111 and 200 SrO peaks were almost the same height, as in the powder. However, for 350 °C and 200 °C, the 200 peak was much smaller, which suggests some preferential orientation for films prepared at lower substrate temperatures. All films deposited in vacuum showed the amorphous structure.

PL spectra for all thin films deposited by spin coating and PLD showed blue emissions at 427 nm with small blue shifted compare with the powder, which attributed to Si diffusion on the structure. Si was responsible for a change in the surrounding structure of the Bi^{3+} ions. There were increase crystallinity of the films deposited in O_2 resulted in an increase in PL emission intensities and then decreased for the highest substrate temperatures due to a consequent loss in Bi^{3+} due to volatile species as a result of the increased substrate temperature. The optimum substrate temperature for maximum PL and CL intensity of the $Sr_{1-x}O:Bi_{x=0.002}$ thin films deposited in O_2 and vacuum were 200 °C and 50 °C, respectively. Spin coating thin films gives a smoother surface roughness compared with deposition by PLD. All surface roughness results indicate there are good optical surfaces and that the statistical relationships for the surface roughness are applicable. The depth profiles for the PLD samples deposited in O_2 and vacuum at the different substrate temperatures were investigated, they look similar, except for a slight thickness variation in the profiles and an increase in Si diffusion into the thin films at the higher substrate temperatures. The 3D depth profiles images show evidence that the SrO:Bi samples deposited by PLD in O_2 and vacuum contained Si, which diffused from the Si substrate into the thin film layer, especially at the higher temperatures. ToF SIMS provided artificial topographic features in the 3D depth profiles of the SrO:Bi films due to the agglomerated particles on the Si substrate's surface.

From results, the balance between the substrate temperature and the background gas pressure was attained at the substrate temperature of 200 °C in O_2.

The sol-gel spin-coating method is effective for growing the thin films which capable of providing homogeneous films at the molecular level, excellent control of film composition and low crystallization temperature. Thus avoid the loss of certain elements of high vapor pressure during the PLD process. The luminescent results suggested that the PLD technique might be a suitable technique to fabricate SrO:Bi films. The PLD is a good technique for synthesizing of the thin films with the ability to transfer the material stoichiometry from a multi-component ablation target to a growing film at lower substrate temperatures, but a lot of parameters have to be used in order to get the best thin film and the correct stoichiometric transfer of the target material to the substrate during deposition.

The results of the SrO:Bi powder and thin films, make it an excellent candidate for efficient applications in the fields of lighting and displays.

9.2 Suggestions for future work

1- In this study, the intervals of 100 °C between measurements might be too large to pinpoint the exact optimized temperature and a more detailed study with smaller temperature intervals between 1000 and 1200 °C is needed before commercialization.

2- Study of the energy transfer between the Bi and lanthanides on the SrO host by co-doped different lanthanides elements.

3- It is well known that the thin films phosphors have more advantages than powders, as a result, our future suggestion prepare more SrO:Bi thin films by spin coating different parameters such as various concentration of Bi, spin speed, liquid viscosity, number of layersand time of annealing. Also in order to obtain the optimized parameters of SrO:Bi PLD thin films, the influence of substrate temperature, the numbers of pulses, a distance between the substrate to target and laser and etc, need to be studied.

4- Thin films of SrO:Bi can be prepared by other preparation techniques and the effect of annealing can be investigated and compared with the results mentioned earlier.

5- From our analysis, the stability for SrO:Bi powder was studied under electron beam irradiation, thus further studies can be done by investigating the CL stability of the synthesized SrO:Bi thin films concentrations during prolonged electron bombardment.

9.3 Research presentations and publications

9.3.1 Presentation at conferences/Workshops

- 10th African Laser Centre Student Workshop (30 Nov – 2 Dec 2017, University of Stellenbosch, Zevenwacht Wine Estate, Stellenbosch, Western Cape, South Africa).
- 63rd Annual Conference of the South African Institute of Physics, (25 - 29 June 2018 University of the Free State, Bloemfontein).

9.3.2 List of publications include

- M. H. M. Abdelrehman, R. E. Kroon, A. Yousif, H. A. A. Seed Ahmed and H. C. Swart. Luminescence properties and cathodoluminescence degradation of Bi doped SrO powder. *J. Vac. Sci. Technol. B* **37** (2019) 011206. DOI: 10.1116/1.5075492.
- M. H. M. Abdelrehman, V. Craciun, R. E. Kroon, A. Yousif, H. A. A. Seed Ahmed and H. C. Swart. Comparison of SrO:Bi phosphor thin films fabricated by spin coating and pulsed laser deposition, (in preparation, January 2019).
- M. H. M. Abdelrehman, R. E. Kroon, A. Yousif, H. A. A. Seed Ahmed and H. C. Swart. Effect of background atmosphere and substrate temperature on SrO:Bi thin films produced using pulsed laser deposition, (in preparation, January 2019).